FREEZE CASTING OF HIERARCHICALLY STRUCTURED HIGHLY POROUS γ-Al_2O_3 MONOLITHS

Hermina Hudelja

Doctoral Dissertation
Jožef Stefan International Postgraduate School
Ljubljana, Slovenia

Supervisor: Assoc. Prof. Dr. Andraž Kocjan, Jožef Stefan International Postgraduate School and Jožef Stefan Institute, 1000 Ljubljana, Slovenia

Evaluation Board:
Prof. Dr. Danjela Kuščer Hrovatin, Chair, Jožef Stefan International Postgraduate School and Jožef Stefan Institute, 1000 Ljubljana, Slovenia
Asst. Prof. Dr. Boštjan Genorio, Member, Faculty of Chemistry and Chemical Technology, University of Ljubljana, 1000 Ljubljana, Slovenia
Dr. Bernd Wicklein, Member, Instituto de Ciencia de Materiales de Madrid, Consejo Superior de Investigaciones Científicas, Madrid, Spain

MEDNARODNA PODIPLOMSKA ŠOLA JOŽEFA STEFANA
JOŽEF STEFAN INTERNATIONAL POSTGRADUATE SCHOOL

Hermina Hudelja

FREEZE CASTING OF HIERARCHICALLY STRUCTURED HIGHLY POROUS γ-Al_2O_3 MONOLITHS

Doctoral Dissertation

KONSOLIDACIJA HIERARHIČNO STRUKTURIRANIH VISOKOPOROZNIH MONOLITOV IZ γ-Al_2O_3 S KONTROLIRANIM ZAMRZOVANJEM

Doktorska disertacija

Supervisor: Assoc. Prof. Dr. Andraž Kocjan

Ljubljana, Slovenia, December, 2021

"We all have dreams. But in order to make dreams come into reality, it takes an awful lot of determination, dedication, self-discipline, and effort."

- JESSE OWENS -

This thesis is dedicated to my parents and sister for their support and unconditional love.

Acknowledgments

"No duty is more urgent
than giving thanks."

- JAMES ALLEN -

First and foremost, I would like to thank Asst. Prof. Dr. Andraž Kocjan, who has not only been my mentor but also my friend. Thank you for all the help, immense patience and most importantly for providing me a relaxed and as non-stressful work environment as possible. You have always found time when I needed help, advice or just some mental support and encouragement. Thank you for believing in me, giving me all the opportunities to improve myself and for sharing all of your knowledge and expertise.

When unpredicted challenges occurred Prof. Dr. Danjela Kuščer was always available for valuable discussions and suggestions regarding my experiments or doctoral thesis. Thank you for all the advice and for encouraging me when I lost inspiration and sight of my goals. It was Dr. Bernd Wicklein who supplied me with endless batches of cellulose nanofibers, and offered help, suggestions and constructive remarks while writing publications and the thesis. In addition, I would like to express my thanks to Asst. Prof. Dr. Boštjan Genorio for his help with SEM analyses and with preparation of this thesis.

My sister's contribution to this work must not be overlooked. Despite her own obligations she always found time to help me with the proof-reading of my dissertation.

I would also like to thank countless people who helped me with my experimental work. Firstly, to my sister Polona, without whose help I would still be in the laboratory preparing my samples. I would also like to thank Prof. Dr. Srečo Škapin for all the XRD and SEM analyses. A special thanks goes to Asst. Prof. Dr. Thomas Konegger for analyzing my samples for permeability and all the help with the interpretation of results. At the beginning of my second year I was given an opportunity to spend two months at Luleå University of Technology (LTU), for which I am very grateful to my supervisor for organizing the exchange and also to Prof. Dr. Farid Akhtar who mentored me during my stay and taught me a lot about freeze casting. A big thanks goes to the employees and students at LTU for making the experience an unforgettable one.

Dare Eterovič and Tomo Pustotnik deserve a big thank you for all the help with my experimental work. Gratitude should also be expressed to all the other coworkers at K7 who made the laboratories a pleasant working environment.

I am also taking this opportunity to express my gratitude to the Slovenian Research Agency (ARRS). This PhD would not have been possible without their funding for which I am very grateful. I am also grateful to the JECS Trust for funding the exchange with LTU and the Centre of Excellence NAMASTE for the use of laboratory equipment.

Lastly, the biggest thanks go to **my family, especially mami Meta, ati Miran and sister Polona** for always encouraging me to achieve any goal I set my mind on.

Abstract

Highly porous ceramic γ–Al_2O_3 monoliths are important in many applications, e.g., catalysis, thermal insulation and adsorption, yet they still have a lot of unrecognized potential. There is a lot of incentive to employ simple and green fabrication processes for the preparation of such porous ceramic materials; however, many challenges, especially the loss of mechanical strength and rigidity due to the increase of porosity, remain unresolved. The presented doctoral thesis was set to establish an unconventional but genuine fabrication approach of highly hierarchically macro-mesoporous alumina (HMMA) monoliths prepared from hierarchically assembled, mesoporous AlN-powder-hydrolysis-derived γ–Al_2O_3 (MA) powder of high surface area (~180 m^2/g) and mesoporosity (0.47 mL/g).

In the first part of the doctoral thesis, the objective was to prepare stable aqueous suspensions containing MA powder and to understand the suspensions' electrokinetic, rheological and sedimentation properties. The evaluation of rheological and sedimentation behaviour of aqueous suspensions containing MA particles dispersed with sodium polyacrylate (NaPAA) showed their proneness to undesired sedimentation and segregation and were as such not suitable for further green body consolidation. Thus, two mechanisms of stabilization were tested in order to delay or completely prevent sedimentation and segregation. The addition of divalent cations (Mg^{2+}, Ca^{2+}) or cellulose nanofibers (CNF) triggered the formation of interparticle association networks in the suspensions via bridging flocculation. While the former only partially prevented sedimentation, in the latter case, long-term stability lasting more than 12 weeks was achieved.

In the second part of the thesis the focus was shifted to the consolidation of as-prepared suspensions into structurally stable and highly-porous MA ceramic monoliths (or foams) with hierarchically distributed pores, high specific surface area, high permeability and low thermal conductivity. For this purpose, freeze casting (FC) was employed as a simple but powerful technique commonly used for fabrication of highly porous, columnar monolithic materials. By unidirectional freezing of aqueous suspension containing NaPAA-dispersed MA powder and CNF hierarchically macro-mesoporous alumina monoliths were successfully prepared. As-prepared, freeze-cast monoliths possessed relatively high surface areas (91–134 m^2/g) and high hierarchical porosity (93.1–99.2 %). Owing to the columnar porosity HMMA monoliths also exhibited high permeability (k_1 =2.39–4.31×10^{-12} m^2 and k_2 =2.23–9.15×10^{-7} m) and low, anisotropic thermal conductivity ranging from 0.039 W/m·K to 0.071 W/m·K that depended on the pore orientation. Despite their high porosity, monoliths still displayed remarkable Young's modulus and high compressive strengths (up to 52.0 kPa).

The bridging flocculation of suspensions with divalent cations did not provide sufficient stability after freeze casting. On the other hand, the CNF turned out to be a superior nanofiller not only in terms of making MA containing suspensions stable but also gave rise to remarkable compressive strengths and rigidness rarely seen in green bodies of such high porosity.

The results of the thesis also showed for the first time how freeze-casting of stable aqueous suspensions containing MA particles can be appropriate for fabrication of hierarchical and highly porous HMMA monoliths that are pivotal in advancing many prominent applications, such as Li-ion batteries separators and inductively heated catalyst reactors.

Povzetek

Visokoporozni keramični monoliti γ-Al_2O_3 so pomembni za številne aplikacije, ki vključujejo katalizo, toplotno izolacijo in adsorpcijo. Kljub temu imajo še vedno veliko neizkoriščenega potenciala. Za razvoj enostavnih in ekološko prijaznih postopkov namenjenih izdelavi poroznih materialov je bilo v preteklosti že veliko pobude. Številni izzivi, zlasti slabše mehanske lastnosti, ki so rezultat povečanja poroznosti v monolitu, ostajajo nerešeni.

Eden od namenov doktorske disertacije je bila vzpostavitev novega, nekonvencionalnega pristopa k izdelavi hierarhično poroznih monolitov iz aluminijevega oksida (HMMA) z visoko vsebnostjo mezo in makro por. Osnovna surovina za pripravo takih monolitov je bil hierarhično strukturiran mezoporozen prah γ-Al_2O_3 (MA). Prah, ki je imel visoko specifično površino (~180 m^2/g) in mezoporoznost (0.47 mL/g), je bil sintetiziran z izkoriščanjem hidrolize AlN prahu v razredčenih vodnih suspenzijah.

Cilj prvega dela doktorske disertacije je bila priprava stabilnih vodnih suspenzij, ki vsebujejo prah MA ter razumevanje elektrokinetičnih, reoloških in sedimentacijskih lastnosti pripravljenih suspenzij.

Karakterizacija reološkega in sedimentacijskega obnašanja vodnih suspenzij MA, ki so vsebovale dispergiran natrijev poliakrilat (NaPAA), je pokazala, da so le-te nagnjene k takojšnji sedimentaciji in segregaciji. Posledično niso bile primerne za nadaljnjo konsolidacijo in pripravo monolitov. Z namenom upočasnitve ali popolne preprečitve neželene sedimentacije in segregacije sta bila uporabljena dva mehanizma stabilizacije, in sicer dodajanje divalentnih kationov (Mg^{2+}, Ca^{2+}) in celuloznih nanovlaken (CNF). Dodatek omenjenih stabilizatorjev je sprožil nastanek meddelčnih asociacij v suspenzijah preko t. i. povezovalne ("bridging") flokulacije. Medtem ko je dodatek divalentnih kationov le delno preprečil posedanje, je dodatek CNF sprožil dolgotrajno stabilizacijo brez opazne sedimentacije tudi po več kot 12 tednih.

Poudarek drugega dela doktorske disertacije je bil na konsolidaciji ter oblikovanju suspenzij v visokoporozne in mehansko stabilne keramične monolite MA, ki jih lahko poimenujemo tudi pene. Pene so imele hierarhično porazdeljene pore, visoko specifično površino ter visoko permeabilnost. V ta namen je bilo uporabljeno kontrolirano zamrzovanje kot preprosta, a zmogljiva tehnika, ki se pogosto uporablja za izdelavo visokoporoznih, cevastih monolitnih materialov z odprto poroznostjo. Z usmerjenim zamrzovanjem vodnih suspenzij, ki so vsebovale NaPAA-dispergiran prah MA in CNF, so bili uspešno pripravljeni hierarhično makro-mezoporozni monoliti na osnovi aluminijevega oksida. Monoliti pripravljeni s kontroliranim zamrzovanjem so imeli relativno visoko specifično površino (91–134 m^2/g) in visoko hierarhično poroznost (93,1–99,2 %). Zaradi cevaste poroznosti so monoliti HMMA imeli tudi visoko permeabilnost (k_1 = 2,39–4,31×10^{-12} m^2 in k_2 = 2,23–9,15×10^{-7} m). Usmerjena visoka poroznost je hkrati botrovala k izredno nizki anizotropni toplotni prevodnosti v območju od 0,039 W/m · K do 0,071 W/m · K, odvisno od orientacije por. Kljub visoki poroznosti so imeli monoliti še vedno znaten modul elastičnosti in spodobne tlačne trdnosti (do 52,0 kPa).

Povezovalna flokulacija suspenzij, dosežena skozi dodatek divalentnih kationov, ni zagotovila zadostne stabilnosti kontrolirano zamrznjenim zelencem. Po drugi strani pa se

je izkazalo, da je CNF perspektivno nanopolnilo, ne le v smislu izboljšanja stabilnosti suspenzij, ki vsebujejo mikronske MA delce, temveč tudi botruje izjemni tlačni trdnosti in togosti, kakršne redko zasledimo pri visokoporoznih monolitih brez postopka sintranja.

Rezultati doktorske disertacije so tudi pokazali, da so lahko enostavne tehnike oblikovanja, kot je kontrolirano zamrzovanje stabilnih suspenzij prahov MA, primerne za izdelavo hierarhično visokoporoznih monolitov. Le-ti bi lahko postali ključni materiali pri izboljšavah številnih tehnoloških aplikacij, kot so na primer separatorji litij-ionskih baterij in indukcijsko ogrevani katalitski reaktorji.

Contents

List of Figures

List of Tables

Abbreviations

AFM	. . . Atomic force microscopy
ACS	. . . American chemical society
BET	. . . Brunauer, Emmett and Teller
BJH	. . . Barret, Joyner and Halenda
BNC	. . . Bacterial nanocellulose
CC	. . . Concentric cylinder
CCD	. . . Charge-coupled device
CIP	. . . Cold isostatic pressing
CNC	. . . Cellulose nanocrystals
CNF	. . . Cellulose nanofibers
CP	. . . Cone-plate
CT	. . . Computed tomography
d_{inner}	. . . Pore's inner diameter
$d_{meas.}$	. . . Pore's diameter measured with mercury intrusion porosimetry
dV/dlog(D)	. . . Differential pore volume distribution
DLVO	. . . Derjaguin, Landau, Verwey and Overbeek
EDL	. . . Electric double layer
e.g.	. . . Exempli gratia (for example)
FC	. . . Freeze-casting
FTIR	. . . Fourier transform infrared spectroscopy
i.e.	. . . Id est (that is)
IEP	. . . Isoelectric point
IR	. . . Infrared spectroscopy
et al.	. . . Et alii (and others)
etc.	. . . Et cetera (and other similar things)
HMMA	. . . Hierarchically macro-mesoporous alumina
MA	. . . Mesoporous (gamma) alumina
MIP	. . . Mercury intrusion porosimetry
MS	. . . Measuring system
NaPAA	. . . Sodium salt of polyacrylic acid
PAA	. . . Polyacrylic acid
pKa	. . . Negative base10 logarithm of the acid dissociation constant
PP	. . . Plate-plate
Per se	. . . By itself
PTFE	. . . Polytetrafluoroethylene

SEM	. . .	Scanning electron microscopy
SSA	. . .	Specific surface area
TEM	. . .	Transmission electron microscopy
TEMPO	. . .	2,2,6,6-tetramethylpiperidin-1-yl)oxyl
TPS	. . .	Transient plane source
V_{susp}	. . .	Volume of suspension
XRD	. . .	X-ray diffraction
YTZ	. . .	Yttria-stabilized zirconia
1.4NaPAA–MA	. . .	MA particles dispersed with 1.4 wt% of NaPAA
2.8NaPAA–MA	. . .	MA particles dispersed with 2.8 wt% of NaPAA
2D	. . .	Two-dimensional
3D	. . .	Three-dimensional
α–Al_2O_3	. . .	Alpha aluminum oxide
γ–Al_2O_3	. . .	Gamma aluminum oxide
μ–CT	. . .	Micro computed tomography

Symbols

A	. . . Surface area
A_N	. . . Molecular cross-sectional area
$A(\lambda)$	. . . Absorbance at a specific wavelength
c	. . . Concentration
C	. . . BET constant
c_p	. . . Specific heat capacity
d_{pore}	. . . Pore's diameter
$d_{avg.}$	. . . Average particle size
d_{10}	. . . Particle size below which 10 % of all the particle sizes lie
d_{50}	. . . Particle size below which 50 % of all the particle sizes lie
d_{90}	. . . Particle size below which 90 % of all the particle sizes lie
E	. . . Young's modulus or modulus of elasticity
F	. . . Force
G	. . . Potential energy
G_A	. . . Van der Walls potential energy
G_E	. . . Double layer potential energy
G_{el}	. . . Free potential energy of interaction
G_{max}	. . . Potential energy maximum
G_{min}	. . . Potential energy minimum
G_{mix}	. . . Potential energy of mixing interaction
$G_{primary}$	. . . Primary energy minimum
G_S	. . . Potential energy of steric interaction
G_{sec}	. . . Secondary energy minimum
G_T	. . . Total potential energy
G^*	. . . Shear modulus
G'	. . . Storage modulus
G''	. . . Loss modulus
I	. . . Intensity in the sample spectrum
I_0	. . . Intensity in the background spectrum
k	. . . Boltzmann constant
k_1	. . . Darcian permeability
k_2	. . . Non-Darcian permeability
Hg	. . . Mercury
l	. . . Length
L	. . . Thickness

m	. . . Mass
m_{MA}	. . . Mass of mesoporous alumina
m_{CNF}	. . . Mass of cellulose nanofibers
M^{2+}	. . . Divalent cation
M^{3+}	. . . Trivalent metal cation
Mg^{2+}	. . . Magnesium cation
$MgCl_2$	. . . Magnesium chloride
N_A	. . . Avogadro constant
p	. . . Fluid's pressure
p_i	. . . Inlet fluid pressure
p_o	. . . Outlet fluid pressure
P	. . . Pressure at equilibrium
P_0	. . . Saturation pressure
Q	. . . Volumetric flow rate
S	. . . Cross-sectional area normal to the flow's direction
T	. . . Temperature
v	. . . Velocity of fluid
v_s	. . . Superficial velocity of fluid
V_a	. . . Volume of adsorbed gas
$V_{cum.}$	. . . Volume cumulative
$V_{incr.}$	. . . Volume incremental
V_m	. . . Monolayer adsorbate volume
V_0	. . . Molar volume of gas
w_{MA}	. . . Mass fraction of MA powder
w_{CNF}	. . . Mass fraction of cellulose nanofibers
$x_{M^{2+}}$	. . . Mole fraction of divalent cations
X	. . . Change in length
α_d	. . . Degree of dissociation
γ	. . . Surface tension
γ_{CNF}	. . . Mass concentration of cellulose nanofibers
γ_{MA}	. . . Mass concentration of mesoporous alumina
$\dot{\gamma}$	. . . Shear rate
δ	. . . Thickness of the adsorbed layer
$\delta_{b.v.}$	. . . Scissoring bond bending vibration
$\varepsilon(\lambda)$	. . . Absorptivity at a specific wavelength
ε	. . . Strain
ζ	. . . Zeta potential
η	. . . Viscosity
η_0	. . . Viscosity of a solvent
$[\eta]$	. . . Intrinsic viscosity
θ	. . . Contact angle
κ	. . . Thermal diffusivity
λ	. . . Thermal conductivity
λ_a	. . . Thermal conductivity in axial direction

λ_r	. . .	Thermal conductivity in radial direction
ν_{as}	. . .	Asymmetric bond stretching mode
ν_s	. . .	Symmetric bond stretching mode
ρ	. . .	Density
$\rho_{b.v..}$	. . .	Rocking bond bending vibration
ρ_A	. . .	Apparent density
ρ_B	. . .	Bulk density
ρ_{CNF}	. . .	Density of cellulose nanofibers
ρ_E	. . .	Envelope density
ρ_{geom}	. . .	Geometric density
ρ_{theor}	. . .	Theoretical density
σ	. . .	Stress
τ	. . .	Shear stress
$\tau_{b.v.}$	. . .	Twisting bond bending vibration
τ_0	. . .	Yield stress
φ	. . .	Volumetric solid fraction
φ_A	. . .	Apparent volume fraction
φ_E	. . .	Envelope volume fraction
φ_m	. . .	Maximum volume fraction
Ψ_d	. . .	Stern potential
Ψ_0	. . .	Nernst potential
$\omega_{b.v.}$	. . .	Wagging bond bending vibration
% T	. . .	Percent transmittance
Δp	. . .	Differential pressure
C=O	. . .	Carbonyl group
R or R'	. . .	Organyl group
R_2–CH_2	. . .	Secondary carbon atom
R_3–CH	. . .	Tertiary carbon atom
R–COO^-	. . .	Deprotonated carboxylic acid/ carboxylate anion
$(R–COO)_2Mg$	. . .	Magnesium carboxylate
–OH	. . .	Hydroxyl group
–COOH	. . .	Carboxylic acid group
$–NH_2$	. . .	Amine group
$–SO_3H$	. . .	Sulfonic acid group

Chapter 1

Introduction

1.1 Highly Porous Ceramics

The simplest definition of porous ceramics describes them as two-phased materials, where continuous gas phase or pores are dispersed in solid ceramic phase or matrix [1]. Pores are to some extent present in all ceramics materials. In many cases, their presence is undesired since they are viewed as defects and considered problematic. In several other cases, however, the introduction of pores is the prime focus of the ceramic material design [1], [2]. For quite some time the interest in porous ceramics was more focused on those that are classified as mesoporous and microporous materials. Mesoporous materials have pores in the size range 2-50 nm while microporous materials have pores with diameter below 2 nm. The presence of such pores in ceramic materials results in enlarged surface area [3]. With the prospect of developing adsorbents and catalysts in the form of monoliths, the interest in the macroporous materials, that is materials with pore sizes above 50 nm, was renewed, not only among material scientists but also in the industry [4].

Highly porous ceramic materials are ceramics with pore volume exceeding 70 % of total material's volume and can be classified as cellular ceramics (with open porosity). Ceramic foams are a subgroup of the latter with a 3D array of voids [5]. The most commonly studied cellular ceramics are alumina, zirconia, titania, silicon nitride, hydroxyapatite, calcium phosphates and silica [6].

In recent years ceramic foams have become increasingly important, since there are numerous applications where the introduction of porosity into a ceramic matrix is necessary [5]. Based on the type of porosity, i.e., pore size, shape and orientation, pore interconnectivity, homogeneity/heterogeneity of porosity [7], ceramic foams find applications in various fields ranging from catalysts, catalyst support, adsorption, thermal insulation, separation and filtration to light-weight structural components [1], [8], [9]. Ceramic foams are also used as bone implants, since the porous structure promotes bone ingrowth and at the same time ensures vascularization [5]. The applicability of a specific porous ceramic material for the above-mentioned applications is governed by a combination of intrinsic (chemical) properties of a ceramic material along with the type of incorporated porosity. The former includes parameters like corrosion, wear, erosion and heat resistances, electronic properties and biocompatibility, while the latter includes surface area, small weight to volume ratio (low density), good thermal insulation properties, permeability and low dielectric constant. [2], [7], [8].

Physical and structural properties of porous ceramics are strongly influenced by the type of porosity [6]. For example, based on the pore structure ceramic foams can be divided into open- and closed-pore foams [2], [10]. If the pore structure is opened, the individual pores are interconnected and such porous ceramics are permeable for air (or fluid) being

suitable as membranes, sensors and majority of catalytic systems [5], [8], [10]. In the case of a closed-pore structure the fluid cannot flow freely through a material. Consequently such porous ceramics are more suitable for applications where the fluid transport is not a prerequisite, such as thermal insulation materials [10]. However, the presence of porosity decreases material's strength, thus the main function of porous materials is seldom of structural nature. In many applications a high mechanical stability is required and often a compromise between strength and degree of porosity must be made [5]. Hence, the characterization of the mechanical properties of porous ceramics is of prime importance [11]. Still, the presence of pores, though deteriorating mechanical properties, can, if carefully tailored, result in a material with unique mechanical properties, which cannot be achieved in dense ceramics [8]. An example of such mechanical property is plastic deformation and collapse of structure in ceramic foams during compression, which makes porous ceramics superior in absorption of impact energy [12].

1.2 Fabrication of Highly Porous Ceramics

Porous ceramics possess a wide range of functional properties for many applications, but there are some (micro)structural requirements [11]. In order to control the microstructure and ceramics' properties, a variety of fabrication routes were developed, since no single processing technique is flexible enough to enable preparation of all the structural variants [6], [7]. The routes can be roughly divided into four groups, where each group consists of a number of variations of a basic process [7]. These general approaches are: (i) partial sintering, (ii) replica templates, (iii) sacrificial fugitives, and (iv) direct foaming [7], [8].

(i) **Partial sintering** is the most frequently used technique for the preparation of porous ceramics and enables preparation of homogeneously distributed pores with narrow size distribution [8]. The size of the pores is controlled by the particle size of the starting ceramic powder. On the other hand, material's porosity depends on the sintering conditions, where with increasing forming pressure, time and temperature of sintering, the final porosity decreases [8]. However, this approach is not suitable for the preparation of cellular ceramics since the final porosity is in most cases below 50 % [8].

(ii) **Replica template** approach is one of the oldest approaches for the fabrication of porous ceramics. It relies on impregnation of a highly porous replica structure with a ceramic slurry [7], [8]. Various synthetic or natural cellular replica templates can be used. The most commonly used are porous polymeric sponges, for example polyurethane [8]. When the ceramic slurry-impregnated template is dry, the organic phase is burnt out. The remaining ceramic layers in contact are sintered and the pores remain in the shape of replica template [7], [8]. As a result, highly porous ceramics (90 %) with interconnected, open-pore structure and large pore sizes are obtained [6], [8]. The pore sizes range from several hundred micrometers up to a few millimeters [8]. The main drawback of this technique is the polymer burning-out phase during which cracking of ceramic struts can occur. This process can diminish the mechanical properties of the final ceramics [7]. A precise control over ceramic slurry's viscosity is required to obtain a uniform ceramic layer covering the template's walls [8]. Irrespective of these challenges, the replica template technique is largely used in industry for the preparation of filters for molten metals [7].

(iii) **Sacrificial fugitive** technique is based on the addition of sacrificial additives to a ceramic powder, with the former acting as a pore forming agent [8]. In a thermal treatment the sacrificial fugitive is removed and in its place the pores are created. The sacrificial agents are commonly in the form of polymer beads or organic fibers. Other materials such as graphite, salicylic acid and liquid paraffin are also used [8]. The shape and size of the sacrificial fugitive determines the size and shape of pores, while its content controls the

final porosity of a material. This technique enables preparation of ceramic foams with pore volumes in the range of 70 to 80 %. The technique is particularly useful for the preparation of materials with open porosity [8]. It also enables preparation of materials with closed porosity. The nature of final porosity depends on the quantity of the sacrificial fugitive added [7]. Yet the challenges of this approach should not be overlooked. The sacrificial template must be homogeneously mixed with ceramic powder in order to obtain uniform pore distribution. The pyrolysis is then used to remove the pore-forming fugitives, which can result in harmful, vaporized by-products. Pyrolysis is a long-termed, energy-consuming process. It is challenging for materials with lower porosities or more closed-pore structure [1], [8].

(iv) **Foaming** technique is based on mechanical agitation of a ceramic slurry by (*in situ*) incorporation of gases [7], [8]. The critical step in foaming is stabilization of gas bubbles, also known as pickering stabilization to prevent fusion of the latter and the formation of larger pores. A variety of novel techniques have been developed for stabilization [8]. The slurry containing bubbles is dried and sintered to obtain porous material [8]. The porosity of a ceramic foam can be as high as 95 % with the pore sizes ranging from 10 micrometers up to a few millimeters [8], [13], [14]. However, the pore size distribution can be very wide. Commonly the difference between the smallest and the largest pores in a single foam is more than ten folds [14], [15]. The pore structure of a foamed ceramic is usually less open than in the case of the replica template approach [7]. The foaming process is thus more suitable for the preparation of materials, where more closed porosity is desired, for example in thermal insulation applications [6].

In the last couple of decades efforts have been invested into development and improvement of new processing approaches for the preparation of cellular ceramic materials, which would enable better control over the pore structure and lead to a considerable improvement of material's properties [8]. Some of these new approaches are freeze-casting (sacrificial fugitive approach) and wood ceramics (replica template approach) [6], [8].

1.3 Freeze-Casting

Freeze-casting (FC) also known as ice-templating [11] is an efficient and cost-effective technique for the preparation of highly porous ceramic materials. It enables tailoring of the pore structure [16]. The materials prepared possess a wide range of porosities ranging from 25 to 90 % [17], [18]. Ceramics with even higher porosities were also reported [19], [20]. FC is used for the preparation of macroporous ceramics, but there are also a few studies demonstrating the preparation of ceramics with hierarchical porosity, that is combining macro and microporosity [21], [22] or macro and mesoporosity [20], [23], [24].

FC is essentially a variation of the sacrificial fugitive approach [8], whereas the only difference is in using ice crystals during freezing instead of polymer beads. FC has been one of the most studied processes in recent years [8], [17], [25]. Likewise, the number of potential applications for as-prepared ceramics and other materials grew significantly. Among proposed applications are batteries, supercapacitors, variety of sensors and biomaterials, with the latter being the most predominantly investigated application [17].

A major advantage of this technique is its universality. It can be used for consolidation of metals, ceramics and polymers [17] as well as their combinations [19], [20], [26]. However, FC is still the most widely used for the preparation of porous ceramics. Mostly used ceramic systems are alumina, hydroxyapatite, yttria-stabilized zirconia, titanium dioxide, mullite and others [17], [18]. FC technique was initially developed using water as a dispersion medium [18]. Yet in later years, a few alternative mediums such as camphene and *tert-*

butanol were also used in order to further modify the pore structure [16], [17]. Another major advantage of FC is the fact that macropores are formed from a dispersion medium, which eliminates the burn-out step of pore-forming organics added as a sacrificial fugitive or replica template. This benefit is especially appealing for the field of biomaterials, where thermally unstable compounds like enzymes and similar biologically active molecules are used [11].

FC technique is based on a solidification of a slurry through freezing. It is crucial that a stable slurry, not prone to sedimentation or segregation, is prepared. This slurry is poured into a PTFE mold, or similar, that acts as a thermal insulator and container, and then is frozen (Figure 1.1). During freezing, liquid dispersion medium is transformed into solid crystals creating the so-called solidification or freezing front. Growing crystals in the freezing front reject any other particles present in the slurry. The particles are entrapped and concentrated between individual crystals, forming solid walls [17], [18]. After the slurry is completely frozen, the dispersion medium is sublimated in the freeze-drying process operating at low temperature and under reduced pressure. After freeze-drying, the ceramic green body is obtained. Sintering is then employed in order to consolidate and densify the ceramic particles which form the pore walls [18]. Both green body as well as sintered monolith possess a pore structure that replicates the shape of the frozen solid crystals [17], [18].

The pore structure obtained by FC can be homogeneous (random) or heterogeneous (directional) depending on the freezing mode which is either isotropic or anisotropic, respectively [16], [18]. Depending on the freezing mode, the microstructure of as-shaped monoliths thus varies greatly. The microstructure is generally quantitatively described for both types by total porosity, pore size, thickness of the pore walls and the structure wavelength. The structure wavelength represents an average width of a single pore and its adjacent wall [27]. However, when the structure is anisotropic, pore and wall sizes are generally described in the terms of width, while for isotropic structure, sizes are given in terms of a diameter [17].

To obtain a homogeneous structure with non-aligned porosity, isotropic FC must be carried out, as illustrated in Figure 1.1A [17]. In this variation of the FC process, slurry is poured into a thermally insulating mold and put into a freezer. There is no directional thermal gradient so the nucleation occurs at random sites throughout the entire slurry. Consequently the crystals grow in random directions with no preferential growth observed (Figure 1.1A) [17]. The pore structure of green and sintered porous ceramic bodies is more or less isotropic [17] ranging from closed, equiaxed pores [28] to a more open-pore, reticular structure [29].

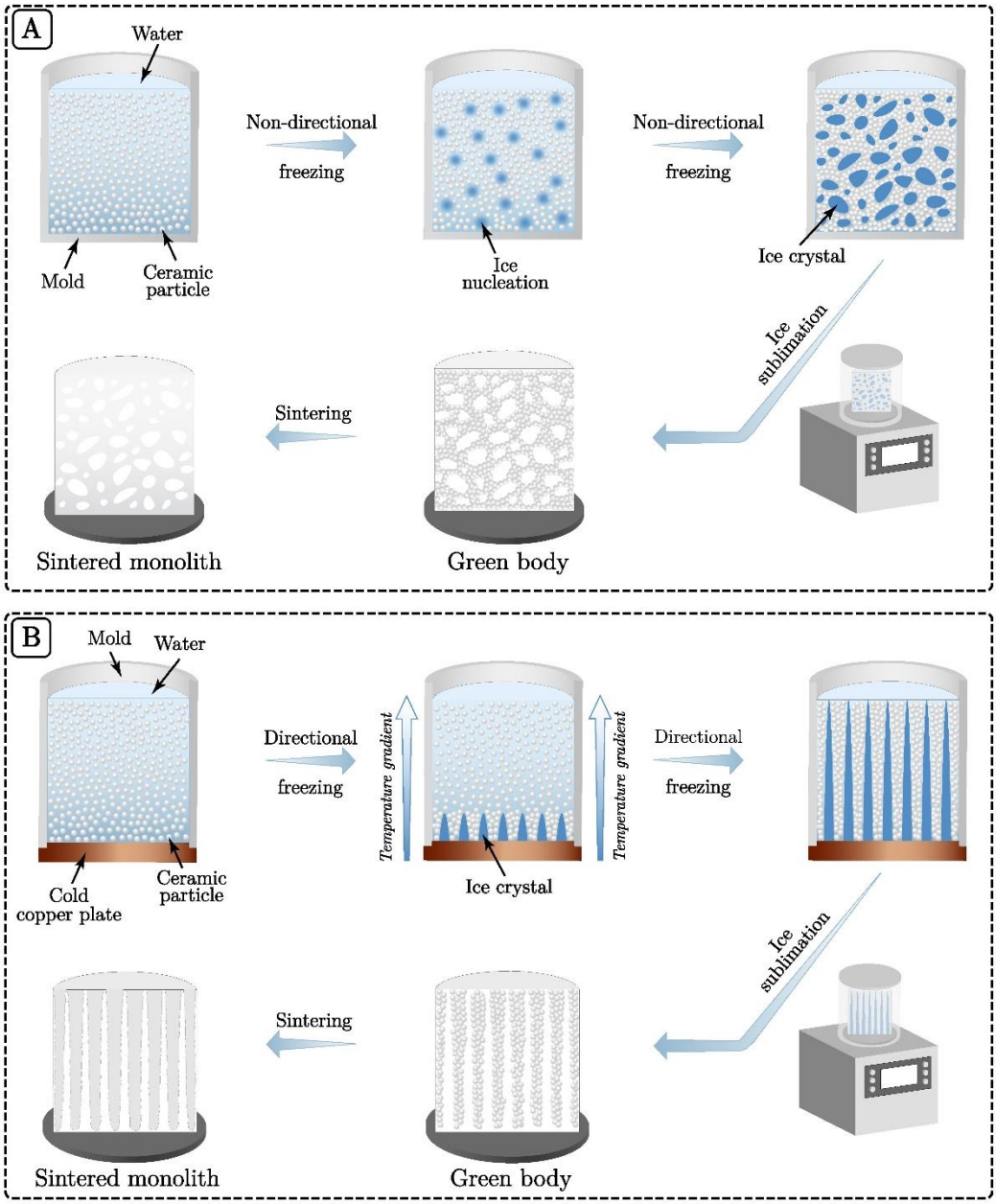

Figure 1.1: Illustration of the consolidation steps of (A) an isotropic freeze-casting and (B) a unidirectional freeze-casting of aqueous ceramic slurries.

On the other hand, aligned or directional porosity is obtained by anisotropic FC of slurries (Figure 1.1B). It is most commonly unidirectional meaning the slurries are cooled vertically from the bottom to the top. This variation of FC is much more widely implemented and researched than the isotropic variation [17]. In a typical FC set-up for unidirectional freezing, the mold is in the shape of a hollow cylinder or a similar shape composed of thermally insulating material. The mold is placed on top of a thermally conductive material (copper rod), which is immersed in cooling medium (liquid nitrogen or dry ice). The temperature at the upper surface of the copper rod directly affects the rate of freezing and is controlled with the help of a heating ring coupled to a thermocouple. A typical freeze-casting set-up for unidirectional freezing is illustrated in Figure 1.2.

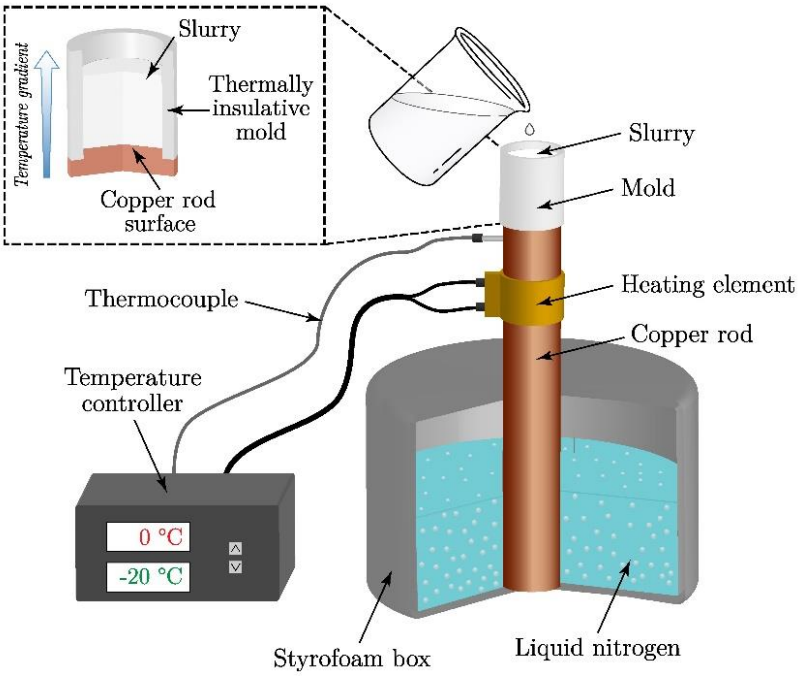

Figure 1.2: Illustration of a setup for the unidirectional freeze-casting process.

On rapid cooling of the copper rod vertical thermal gradient is induced in the slurry causing nucleation and directional growth of the freezing front [17] as illustrated in Figure 1.1B. The most commonly observed anisotropic pore structures are lamellar, dendritic and honeycomb [17] (Figure 1.3), although some other shapes such as columnar [30], [31] and needle-like [32] were also reported.

The pore structure obtained by directional FC process causes anisotropy of material's properties regardless of its shape. The influence of anisotropy is especially noticeable in mechanical properties [11]. However, anisotropic pore structure also results in anisotropy of some other functional properties such as thermal conductivity, permeability, piezoelectric properties and electric conductivity [11], [25].

1.3.1 Processing parameters

FC is a very flexible technique enabling the preparation of porous (ceramic) materials with a wide variety of pore volumes, pore sizes, morphologies and orientations. To obtain a material with desired porosity an appropriate slurry formulation such as type of dispersion medium, solid volume fraction, additives and size of ceramic particles, as well as appropriate freezing conditions must be carefully chosen [18]. Determination of the appropriate processing parameters for FC of a given system is challenging, but some general trends can be observed [11].

Many parameters influence the total porosity and pore structure of the freeze-cast materials. One should not overlook the most important processing parameter, which is slurry's stability. Stability should be carefully controlled to prevent sedimentation and segregation effects throughout the entire duration of the freezing process, since both cause non-homogeneous structure, i.e., unequally distributed density and porosity, which lead to different properties across the final material [16], [18].

1.3.1.1 Dispersion medium

A suitable dispersion medium must have an appropriate freezing temperature, and high vapor pressure to enable sublimation under acceptable conditions [18]. In FC, three dispersion mediums are commonly used; these are water, *tert*-butanol and camphene. Water is the most widely used dispersive medium in FC [18]. *Tert*-butanol and camphene are less commonly used, although more literature exists, where the former is used [17].

The choice of dispersion medium affects the pore morphology evolution [18], as shown in Figure 1.3, where different anisotropic pore structures are illustrated. When aqueous ceramic slurries are unidirectionally frozen, in most cases lamellar porosity is obtained [31], [33]–[35]. Anisotropic lamellar structure consists of plate-like ceramic walls with lamellar channels between them aligned parallel to the freezing direction [18]. Lamellar structures are usually observed and represent around 60 % of all reported anisotropic FC structures [17]. When lamellas exhibit tree-like branching in the form of dendrites, we speak about dendritic pore shapes (Figure 1.3B) [17]. Such structures are characteristic for materials prepared by a directional FC of camphene-based slurries [36]–[40].

The third anisotropic pore structure encountered is a honeycomb structure, where pores in the shape of hexagonal columns can be observed (Figure 1.3C) [17]. One of the possible ways of obtaining a ceramic honeycomb structure is to disperse the ceramic particles in *tert*-butanol [41]–[43].

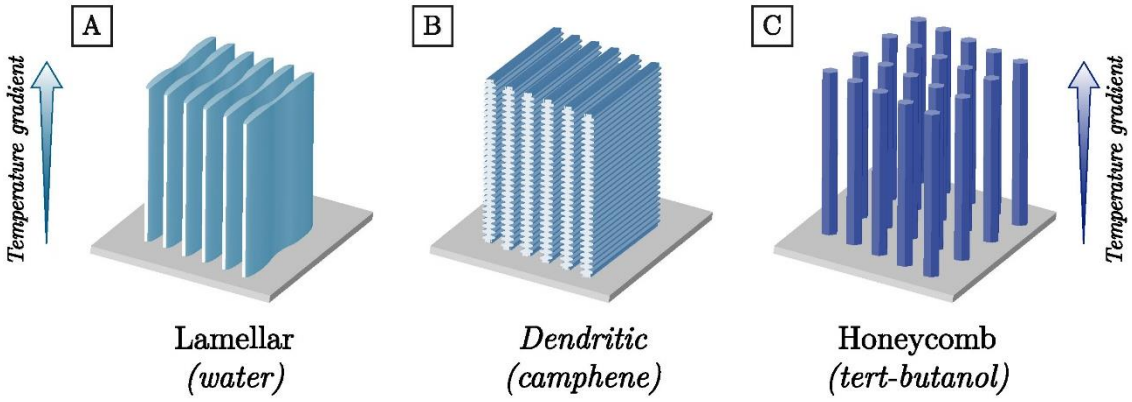

Figure 1.3: Illustration of different types of (anisotropic) structures formed during unidirectional freezing of slurries prepared with different dispersion mediums [17].

1.3.1.2 Solid volume fraction

Volume fraction of ceramic powder in a slurry has the highest impact on the amount of final porosity. Higher solid volume fraction lowers the amount of dispersion medium that transforms into pores [11], [18]. This direct correlation is observed for all dispersion mediums [11]. However, an enormous scattering of final porosities values can be observed for a single solid volume fraction. For example, with volume fraction of 20 % materials with porosities ranging from 25 to 80 % were reported [11]. Therefore, a number of other parameters must also be tuned to obtain a desired final porosity.

In the FC process, moderate solid volume fractions are generally used, ranging from 10 to 40 vol% [11], [18]. When volume fractions outside of this range are used, two problems arise: i) lower volume fractions result in green bodies with low strength [11], ii) solid volume fractions exceeding 40 vol% increase the viscosity resulting in atypical pore morphologies [11]. At high volume fractions, particle redistribution is extremely hindered, and the crystals cannot grow continuously along the direction of the temperature gradient [11], [27].

1.3.1.3 Properties of ceramic powder

The properties of ceramic powder, for example particle size and size distribution, particle shape and surface roughness, influence the outcome of the FC process. Each property modifies the pore structure to a different extent, but the influence of particle size is the most commonly discussed [18]. It has been reported that the anisotropic pore morphology is less likely to disappear at higher freezing rates when slurries with smaller ceramic particles are used [44]. The same study also demonstrated that with smaller particles well defined, dense lamellar walls were obtained, while bigger particles resulted in walls (or struts) with higher porosity.

1.3.1.4 Additives

Inclusion of certain additives during slurry preparation is necessary for a successful performance of the FC process. These additives are of organic nature, such as polyelectrolytes, which are used as dispersants or a variety of binders which prevent the freeze-cast green bodies to collapse during the freeze-drying stage [11], [18].

Additives represent from 5 to 10 % of the solid fraction and can help in the formation of meso- or microporosity. However, the majority of these pores are then removed together with all of the organic matter during the sintering step [11].

Additives also affect the shape of macropores. For instance the addition of zirconium acetate [45], [46] or cellulose, polytetrafluoroethylene and polyacrylic acid [20], [47], [48] changed the pore structure from lamellar to a honeycomb-like ceramic structure. The same effect was also observed after the addition of gelatin prior to the freezing step [49], [50].

1.3.1.5 Freezing conditions

The most critical step in determining the pore structure are the freezing conditions of the slurry, since they dictate the shape of the growing dispersion medium crystals. It follows that the majority of the porosity's final features are created during this stage [18]. For example, if the freezing temperature is carefully controlled, pore channels can run throughout the entire length of the material, but only in the direction of the imposed temperature gradient [18].

Freezing conditions include parameters like non-directional or directional freezing, starting freezing temperature and freezing kinetics (freezing rate) [17], [18]. Each of these conditions has a unique influence on the pore structure.

Freezing technique determines whether the pore structure will be non-directional or directional. The former is achieved when slurries are frozen without an imposed temperature gradient, resulting in pore structures with no specific orientation or long-range order. Directional pore structure is on the other hand obtained with temperature-gradient-imposed freezing. Directional freezing yields pore structures oriented along the direction of the temperature gradient [18].

The starting and the final freezing temperatures have little effect on the pore structure and are roughly dictated by the choice of the dispersion medium [18]. Aqueous ceramic particle slurries are solidified (frozen) at temperatures below 0 °C, while tert-butanol and camphene are solidified at higher temperatures, around 8 °C and 50 °C, respectively [18].

Freezing rate is a kinetic parameter with a major role in the determination of the final pore structure. The freezing rate is controlled by a heating ring placed beneath the top of a copper rod (Figure 1.2) or the type of coolant used (liquid nitrogen or mixture of ethanol/dry ice). With increasing freezing rate, the speed of freezing front's growth increases. This leads to a faster growth of crystals resulting in a finer crystal structure, which further leads to a finer microstructure of resulting pores. For example, thinner cell

walls and considerably narrower channels are obtained at higher freezing rates [51] as seen in Figure 1.4.

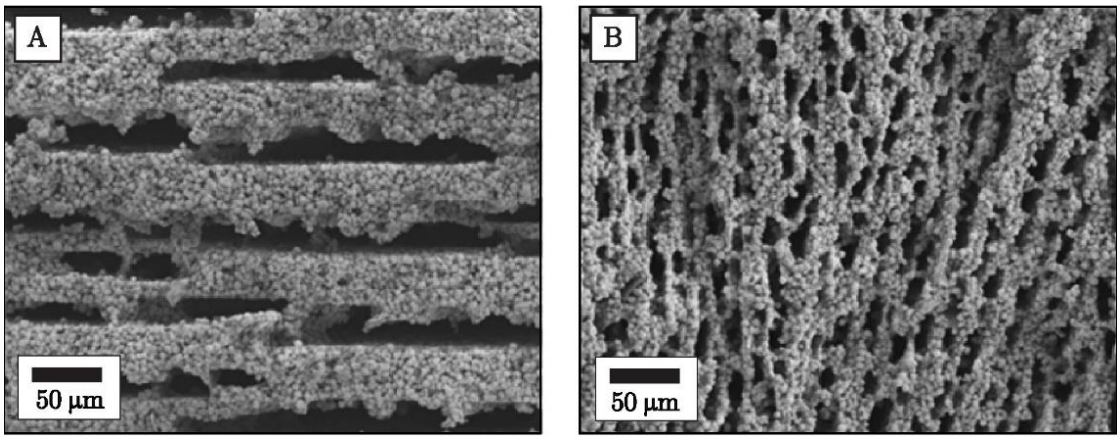

Figure 1.4: SEM images of freeze-cast zeolites frozen at 0.5 °C/min (A) and 5 °C/min (B). Images are adopted from *Ojuva et. al.* [22].

It is important to know that in a unidirectional FC process the freezing front velocity decreases with increasing the distance from the freezing surface. As a result, wall thickness and pore size may vary with the monolith height [52], [53].

1.3.1.6 Sintering conditions

Sintering is a final stage of the consolidation of FC body, where ceramic particles in the struts/walls are densified leading to an increase of the strength of the freeze-cast porous ceramics. However, the densification of ceramic walls also means that micro- and mesopores are removed. Consequently, only macropores created by a frozen dispersion medium (crystals) remain in the microstructure [18].

Conventional sintering techniques are applied for freeze-cast green monoliths, since their strength is too low to allow the use of pressure-assisted sintering techniques [18]. The effects of sintering on the final porosity are yet to be systematically studied, where the mechanism leading to monolith's shrinkage still need to be determined [18]. Additionally, optimization of sintering conditions offers some control over the pores and over the density of sintered material [21].

1.4 Stabilization of Particles in Aqueous Media

Aqueous suspensions are heterogeneous systems consisting of a water phase in which solid particles are dispersed. When these particles are in a sub-micron size region (1 – 1000 nm) the system is referred to as colloid suspensions. In principle, these particles are too small for their mass to be pulled by the gravitational force and such systems are able to resist the sedimentation in longer time periods and thus remain homogenious over longer time periods. On the other hand, in suspensions containing larger particles, exceeding diameter of 1 µm, the gravitational pull on the particles is considerable and such systems undergo sedimentation.

When a ceramic particle is immersed in a polar liquid such as water, a charge is formed on its surface. There are many mechanisms for the development of surface charge, like ion adsorption, ion dissolution and ionization of surface groups, e.g., carboxyl groups (–COOH), amine groups ($–NH_2$), sulfonic acid groups ($–SO_3H$) and hydroxyl groups (–OH)

[54]. For example, in the case of metal-oxide ceramic materials, the surface groups ionization is the prevailing mechanism of surface charge formation [55]. The hydroxyl groups on the particles surface in contact with water either become protonated or deprotonated depending on the pH and develop surface charge according to the following reactions [56]:

$$M - OH \; + \; H^+ \; \rightleftharpoons \; M - OH_2^+ \tag{1.1}$$

$$M - OH \; + \; OH^- \; \rightleftharpoons \; M - O^- + H_2O \tag{1.2}$$

Controlling the behavior of suspensions, such as their stability, is an important industrially relevant scientific field [57]. Dispersed particles are considered stable when the agglomeration is prevented or at least prolonged [58]. Stability depends on the balance between short-range Van der Waals forces, which are always attractive between like-particles [59] and repulsive forces. When the former prevail over the latter, flocculation or coagulation occurs, which leads to particle agglomeration causing formation of clusters [60]. On the other hand, when repulsive interactions prevail (kinetically), stable suspensions are obtained [61].

Sedimentation is another process that must not occur in order for a suspension to be considered stable. Sedimentation causes unequal distribution of solid phase throughout the dispersion medium, leading to a non-homogenous system. This parameter must however be controlled only in suspensions, since sub-micron particles in colloid suspensions are not affected by the gravitational pull due to their small size.

Stability of particles dispersed in a polar media governed by the relationship between the attractive Van der Walls forces and the repulsive electrostatic interactions is predicted by the DLVO theory. The theory is named after its authors Derjaguin, Landau, Verwey and Overbeek [57], [60]. DLVO theory is widely accepted as the foundation of the modern colloid science [57], [59], though it should be emphasized that the DLVO theory has been developed for diluted systems. Therefore, if DLVO theory is applied to a concentrated system, some modifications should be made [60].

Van der Walls forces are always present between dispersed particles and occur due to the (high) positive Gibbs energy of the interfaces. On the contrary, the repulsive forces have many origins such as electrostatic potential, steric barrier or a combination of both [59], [61], [62].

The repulsive forces can be modified through suspension's parameters such as pH, ionic strengths or addition of surface-active agents. These modifications are exploited as a way of suspension stabilization. There are three main approaches for stabilization, namely, electrostatic stabilization, steric stabilization and electrosteric stabilization.

1.4.1 Electrostatic stabilization (DLVO theory)

Electrostatic stabilization is based on the development of a charge on the surface of a particle dispersed in a polar medium. Due to this charge a reorganization of ions in the dispersion medium occurs in order to ensure electrical neutrality of the suspension [61]. Therefore, a layer of ions known as electric double layer (EDL) forms around each particle. EDL is composed from an excess of ions charged oppositely as the particle surface and a deficiency of ions carrying the charge of the same sign [61], [63]. The development and composition of EDL is described in detail in Appendix C.2. Here only a quick overview is given. As the name indicates, EDL is composed of two layers: Stern layer and diffusive layer. The Stern develops right next to the particle surface and consists of ions that are assumed to be immobilized [64]. On the other hand, the diffusive layer consists of the inner

part where ions are also assumed to be immobilized and the outer part where ions are mobile. The inner and outer part of diffusive layer are separated by a sharp boundary named slip plane [65]. The potential on the surface of particles cannot be measured, while the potential on the slip plane, known as zeta potential (ζ), can be successfully determined [59], [65].

Since like-charged particles repel each other, a generation of a surface charge of sufficient magnitude should in principle prevent particle agglomeration. Zeta potential can thus be used as a tool for the estimation of surface charge that can reflect on the suspensions stability [66]. A general rule states that when the value of zeta potential exceeds ±30 mV, dispersed particles repel each other enough to prevent agglomeration. Such suspensions are considered stable [67], [68]. The charge on the particles surface can be modified by several factors. The most commonly used one is a change of suspension's pH, hence enabling the control over suspension's stability.

The original DLVO theory was developed for electrostatically stabilized systems. It combined the Van der Waals attraction potential (G_A) with the electric double-layer repulsion potential (G_E). The change of the total energy of interaction (G_T) with the interparticle distance (h) is shown in Figure 1.5 [57], [60]. This curve describes the conditions of suspension's (in)stability [57].

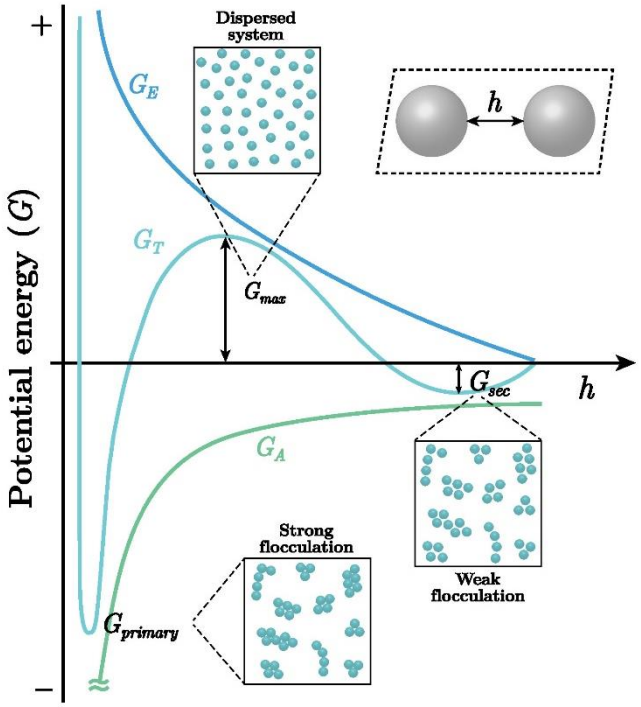

Figure 1.5: Schematic representation of the potential energy–interparticle distance curves (G_T–h), showing the variation of the Van der Waals potential energy (G_A), the electric double-layer repulsion potential (G_E) and the total potential energy (G_T) with interparticle distance (h) according to the DLVO theory.

According to the DLVO theory, the total potential energy of interaction between two particles (G_T) is determined by the sum of G_E and G_A at all interparticle distances as represented by Equation 1.3 [57]:

$$G_T = G_A + G_E \tag{1.3}$$

As can be seen from Figure 1.5, the double layer repulsion potential G_E shows an exponential decay with an increasing interparticle distance, approaching zero at large particles separations [57]. The exponential function order depends on the properties of EDL [60].

On the other hand, the function describing the negative potential occurring due to the attractive Van der Walls potential (G_A) exhibits an inverse power-law dependence from the particle distance. Its strength is a function of the Hamaker constant of matter (particles) and the dispersion medium [59]. As can be seen from Figure 1.5, Van der Waals force becomes significant at short interparticle distances (≤10 nm), where the potential energy reaches large negative values [57], [60]. However, unlike G_E, G_A does not reach zero even at long interparticle distances [57].

The form of the total potential energy (G_T) - interparticle distance (h) curve shown in Figure 1.5 exhibits one maximum (G_{max}) and two minimums ($G_{primary}$ and G_{sec}). The maximum occurs at intermediate distances and is also referred to as the energy barrier [57]. The higher the value of the energy barrier G_{max}, the higher the force needed for the particles to overcome it and fall into primary minimum. The consequence is the transition from dispersed state to the strongly flocculated state (Fig. 1.5). A general rule is that if particle flocculation is to be avoided, this barrier should be higher than $25kT$ (kT stands for thermal energy of a particle, where k is the Boltzmann constant and T the temperature) [57], [69].

The value G_{max} depends on the value of surface potential and the concentration and valency of the ions in the suspension. With increasing electrolyte concentration, EDL starts to compress resulting in a reduction of G_E. As a consequence, G_{max} also starts to decrease. When the value of G_{max} eventually becomes lower than 5 kT, a slow flocculation starts. However, if the energy barrier entirely disappears, a rapid flocculation occurs [60], [70]. The former occurs when G_E is so low that the value of G_A exceeds it. Regardless of the electrolyte concentration, G_{max} will always decrease if the electrolyte valency is increased. In order to prevent flocculation of electrostatically stabilized particles, the value of zeta potential should be increased above the absolute value of 40 mV and the concentration of electrolyte (preferably with the valence of 1) should be decreased below 0.01 mol/L [57].

The primary minimum ($G_{primary}$) occurs at very short interparticle distances. It is much deeper as the shallow secondary minimum (G_{sec}) occurring at larger particle separations [57]. The latter occurs because at large interparticle distances G_A decays much slower than G_E. The depth of G_{sec} depends on the shape and size of dispersed particles and the Hamaker constant [57], [60]. Electrolyte concentration also affects the depth of the secondary minimum, namely the higher the electrolyte concentration, the deeper the minimum [60]. Under specific conditions this secondary minimum can become sufficiently deep (reaching 2-20 kT units) to enable weak flocculation of the suspension [57], [59]. Unlike strong flocculation, the former is reversible. By changing suspension parameters, for example, diluting the electrolyte concentration, can increase the G_E and the particles return back to the dispersed state.

If interparticle forces in an electrostatically stabilized system are carefully controlled through parameters such as pH, electrolyte concentration and electrolyte valency, suspensions can be prepared in three forms as depicted in Figure 1.5. One is a strongly flocculated state, where particles form “touching” aggregates. The second is a dispersed state, where particles repel one another on close approach thus existing as individual entities. The last is a weakly flocculated state, where particles are connected into loosely aggregated flocs or particle networks that can be readily broken under sufficient stress (yield stress) [59].

1.4.2 Steric stabilization

The steric stabilization is based on the adsorption of organic molecules such as long polymer chains on the surface of dispersed particles [70]. These molecules, when adsorbed, represent a steric barrier preventing particles to approach each other on a close enough distance where attractive Van der Waals forces would operate to trigger flocculation.

In order to achieve adequate steric stabilization, a couple criteria must be met. Firstly, the adsorbed layer must be sufficiently thick (at least 5 nm) and dense enough to completely cover the particles surface. Any "bare" zones can cause flocculation [57], [59]. Secondly, the polymer must be strongly adsorbed on the particle surface [57]. Thirdly, the chains must be highly soluble and solvated by the dispersion medium [57], [70].

The DLVO theory was later extended to also explain the origin of stability resulting from adsorption of polymer chains [57]. When steric forces are combined with Van der Waals attraction forces, a modified version of the classical DLVO potential energy – interparticle distance curve is obtained [57]. The modified G_T–h curve for sterically stabilized systems is shown in Figure 1.6. It can be seen that the shape of G_T curve differs significantly from the shape of the G_T curve predicted by the original DVLO theory.

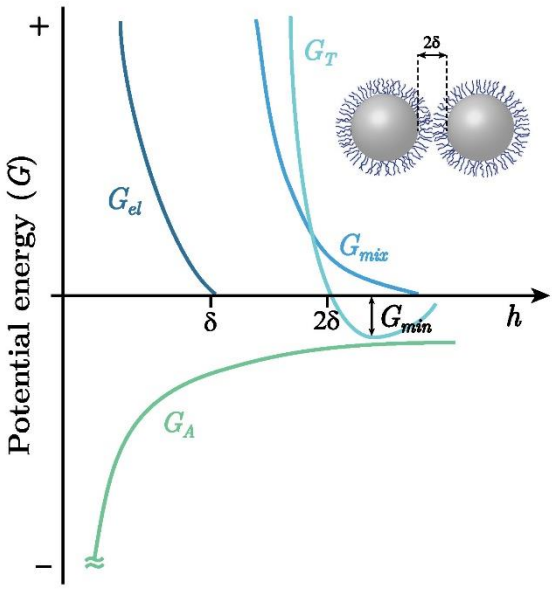

Figure 1.6: Schematic representation of the potential energy–interparticle distance curves (G_T–h) according to the extended DLVO theory for sterically stabilized particles. δ represents thickness of the adsorbed layer, G_{mix} the variation potential energy of the mixing interactions and G_{el} the variation of free potential energy of interaction with the interparticle distance.

When two particles with an adsorbed polymer layer of thickness δ come to an interparticle distance of twice the thickness of the adsorbed layer (2δ) or less, polymer layers interact with each other causing the repulsive steric interactions [57], [59]. In the interaction zone, a local increase in the density of the polymer chains occurs. The result is a strong repulsion described by the potential energy of the mixing interactions curve (G_{mix}) [57]. The latter curve increases very steeply when interparticle distance becomes smaller than 2δ.

Due to the overlapping (or compression) of polymer layers, the volume available to an individual chain decreases. This volume restriction results in a repulsive interaction described by the free potential energy of interaction (G_{el}) [57]. Similar as G_{mix} curve also

G_{el} curve increases abruptly when particles come too close together. However, unlike in the former case, this distance must be shorter than the thickness of a single adsorbed layer (δ) [57].

The sum of contributions of G_{mix} and G_{el} is referred to as the potential energy of steric interaction G_S (Equation 1.4): [57]

$$G_S = G_{el} + G_{mix} \tag{1.4}$$

If the potential energy of steric interaction G_S is combined with the attractive Van der Waals potential G_A, the total energy of interaction G_T is obtained (Equation 1.5): [57]

$$G_T = G_S + G_A \tag{1.5}$$

G_T–h curve exhibits a steep increase when $h < 2\delta$, due to the repulsion forces occurring as a consequence of the overlapping of adsorption layers [60]. At distances of few tens of nanometers, the Van der Waals forces are still relatively weak [60].

Unlike the curve illustrating the G_T–h relationship predicted by the original DLVO theory, the curve describing the G_T–h relationship in a sterically stabilized system has only one (shallow) minimum (G_{min}). The latter occurs at interparticle distances slightly larger than 2δ, with the depth usually not exceeding a few kT units [57], [60]. The depth of G_{min} is determined by three parameters: particle size (radius), Hamaker constant and thickness of the adsorbed layer. If the latter is decreased by decreasing the molecular weight of the stabilizing chains, the G_{min} will increase [57]. For example, calculations have shown that if polymers with a high enough molecular weight are used, the G_{min} will be shallow to the extent of not being visible on the G_T–h curve. Such suspensions approach thermodynamic stability. On the other hand, if the molecular weight is so low that the layer thickness falls below 5 nm, the G_{min} will be deep enough for the weak flocculation to occur [57].

1.4.3 Electrosterical stabilization

Electrosterical stabilization is the third most common type of stabilization. The repulsion between two particles is caused by the sterical hindrance as well as the electrostatical repulsion [59]. It is achieved by adsorption of polyelectrolytes, which are charged polymeric species containing at least one type of ionizable group [60], [71]. This group can be either cationic, for example amino (–NH_3) groups, or anionic, for example carboxylic (–COOH) or sulfonic (–SO_3H) acid groups [59], [72]. Polyelectrolytes with only one type of ionizable group are known as homopolymers, for example polyacrylic acid (PAA), while in the case of polyelectrolytes containing several different types of ionizable groups we are speaking about block copolymers [59]. In adsorption, a general rule applies that the negatively charged polyelectrolytes adsorb on positively charged particle surface and vice versa [59]. Yet some polyelectrolites can also attach on the surface where the predominate charge is of the same sign [56]. For example, adsorption of PAA on the negatively charged surface of alumina particles [72], [73].

The shape of the G_T–h curve for electrosterically stabilized particles is shown in Figure 1.7. Here the total energy of interaction (G_T) is given by Equation 1.6:

$$G_T = G_E + G_S + G_A \tag{1.6}$$

The G_T–h curve possesses one shallow minimum (G_{min}) at larger interparticle distances and one poorly defined maximum (G_{max}) at intermediate distances. The latter arises due to the electrostatic type of interactions. At small interparticle distances a steep increase of G_T

can be observed as a contribution of steric interactions. Essentially the G_T–h curve for electrosterically stabilized particles is a combination of the features of G_T curves for electrostatically and sterically stabilized systems [60].

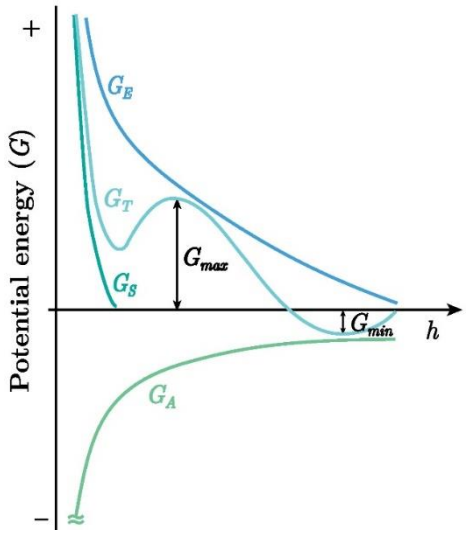

Figure 1.7: Schematic representation of the potential energy–interparticle distance curves (G_T–h), according to the extended DLVO theory for electrosterically stabilized particles. G_E represents the variation of electric double-layer repulsion potential and G_S the variation of potential energy of steric interaction with the interparticle distance.

When exploiting polyelectrolytes for stabilization of ceramic particle suspensions, the influences on their stabilization capacity should be considered. Stabilization capacity is mainly a function of the polyelectrolyte chains conformation, but other parameters such as the strength of adsorption and the adsorption density also play a significant role. A polyelectrolyte chain has many possible conformations, with a coiled (compact) and an extended (open) conformation representing the two borderline possibilities [59], as illustrated in Figure 1.8. With the change in the chain conformation the thickness of the adsorbed polymer layer (δ) also changes. The lowest δ is obtained for the coiled conformation. Aside from the chains conformation, the adsorbed polymer layer thickness is also determined by the polyelectrolyte's molecular weight [57].

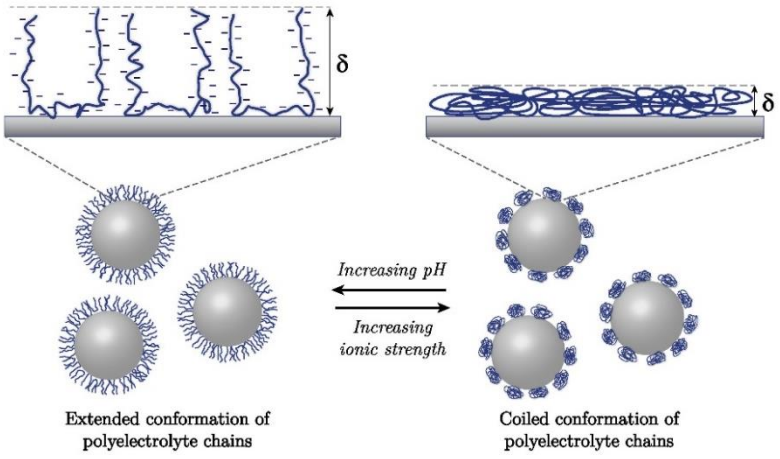

Figure 1.8: Illustration of the influence dispersion medium's ionic strength and pH have on the conformation of negatively charged polyelectrolyte chains adsorbed on the particle surface.

The conformation of polyelectrolyte chains depends on pH and ionic strength of the dispersion medium [59]. At high ionic strengths the charge on polyelectrolyte chains is shielded by the ions present in the dispersion medium. Due to the lack of repulsion between like-charged groups on the polyelectrolyte chains, the conformation of the latter changes from extended to coiled.

A similar effect can be observed with the change in the pH value. For an anionic polyelectrolyte the degree of ionization (deprotonation) is low at acidic pH values and high in the alkaline pH region. The opposite trend of pH dependence can be observed in the case of cationic polyelectrolytes. In both cases at low ionization the lack of charged groups and the repulsion between same-charged species result in a coiled chains conformation. With varying the pH value, the degree of ionization can be increased and the polyelectrolyte chains will unfold [59]. An extended, charged polyelectrolyte conformation provides both the electrostatic and steric stabilization. Hence, the suspension's pH and ionic strength should be carefully monitored to obtain the highest possible level of stabilization [59].

Another aspect when using polyelectrolyte stabilization that has to be considered is the amount of added polyelectrolyte. When the added amount is insufficient, polyelectrolytes can adsorb on more than one particle resulting in the formation of agglomerates via the phenomena known as bridging flocculation [59]. On the other hand, an excessive amount of added polyelectrolyte can have adverse effects on the suspension's rheological properties [59], [74].

The three above-mentioned stabilization mechanisms are highly efficient in endowing the colloid suspensions with required stability. In such suspensions, particle agglomeration and subsequent sedimentation are prolonged over extended time periods. The former is however not true in the case of suspensions, which contain micron-sized particles.

1.4.4 Sedimentation behavior of aqueous suspensions

In the case of suspensions containing sub-micron particles (colloid suspensions), gravitational pull on the particles is negligible and cannot induce particle sedimentation. It follows that the above-described stabilization mechanisms are sufficient to prepare reasonably stable colloids. However, in the case of suspensions containing particles with sizes exceeding one micrometer, gravitational pull on the particles is considerable and can cause fast sedimentation rates. In such cases, additional stabilization mechanisms can be employed in order to hinder gravitational pull and slow down or completely prevent sedimentation.

In the past, activation of interparticle associations in the aqueous ceramic suspensions proved beneficial. Suspensions in which interparticle associations are triggered possess a type of structure or particle network capable of efficient resistance towards suspension sedimentation and particle size segregation. This is the most commonly achieved by a weak flocculation of electrostatically and electrosterically stabilized suspensions [59], [69], [75]. In the latter case, the existence of a G_{min} (Figure 1.7) is a requirement for the onset of interparticle association [69]. However, when dealing with systems where particles are electrosterically stabilized with long polymer molecules, such as polyacrylic acid (PAA), this minimum no longer exists. In such suspensions, alternative approaches for the minimization of sedimentation should be implemented. Two mechanisms are especially suitable for the triggering of interparticle associations between micron-sized particles stabilized by long polyelectrolytes, namely the addition of multivalent cations and the addition of secondary fibrous phases.

1.4.4.1 Addition of divalent cations

Addition of divalent (M^{2+}) or trivalent (M^{3+}) cations can prevent sedimentation in electrosterically stabilized aqueous ceramic suspensions. This phenomenon has been extensively studied, but its mechanism is still not entirely clear [76]–[79]. The most likely mechanism involves a non-covalent cross-linking, also known as (salt) bridging flocculation. It was proposed that two or three negatively charged groups, mostly carboxylic ($R–COO^-$) or sulfonic ($R–SO_3^-$) groups, from the different polyelectrolyte chains coordinate on a positively charged multivalent cation as illustrated in Figure 1.9 [75]–[78], [80]–[82].

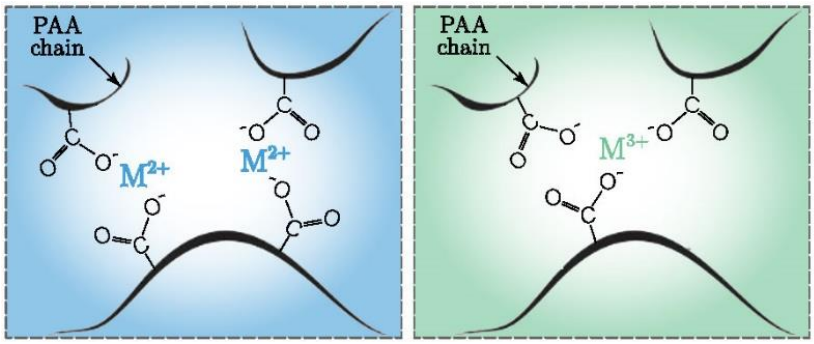

Figure 1.9: Illustration of cross-linking (salt-bridging) of different polyacrylic acid (PAA) chains through divalent cation addition (left) or trivalent cation addition (right).

Consequently, a network consisting of interconnected polymer chains, adhered to ceramic particles, is formed. The as-formed network minimizes any potential size segregation and decreases sedimentation rates, due to the formation of a structure able to resist the gravitational pull [75], [76], [80]–[82].

It has been reported that the presence of multivalent cations enhances the adsorption of polyelectrolyte chains on the surface of a ceramic particle when pH is above the particle's IEP. The majority of the ceramic materials possess negative surface charge above the IEP, hence the adsorption of negatively charged polyelectrolytes is hindered. Multivalent cations, on the other hand, provide a sort of bridges between negatively charged surface of ceramic particles and negatively charged functional groups on the polyelectrolyte chains. As a result, the amount of adsorbed polyelectrolyte is increased [83]–[85].

While in smaller amounts multivalent cations enhance the adsorption of polyelectrolyte on the particle surface, in higher concentrations the same cations trigger a formation of a 3D gel network. The latter can considerably improve suspension's resistance toward sedimentation, resulting in an enhanced long-term storage capacity.

However, while the formation of a cation-polyelectrolyte network has been widely studied in pure polyelectrolyte-cations systems [77], [78], [86], there is a limited number of studies on the systems containing polyelectrolytes, cations and ceramic particles [83], [87]. Further studies are needed in order to better understand the benefits of this approach in regards to the minimization of sedimentation and consequent assurance of long-term homogeneity of suspensions.

1.4.4.2 Addition of a secondary fibrous phase

Sedimentation can also be limited if a suspension is sufficiently viscous. The addition of a secondary (fibrous) phase can be employed to prevent sedimentation of bigger particles [88]. As secondary phase polymeric agents such as cellulose or other polysaccharides such as latex and xanthan are usually added [88]–[91]. Especially cellulose has a long history of use as a rheological modifier in the food industry [92].

The polymeric agents work as thickeners producing high zero shear rate viscosity which then hinders the gravitational force [90]. Aside from increasing the viscosity at zero shear rate thickeners also commonly work as flocculants, causing the formation of a 3D gel network by bridging flocculation throughout the entire suspension. As a result such suspensions are endowed with good resistance toward sedimentation [89], [90].

In recent years, the interest of scientific community in nanocellulose has greatly increased. Nanocellulose is a type of cellulose where at least one of the material's dimensions is in the nanometer range. Nanocellulose combines the beneficial properties of cellulose with the advantages of nanomaterials, such as high surface area, low density and improved mechanical properties [92], [93].

There are three main subgroups of nanocellulose, namely bacterial nanocellulose (BNC), cellulose nanofibers (CNF), and cellulose nanocrystals (CNC) [94]. Different subgroups of nanocellulose also possess a different set of properties [92]. For example, CNF usually possess a cross-section diameter between 5 and 60 nm, while the length of a single fiber stretches from a hundred nanometers up to a several micrometers [92].

However, it has to be emphasized that cellulose nanoparticles have a strong tendency for agglomeration, due to the inter-particle interactions through surface hydroxyl groups [95]. Such aggregation can have undesirable effects on the properties of the final material. For example it can limit the mechanical reinforcement nanocellulose could provide in an un-aggregated form [95].

Yet the flocculation of nanocellulose can be controlled either by the addition of other polymers, which if adsorbed can provide steric stabilization [92], or by various surface chemical modifications [95]–[97]. Among many possible chemical modifications oxidation with 2,2,6,6-tetramethylpiperidinyloxyl, also known as TEMPO–oxidation, is among the most frequently used [96]–[98]. TEMPO–oxidation under alkaline aqueous conditions is a process developed by de Nooy et al. [97], which turns the primary hydroxyl group on C6 atom into carboxylate groups (Figure 1.10). Consequently nanocellulose with a high negative charge is obtained (500-1500 μmol/g) [98], which results in a strong repulsive effect between individual nanocellulose fiber, preventing their agglomeration [98].

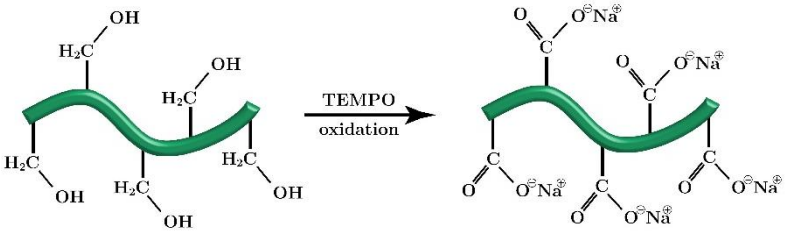

Figure 1.10: Ilustration of the TEMPO–oxidation process of cellulose nanofibers.

In recent years a number of research projects demonstrated a great potential of CNF in various fields (especially when TEMPO–oxidized), among which is also the area of wet-forming aids [96], [99]–[101]. For example it was shown that CNF is a superior aqueous dispersing agent for a variety of materials, able to endow suspensions with stability by providing a high negative ζ on the particles [96], [99]–[102]. Furthermore, advantageous properties of CNF such as their sustainability, gel-forming ability, high aspect ratio and excellent ability to form hydrogen bonds have further boosted its wide applicability [92], [99], [103]–[105].

It was shown that CNF incorporation has a great potential in the field of preparation of advanced lightweight cellular-structured ceramic monoliths and foams [94], [96], [106], [107]. CNF has also shown a great promise as a green body reinforcement due to their ability to considerably improve the mechanical properties of the latter [19], [96], [105].

1.5 Mesoporous Alumina (MA) Ceramics

Mesoporous γ–Al_2O_3 (MA) is one of the most important transition aluminas [108], since it exhibits nanocrystallite size, high (meso)porosity, large surface area and a high surface density of the hydroxyl groups [109] [110]–[112]. The convenient combination of properties makes it an important precursor for the fabrication of catalysts, catalyst support, filtration membranes and adsorption components [113]. More recently, its potential use in medicine as biomaterial, with increased osteoblast cytocompatibility properties [114] or as carriers and adjuvants [115], was also recognized. However, due to a slightly poorer chemical and hydrothermal stability, wide applicability of MA, especially in catalysis, is still rather limited [108].

MA powders are typically obtained through the thermal dehydration of aluminum oxyhydroxide (γ–AlOOH, boehmite), retaining the latter's morphological and surface features due to a topotactical transformation [110]. In as-prepared MA powders, a hierarchical structure is obtained. Several morphologies of hierarchically assembled boehmite and consequently MA powders were reported, e.g., nanofibers and nanotubes [116], nanorods or nanoplates [117]–[120] and hollow nanospheres [121]. The literature is full of a variety of different terms for the building blocks of hierarchically assembled MA entities, such as nanosheets or nanoleaves [122], nanoflakes [123] and nanoflowers [124], but essentially having similar morphologies to those already mentioned.

Controlled hierarchical assembly on the mesoscale has been recognized as a powerful strategy to obtain superstructures with various morphologies and sizes [125], [126] these can improve the catalytic, selective and adsorptive properties of hierarchically assembled MA [127], [128]. It should be emphasized that hierarchically assembled materials retain their intrinsic nanoscale properties, but are environmentally friendlier, less hazardous [129] and easier to handle [130]. Additional benefit of the hierarchically assembled powders is easier processing in comparison to classical nano-powders. Unlike nanopowders, where the occurrence of agglomerates and aggregates is very common, hierarchically assembled supraparticles display a uniform shape and size distribution, making them superior candidates, especially in sintering applications [131]. Additionally, hierarchically assembled particles also have a wide variety of characteristics, and a broader spectrum of functionalities and possible applications than their bulk form.

1.5.1 Synthesis of MA powder

Two ultimate goals are being followed in the synthesis of MA hierarchical structures: i) to prepare a finely porous and crystalline hierarchical structures, which result in increased specific surface area and pore volume, and ii) to employ a facile-like, energy-efficient and environmentally friendly synthesis. However, these two goals are rarely achievable at the same time.

Hierarchical MA powder is obtained by dehydration/decomposition of an aluminum oxihydroxide, known as boehmite (γ-AlOOH) [111]. Transformation between both forms is topotactic, meaning the characteristics such as crystallographic orientations of as-obtained γ-Al_2O_3 are very similar to the characteristics of the starting boehmite powder [110], [111]. Thereby, the evolved texture and porosity of MA are mainly influenced by the nature of the boehmite precursor. Thus the first step in the preparation of MA powder is the synthesis of boehmite which possess properties, desired in the MA powder.

There are several well established synthesis routes for the preparation of hierarchically assembled boehmite of high purity and high surface area, for example hydrolysis of aluminium alkoxides (sol-gel method) [132]–[138] and hydrothermal/solvothermal transformation of gibbsite ($Al(OH)_3$) [139], [140] or other aluminum salts, such as $Al(NO_3)_3$

[123], [141]–[148], $AlCl_3$ [122], [149]–[153] and aluminum alkoxide [154]–[157]. A few studies on the preparation of highly pure hierarchically assembled boehmite by homogeneous precipitation from $Al(NO_3)_3$ [158]–[162] and $Al(OH)_3$ [163], [164] have also been reported.

However, these γ-Al_2O_3 synthesis routes include either lengthy and complex multiple-step synthesis routes or require the usage of alkoxides and organic solvents along with the addition of various surfactants or structure-directing agents for the purpose of gelation initiation or phase separation. Aqueous methods also require additional extensive washing of the precipitated cake due to the presence of cationic and anionic impurities (Na^+, K^+, Mg^{2+}, Cl^-, SO_4^{2-}, NO_3^-, etc.), formed as a side-product of neutralization of aluminum salts [110], [113]. Furthermore, in mentioned synthesis paths not only limited amounts of γ-AlOOH are obtained, but also physical characteristics, such as particle size distribution and degree of agglomeration, are rarely reported. However, these properties are of crucial importance for further processes and ultimately determine the possible applicability of as-synthesized MA powder [110].

1.5.1.1 Hydrolysis of AlN powder

At the beginning of the 21st century, an alternative, straight-forward and versatile aqueous synthesis route for the preparation of abundant amounts of γ-AlOOH powder of high purity was explored and characterized by Kocjan et al., that is exploiting the peculiar process of AlN powder hydrolysis in diluted aqueous suspensions at elevated temperatures (<90 °C) [165], [166]. Beforehand Kosmač et al. showed how AlN hydrolysis process can also be exploited for hydrolysis-assisted solidification process [167], [168] of aqueous ceramic slurries or for the synthesis of nanostructured coatings [169], [170].

In the past, AlN powder hydrolysis used to be exploited for the production of ammonia by the Serpek process before the invention of the Haber-Bosch process at the beginning of the 20th century [166]. Ever since the hydrolysis of AlN powder has been mostly regarded as an undesired process, which only deteriorates properties of AlN-based materials [166]. Therefore, the majority of research regarding AlN hydrolysis was conducted in the light of the inhibition of the latter [171]–[173].

Bowen et al. carried out the pioneering work on the mechanisms of AlN powder degradation during hydrolysis and established the process kinetics [174]. According to the experimental results, they proposed the following reaction model for diluted AlN powder aqueous suspensions:

$$AlN + 2H_2O \longrightarrow AlOOH_{amorph} + NH_3 \tag{1.7}$$

$$NH_3 + H_2O \rightleftharpoons NH_4^+ + OH^- \tag{1.8}$$

$$AlOOH_{amorph} + H_2O \xrightarrow{OH^-} Al(OH)_{3\,(xstal)} \tag{1.9}$$

According to their findings, after AlN powder reacts with water, an amorphous aluminum oxide hydroxide (AlOOH) known as pseude is formed (Eq. 1.7).

The kinetics of AlN hydrolysis represented by Equation (1.7) were described by the unreacted core model proposed by Levenspiel [175]. According to this model, the chemical reaction starts on the outmost layer of a solid particle and then continues towards the most inner part of a particle. Accordingly, the hydrolysis reaction takes place at the interface between unreacted AlN core and the reaction-product (boehmite) layer. This stage is the rate-controlling-step [166], [176].

From the chemical perspective, the reaction converting AlN to boehmite occurs at the surface of the AlN particles by binding of hydroxyl anion to aluminum cation and consequent displacement of the afore bonded nitrogen anion. The latter reacts with

remaining hydroxyl cations, forming ammonia (Equation 1.7). It thus follows that the reaction of AlN hydrolysis is basic-catalyzed. The hydroxyl anions, formed after the dissociation of ammonia (Equation 1.8) will accelerate the further conversion of AlN to AlOOH. This means the reaction is self-catalyzed [166], [177]. The latter was additionally confirmed by observations of hydrolysis at room temperature, where at elevated pH values (≈11) the rate of the reaction increased, while at acidic pH values (pH≈1), the conversion did practically not occur [178].

In the last, so-called ageing step, the formation of bayerite ($Al(OH)_3$) occurs. Reaction of crystalline bayerite formation, given by Equation (1.9), assumes the dissolution-precipitation process of pseudoboehmite to bayerite [166], [176], [179]. However, the precise crystallization course during the AlN hydrolysis and subsequential ageing of the precipitated γ–AlOOH remains unclear [180].

It should be noted that Bowen et al. [174] conducted their experiments at room temperature. Consequently, the proposed mechanism and the corresponding reaction kinetics cannot be generalized for hydrolysis reactions carried out at elevated temperatures, especially above 80 °C [166]. For example, the research carried out by Fukumoto et al. [178] and Yoldas [181] demonstrated that at higher temperatures (above 80 °C) crystalline bayerite is not formed, but rather precipitation of crystalline boehmite is the predominant process.

It was also shown that ammonia's temperature-dependent solubility, which is reversibly proportional to the temperature, ensures that the pH of the suspension throughout the hydrolysis remains below 10. As a result, the formation of a single-phased γ-AlOOH with no aluminum trihydroxides residues is facilitated [180].

Kocjan et al., who conducted an in-depth study of AlN powder hydrolysis at room and at elevated temperatures, suggested that the course of AlN hydrolysis consists of three main stages: the induction period (first stage), the growth of boehmite (second stage) and the growth of bayerite (third stage). When hydrolysis was performed at lower temperatures, i.e., 22 °C and 50 °C, all three stages were observed. On the other hand, when the process was carried out at temperatures above 90 °C, only the second stage (growth of boehmite) was observed.

The induction stage, where the reaction rate is slow, occurs due to the formation of a thin aluminum hydroxide gel ($Al(OH)_3(H_2O)$) layer. The latter forms on the surface of AlN particles [166], [177]. This layer was observed only if the reaction temperature was kept below 70 °C [177]. The absence of the induction period at higher temperatures (above 90 °C) was ascribed to the aluminum hydroxide gel's thermodynamic instability. Consequently, at such temperatures, the formation of boehmite starts immediately after the AlN surface is exposed to the hot water [166], [177].

The onset of the second hydrolysis stage, where the growth of boehmite is the predominant process, can be observed after the supersaturation of $[Al(OH)_4]^-$ in the suspension is achieved [177]. The supersaturation is reached as a consequence of the dissolution of aluminum hydroxide gel layer, formed on the surface of AlN particles during the induction period, or via direct Al-N bond decoupling at elevated temperatures. Supersaturation of $[Al(OH)_4]^-$ then triggers the nucleation and subsequent growth of poorly crystalline boehmite particles in the shape of porous 2D nanosheets. As-formed boehmite nanosheets form a porous shell layer on the surface of AlN particles [166].

The kinetics of AlN hydrolysis are mechanistically described by an un-reacted-core model [175], [177]. The proposed model can however only adequately describe the hydrolysis mechanism in the second reaction step, where boehmite forms and grows on the surface of a shrinking AlN particle [177]. During the second stage, the reaction's rate is limited by either the kinetics of the reaction between AlN and water or by the diffusion of the reactants (hydroxyls) through the product layer of boehmite [177]. The diffusion of species

is the rate-controlling step in the case of suspensions with temperature between 22 °C and 70 °C, while the reaction itself determines the conversion rate in the case of suspensions where the temperature is above 90 °C [177].

For the third and last stage of the AlN hydrolysis, the recrystallization of boehmite to bayerite takes place [166]. This step was only observed if the reaction temperature was below 90 °C [177]. Above this temperature in the research carried out by Kocjan et.al. no bayerite was observed even after more than 12 days of suspension aging [180].

Kocjan et al. [166] also reported that an increase of the starting hydrolysis temperature immensely accelerated the hydrolysis rate. For example, a 50 % conversion rate was achieved more than 500 times faster at 90 °C in comparison to 20 °C. Aside from the temperature it was also observed by the same research group [177] that the initial pH value can also fasten the rate of the hydrolysis. While the pH value cannot accelerate the rate of hydrolysis *per se*, it was observed that when the initial pH value of suspensions was around 10, the induction period could be avoided even at temperatures below 90 °C. This was ascribed to the instability of the aluminum hydroxide ($Al(H_2O)(OH)_3$) gel layer at such high pH values.

All of the carried out work demonstrates that the hydrolysis of AlN powder is indeed a suitable path for the preparation of hierarchically assembled MA. It therefore represents a promising alternative to the already established synthesis paths. Additionally, the experimental results suggest that the temperature is the only critical parameter determining whether the predominant product will be in the form of bayerite or boehmite. Hence, the temperature should be carefully controlled throughout the entire synthesis process.

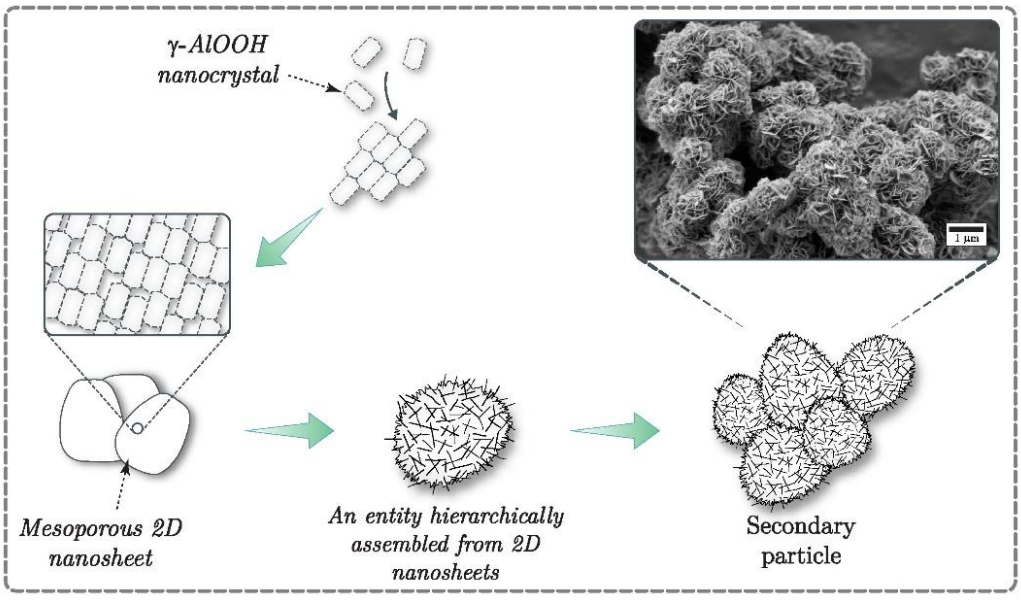

Figure 1.11: The proposed mechanism of hierarchical assembly of γ–AlOOH nanocrystals to secondary particles.

MA powder obtained through the calcination of boehmite prepared by AlN hydrolysis is of high purity, has a controlled (meso)porosity with pore sizes around 4 nm and mesopore volume of ≈ 0.65 mL/g, and a high surface area exceeding 200 m^2/g. An individual MA particle has a hierarchical structure, where a secondary entity is composed of micron-sized, aggregated globular spheres with a flower-like structure formed through a repeatable self-assembly of nanocrystalline 2D nanosheets (Figure 1.11) [110], [166], [177]. Additionally,

unlike the traditional processes for the production of γ–Al_2O_3 of high purity, where reaction yields are relatively low, the AlN powder hydrolysis enables preparation of abundant amounts of MA powder in a single reaction step [177], [182]. It should also be noted that AlN hydrolysis approach does not require any organic solvents, hazardous surfactants, lengthy ageing steps or hydrothermal/solvothermal treatments, needed in alternative synthesis paths to obtain similar hierarchically structured MA powders [116], [122], [123], [177].

1.5.2 Hierarchically macro-mesoporous alumina (HMMA)

The benefits of hierarchical porosity, i.e., presence of micro- and macropores or meso- and macropores inside a single ceramic monolith have been recognized [4], [23], [183], [184]. Advantage of hierarchically porous ceramic monoliths lies in the balance between two pore size groups, each providing or improving different material's advantageous properties [8]. The presence of macropores considerably enhances material's mass transport capacity and diffusion properties [23], [185], [186]. On the other hand, the presence of micro- and mesoporosity substantially increases the accessible surface area of the material and consequently the number of active sites [22], [183], [186], [187]. When a hierarchically macro-mesoporous material is to be used in a flow-catalysis application, the macropores will ensure a good fluid permeability. Mesopores will be the active sites where chemical reaction occurs [165].

Various methods for the preparation of hierarchically porous materials have already been reported, such as freeze casting [23], sol-gel processing [184], polymer foam filling [188], and phase separation [189]. Attempts at a simplified consolidation path for preparation of hierarchically porous ceramics have also been made. An example is a one-pot synthesis like single step pyrolysis [8].

Mesoporous alumina is one of the materials that has already received a lot of attention as a prosperous candidate for the fabrication of hierarchically macro-mesoporous materials [183], [184], [188]–[192]. The great potential of MA powders for the preparation of hierarchically porous materials lies in its intrinsic mesoporosity and hierarchical structure. When MA is consolidated with a technique enabling the formation of macropores, a hierarchically maco-mesoporous material can be readily obtained [111], [193], [194]. The non-spherical shape of MA powders may offer an advantage in the formation of porous materials [195].

However, despite the abundance of literature on the preparation of HMMA monoliths, structural properties, such as mechanical strength, thermal properties, pore size distribution or permeability are rarely reported [165].

In the fabrication of HMMA monoliths, two procedures are commonly used. In the first approach a sol-gel MA synthesis is combined with the phase separation process by the addition of porogen [136], [138]. Macropores are generated when porogen is mixed together with the aluminum sol-gel precursor [183], [189]. The second procedure consists of impregnation of macroporous polymer template with alumina hydrosol [188], [191]. Both procedures have some drawbacks. Cracking of monolith during the drying phase may occur in the sol-gel process [146], while the second route requires a burn-out step to remove the sacrificial template. The latter can have adverse effects on the final material's surface area and porosity. In addition, the control over macropore insertion via second route is usually rather difficult.

A limited number of suitable techniques for the preparation of HMMA monoliths derives from the relatively low thermal stability of MA. At temperatures above 700 °C the high surface area and mesoporosity start to gradually disappear. Both properties completely vanish above the temperature of 1200 °C, where the transformation to α–Al_2O_3

occurs [109]. The relatively low temperature stability means that HMMA monoliths cannot be sintered like traditional porous ceramics without loosening of the surface properties. This greatly limits the number of techniques suitable for the preparation of HMMA materials. A method for the preparation of HMMAs that would not require any sintering steps is therefore needed.

Aside from a very limited number of suitable techniques, some other challenges are yet to be met in the preparation of HMMA monoliths [165]. One problem is the already mentioned limited synthesis strategies to obtain abundant amounts of MA powder with controlled surface properties. The second problem lies in the installation of macropores into the HMMA material. Although the latter enhances the mass transport properties, it also causes a considerable loss of the mechanical strength [165]. Therefore, to the best of our knowledge a suitable highly porous ceramic material, where incorporation of macropores would not cause a too discernable deterioration of mechanical properties, is yet to be fabricated.

Chapter 2

Aims and Hypothesis

2.1 Aims

The first aim of this doctoral dissertation was to adjust the AlN powder hydrolysis process to facilitate production of larger amounts of hierarchically assembled MA powder. For this purpose, different hydrolysis parameters were investigated and adjusted to obtain the highest yield of boehmite powder (MA precursor). The as-prepared powder was thoroughly characterized in order to determine crystal the structure, porosity, bulk and apparent density, particles size distribution, particle shape and surface area.

The second aim was to study the dispersibility behavior of as-synthesized MA powder in water using NaPAA. Suspensions were characterized for zeta potential, rheological properties and sedimentation behavior.

The third aim was to study different mechanisms for inducing weak (bridging) flocculation to facilitate long-term stability of the suspensions, which were prone to immediate sedimentation and segregation after MA suspension. A possibility of achieving long-term stability by the addition of divalent cations (Mg^{2+} and Ca^{2+}) or fibrous second phase (CNF) to NaPAA dispersed MA particles was investigated. The effectiveness of both mechanisms was evaluated in detail through zeta-potential and rheological characterization and determination of sedimentation behavior.

The fourth and the last objective of this dissertation was to employ freeze-casting for consolidation of aqueous suspensions containing NaPAA dispersed MA powder to prepare highly-porous MA monoliths. The main focus was on the improvement of poor mechanical properties (fragility) commonly observed in highly porous materials. This problem was by incorporation of divalent cations or CNF into NaPAA-dispersed-MA-powder suspensions, serving as a green body reinforcement. HMMA monoliths were tested for porosity, surface area, permeability, thermal conductivity and compressive strength. The nature of triggered associations (weak bridging flocculation) was also investigated by FTIR analysis.

2.2 Hypothesis

The following hypotheses were set for this doctoral dissertation:

- ∴ Hydrolysis of the AlN powder in diluted aqueous suspensions can be used as a simple synthesis method for the preparation of abundant amounts of pure, micron-sized, mesoporous boehmite powder hierarchically assembled from 2D nanosheets that can be readily re-dispersed in water as γ–Al_2O_3 after dehydration.
- ∴ Aqueous suspensions containing hierarchically assembled, micron-sized MA particles must be dispersed and stabilized prior to consolidation. Otherwise

sedimentation and particle segregation occur, both leading towards undesired properties of final material. We hypothesize that polyacrylic acid (PAA) with MW 225 000 g/mol will adequately disperse and sufficiently stabilize MA particles.

∴ Triggering interparticle associations (bridging flocculation) in aqueous suspensions containing PAA-dispersed MA particles via the addition of divalent cations (Mg^{2+} and Ca^{2+}) or cellulose nanofibers (CNF) will endow the suspensions with long-term stability, i.e., prevent sedimentation and segregation through bridging flocculation.

∴ Addition of divalent cations (Mg^{2+} and Ca^{2+}) or cellulose nanofibers (CNF) to NaPAA-dispersed MA powder suspensions will also provide mechanical rigidness to the consolidated MA green bodies. We hypothesize that provided stability will be high enough to avoid sintering, which would have adverse effects on material porosity and surface area.

Chapter 3

Materials and Methods

3.1 Chemicals

- ∴ Aluminium nitride powder, AlN (Grade C, H.C. Starck, Goslar, Germany).
- ∴ Isopropanol, CH_3–CH(OH)–CH_3 (99.8 %, pure for analysis, Sigma–Aldrich GmbH, Germany)
- ∴ Sodium polyacrylate, –[–CH_2–CH–COONa–]–$_n$ (molecular weight 225 000 g/mol, 20 wt% aqueous solution, Polysciences Europe GmbH, Germany), denoted as NaPAA.
- ∴ Magnesium nitrate hexahydrate, $Mg(NO_3)_2 \cdot 6H_2O$ (ACS reagent grade, Merck & Co., Kenilworth, New Jersey, USA).
- ∴ Magnesium chloride hexahydrate, $MgCl_2 \cdot 6H_2O$ (ACS reagent grade, Sigma–Aldrich, St. Louis, Missouri, USA).
- ∴ Magnesium acetate tetrahydrate, $Mg(CH_3COO)_2 \cdot 4H_2O$ (98 %, Sigma–Aldrich, St. Louis, Missouri, USA).
- ∴ Calcium chloride, $CaCl_2$ (97 %, Sigma–Aldrich, St. Louis, Missouri, USA).
- ∴ Hydrochloric acid, HCl (37 %, Carlo Erba Reagents, Barcelona, Spain).
- ∴ Sodium hydroxide, NaOH (99 %, Neolab Migge GmbH, Heidelberg, Germany).

3.1.1 Preparation and characterization of cellulose nanofibers gel

Cellulose nanofibers (CNF) were provided by the Instituto de Ciencia de Materiales de Madrid [50]. According to their procedure CNF were obtained from the bleached *Eucalyptus globulus* kraft pulp. An aqueous suspension of wood pulp was subjected to chemical nanofibrillation by TEMPO-mediated oxidation and a subsequent mechanical defibrillation in a high-pressure microfluidizer (Microfluidics Corp., USA). As a result, a 1.55 wt% CNF gel was obtained with an approximate fiber thickness of 2 nm. Due to the TEMPO-mediated oxidation, the cellulose nanofibers were carboxylated (900 µmol/g charge) [98].

CNF were characterized by atomic force microscopy (AFM) using a Cervantes instrument (Nanotec electrónica S.L., Spain). The microscope was equipped with PPP-FMR cantilevers (Nanosensors, Switzerland), with a 75-kHz resonance frequency and a 1.5-N/m spring constant. Images were acquired under ambient conditions in a modulated amplitude mode. Detailed process of CNF synthesis and characterization is described elsewhere [50].

3.2 MA Powder Synthesis and Characterization

3.2.1 Hydrolysis of AlN

Hydrolysis of commercially available AlN with a 2.54 µm mean particle size was used to prepare the MA powder. Firstly, distilled water was heated to a temperature above 95 °C in a glass beaker. Then during constant mixing 10 wt% of AlN powder was added. The glass beaker was covered with aluminium foil, placed in an oven and left to boil for 7h.

During this time, hot water was added to the reaction mixture several times in order to maintain the suspension concentration. After 7 hours the conversion of AlN to boehmite was completed. The reaction mixture was then filtered through filter paper (Grade 393, Sartorius AG, Germany), washed with isopropanol and dried in an oven at 120 °C for 24 h. The dried powder was sieved through 230 mesh to eliminate any larger aggregates formed during hydrolysis. The as-synthesised powder was finally treated at 500 °C for 1 hour (heating rate 10 °C/min) in an oven with air to achieve the conversion of boehmite to γ–Al_2O_3.

3.2.2 Powder characterization methods

3.2.2.1 X-ray diffraction

Intermediate (boehmite) and final (MA) powders were characterized by X-ray diffraction (XRD). To obtain XRD patterns, a Bruker diffractometer (AXS-D4 Endeavor, Bruker, USA) using a Cu–$K_{\alpha 1}$ radiation source with a wavelength of 1.542 Å was used. The machine was set to a continuous mode in the 2θ range 10–70°, with a 0.02° step and an integration time of 3 seconds. For the processing of XRD spectra the Eva software (version 12.0) and the PDF-2 database (released 2006) were used. ICDD-JCPDS card number 83-2384 was used to identify boehmite, while card number 74-2206 was used for the identification of MA powder. To estimate average crystallite sizes, the Scherrer equation was applied.

3.2.2.2 Particle-size distribution

For AlN and MA powder particle size determination, a laser-scattering particle-size-distribution analyser (LA-920, Horiba, Japan) was used. Measurements of AlN powder were conducted in isopropanol, while for all the measurements of MA deionized water was used as a dispersion medium. Before the addition of MA powder, 3-basic ammonium citrate was added to the water as a dispersion agent. No dispersant was used in the case of isopropanol-based suspensions. Prior to all the measurements, the suspensions in the measuring chamber were stirred and ultra-sonicated for 5 minutes.

3.2.2.3 Scanning and transmission electron microscopy

Scanning electron microscopy (SEM) and transmission electron microscopy (TEM) were used to characterize the morphology of a pure MA powder. Additionally, SEM was also used to characterize the MA powder with added NaPAA and CNF. Scanning electron microscopy (SEM) was carried out on the ULTRA plus microscope by Carl Zeiss SMT, Germany, at an accelerating voltage of 2 kV. TEM analyses were carried out on a JEM 2100 microscope by Jeol, Japan. Due to the low electron conductivity, the MA powder was sputtered with gold prior to the analyses.

3.2.2.4 Nitrogen sorption

A Nova 2000e (Quantachrome GmbH & Co. KG, USA) nitrogen-sorption analyser was employed to obtain nitrogen adsorption/desorption isotherms. Before the measurement

powders were degassed at 200 °C in a vacuum for at least 12 h. The specific surface areas were calculated using the Brunauer–Emmett–Teller (BET) equation with the data in the P/P0 range 0.05–0.3. The pore size distributions and pore volumes were obtained using the Barrett–Joyner–Halenda (BJH) model from the desorption curve of the isotherms.

3.2.2.5 Mercury porosimetry

The bulk, envelope and apparent densities of the MA powder along with the MA powder's total porosity and pore size distribution were determined using mercury-intrusion porosimetry (Pascal 140 and Pascal 440, Thermo Fisher Scientific, USA), with pressures ranging from 10 kPa to 400 MPa. The surface tension and the contact angle of mercury were set to standard values (0.485 mN/m and 130°, respectively). Prior to the measurement powders were dried in an air oven at 200 °C for at least 12 h.

3.3 Preparation and Characterization of MA Powder Aqueous Suspensions

3.3.1 Suspensions preparation

All of the MA powder quantities in the aqueous suspensions are expressed as apparent volume fractions φ_A, unless otherwise stated. For the calculation of the latter MA powder's apparent density (ρ_A), determined by mercury intrusion porosimetry, was used.

3.3.1.1 Rheological properties

Aqueous suspensions of different compositions were prepared for the determination of rheological properties. Sodium polyacrylate (NaPAA) in the quantity of 0.16–7 wt% (based on the mass of the MA powder) and predetermined quantity of water were placed into a glass bottle and mixed with a magnetic stirrer. Next, the MA powder was slowly added to the solution during constant mixing. For the purpose of studying the influence the addition of different amounts of NaPAA or the addition of divalent cations have on suspension's properties, the MA powder volume fraction (φ_A) was set to 0.082. For the determination of the influence the amount of added MA powder has on rheological behaviour of suspensions volume fractions between 0.013 and 0.126 were tested. If not otherwise stated, the volume fractions of the MA powder in the suspensions are expressed as apparent volume fractions φ_A (calculated using apparent powder density ρ_A).

For the determination of the influence divalent cations have on suspension's properties, $Mg(NO_3)_2$, $MgCl_2 \cdot 6H_2O$, $Mg(CH_3COO)_2 \cdot 4H_2O$ or $CaCl_2$ in amounts of 1–70 mmol/mol were added during intense mixing to the suspensions already containing 1.4 wt% NaPAA-dispersed MA powder. The quantity of cations is given in mmol of M^{2+} per 1 mol of MA powder.

The influence of CNF addition to the aqueous suspensions containing 1.4 wt% NaPAA-dispersed MA powder was also studied. For this purpose, the CNF in amounts of 0.5 to 10 wt% based on the mass of the dry MA powder was added prior to MA powder addition and thoroughly mixed. Subsequently, into this suspension, the MA powder was slowly added during mixing. The MA volume fractions (φ_A) were between 0.013 and 0.097.

The pH value of the suspensions was set to either 6 or 9 (SevenMulti pH meter equipped with an InLab expert pro electrode, Mettler Toledo, International Inc., USA) with HCl or NaOH, respectively. The influences of the addition of divalent cations and CNF were only determined at pH value of 9. On the other hand, for the purpose of studying the influence of optimal NaPAA addition and the influence of MA volume fraction on suspensions

properties two separate sets of suspensions were prepared. The pH value of one part was set to 6 and of the other to 9.

In the last step, the suspensions were homogenized with a 24-hour ball milling. YTZ (yttria-stabilized zirconia) balls (purchased from Tosoh Europe B.V.) with 3 mm diameter were used in the amount of approximately 12 balls per 1 g of dry MA powder. After homogenization the pH of suspensions was checked again and if necessary corrections to the pH value were made.

3.3.1.2 Sedimentation rates

Sedimentation rates of selected suspensions were determined in order to establish how the addition of NaPAA, divalent cations, CNF or pH influence settling of MA particles over predetermined time periods.

For this purpose, suspensions containing 1.4NaPAA dispersed MA powder in volume fraction (φ_A) of 0.027 and pH value of 9 were prepared. One suspension was prepared without NaPAA addition (contained only MA powder) in order to determine the influence NaPAA has on sedimentation rates.

To determine the influence of divalent cations Mg^{2+} ions (as $MgCl_2 \cdot 6H_2O$) in quantities of 30 and 70 mmol/mol were added.

Influence of CNF addition was determined by letting suspensions containing 1.4NaPAA dispersed MA powder and from 0.5 to 5 wt% of CNF to settle.

To determine the influence of pH, two suspensions containing MA powder ($\varphi_A = 0.027$) with pH 6 were prepared. One contained only MA powder while to the other prior to MA powder 2.5 wt% of NaPAA was added.

Prior to the sedimentation test, the suspensions were homogenized with a 24-hour ball milling. YTZ balls with 3 mm diameter were used in the amount of approximately 12 balls per 1 g of dry MA powder. After homogenization, the pH of suspensions was checked again and where necessary corrected to the predetermined value.

3.3.1.3 Zeta potential

For the determination of zeta potential diluted suspensions with a MA volume fraction (φ_A) of only 0.00005 (0.017 wt%) were prepared. Prior to all of the measurements, the suspensions were mixed with a magnetic stirrer, while the pH was adjusted with HCl or NaOH.

Firstly, the zeta potential of MA particles was measured in the pH range from 2 to 12. To determine the influence, the NaPAA addition has on the zeta potential of dispersed MA particles, NaPAA in five different amounts ranging from 0.4 to 2.2 wt% was added. The zeta potential for all five suspensions was determined inside the pH range 2–6. The exception was the suspension containing 1.4 wt% NaPAA, where additional points were determined in order to characterize the zeta potential inside pH range from 2 to 12.

To other suspensions either $MgCl_2 \cdot 6H_2O$ in amounts of 5–70 mmol/mol or CNF in amounts of 0.5–7 wt% was added. The zeta potential of suspensions containing either Mg^{2+} cations or CNF was measured only at the pH value of 9. The exception was the suspension containing 5 wt% of CNF, where the zeta potential was determined in the pH range 3.5–12.

For the determination of zeta potential of pure CNF and the mixture containing only CNF and NaPAA, firstly the diluted suspension of CNF with a mass fraction of 0.04 wt% was prepared. After thorough mixing with magnetic stirrer, the suspension was divided into two parts. To the first part of the suspension, pH was set to 9 with the addition of NaOH, followed by a zeta potential measurement. To the second part, NaPAA was added (28 wt% of the CNF mass). After mixing, pH was set to 9 and zeta potential measured.

The mass ratio between CNF and NaPAA was the same as in the case of suspension containing 1.4NaPAA–MA and 5 wt% of CNF.

3.3.2 Suspensions characterization methods

3.3.2.1 Rheological properties

The rheological properties were determined on a rotational rheometer (Physica MCR 301, Anton Paar, GmbH, Graz, Austria). For the MA suspensions with $\varphi_A \leq 0.119$ and distilled water a CC 17 cylindrical system was used, while the suspensions with $\varphi_A = 0.126$ was measured using a CP 50-2 con-plate system with a diameter of 50 mm and an angle of 2°. The viscosity of the suspensions was measured in the shear-rate range of 1 s^{-1} to 200 s^{-1} at a constant temperature (23 ± 0.1 °C).

3.3.2.2 Sedimentation tests

For the determination of sedimentation rates 17 mL of selected suspensions were poured into glass test tubes with a diameter of 1.2 cm and left to settle for 12 weeks. The readings of sediments height were performed at predetermined times ranging from 5 minutes to 12 weeks.

3.3.2.3 Zeta-potential

Zeta-potential measurements were performed at room temperature on the ZetaPALS Zeta Potential Analyzer (Brookhaven Instruments Ltd, USA). The calculations were made according to the Smoluchowski model.

3.4 Freeze-Casting

3.4.1 Preparation of MA powder aqueous suspensions without or with added Mg^{2+}

1.4 wt% of NaPAA (based on the mass of the MA powder) and a predetermined quantity of distilled water were added to a plastic bottle and mixed with a magnetic stirrer. Then MA powder ($\varphi_A = 0.082$) was slowly added during constant mixing. Suspension was thoroughly mixed, divided into two parts and placed into two plastic bottles. To one part, no additional components were added. To the remaining part, a solution of $MgCl_2$ (3.5 M) was added dropwise. The final amount of Mg^{2+} cations was 30 mmol/1 mol of MA powder.

3.4.2 Freeze-casting of MA powder aqueous suspensions without or with added Mg^{2+}

Approximately 16 mL of aqueous suspension was poured into a cylindrical PTFE mold with an inner diameter of 25 mm. The PTFE mold was placed on top of a copper rod immersed in liquid nitrogen (Figure 1.2). At the beginning of the freezing process, the temperature at the top of the rod was set to 5 °C. The suspensions were freeze-cast at 6 K/min (linear freezing regime) till the final temperature of –50°C was reached. Throughout the freezing process, the temperature was controlled by a thermometer and a heating ring.

After the suspensions were completely frozen, the freeze-cast samples were taken from the mold and placed in a freeze dryer (2–4 LSCbasic, Martin Christ Gefriertrocknungsanlagen GmbH, Germany) set to T = –80 °C and p = 0.001 mbar for approximately 72 h for the ice to sublimate.

3.4.3 Preparation of MA-CNF aqueous suspensions

1.4 wt% of NaPAA (based on the mass of the MA powder) and a predetermined quantity of distilled water were added to a plastic bottle and mixed with a magnetic stirrer. Next, the CNF in mass fractions (w_{CNF}) between 1 and 10 % (based on the mass of the MA powder) was added to the aqueous solution of NaPAA and thoroughly mixed again. In the third step, MA powder in volume fractions (φ_A) between 0.013 and 0.082 was added during mixing. The suspensions were homogenized with a 24-hour ball milling using YTZ balls of 10 mm diameter (approximately 2 balls per 10 mL of suspension). In the last step, if needed, NaOH was added to set the pH value to 9.

For all suspensions, the amounts of NaPAA and CNF were calculated based on the dry MA powder mass. The exception was suspension used for consolidation of monolith FZC–1 (prepared without MA powder), where the components amounts, i.e., mass fractions of NaPAA and CNF were calculated based on the mass of water instead of MA powder. The suspension FZC–1 was prepared according to the above-described process with the following components ratio: per 10 mL of water 0.013 g of NaPAA and 0.066 g of CNF were added (masses of CNF and NaPAA per 10 mL of suspension were the same as in the case of monolith FZC–5).

3.4.4 Freeze-casting of MA-CNF aqueous suspensions

For freeze-casting, suspensions were poured into three differently shaped PTFE molds, namely a cylindrical mold with an inner diameter of 25 mm, a cylindrical mold with an inner diameter of 10 mm or in a square-shaped mold with a side length of 20 mm. For the first type of mold, a suspension volume of approximately 16 mL was needed, while for the second and the third type of mold volumes of suspensions were either 1.5 or 10 mL, respectively.

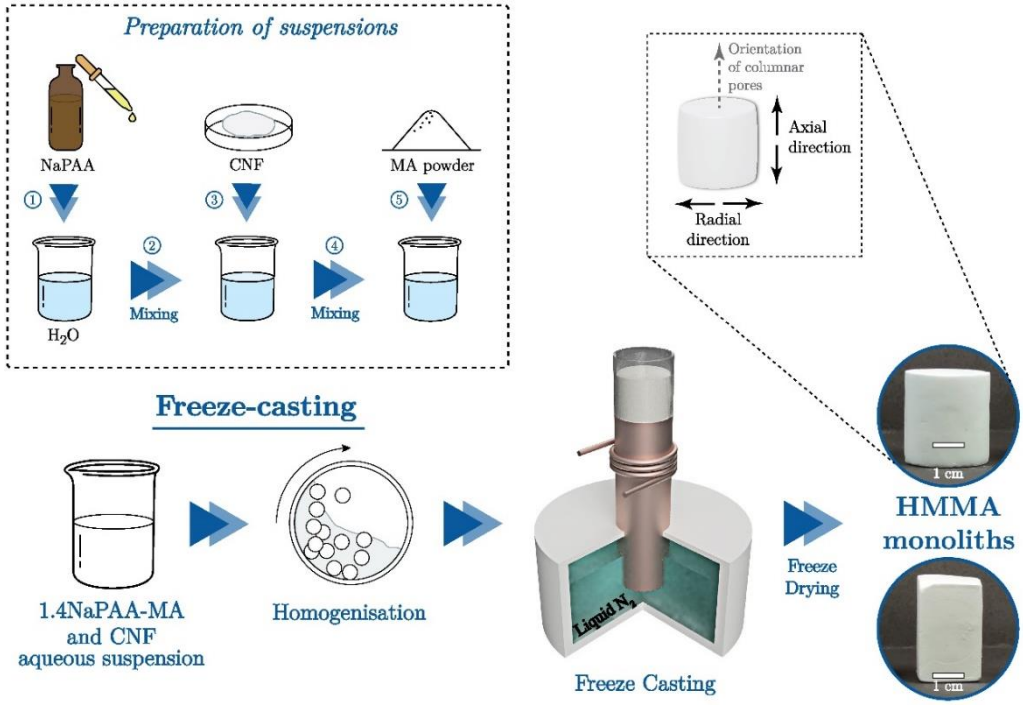

Figure 3.1: Illustration of the preparation of HMMA monoliths by freeze-casting.

The PTFE mold was placed on top of a copper rod immersed in liquid nitrogen. The temperature at the top of the rod was controlled by a thermometer and a heating ring. The suspensions were freeze-cast at two different (linear) freezing regimes, i.e., 1 K/min or 6 K/min. The temperature of the top of the copper rod at the beginning of the freezing process was 5 °C, while the end temperature was –50°C. After the suspensions were completely frozen, the freeze-cast samples were taken from the mold and placed in a freeze dryer (2–4 LSCbasic, Martin Christ Gefriertrocknungsanlagen GmbH, Germany) set to T = –80 °C and p = 0.001 mbar for approximately 72 h for the ice to sublimate.

In Table 3.1 an overview of the suspensions parameters used in the freeze-casting is given. Since the monoliths FZC–1 were prepared without MA powder, and thus the amounts of individual components could not be calculated based on MA powder weight the preparation parameters for this suspension are not part of Table 3.1.

Table 3.1: Overview of suspension parameters and consolidation conditions used in freeze-casting of cellulose-nanofiber-reinforced MA monoliths.

Monolith	**MA volume fraction (φ_A)**	**γ_{MA} (mg/mL)‡**	**γ_{CNF} (mg/mL)‡**	**w_{CNF} (wt%)§**	**MA/CNF (mass) ratio**	**Freezing rate (°C/min)**
FZC–1	/	/	/	/	/	1
FZC–2	0.013	46.0	4.6	10.0	10:1	1
FZC–3	0.013	46.0	4.6	10.0	10:1	6
FZC–4	0.027	92.0	4.6	5.0	20:1	1
FZC–5	0.027	92.0	6.6	7.0	14:1	1
FZC–6	0.027	92.0	6.6	7.0	14:1	6
FZC–7	0.054	190.0	4.0	2.0	50:1	1
FZC–8	0.054	0190.0	4.0	2.0	50:1	6
FZC–9	0.082	289.0	3.0	1.0	100:1	1

‡ γ_{MA} and γ_{CNF} are mass concentrations of MA powder and CNF, respectively (CNF mass per 1 mL of suspension).
§Mass fraction of CNF was determined according to the equation: $w_{CNF} = m_{CNF}/(m_{CNF} + m_{MA})\cdot 100$.

3.4.5 Cold isostatic pressing

Dry-pressing was used to prepare disk-shaped HMMA specimens according to the following procedure: firstly, the MA powder was dried at 200°C. Then either 2.4 or 5 g of powder was placed in a steel die with 25 mm diameter and uniaxially dry-pressed at 100 MPa, followed by a subsequent cold isostatic pressing (CIP) step using a final pressure of 200 MPa (MA–CIP200). Preparation and characterization of monoliths via CIP of hydrolysis-derived-MA powder was already reported elsewhere [110].

3.4.6 Characterization of HMMA monoliths

All monoliths were conditioned in a vacuum dryer at 40 °C for at least 24 h prior to all the measurements. If not otherwise stated aside from drying, no sample treatment was carried out prior to the below analyses.

To describe the orientation of pores inside the monoliths, the terms axial and radial direction are used. The term axial direction refers to the direction parallel to the orientation of columnar pores, i.e., parallel to the direction of freezing, while the term radial direction refers to the direction perpendicular to the orientation of columnar pores.

3.4.6.1 Scanning electron microscopy

Scanning electron microscopy (SEM; ULTRA plus, Carl Zeiss SMT, Germany) was used to determine the approximate size and shape of the macropores evolved during the freeze-casting process. To reduce the electric charging, the samples were coated with gold particles prior to analysis. The analysis was performed at an accelerating voltage of 5 kV. Samples were prepared by cutting thin sections from the middle part of monoliths with a sharp scalpel perpendicular and parallel to the ice growth direction.

3.4.6.2 Nitrogen sorption

The nitrogen adsorption/desorption isotherms were obtained using a Nova 2000e (Quantachrome GmbH & Co. KG, USA) nitrogen-sorption analyser. The Brunauer–Emmett–Teller (BET) equation with the data in the P/P_0 range of 0.01–0.3 was used for the calculations of a specific surface area of individual monoliths. For analyses cylindrical monoliths with a diameter of 10 mm and a height of approximately 20 mm were firstly cut in half in the radial direction and then each half was additionally cut into four pieces in the axial direction to accommodate the dimensions of measuring cells. All pieces were transferred into a measuring cell and degassed at 150 °C for 24 h prior to the measurement.

3.4.6.3 Mercury porosimetry

Mercury-intrusion porosimetry (Pascal 140 and Pascal 440, Thermo Fisher Scientific, USA) was used to determine the total porosities and pore size distribution of HMMA green bodies. The measurements were performed inside the pressure range 10 kPa–400 MPa. This pressure interval enables the characterization of pores with diameters ranging from 115 μm to 3.2 nm. The surface tension and the contact angle of the mercury were set to the standard values of 0.485 mN/m and 130°, respectively. Two measurements per sample were carried out and the results are given as an average value. The mass of monoliths used for one analysis had to be adjusted so that the approximate volume of pores was between 250 and 350 mm^3. To obtain the needed amounts, the cylinders (diameter of 10 mm) were firstly cut to adjust their height to 14 mm (equal parts were cut from the upper and bottom side of the cylinders). Then the samples were cut in the axial direction into three approximately equal parts. For the analysis of monoliths FZC–1, FZC–2 and FZC–3 all three parts had to be placed into the measuring cell to achieve the adequate volume of pores, while for other monoliths, only one third of the cylinder was enough.

3.4.6.4 Geometrical density

Geometric densities (ρ_G) were determined based on the relationship between the weight of the dried monoliths (weighing was performed with a precision of ±0.001 g) and their volume. The volume was calculated from the monoliths height and diameter measured using a digital caliper with a precision of ±0.01 mm.

For each monolith composition the mass and volume of two samples were measured, namely of one cylindrical monolith with a diameter of 25 mm and one cubic monolith with a side of 20 mm. Where needed, the upper surface of monolith was gently polished using silicon carbide grinding paper (2400 grit) to make it parallel to the bottom plate. The average value of both calculated ρ_G is given as a result.

3.4.6.5 µ–CT

X-ray micro-computed tomography (µ–CT) was performed with the XRadia MicroXCT-400 tomograph (XRadia, Concord,CA, USA) in order to investigate the characteristics of the pore structure of freeze-cast monoliths. For this analysis monoliths with a diameter of 10 mm and approximate height of 15 mm were used. The beam energy was set to 40 kV, while the beam's intensity was set to 176 µA. A filter was not used. A charge-coupled device (CCD) camera acquired 500 projection images at an exposure time of 5 s per projection. The resolution of scanned samples using macro objective (0.39x) was 10.6 µm per pixel.

3.4.6.6 Thermal conductivity

Thermal conductivity (λ) and specific heat capacity (c_p) were measured on a Hot Disk thermal constant analyzer TPS 2500 S (HotDisk AB, Gothenburg, Sweden). Freeze-cast as well as CIP consolidated monoliths were characterized. A Kapton sensor with a diameter of 6.4 mm, sandwiched between a pair of samples, was used for the determination of λ. If needed, the upper surface of a monolith was gently polished using silicon carbide grinding paper (2400 grit) to make it parallel to the bottom plate. The measurements were performed in an anisotropic module. Monoliths of cylindrical shape were used for the determination of thermal conductivity in axial direction (λ_a), while cubical monoliths were used to determine thermal conductivity perpendicular to the pore orientation, i.e., in radial direction (λ_r) as illustrated in Figure 3.2. Cylinders with a diameter of 25 mm and minimum height of 20 mm were used in the case of freeze-cast monoliths, while the height was 12 mm in the case of monoliths MA–CIP200. For the determination of radial thermal conductivity (only for freeze-cast monoliths) cubes with a side dimension of 20 mm were used.

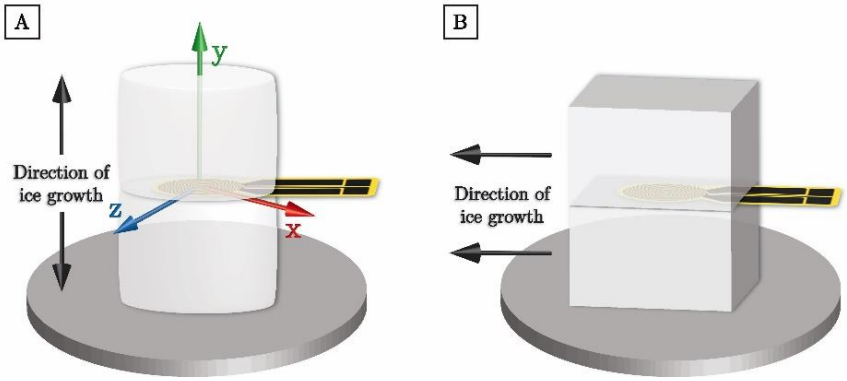

Figure 3.2: Illustration of a measurement setup for the determination of axial (A) and radial (B) thermal conductivity. Arrows in the left figure indicate an in-plane (xy) and out-of-plane (xz) measuring direction.

The determination of specific heat capacity of monoliths was performed using a special sensor-cell, consisting of a hollow gold cylinder. Firstly, a reference measurement was performed, where an empty cylinder was thermally insulated with polyurethane foam and carefully heated with an applied power of 90 mW for 80 seconds. Under these conditions, the temperature inside the empty cylinder increased from 22.2 °C to 30.1 °C. Then the polyurethane thermal insulation was removed and the cylinder was left to cool down. In the next step, a sample of known mass was placed inside it, and then the cylinder was again thermally insulated with polyurethane foams and heated. Electrical heating power was adjusted, so that the temperature increase was the same as in the reference

measurement (≈ 8 °C). Five independent measurements with a 2-hour conditioning time between measurements were performed.

All of the results are given as an average value of five measurements per sample with a 1-hour conditioning time between individual measurements for thermal conductivity and 2-hour conditioning time for heat capacity measurements.

3.4.6.7 Thermographic imaging

An infrared thermal camera from Fluke (Ti55FT IR FlexCam) with a thermal sensitivity of 0.05 °C was used to capture thermographic images. Cylindrical samples with a 25-mm diameter and approximate height of 25 mm were placed on a plate made of mullite fiber wool as illustrated in Figure 3.3. Through a round hole in the middle of the plate, a heating source in the shape of a small copper cylinder with a 10 mm diameter was placed. The temperature at the top of the copper cylinder was approximately 180 °C.

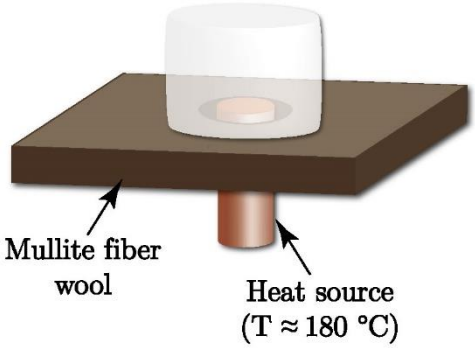

Figure 3.3: Illustration of a measurement setup used to capture thermographic images.

3.4.6.8 Permeability

Cylindrical samples with a 10-mm diameter and a height (L) between 25 and 30 mm were used to perform permeability testing. The latter were conducted at room temperature using filtered compressed air as fluid. The specimens were radially sealed using a heat shrink tubing. The volumetric gas flow (Q) was recorded as a function of the differential pressure (Δp) between upstream (p_i) and downstream (p_o) side of the specimen. A minimum of 12 sets of pressure drop and Q values were recorded per sample. The measurements were performed inside the Δp range 0.6 and 2.4 bar, with the maximum pressure depending on the monolith tested, i.e., the samples integrity during testing. Three samples were tested per batch.

Forchheimer's equation for compressible fluids (Eq. 3.1) [196] was used to determine the Darcian (k_1) and non-Darcian permeability (k_2):

$$\frac{p_i^2 - p_o^2}{2p \cdot L} = \frac{\eta}{k_1} \cdot \left(\frac{Q}{A}\right) + \frac{\rho}{k_2} \cdot \left(\frac{Q}{A}\right)^2 \tag{3.1}$$

An air's viscosity η of 1.84×10^{-5} Pa · s and air density ρ of 1.16 kg · m^{-3} were assumed (p = 1004 mbar and T = 22 °C). In order to determine k_1 and k_2, a quadratic function was fitted to (p_i^2-$p_o^2/2pL$) versus Q/A, using the least-squares method.

3.4.6.9 Compressive testing

To determine the compressive strength of freeze-cast monoliths Quasar 100 (Galdabini, Cardano al Campo, Italy) with a 100 N load cell was used. Cylinders with a diameter of 25 mm and an approximate height of 25 mm were used to determine compressive behaviour in the axial direction, while cubic monoliths with a side of 20 mm were used to determine

compressive behaviour in the radial direction (Figure 3.4). The monoliths were compressed at a constant speed of 0.5 mm/min.

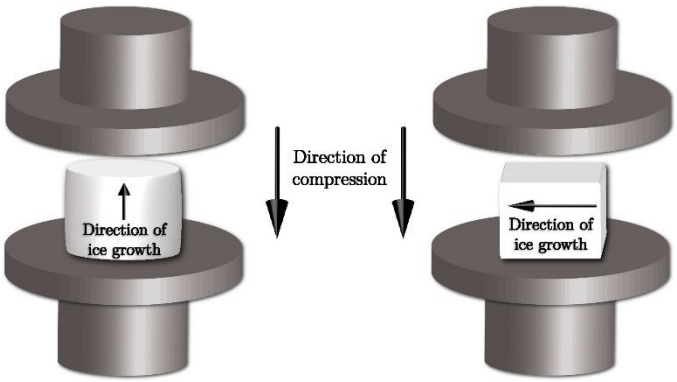

Figure 3.4: Illustration of a measurement setup for the determination of axial (left) and radial (right) compressive properties of freeze-cast monoliths.

A maximum of two samples per batch were tested and the results were averaged. Results where only one sample per batch was compressed are marked. Thus the obtained results should be regarded as an estimation. However, the results are sufficient to evaluate the influence of individual processing parameters on compressive properties.

3.5 FTIR Analyses

FTIR spectra of pure MA powder, freeze-dried CNF gel (1.55 wt%), a sample containing only CNF and NaPAA (FTIR–1) and sample containing only CNF and MA powder (FTIR–2) were recorded. Prior to the FTIR analyses, all samples were treated at 120 °C for 12 h to remove any water residues. The exception was pure MA powder, which was treated at 200 °C.

FTIR was performed on Spectrum 100 (Perkin Elmer, Waltham, Massachusetts, USA). The spectra were recorded in the range 500–4000 cm^{-1} with a resolution of 4 cm^{-1}. Eight scans were collected for each measurement.

3.5.1 Sample preparation for FTIR measurements

Sample FTIR–1 was prepared by mixing of 0.02 g of NaPAA, 6.5 g of 1.55 wt% CNF gel and 15.5 mL of distilled water in a plastic bottle with a magnetic stirrer. To prepare the sample FTIR–2 6.5 g of CNF gel (1.55 wt%) and 15.5 mL of distilled water were placed in a plastic bottle and mixed with a magnetic stirrer. Then 1.0 g of MA powder ($\varphi_A = 0.013$) was slowly added during mixing. Both suspensions were homogenized with a 24-hour ball milling. YTZ balls of 10 mm diameter were used (approximately 5 balls). In the last step, a small amount of NaOH (Neolab Migge GmbH, Germany) was added to set the pH value to 9 (SevenMulti pH meter equipped with an InLab expert pro electrode, Mettler Toledo, International Inc., USA). After ball milling plastic bottles containing suspension were immersed into liquid nitrogen for 5 minutes and then placed into a freeze dryer (2–4 LSCbasic, Martin Christ Gefriertrocknungsanlagen GmbH, Germany) set to T = –80 °C and p = 0.001 mbar for the ice to sublimate.

Chapter 4

Results and Discussion

4.1 Outline of the Research

I. MA powder synthesis and characterization: Hydrolysis of AlN powder was exploited to prepare abundant amounts of hierarchically assembled MA powder. As-prepared powder was characterized in detail by determining its crystal structure, particles size distribution, porosity, bulk, envelope and apparent density, particle shape and surface area.

Description of synthesis path and detailed powder characterization is part of C*hapter 4.2* and research article: H. Hudelja, B. Wicklein, D. Kuščer and A. Kocjan: Triggering the aqueous interparticle association of γ-Al_2O_3 hierarchical assemblies using divalent cations and cellulose nanofibers. *J. Eur. Ceram. Soc.*, 41, 590–598 (2021).

II. Preparation of stable MA powder aqueous suspensions: In the first step, the dispersibility of AlN-hydrolysis-derived-MA powder in water using NaPAA was optimized through characterization of zeta potential, rheological properties and sedimentation behavior. In the second step, interparticle interactions between NaPAA-dispersed MA particles (bridging flocculation) were triggered. The latter was achieved via the addition of divalent cations (Mg^{2+} and Ca^{2+}) or cellulose nanofibers (CNF). The effectiveness of both mechanisms was evaluated in detail.

This topic is addressed in C*hapter 4.2* and research article: H. Hudelja, B. Wicklein, D. Kuščer and A. Kocjan: Triggering the aqueous interparticle association of γ-Al_2O_3 hierarchical assemblies using divalent cations and cellulose nanofibers. *J. Eur. Ceram. Soc.*, 41, 590–598 (2021).

III. Processing of stabilized MA powder aqueous suspensions: Hierarchically macro-mesoporous alumina monoliths were prepared for the first time by freeze-casting of MA powder suspensions stabilized by the addition of NaPAA and Mg^{2+} or CNF.

Further on, the suspensions containing different amounts of NaPAA-dispersed MA powder and CNF were frozen at two different freezing rates. The influence of process parameters (MA powder volume fraction, CNF content and freezing rate) on density (porosity), permeability, thermal and mechanical properties were studied in detail.

The preparation of hierarchically porous monoliths from MA powder and CNF via freeze-casting, enhancement of their mechanical properties and detailed characterization of as-shaped monoliths is addressed in C*hapter 4.4* and research article: H. Hudelja, T. Konegger, B. Wicklein, J. Čretnik, F. Akhtar, A. Kocjan: Freeze-casting of highly porous cellulose-nanofiber-reinforced γ-Al_2O_3 monoliths. *Open Ceram.*, 5, 100069 (2021).

The nature of interactions between MA powder, NaPAA and CNF were investigated by FTIR (*Chapter 4.4.1*). An attempt to define the nature of interactions between NaPAA-

dispersed MA particles and CNF was made in order to establish whether any new chemical or hydrogen bonds are formed or if the interactions are only of a mechanical origin (entrapment).

4.2 AlN-Hydrolysis Derived MA Powder

The hydrolysis of AlN powder in diluted aqueous suspension was used to prepare MA powder, as already demonstrated by Kocjan et al. [110], [166]. However, slight changes of the described synthesis conditions had to be made. Firstly, the concentration of AlN powder in the suspension was increased from the originally suggested 3 wt% to 10 wt% to obtain larger quantities of MA powder. Secondly, the time of hydrolysis had to be increased from 4 to 7 hours in order to achieve a complete conversion of AlN to boehmite. This increase was needed due to the slightly larger size of AlN particles used in the present doctoral dissertation [197]. Although the material was provided by the same manufacturer, the mean particle size of AlN powder was 2.54 μm in comparison to the 1.2 μm average particle size used by Kocjan et al. [110], [166].

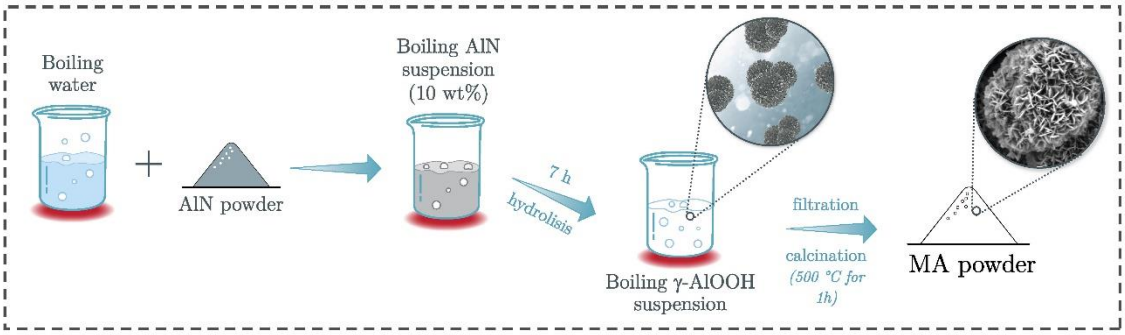

Figure 4.1: An illustration of MA powder synthesis process through hydrolysis of AlN powder.

The hydrolysis was conducted by dispersing AlN powder in boiling water and tempered for the required amount of time, as illustrated in Figure 4.1. A complete conversion of the AlN to single-phase boehmite was achieved after 7 hours, as can be seen from the XRD pattern of a filtered and dried powder shown in Figure 4.2A, where no peaks of AlN nor aluminum trihydroxides were present. The obtained boehmite powder was then calcined at 500 °C for 1 hour in air, where a topotactic transformation to mesoporous γ–Al_2O_3 (MA) occurred (Figure 4.2A) [198].

According to the Scherrer equation, the average crystallite size of the boehmite powder was 9.5 nm (d_{010}), while a smaller size of 4.2 nm (d_{100}) was obtained for MA powder. The nanocrystallinity was additionally supported by the TEM analysis (Figure 4.2B). As can be seen from the TEM micrograph, a MA particle consisted of stacked 2D nanosheets with the thickness of approximately 6 nm. The presence of mesopores in a single nanosheet can be observed in Figure 4.2C.

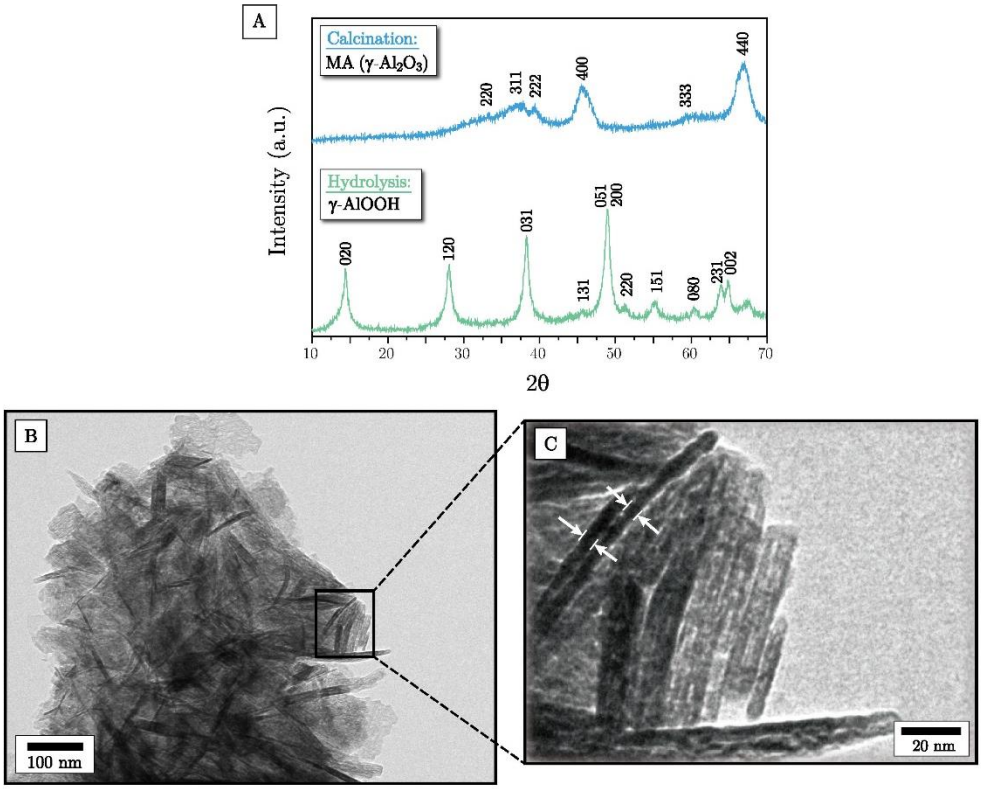

Figure 4.2: A) XRD patterns of the AlN-hydrolysis-derived boehmite and MA powder obtained after the calcination of boehmite at 500 °C. B) TEM micrograph of a part of hierarchically assembled MA particle. Arrows mark the thickness of a single 2D nanosheet.

High mesoporosity of the as-synthesized MA powder was confirmed by the nitrogen adsorption/desorption measurements. The obtained type-IV isotherm, shown in Figure 4.3, is representative of mesoporous materials. When BJH method was implemented to the desorption part of the isotherm, pore volume of 0.47 mL/g and an average pore size opening of 2.4 nm were obtained. The MA powder also possessed a relatively high BET surface area of ≈180 m^2/g.

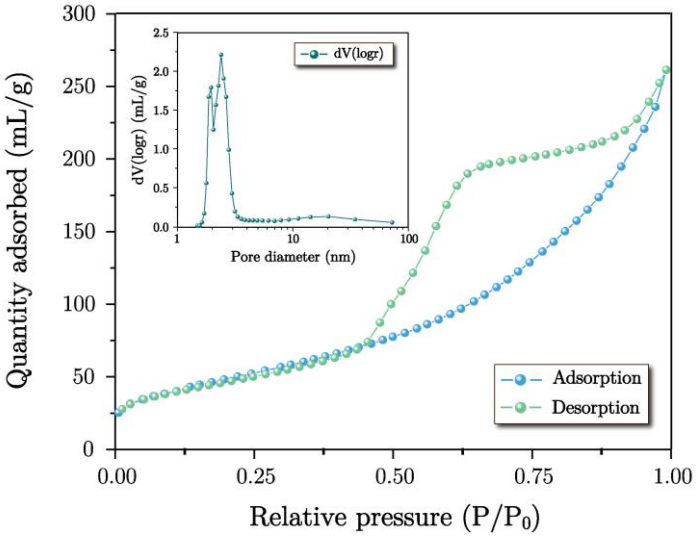

Figure 4.3: Nitrogen adsorption and desorption isotherms of MA powder. Inset: Size distribution of mesopores in MA powder.

To determine the size and shape of the secondary MA particles consisting of aggregated 2D nanosheets, the SEM and particle-size-distribution analyses were performed, respectively (Figure 4.4A and 4.4B). The MA powder had the average particle size of 8.9 µm and possessed a negatively skewed normal particle size distribution with sizes ranging from 0.5 µm and up to around 30.0 µm. In more detail, the d_{10}, d_{50} and d_{90} diameters of the particle size distribution were equal to 3.4 µm, 8.6 µm and 14.5 µm, respectively (Figure 4.4A). The SEM imaging confirmed that the MA powder was composed of spherical particles with a diameter of a few micrometers, i.e., entities hierarchically assembled from 2D nanosheets (Figure 4.4B) forming a "hedgehog"- or "flower-like"-shaped secondary particles. A number of these entities further aggregated forming a more complex secondary MA particle as illustrated in the hierarchical assembly process of a single MA particle (Figure 4.4C).

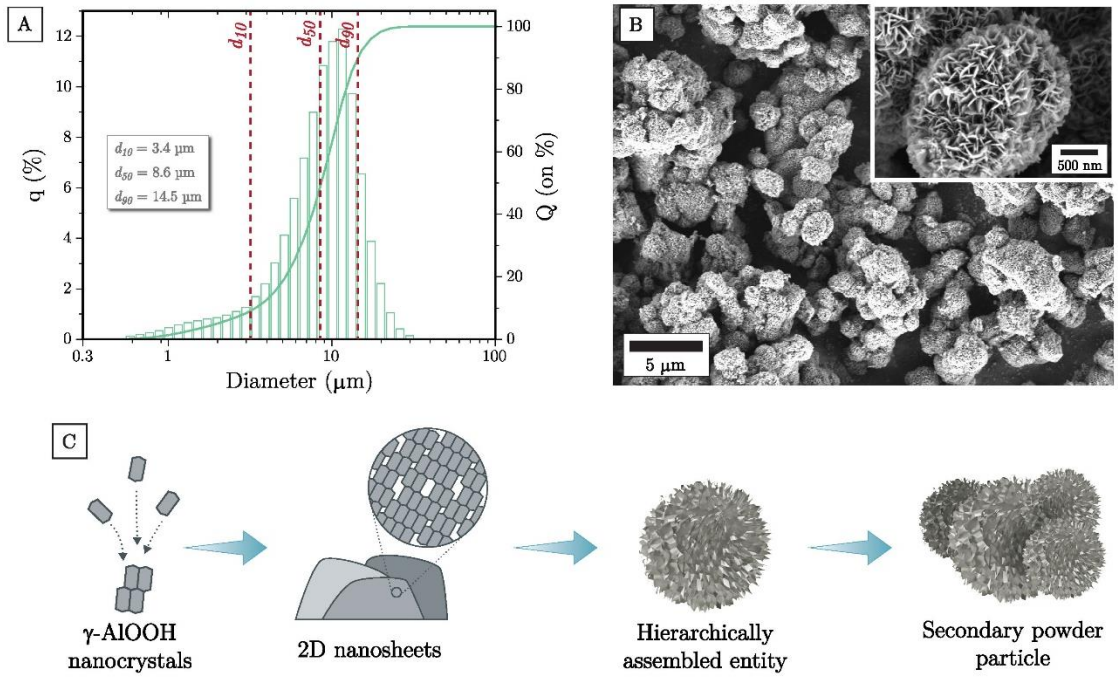

Figure 4.4: A) SEM micrograph of MA powder. B) Particle size distribution of MA powder. C) Illustration of proposed mechanism of γ–AlOOH nanocrystals assembly to a hierarchical particle.

The MA powder was further characterized by mercury-intrusion porosimetry (Figure 4.5) yielding pore size distribution with respect to the distribution of pores opening diameter. The distinction between pore diameter and pore's opening diameter is explained in Appendix's Section A.3. The intrusion curve showed two distinctive peaks, one in the mesopore region at around 3 nm and the other in the macropore region around 6 µm. While the latter peak is characteristic for the mercury volume intruded into inter-particle space, the former points towards intra-particle intrusion again corroborating the mesoporous nature of a single MA entity.

Mercury intrusion curve was also used to obtain the MA powder's bulk (ρ_B) and apparent (ρ_A) density. The values were 0.42 mL/g and 3.35 mL/g, respectively. Envelope density (ρ_E) was also estimated in order to account for the porosity of individual particles. To obtain ρ_E the volume of mercury intruded into the interparticle space was first determined as indicated by the cross-section of the dashed lines in Figure 4.5. Accordingly, the mercury intrusion volume obtained inside the pressure interval 0.014–0.42 MPa

(corresponding to the pore sizes between 103.0–3.5 μm) corresponded to the interparticle porosity. Then the latter value was subtracted from the total intruded volume of mercury. As a result, the mercury volume intruded into intra-particle space, i.e., pure particles porosity, was obtained. The as-calculated ρ_E was 0.92 mL/g, which was more than 3-times lower than the value of ρ_A and corresponded to ≈23 % of the alumina's theoretical density.

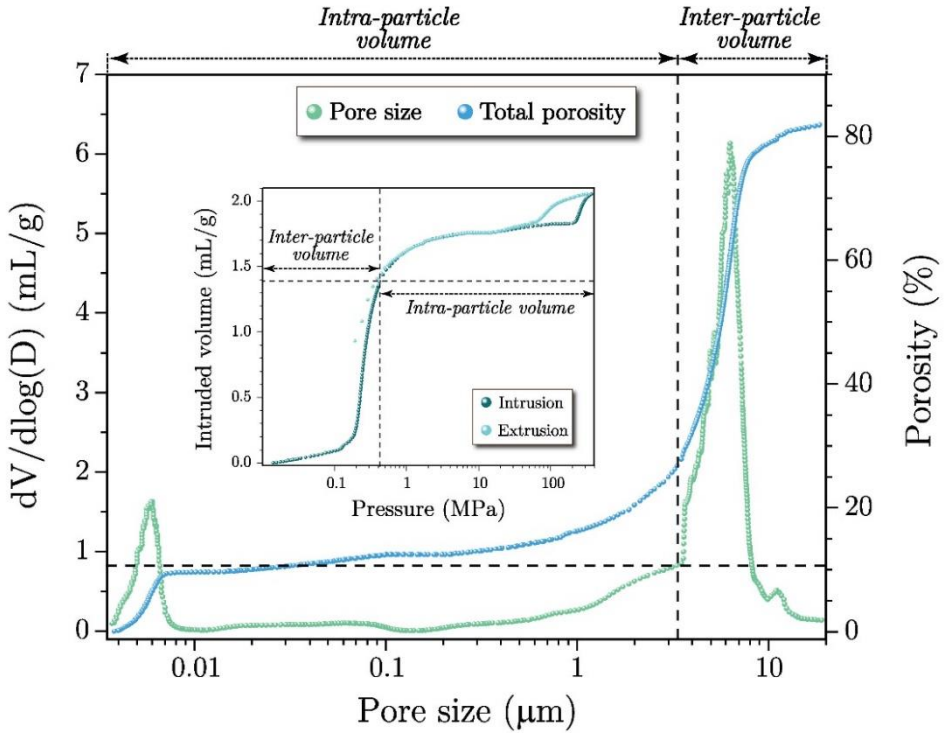

Figure 4.5: Pore size distribution and total porosity of MA powder determined by mercury-intrusion porosimetry. Dashed lines approximately divide the pores by their size into the inter-particle porosity and intra-particle porosity. Inset: Total mercury-intrusion and extrusion volumes. Dashed lines approximately divide the total intruded volume into the volume intruded into the inter-particle and into the intra-particle space.

The characterization of surface and structural properties of the MA powder proved that AlN powder hydrolysis is an interesting and simple synthesis procedure for hierarchically assembled MA powder.

4.3 MA Powder Aqueous Suspensions and Their Stabilization

Aqueous suspensions containing dispersed AlN-hydrolysis-derived MA powder were prepared. In order to prevent uncontrolled suspensions flocculation and thus pronounced sedimentation rates the MA particles were firstly dispersed by the electro-steric stabilization. The latter was achieved by the addition of sodium polyacrylate (NaPAA) with molecular weight of 225 000 g/mol. Since MA particles were in micro-size range additional mechanisms had to be implemented to hinder the gravitational pull on individual particles. Suitability of two mechanisms was evaluated, namely, the addition of divalent cations (M^{2+}) and the addition of cellulose nanofibers (CNF) to NaPAA dispersed MA particles as illustrated in Figure 4.6.

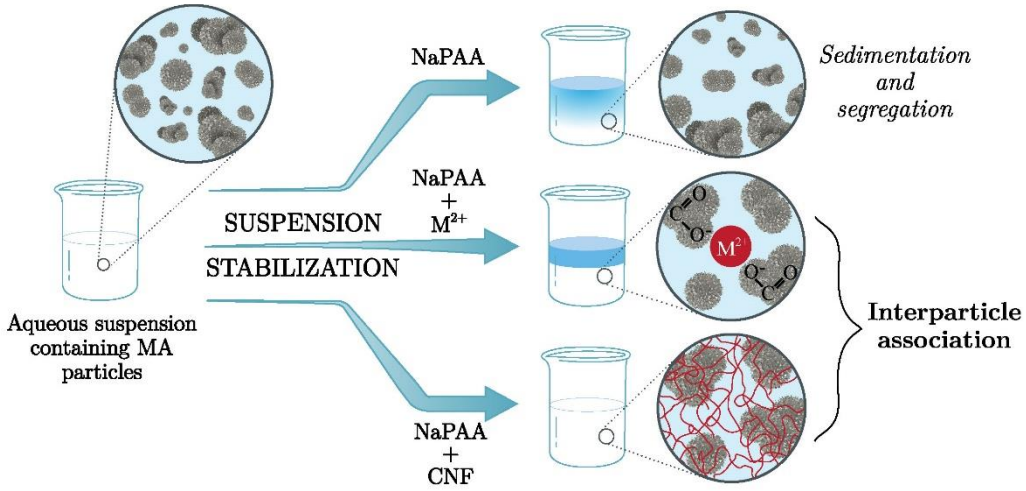

Figure 4.6: An overview of mechanisms implemented against sedimentation and size segregation of aqueous MA powder suspensions.

4.3.1 Aqueous suspensions containing NaPAA-dispersed MA particles

NaPAA was used to endow suspended MA particles with higher surface charge and to provide sterical barrier between individual particles, thus hindering their agglomeration. The pH value of 9 was chosen as the main suspensions pH, since at this value NaPAA chains are extended and highly charged (degree of dissociation α_d is approximately 0.99998) [199], thus yielding a better electrosterical repulsion and a better dispersion in comparison to lower pH values [59]. To experimentally confirm that pH value of 9 was indeed a more suitable choice than lower pH values, suspensions containing NaPAA-dispersed MA particles at pH 6 were also characterized.

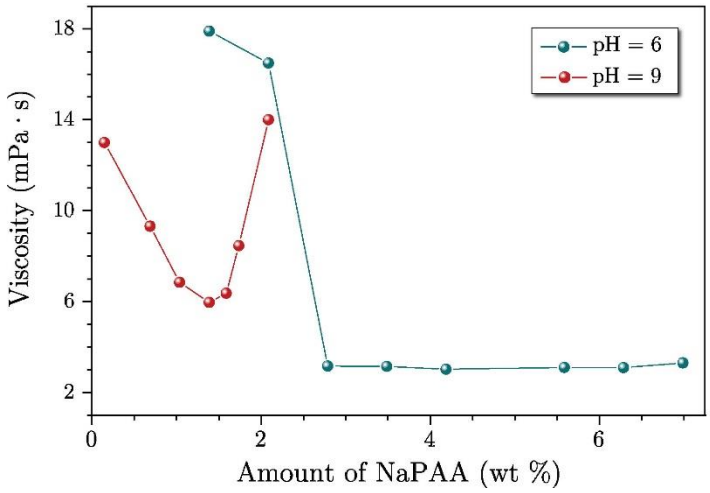

Figure 4.7: Viscosity of MA aqueous suspensions (φ_A=0.068) at pH 6 and 9, dispersed with different amounts of NaPAA measured at a shear rate of 50 s^{-1}.

Different amounts of NaPAA were added to the MA powder aqueous suspensions and the pH value was set to either 9 or 6. An optimal amount of added NaPAA was determined by measuring the viscosity of suspensions at a constant MA powder's apparent volume

fraction φ_A of 0.068. The suspension containing optimal amount of NaPAA, i.e., where a monolayer surface coverage is achieved [200], is the one with the lowest viscosity. The results for both chosen pH values are presented in Figure 4.7.

At pH 9, the lowest viscosity (≈ 6 mPa·s) was obtained when suspension contained MA particles dispersed with 1.4 wt% of NaPAA (1.4NaPAA–MA). For comparison the viscosity of suspension containing only MA particles of the same volume fraction was 2.1 mPa·s (at shear rate of 50 s^{-1}). Addition of NaPAA increased viscosity, since the extended polyelectrolyte tails, together with the unbound NaPAA hinder particle movement and therefore increase suspension's viscosity. In the case of lower NaPAA concentrations (< 1.4 wt%), a more than twofold increase of the viscosity value was observed. It can be ascribed to the bridging flocculation. The latter occurs when the concentration of added polymer (dispersant) is below the amount needed for monolayer coverage, i.e., the surface of the particles is only partially covered. In such cases a single molecule of dispersant can adhere to two particles simultaneously, thus connecting them together and causing flocculation [201]. On the other hand, when the addition of NaPAA was above 1.5 wt%, an even steeper increase in the viscosity of the suspension could be observed. The reason lies in excess NaPAA molecules which were not bound to the surface of the particles, but remained free-flowing. These molecules forced the particles closer together, causing depletion flocculation, which was manifested as an increase of the suspensions viscosity [59], [74].

For pH 6, the lowest viscosity (≈ 3 mPa·s) was achieved at the addition of 2.8 wt% of NaPAA. The viscosity of suspension (φ_A=0.068) containing only MA particles at pH 6 was 1.4 mPa·s (at shear rate of 50 s^{-1}). The optimal addition of NaPAA was twice as high as in the case of suspensions with pH value of 9. The difference occurred due to the MA particles surface charge, which is pH dependent. At pH values above the isoelectric point (IEP for γ–Al_2O_3 is around 7.5) predominant charge on the surface of MA particles was negative, while below IEP positive charge prevailed. Therefore, at pH 9, negatively charged NaPAA chains were repulsed by negatively charged surface of the MA particles. NaPAA chains could thus only attach on a limited amount of positively charged sites on the MA surface [72], [202]. On the other hand, positively charged MA surface at pH 6 offered many areas where polymer chains could adsorb readily. Consequently, the amount of NaPAA needed to achieve a complete monolayer surface coverage was larger at pH 6.

While an excess addition of NaPAA at pH 9 led to an abrupt increase of viscosity, due to the unbound chains of NaPAA, moving freely in suspension and causing additional interferences of particle movement, at pH 6 practically no increase of viscosity could be observed after the addition of over twice the optimal amount. This was ascribed to the pH-dependent conformation of PAA chains. At pH 9, chains were highly charged, while at pH 6 the degree of dissociation was slightly lower, i.e., at pH 6 α_d is 0.9693, which is considerably lower than at pH 9 [199]. This led to notable differences in the 3D configuration of polymer chains. At pH 9, the chains were extended and stretched into the suspension, due to the charged carboxylate groups. On the other hand, the configuration of PAA chains at slightly acidic pH value of 6 was more coiled, since the chains carry less charge, due to fewer deprotonated carboxylic groups [59], [203], [204]. Extended PAA chains caused more hindrance of particle movement than PAA chains in coiled conformation, thus explaining why at pH 9 an abrupt increase in viscosity was observed after the addition of excess NaPAA. A more or less constant viscosity could be observed in the case of suspensions with pH 6.

The optimal amount of NaPAA added at pH 9 was additionally determined by measuring zeta-potential (ζ) of diluted MA suspensions ($\varphi_A = 0.00005$) containing different amounts of NaPAA. As seen in Figure 4.8A an increasing amount of NaPAA caused IEP to steadily shift towards lower pH values until at NaPAA addition >1.4 wt% a constant

value of approximately 3.0 was reached. With even higher addition of NaPAA, the values of zeta-potential were comparable throughout the entire investigated pH range. The amount of NaPAA needed for optimal dispersion determined with ζ measurements was thus in accordance with rheologically obtained results.

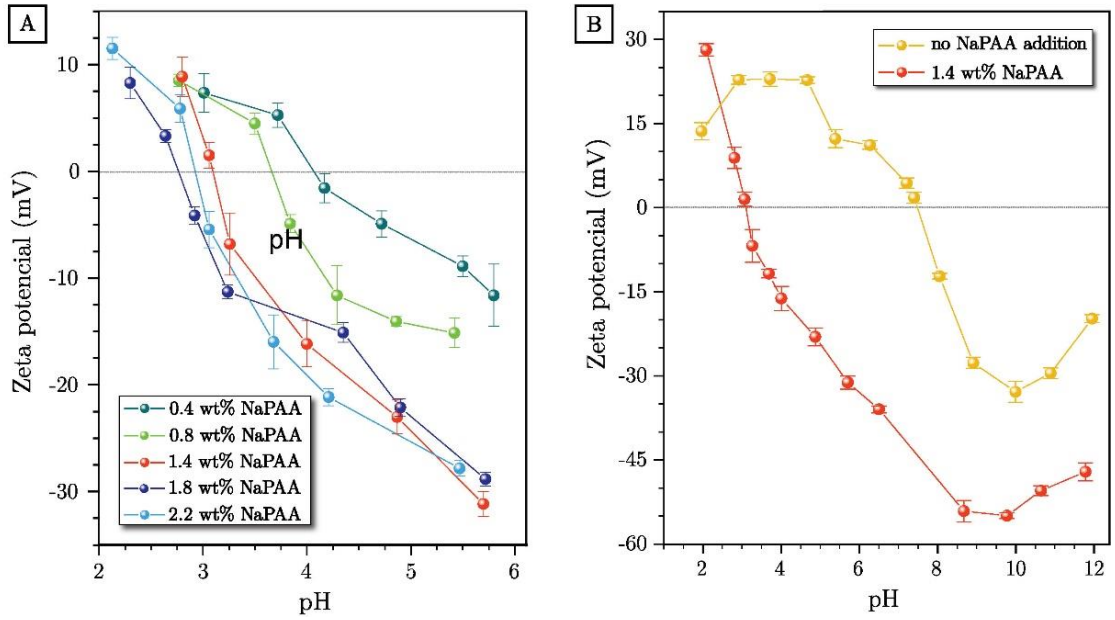

Figure 4.8: A) Zeta-potential of MA particles in diluted suspensions at different additions of NaPAA amounts and at different pH values. B) Comparison of zeta-potential curves of MA particles in diluted suspensions with and without the addition of 1.4 wt% NaPAA as a function of pH.

The ζ of the suspended MA particles without added NaPAA was also determined and compared with the ζ of the particles dispersed with 1.4 wt% of NaPAA. Results are shown in Figure 4.8B. A positive ζ of $\approx$ 23 mV was measured for the MA particles in the acidic pH range (from 2 to 5), while in the alkaline pH region (8.5–12) a negative potential between -25 and -30 mV was measured. The IEP was positioned between pH values 7.5 and 8, which was in accordance with the literature [203], [205]. On the other hand, after the addition of 1.4 wt% of NaPAA, the IEP shifted to considerably lower pH values (pH $\approx$ 3), while the absolute values of ζ considerably increased throughout the alkaline pH range (8–10), exceeding -50 mV indicating on a strong negative repulsive potential of the NaPAA-coated-MA particles.

4.3.2 Influence of MA volume fraction on the rheological behavior

The influence of MA powder volume fraction φ on viscosity and rheological behavior of 1.4NaPAA–MA suspensions (pH=9) and 2.8NaPAA–MA suspensions (pH=6) was evaluated. Suspensions in the MA volume fraction range (φ_A) from 0.013 to 0.126 were tested. Results are shown in Figures 4.9 and 4.10.

An almost linear increase of the viscosity values with an increasing MA powder volume fraction up to $\varphi_A = 0.112$ for pH 9 can be observed, while at pH 6, the linear increase could be observed to even higher MA volume fractions, i.e., $\varphi_A = 0.119$. Above these volume fractions, the viscosity began to increase abruptly (Figure 4.9).

Viscosities obtained for suspensions with pH 6 were lower than the values obtained for optimally dispersed MA particles at pH 9 for all MA volume fractions. The reason for the

difference could lie in i) the pH-dependent conformation of NaPAA chains and ii) the pH-dependent mechanism of NaPAA adsorption. As already mentioned at high pH values, PAA chains exist in extended conformation and at lower values (pH = 6) in more coiled conformation. PAA chain tails that extend into the suspension cause more hindrance of particle movement than the coiled ones, thus resulting in a higher increase of viscosity.

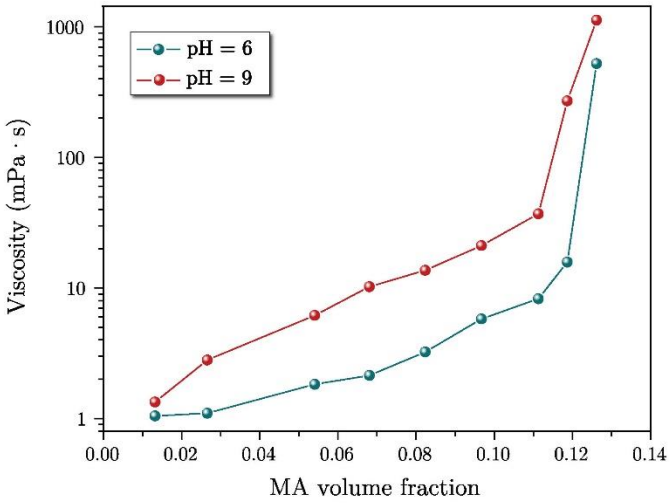

Figure 4.9: Viscosity (at 50 s^{-1} shear rate) versus volume fraction of MA powder in water, dispersed with either 2.8 wt% NaPAA (pH=6) or 1.4 wt% NaPAA (pH=9).

Higher viscosity at pH 9 can also be explained by the type of NaPAA adsorption, which is pH-dependent. At high pH values, PAA adsorb through hydrogen bonds, while in the case of lower pH electrostatic adsorption is possible [74], [206]. At the lower pH, there is the so-called high-affinity type of PAA adsorption, where PAA is completely adsorbed on the particle's surface. In the case of higher pH 9 value (above IEP), an adsorption barrier occurs due to the same charge on the surface of particles and PAA chains. Consequently, high-affinity type adsorption is not possible and an equilibrium between adsorbed and non-adsorbed, free-moving polymer chains is established. In the suspension with pH 9, where the equilibrium existed, the unabsorbed NaPAA hindered particles movement causing higher viscosities than in the case of suspensions with pH 6 where practically no free-flowing PAA chains were present [74].

A volume fraction φ_A =0.126 represented the maximum volume fraction (φ_m) of aqueous suspension experimentally achievable with this MA powder. The low maximum volume fraction can be ascribed to the high porosity of MA particles. To account for the MA particles intrinsic porosity predetermined ρ_E (0.92 g/mL) was used to calculate the envelope solid volume fractions (φ_E), which gave a rough estimation of the solid volume fractions the prepared suspensions would possess in case MA particles were non-porous (Table 4.1).

A porous secondary MA particle (Figures 4.4B and 4.4C) was able to accommodate substantial amounts of water, i.e., approximately 0.5 mL of water per 1 g of MA powder. This part of the total water's volume could not contribute to the suspension's fluid dynamics.

A rough approximation of the MA powder's volume fractions, where the volume of water contained inside the MA particles was subtracted from the total water's volume, yielded the envelope volume fractions φ_E in the range from 0.048 to 0.453 (corresponding to φ_A =0.013-0.126) as can be seen in Table 4.1. If envelope density was used for the calculation of the maximum MA powder's volume fraction φ_m, the value was considerably higher, i.e., 0.453 (φ_E) instead of 0.123 (φ_A).

Table 4.1: Comparison between MA powder's volume fractions calculated by using apparent density (apparent volume fraction, φ_A), envelope density (envelope volume fractions, φ_E), bulk density (bulk volume fraction, φ_B) and the corresponding mass fractions (w_{MA}).

Apparent volume fraction (φ_A)	Envelope volume fraction (φ_E)	Bulk volume fraction (φ_B)	Mass fraction (w_{MA})
0.013	0.048	0.097	0.043
0.027	0.097	0.179	0.084
0.054	0.196	0.251	0.161
0.068	0.247	0.313	0.197
0.083	0.298	0.368	0.231
0.097	0.349	0.417	0.264
0.112	0.401	0.460	0.296
0.119	0.427	0.500	0.311
0.126	0.453	0.518	0.326

*$\rho_A = 3.347$ g/mL, $\rho_E = 0.917$ g/mL, $\rho_B = 0.421$ g/mL

Even when the maximum solid volume fraction was expressed as φ_E, the maximum volume fraction of MA powder experimentally achievable (φ_m=0.453) was still lower than the maximum volume fractions reported for aqueous suspensions containing spherical, dense α–Al_2O_3 particles, where φ_m was approximately 0.65 [207], [208]. However, the obtained φ_m for MA powder was similar to the maximum solid loadings already reported for spheroid-like particles (φ_m = 0.32 – 0.58) [209]. Higher maximum volume fraction obtainable in the case of spherical particles in comparison to the φ_m of MA particles can be explained by the irregular shape of the latter, i.e., randomly staked globular particles as seen in Figure 4.4B. The non-spherical particle's shape led to a poorer space filling efficiency and consequently the maximum volume fraction was lower [210].

The φ_m for the AlN-hydrolysis-derived MA powder was also slightly lower than the values reported for similar MA powders. Zamorategui et al. used fibrillar MA particles to prepared aqueous suspensions with 35 wt%, while in the case of MA powder consisting of spherical particles a slightly higher maximum solid fraction of 45 wt% was obtained. If aforementioned mass fractions are expressed as apparent volume fractions φ_A (calculated using 3.4 g/mL as the apparent density) values of 0.137 and 0.194 were obtained, respectively [211].

The rheological behaviour inside the shear rate range 1–200 s^{-1} of suspensions containing different volume fractions of MA powder dispersed at different pH values is presented in Figure 4.10. Note that for suspensions with volume fractions (φ_A) below 0.082 rheological behaviour at shear rates below 10 s^{-1} was not determined, due to the limitations of the measurement system used.

The viscosities of the suspensions with the MA volume fractions between 0.013 and 0.097 for suspensions at pH 9 and volume fractions from 0.013 to 0.112 for suspensions with pH 6 were more or less constant and exhibited near-Newtonian behavior. Above these volume fractions, a change of the rheological behaviour was observed. In the case of suspensions with pH 9, the behaviour changed from a near-Newtonian to shear thickening, while at pH 6, the rheological behavior changed to shear-thinning.

Shear-thickening occurred at low shear rates, while at slightly higher shear rates, a plateau value was reached (Figure 4.10A). Shear thickening mostly occurs at shear rates above 100 s^{-1}, even when suspensions contain a high solid volume fraction [212]. However, in the present case, shear thickening occurred at considerably lower shear rate values, e.g., at 40 s^{-1} when φ_A was 0.112. The on-set of shear thickening shifted to even lower shear rates with an increase in the MA volume fractions, occurring at approximately 1 s^{-1} at φ_A =0.126. Shear thickening observed at low shear rates can be ascribed to the friction between the MA particles occurring due to the high solid contents. The interactions were most likely additionally enhanced due to the non-spherical shape of MA particles and their rough surface area [213]. However, the phenomenon of shear-thickening at low shear rates could also be caused by the entanglement of the unabsorbed NaPAA chains in the MA particles at higher volume fractions [214].

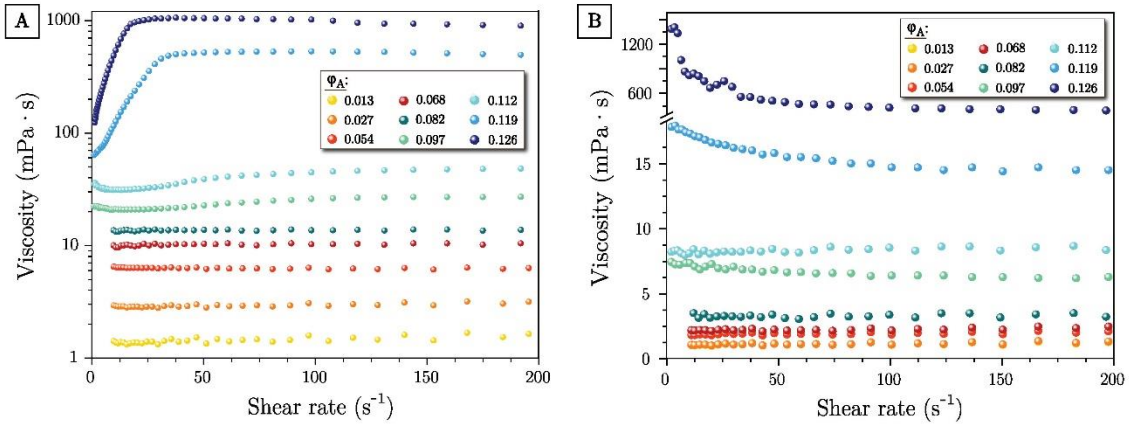

Figure 4.10: A) Rheological behaviour of the suspensions with different volume fractions of MA powder dispersed with 1.4 wt% NaPAA at pH 9. B) Rheological behaviour of the suspensions with different volume fractions of MA powder dispersed with 2.8 wt% NaPAA at pH 6.

On the other hand, a transition to shear-thinning at low shear rates (< 100 s^{-1}) observed for suspensions with pH 6 could be related to an agglomerate break-down and the orientation of particles in the direction of the flow [215], [216]. Unlike in the case of suspensions with pH 9, the NaPAA chains were in coiled conformation and were almost in its entirety adsorbed on the surface of MA particles ("high-affinity" type of adsorption). Consequently, the formerly mentioned entanglement between MA particles and NaPAA chains occurring at pH 9 was not possible in the systems with lower pH values.

It was evident that the pH value played a significant role in the type of rheological behavior. Since at the same high enough MA volume fractions but at different pH values two types of rheological behavior were observed, it can be stated that the shear-thickening of suspensions at pH 9 was not so much a consequence of friction between rough surface of non-spherical particles, but occurred mainly due to the entanglement of the unabsorbed, extended NaPAA chains and MA particles.

4.3.2.1 Krieger-Dougherty model

For the suspensions containing either 1.4NaPAA–MA powder (pH=9) or 2.8NaPAA–MA powder (pH=6), the Krieger-Dougherty model was used (Figure 4.11 and 4.12, respectively) in combination with the least-square method to predict the maximum MA volume fraction φ_m in aqueous suspensions and to establish whether the pH value carries any significant influence on the latter. Furthermore, a comparison between the theoretical viscosity values

calculated from the Krieger-Dougherty model and the experimentally determined values was performed in order to establish the suitability of Krieger-Daugherty model for the aqueous NaPAA-MA systems.

The Krieger-Dougherty model is used to predict the suspension's viscosity (η) at a specific solid volume fraction (Equation 4.1) [217].

$$\frac{\eta}{\eta_0} = \left(1 - \frac{\varphi}{\varphi_m}\right)^{-[\eta]\cdot\varphi_m} \tag{4.1}$$

In the Krieger-Dougherty equation, η_0 represents the viscosity of the chosen solvent, i.e., in the case of distilled water at 23°C, sheared at 50 s^{-1}, the value is 0.79 mPa·s. φ is the actual solid volume fraction, while φ_m is the maximum achievable solid volume fraction. Parameter $[\eta]$ is known as the intrinsic viscosity and accounts for the influence of particle's shape on the viscosity.

Krieger-Dougherty model was already used for the theoretical predictions of intrinsic viscosity and maximum solid fractions of aqueous suspensions containing non-porous, spherical particles with monomodal, narrow particle size distribution [217], [218]. On the other hand, an accurate theoretical prediction of $[\eta]$ and φ_m for systems containing particles with a complex shape in addition to a broad particle size distribution is not possible.

Still, values of [η] and φ_m can be estimated through the implementation of the Krieger-Dougherty equation on the experimentally obtained data. The goal is to obtain the best fit between viscosity calculated through Equation 4.1 and experimentally obtained viscosity at different solid volume fractions [219], [220].

Results of the Krieger-Dougherty model implementation for suspensions containing either 1.4NaPAA–MA powder (pH=9) or 2.8NaPAA–MA powder (pH=6) are presented in Figures 4.11 and 4.12, respectively. The best fit between experimentally determined viscosity values and the Krieger-Dougherty calculated results was obtained by the least-square method.

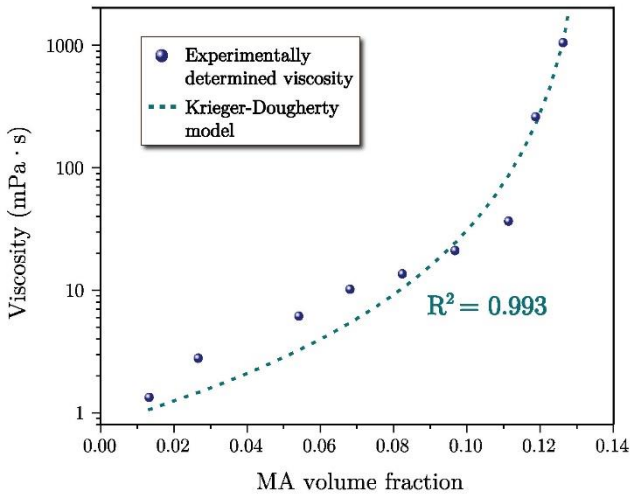

Figure 4.11: Viscosity versus volume fraction of 1.4NaPAA–MA powder in water at pH 9 (50 s^{-1} shear rate) as predicted by the Krieger-Dougherty model. Spheres mark the experimentally determined viscosity values.

For the aqueous suspensions containing 1.4NaPAA–MA particles, the least square method yielded the best fit ($R^2 = 0.993$) when maximum solid volume fraction (φ_m) was set to 0.136. Additionally, the best fit was obtained when intrinsic viscosity was set to either 0.056 if MA was expressed in envelope volume fractions (φ_E) or 19.9 if MA volume

fractions were expressed as apparent volume fractions (φ_A). Apparently, the particle density used for the determination of solid volume fraction also has an influence on the intrinsic viscosity. Thus, the latter parameter should not be used as an absolute but rather as a relative value. For example, the values of [η] obtained for dense spherical α-Al_2O_3 should not be compared to the values obtained for porous, non-spherical MA particles in order to determine the influence particle's shape has on the intrinsic viscosity. Valid comparisons can only be made between [η] obtained for slurries containing particles of at least similar densities, e.g., two suspensions containing α-Al_2O_3 particles of a different shape.

Comparison between experimentally obtained and theoretically calculated viscosity values at different MA volume fractions (pH=9) is given in Table 4.2. As can be seen from Figure 4.11, a slightly higher maximum volume fraction in comparison to the one determined experimentally was obtained, i.e., $\varphi_m = 0.136$ in comparison to 0.126 determined experimentally. Still the values were very similar, suggesting a satisfactory fit between theoretically predicted and experimentally obtained viscosity behavior of 1.4NaPAA–MA suspensions.

Table 4.2: Comparison of viscosities obtained experimentally and by implementation of the Krieger-Dougherty model at different 1.4NaPAA–MA powder volume fractions in suspensions with pH 9.

MA volume fraction (φ_A)	**η_{exp}* [mPa·s]**	**η_{cal}** [mPa·s]**	***Δn sqr²***
0.013	1.34	1.06	0.1
0.027	2.80	1.47	1.8
0.054	6.16	3.27	8.4
0.068	10.20	5.48	22.3
0.083	13.60	10.47	9.8
0.097	21.10	24.73	13.1
0.112	36.60	88.69	2713.3
0.119	259.00	235.28	562.4
0.126	1040.00	1100.12	3614.5

*Experimentally determined viscosity.
**Viscosity calculated using Equation 4.1.

Results in Table 4.2 show that the best fit between experimental and theoretical viscosity values was obtained at MA volume fractions (φ_A) lower than 0.097. Still in the case of lower MA volume fractions, calculated viscosity was lower than the experimentally obtained values. The Krieger-Daughterly model only accounts for particle shape. It does not consider the impact of particle's surface roughness or the surface charge. It follows that the deviations of the predicted viscosity values from the experimental results could be attributed to the rough surface of MA particles and a considerable surface charge that develops when suspended in water. However, the deviations of the experimentally obtained results from the Krieger-Daughterly model predicted values could also be caused by the unbound NaPAA molecules, which hinder particle movement and thus cause higher viscosity than theoretically predicted.

On the other hand, in the case of suspensions containing 2.8NaPAA–MA particles (pH=6) the situation was slightly different. As can be seen from Figure 4.12 two sets of values were predicted by the Krieger-Daugherty model. To obtain the first set of values all of the experimentally determined viscosity values were used in the determination of the best fit by the least square prediction method (Figure 4.12A). The second set of values was obtained when only viscosity obtained for MA volume fractions including 0.119 was used (the viscosity obtained at the highest MA volume fraction, i.e., 0.126, was excluded from the model) as can be seen in Figure 4.12B.

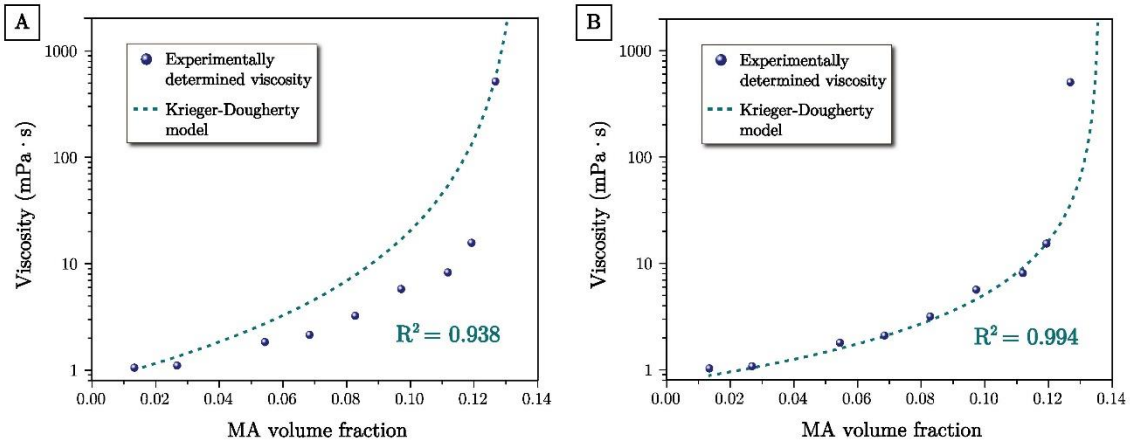

Figure 4.12: A) Viscosity versus volume fraction of 2.8NaPAA–MA powder in water at pH 6 (50 s^{-1} shear rate) as predicted by the Krieger-Dougherty model, when all of the nine experimentally determined viscosity values were considered (first set of data). B) Viscosity versus volume fraction of 2.8NaPAA–MA powder in water at pH 6 (50 s^{-1} shear rate) as predicted by the Krieger-Dougherty model, when only eight out of nine experimentally determined viscosity values were considered (second set of data). Spheres mark the experimentally determined viscosity values.

Interestingly, in both cases, the best fit was obtained when maximum solid volume fraction of $\varphi_m = 0.136$ was used, which is the same as in the case of suspensions with pH 9. It can be claimed that pH value (and with it connected conformation of NaPAA chains) has a negligible effect on the maximum amount of MA powder that can be dispersed in a given volume of water.

However, the values of intrinsic viscosity $[\eta]$ (determined if MA content was expressed as φ_A) differed considerably between both sets, i.e., the value of 0.049 yielded the best fit in the case of the first set of calculated data, while the value of 0.029 resulted in the best fit for the second set of data. If MA was expressed in envelope volume fractions, intrinsic viscosity values of 18.0 and 10.5 were obtained for the first and second set of data, respectively.

The match between experimentally obtained viscosity and the first set of the Krieger-Daughterly model predicted values (Figure 4.12A and Table 4.3) was considerably poorer in comparison to the match with the second set of calculated data (Figure 4.12B and Table 4.3). The obtained R^2 was only 0.938 for the first set of values, while the values were significantly higher (R^2=0.994) for the second set of calculated viscosity values. As can be seen from Table 4.3, the second set of calculated values was practically the same as the experimentally obtained viscosity values. However, the first set of data much more accurately predicted the viscosity at the highest MA volume fraction. According to the second set of calculated data, viscosity at MA volume fraction of 0.126 should be around 35 mPa·s (Figure 4.12B) which is almost 20 times lower than the experimentally

determined value (≈516 mPa·s). The most likely reason for the misfit between both values is the rough surface of MA particles. As already stated, the Krieger-Daughterly model does not account for the particle surface roughness. Yet at the highest volume fractions where the friction between particles is greater, the rough particle surface could contribute to the overall increase of the suspension's viscosity. Accordingly, we propose that the deviation observed between experimental and calculated viscosity at the highest MA volume fraction was most likely a consequence of an increased friction between MA particles due to the rough surface which is not considered by the Krieger-Daughterly model.

Table 4.3: Comparison of viscosity values obtained experimentally and by implementation of the Krieger-Dougherty model at different 2.8NaPAA–MA powder volume fractions in suspensions with pH 6.

MA volume fraction (φ_A)	η_{exp}* **[mPa·s]**	η_{cal}** **[mPa·s]**	***Δn sqr²***	η_{cal}** **[mPa·s]**	***Δn sqr²***
		First set of data‡		Second set of data§	
0.013	1.05	1.02	0.0	0.92	0.0
0.027	1.10	1.35	0.1	1.08	0.0
0.054	1.83	2.74	0.8	1.63	0.0
0.068	2.14	4.34	4.9	2.13	0.0
0.083	3.23	7.75	20.5	2.99	0.1
0.097	4.72	16.71	143.7	4.68	0.0
0.112	8.25	52.46	1954.8	9.13	0.8
0.119	15.70	126.52	12280.9	15.26	0.2
0.126	516.00	519.91	15.3	/	/

*Experimentally determined viscosity.
**Viscosity calculated using Equation 4.1.
‡ The first set of values was calculated based on the parameters obtained for the best fit of the Krieger-Dougherty model when all of the nine experimentally determined viscosity values were considered.
§The second set of values was calculated based on the parameters obtained for the best fit of the Krieger-Dougherty model when only eight out of nine experimentally determined viscosity values were considered (the viscosity obtained at the highest MA volume fraction was excluded from the calculations).

When comparing the fits between theoretical and experimental values obtained at pH=6 (second set of calculated data) and pH=9 an interesting observation can be made. Namely, the Krieger-Daughterly model more accurately described the values obtained at the lower pH. This suggests that the misfit between experimental and theoretical values observed at pH 9 was not a consequence of either the rough particle surface or a complex particle shape. The same model gave a perfect fit between the experimental and the theoretical values for the same particles at pH= 6 (exception is the highest MA volume fraction). Accordingly, it can be claimed that the deviations from the model at pH 9 are a sole consequence of the NaPAA chains conformation and the unabsorbed NaPAA chains which hinder the particles movement.

4.3.2.2 Sedimentation behavior of aqueous MA suspensions

Observing the proneness of suspensions towards sedimentation is the most straightforward merit for the evaluation of suspensions' stability. The influences of the pH value and NaPAA addition on the sedimentation behavior (kinetics and possible segregation) at three different times of 1 h, 6 h and 24 h were monitored. Suspensions containing particles without added dispersant and suspensions containing MA particles dispersed with NaPAA were studied at two different pH values.

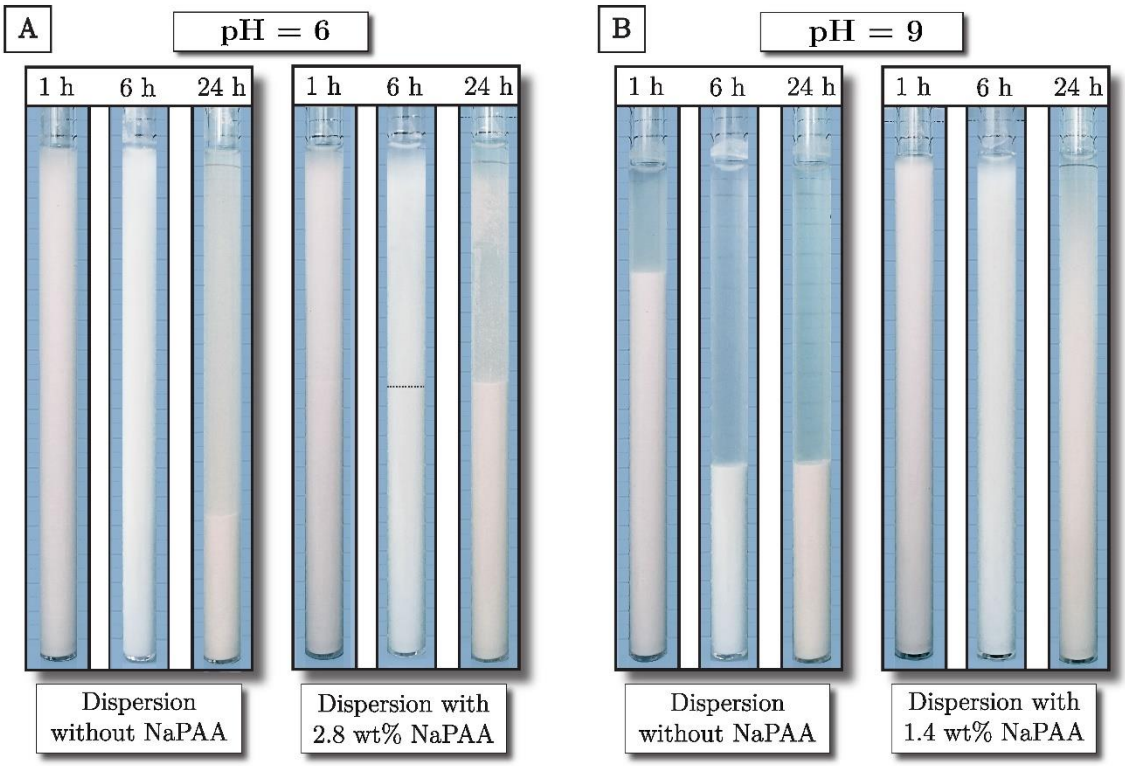

Figure 4.13: A) Pictures of sedimentation tests of $\varphi_A = 0.054$ MA aqueous suspensions at pH 6 without (left) and with (right) added NaPAA. B) Pictures of sedimentation tests of $\varphi_A = 0.054$ MA aqueous suspensions at pH 9 without (left) and with (right) added NaPAA.

At pH=6, the pure MA suspension was more stable (up to 6 h) than the suspension with added NaPAA (Figure 4.13A), as in accordance with Chibowski et al. who studied PAA-Al_2O_3 systems [203]. After 6 h, the suspension containing 2.8NaPAA–MA particles exhibited a phase separation between sedimented particles and turbid supernatant (indicated in Figure 4.13A by a dotted line). Pure MA particles suspension appeared homogeneous. For both suspensions, the supernatant was cloudy even after 24 h due to the presence of fully stabilized MA particles of colloidal size, indicating the absence of flocculation. However, after 24 h the sediment height was lower in the suspension without added NaPAA (29 % of the initial suspension's height) in comparison to the suspension containing NaPAA (53 % of the initial suspension's height). The higher sediment height indicated a less efficient packing of particles, which can be explained by the higher surface charge of NaPAA-dispersed MA particles (Figure 4.8) and the presence of NaPAA chains preventing MA particles to come in close contact, thus enabling efficient packing.

At pH=9, the situation was reversed. The MA particles dispersed with NaPAA showed a better resistance towards sedimentation than the pure MA suspension (Figure 4.13B). At pH 9, despite their relatively high measured zeta potential (-28 mV, Figure 4.8), pure

MA particles underwent immediate agglomeration, which resulted in the complete sedimentation after 6 h. A clear supernatant was a result of flocculation. The suspended particles were apparently too close to their IEP (7.5-8) (Figure 4.8) and obviously ended in the IEP soon after dispersion. Zeta potential was determined in a very diluted system (φ_A=0.00005). In a more concentrated system, as used for sedimentation experiments, a shift of the pH towards lower values or an increase in ionic strength of suspension could have taken place due to the powder's characteristics (adsorbed residues, hydroxylation) and due to potential dissolution of MA, which becomes meaningful at pH values of 9 or greater [221]. In contrast, 1.4NaPAA–MA suspension consisting of MA particles, which were far removed from their IEP (≈3) exhibited a superior stability [68] compared to all conditions tested.

On the other hand, when comparing suspensions at different pH values after NaPAA addition, the more stable suspension was obtained at pH=9. Even after 24 h no phase separation (clear sediment line) could be observed. The latter indicated that the smallest (colloidal) MA particles stayed dispersed over a longer time-period. NaPAA dispersed MA particles in suspension with pH=6 possessed lower absolute value of ζ (-25 mV) than the particles dispersed with NaPAA at pH=9 (-55 mV). Additionally, at pH=9, the NaPAA chains were in a more extended conformation in comparison to pH=6. Consequently, the steric stabilization provided by NaPAA was better in the case of suspension with pH=9. Correspondingly, NaPAA provided poorer stabilization of MA particles at pH=6, therefore explaining the faster sedimentation observed in the case of 2.8NaPAA–MA particles in comparison to 1.4NaPAA–MA particles.

Based on the above results, the suspension containing 1.4NaPAA–MA particles at pH=9 was chosen for further studies of the possible additional stabilization. Sedimentation behaviour in terms of sedimentation rates (Figures 4.14A and 4.14B) and segregation (sediment versus supernatant, Figure 4.14C) were then studied in more detail.

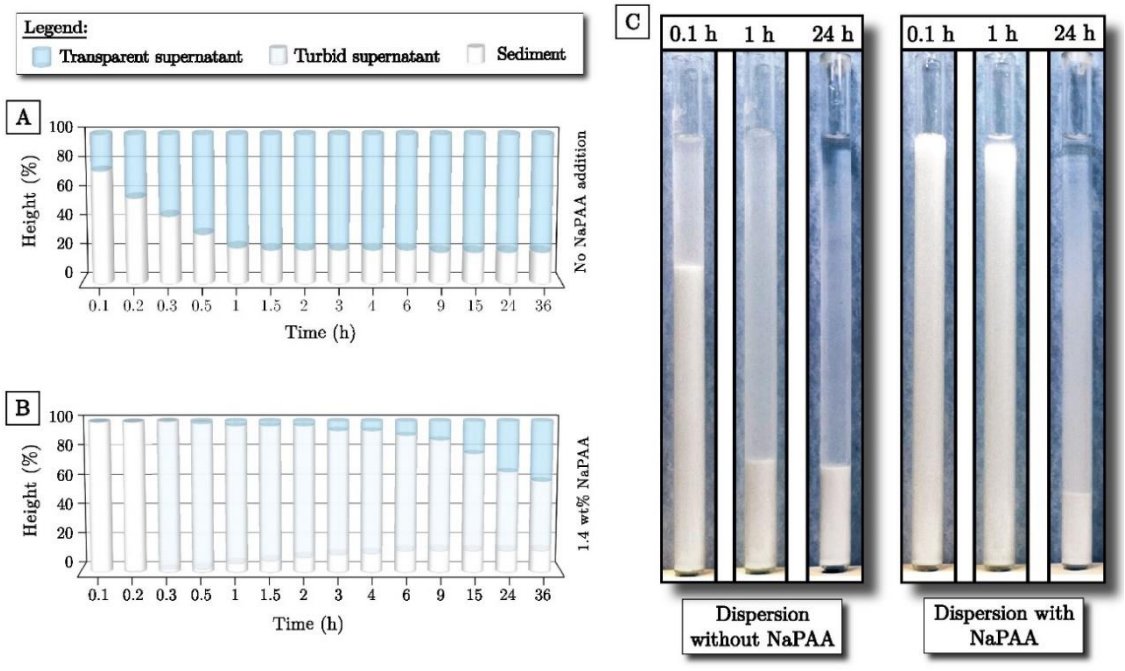

Figure 4.14: A) Sedimentation rates of φ_A = 0.027 MA aqueous suspensions (pH = 9) without the NaPAA addition. B) Sedimentation rates of φ_A = 0.027 MA aqueous suspensions (pH = 9) with added 1.4 wt% NaPAA. C) Pictures of sedimentation tests of φ_A = 0.027 MA aqueous suspensions at pH 9 without added NaPAA (left) and with 1.4 wt% of NaPAA addition (right).

At lower MA volume fractions (φ_A=0.027), the more or less instantaneous sedimentation of pure MA particles was even more obvious (Figures 4.14A and 4.14C) than in the case of higher volume fraction (Figure 4.13B). At lower MA volume fraction, the supernatant was only slightly turbid after 1 hour, with the sediment reaching approximately 24 % of the initial suspension's height. From relatively clear supernatant after 24 h it can be concluded that even the smallest MA particles had agglomerated and consequently sedimented due to the gravitational force.

On the other hand, 1.4NaPAA–MA particles exhibited a much slower sedimentation rate, reaching final sediment height after more than 36 hours (Figure 4.14B). However, unlike in the case of pure MA powder suspension, which sedimented into a two-phased system consisting of a sediment and a more or less transparent supernatant, the suspension containing 1.4NaPAA–MA particles segregated into three distinct phases after around 10 minutes. The three phases were represented by a transparent supernatant, a turbid supernatant and a denser sediment. The turbid supernatant was formed from the stable fraction of the smallest MA particles. Although, in both suspensions (with and without added NaPAA), the supernatant was still turbid after 24 hours, the transparency was considerably lower for the 1.4NaPAA–MA suspension (Figure 4.14C). In the case of pure MA particles, the supernatant was only slightly turbid.

Based on the observed sedimentation behaviour it can be concluded that the MA particles dispersed with NaPAA possessed a better resistance towards sedimentation than the pure MA particles. The improved stability and thus slower sedimentation rate of 1.4NaPAA–MA suspension was a result of a higher absolute value of ζ (-55 mV in comparison to –28mV for pure MA particles at pH=9; Figure 4.8B). A higher absolute value of ζ together with the sterical barrier provided by the extended NaPAA chains hindered the agglomeration of dispersed 1.4NaPAA MA particles. It was expected for even the smallest of pure MA particles (with sizes in the colloid range) to agglomerate and therefore readily sediment in comparison to the more stable 1.4NaPAA–MA colloid particles [68].

When MA particles were dispersed with NaPAA, the final sediment height was also considerably lower, i.e., 15 % of the initial suspension's height in comparison to 21 % obtained after sedimentation of MA powder without added NaPAA. The latter can be readily explained by the lower stability of the MA particles dispersed without the addition of NaPAA. Consequently, the rate of agglomeration was substantially faster, resulting in a faster sedimentation rate, causing lower particle packing density.

4.3.3 Addition of divalent cations

To minimize or even prevent sedimentation and particle size segregation by inducing interparticle association, divalent cations (Mg^{2+} and Ca^{2+}) were added to 1.4NaPAA–MA aqueous suspensions at pH 9. Effectiveness of cations addition against sedimentation was then evaluated through characterization of rheological properties and sedimentation rates determination. Results are shown in Figures 4.15 and 4.16, respectively.

The addition of divalent cations that differed in the size, such as Mg^{2+} and Ca^{2+}, when added in small amounts (< 20 mmol/mol), decreased the viscosity regardless of the cations size, as is clearly evident from Figure 4.15A. The viscosity also exhibited a decreasing trend for different anion sizes in the case of magnesium salts (Figure 4.15B). The observed can be explained by either of the two possible mechanisms. Firstly, the addition of divalent cations caused the maximum amount of NaPAA adsorbed on the surface of MA particles to increase. Secondly, the 3D structure of the NaPAA chains changed from extended to coiled after divalent cations were added. Both mechanisms most likely occurred simultaneously and thus each partly contributed to the decrease of the viscosity.

Divalent cations can create bridges between the negatively charged carboxylate groups on polyacrylate's chains and negatively charged sites on the surface of suspended MA particles, causing an increase in the maximum amount of NaPAA able to adsorb on the particles surface [83]. As a consequence, the amount of unadsorbed NaPAA chains, moving freely through the dispersion medium, was decreased, thus lowering the depletion forces and causing a reduction of the viscosity [74]. Divalent cations also caused a more or less effective shielding of the carboxylic group's negative charge. The latter resulted in a change of the NaPAA chains conformation from an extended shape to a more coiled form. A coiled NaPAA chain caused less steric hindrance than an extended form, and as a consequence the particle movement was less obstructed, leading to a decrease of the viscosity [222].

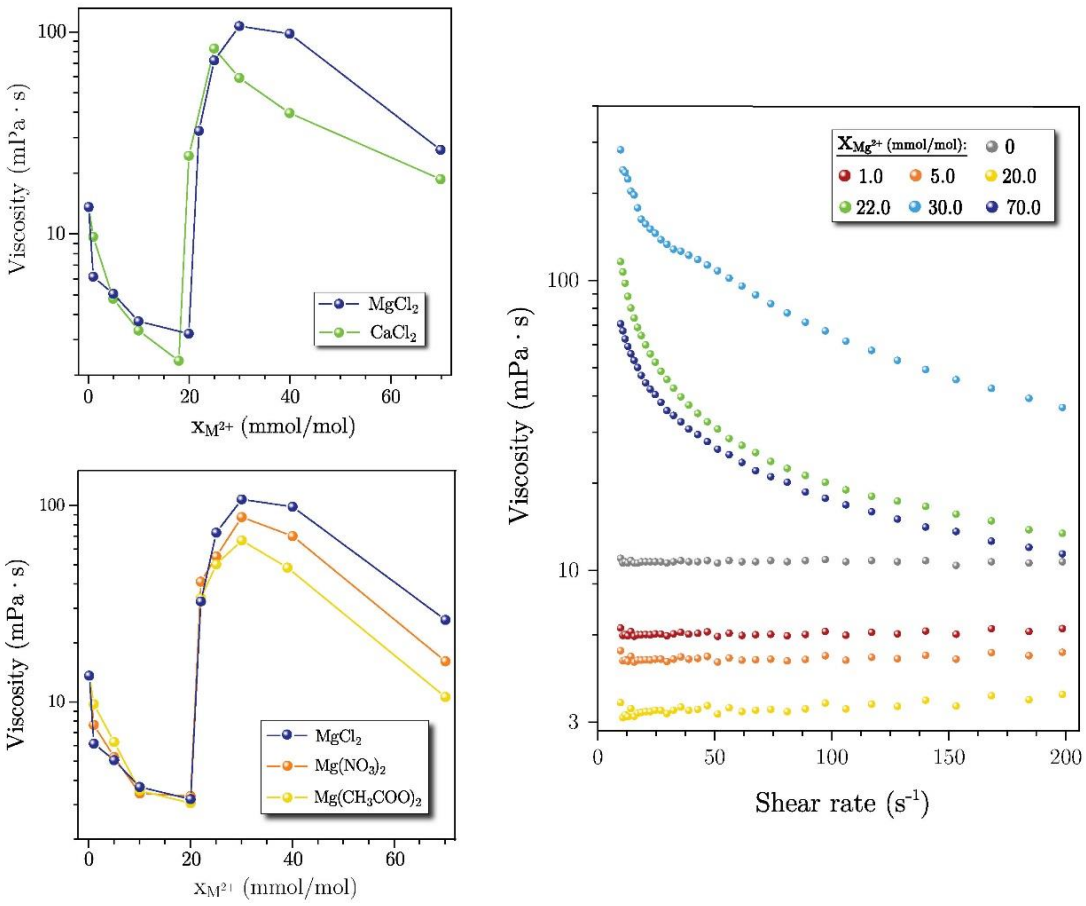

Figure 4.15: A) Viscosity as a function of divalent cations addition to 1.4NaPAA–MA aqueous suspension ($\varphi_A = 0.082$) at pH 9, measured at a shear rate of 50 s^{-1}. B) Influence of type and amount of monovalent anions on the viscosity 1.4NaPAA–MA aqueous suspension with added Mg^{2+} cations. Volume fraction φ_A was set to 0.082 and pH to 9, while shear rate was 50 s^{-1}. C) Effect of different amounts of $MgCl_2$ on rheological behaviour of 1.4NaPAA–MA suspensions ($\varphi_A = 0.082$, pH = 9) at different shear rates.

A minimum viscosity value was reached at 20 mmol/mol for Mg^{2+} cations (≈3.2 mPa·s) and 16 mmol/mol for Ca^{2+} cations (≈2.3 mPa·s). With an additional increase of the amount of divalent cations the viscosity increased abruptly. In parallel, the rheological behaviour changed from a near-Newtonian to a shear thinning behaviour (Figure 4.15C).

Evidently, a critical value of divalent cations was needed to trigger the formation of salt bridges, triggering bridging flocculation. The latter occurs when two carboxylate groups coordinate on one divalent cation: $2R–COO^- + M^{2+} \rightleftharpoons (R–COO)_2M$. When Mg^{2+}

cations were used, salt bridges started to form at a threshold value of 22 mmol/mol (Figures 4.14A and 4.14C). The viscosity continued to increase even after the onset of bridging, until a maximum value (≈107.0 mPa·s) was reached after the addition of 30 mmol/mol of magnesium cations.

After reaching the maximum values, the viscosity started to decrease again with viscosity values after the addition of Mg^{2+} in molar fraction of 70 mmol/mol approaching the values obtained for the system prior to the addition of divalent cations yielding (≈26.0 mPa·s). This last transition can be explained by the dissolution of formed salt-bridges caused by an excessive addition of divalent cations, which decreased short-range electrostatic attractions by a more effective charge screening [78].

The amount of Ca^{2+} cations needed for the on-set of bridging flocculation as well as to reach the maximum viscosity (≈82.9 mPa·s) was lower in comparison to the Mg^{2+}, i.e., 20 mmol/mol and 25 mmol/mol, respectively (Figure 4.15A). This is in agreement with the literature data for pure polyacrylate aqueous systems, where it was also demonstrated that an increase of the cation size resulted in a lower amount of cations needed for the onset of salt-bridging [77], [222].

On the other hand, the size of anions did not exhibit any effect on the bridging initiation. It did however affect viscosity values after the onset of the latter and determine the maximum value of viscosity. The viscosity values and anion sizes were reversibly proportional to the size of the anions, that is $Cl^- < NO_3^- < CH_3COO^-$, as can be clearly seen in Figure 4.15B. The effect of anion size on the overall viscosity after the beginning of bridging can be explained by a better effectiveness in screening of the cations positive charge by larger anions. Better screening resulted in a weaker repulsion between individual cations and consequently in a more compact and less extended configuration of NaPAA chains. As mentioned earlier, the more coiled are the chains, the less steric hindrance of particle movement is invoked, leading to a smaller increase of the viscosity [223].

In addition to the rheological measurements, the effectiveness of the bridging triggered by the addition of divalent cations was evaluated by the sedimentation tests, where 30 mmol/mol or 70 mmol/mol of $MgCl_2$ was added to 1.4NaPAA–MA suspensions (Figure 4.16).

When sedimentation rates of suspensions containing only 1.4NaPAA–MA particles (Figure 4.14B) were compared to the rates obtained for suspensions containing 1.4NaPAA–MA and Mg^{2+} cations (Figure 4.16), it was clear that in the latter case initial sedimentation was considerably faster. However, the final sediment height, achieved after 24 hours, was more than three times higher when Mg^{2+} cations were added. The formation of salt bridges prevented the MA particles from settling into a more densely packed sediment.

It is worth mentioning that after the addition of Mg^{2+} cations no "phase" separation, i.e., occurrence of a turbid supernatant caused by a severe particle size segregation was observed (Figure 4.16C) like in the case of suspension containing only 1.4NaPAA–MA particles (Figure 4.14C). The supernatant was completely transparent when Mg^{2+} cations were added. This indicated that particle association was achieved between 1.4NaPAA–MA particles within the suspension.

When the amount of Mg^{2+} was increased from 30 mmol/mol to 70 mmol/mol, the initial sedimentation was even faster, while the height of sediment after 24 h decreased by approximately 30 %. This decrease could be explained by a re-dissolution of a segment of the formed salt-bridges, since a lower number of these bridges could indeed cause a decrease of the final sediment height. This observation corroborated with the rheological observations, demonstrating that an excess of divalent cations caused a partial re-dissolution of salt-bridges.

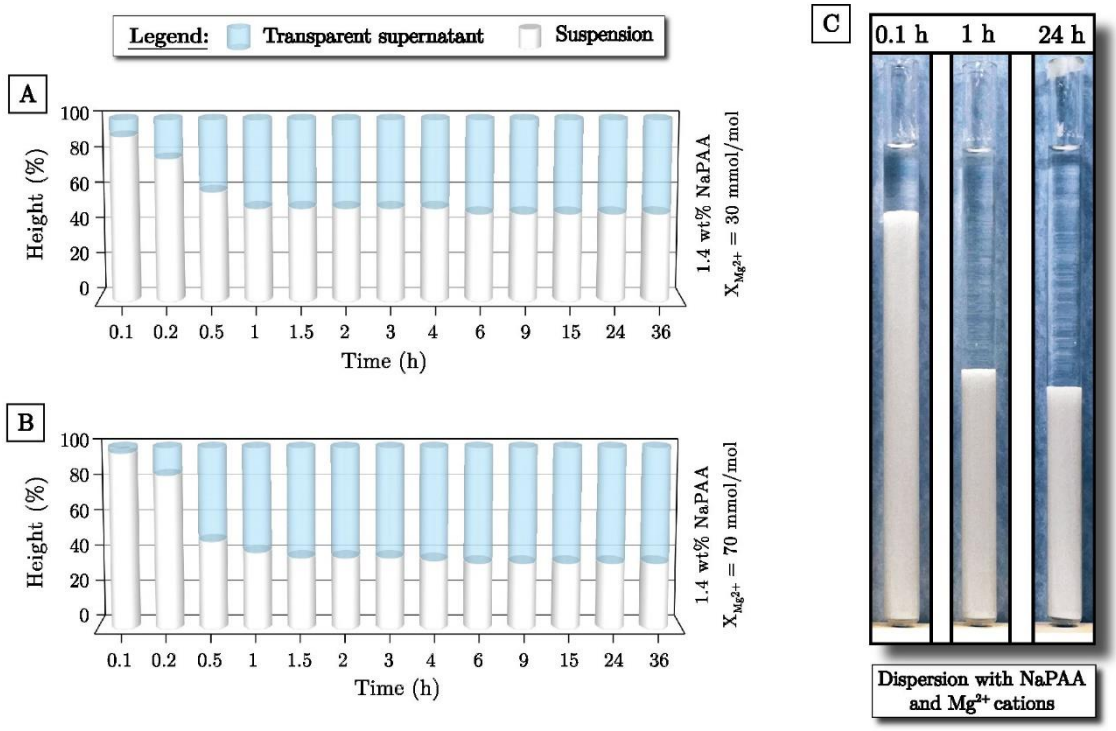

Figure 4.16: A) Sedimentation rates of $\varphi_A = 0.027$ 1.4NaPAA–MA aqueous suspensions (pH = 9) with added 30 mmol/mol of Mg^{2+} cations. B) Sedimentation rates of $\varphi_A = 0.027$ 1.4NaPAA–MA aqueous suspensions (pH = 9) with added 70 mmol/mol of Mg^{2+} cations. C) Pictures of sedimentation test of $\varphi_A = 0.027$ MA aqueous suspensions dispersed with 1.4 wt% of NaPAA at pH 9 and added 30 mmol/mol of Mg^{2+} cations.

The final sediment height of both tested suspensions was re-checked three months after the on-set of sedimentation, and it must be noted that it has not changed, indicating that the formed network indeed prevented complete sedimentation in the long time periods.

Findings gathered by the sedimentation testing imply that after the addition of divalent cations 1.4NaPAA–MA particles were no longer individual entities, but rather formed an interconnected ceramic-polymer-divalent cation network.

4.3.4 Addition of cellulose nanofibers (CNF)

Another promising additive that can prevent sedimentation and segregation of micron-sized particles in aqueous suspensions by the formation of a fibre network is CNF. CNF was added to the aqueous 1.4NaPAA–MA suspensions. The CNF used for this purpose was TEMPO-oxidized to ensure a better dispersion in the aqueous medium [96], [97]. An approximate thickness of a single fibre was estimated by AFM to be around 2 nm (Inset of Figure. 4.17A).

A strong dependence between the viscosity of the 1.4NaPAA–MA suspensions and different CNF contents and MA volume fractions can be discerned from Figure 4.17B. A connection can be observed between the maximum amount of CNF and MA powder that could be added to the suspension prior to the viscosity reaching an infinite value. The amount of added CNF decreased gradually with an increasing MA volume faction, i.e., if the volume fraction was increased from 0.013 to 0.082, the maximum CNF amount that could be added decreased from 10 wt% to 1 wt% (of the MA powder's mass).

Viscosity of suspensions containing MA powder in the volume fraction of $\varphi_A = 0.013$ increased from approximately 1.5 mPa·s to over 1200 mPa·s after 10 wt% of CNF was

added. Such viscosity was close to the value observed in the suspension containing the maximum volume fraction (φ_A=0.126) of 1.4NaPAA–MA (Figure 4.9A). It can be observed that the viscosity was more influenced by the amount of added CNF than by the increase of MA powder's volume fraction.

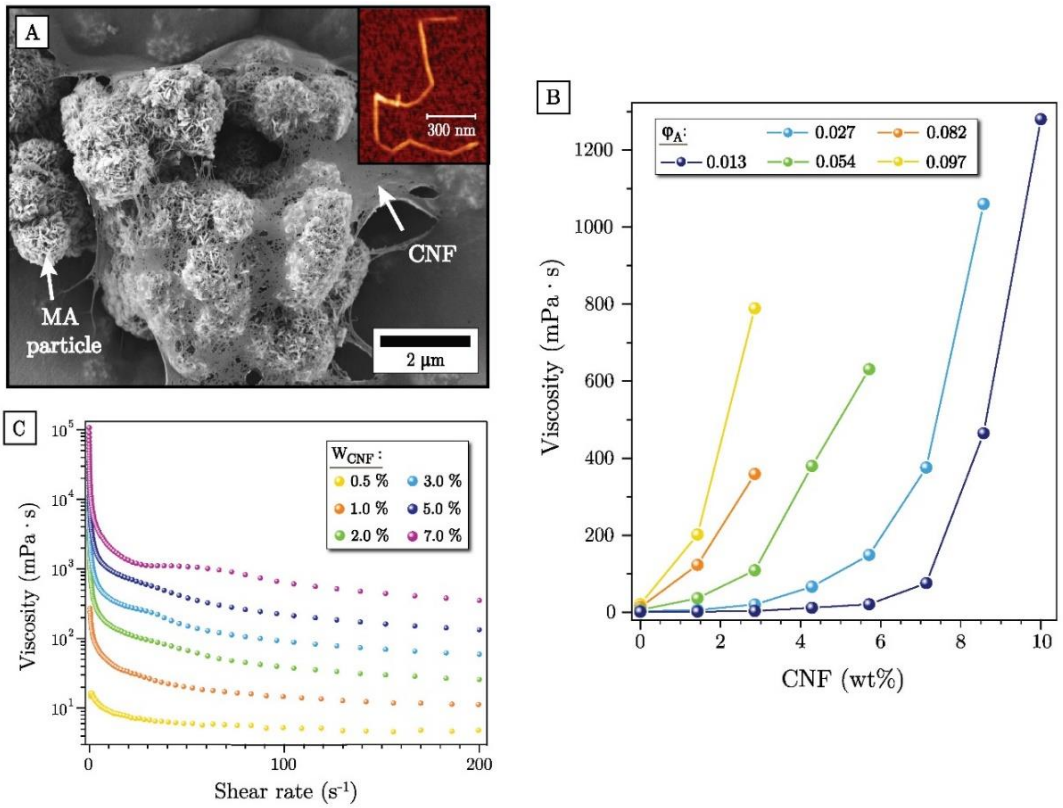

Figure 4.17: A) Viscosity of 1.4NaPAA–MA aqueous suspensions (pH = 9) with different powder volume fractions as a function of CNF addition measured at a shear rate of 50 s^{-1}. B) SEM image of 1.4NaPAA–MA particle with added CNF. Inset: AFM image showing a single cellulose nanofiber. C) Effect of the CNF amount on rheological behaviour of 1.4NaPAA–MA suspensions (φ_A = 0.027) at pH 9 as a function of shear rate.

At the lowest MA volume fractions, i.e., 0.013 and 0.027, the viscosity was increasing gradually until the CNF amount exceeded 7 wt% or 3 wt%, respectively. Afterwards, the viscosity started to increase abruptly. At lower MA volume fractions ($\varphi_A \leq 0.054$), a threshold occurred at the viscosity around 100 mPa·s. Above it, the viscosity also began to increase abruptly, following the trend – the higher the MA volume fraction, the steeper the increase of the viscosity. In addition, the amount of CNF at which this threshold was reached was MA-volume-fraction-dependent: the higher the volume fractions, the lower the amount of CNF needed to reach this threshold.

At lower shear rates, i.e., below 100 s^{-1}, the viscosity values grow a few orders-of-magnitude when the CNF amount was increased (Figure 4.17C), displaying the strong effect CNF had on the rheological properties. Addition of CNF also caused a change of the rheological behaviour from near-Newtonian to shear thinning, as was already reported by Liu et al. [224]. On the curve depicting the viscosity's dependence from shear rate (Figure 4.17C) of suspension containing MA powder (φ_A=0.027) and 7 wt% of CNF, a short plateau region can be discerned at the approximate shear rate of 30 s^{-1}. This phenomenon was already observed and described in the literature as breakdown of CNF structure occurring at a critical shear rate and high enough CNF concentrations [107].

Sedimentation tests (Figure 4.18) showed that the addition of CNF improved suspensions resistance towards sedimentation and particle segregation. However, the addition of only 0.5 wt% of CNF was not sufficient to prepare a suspension able to resist sedimentation or segregation for longer time periods. As can be seen from the pictures taken during sedimentation testing (Figures 4.18A and 4.18E), after only 10 minutes, a clear sediment boundary was visible, while the supernatant was notably turbid, indicating the smaller particles remained dispersed. On the other hand, a turbid supernatant could not be observed in suspensions containing 1 wt% or more of CNF. In the latter cases, the supernatant was completely clear and transparent. This suggested that smaller, colloidally stable particles were trapped inside the CNF network. It is surmised that MA particles are entrapped/adhered into CNF network which acts as a scaffold. Consequently, an interconnected CNF-MA particle network is created through bridging flocculation, which in turn helps to limit or even entirely prevent sedimentation over longer time-periods.

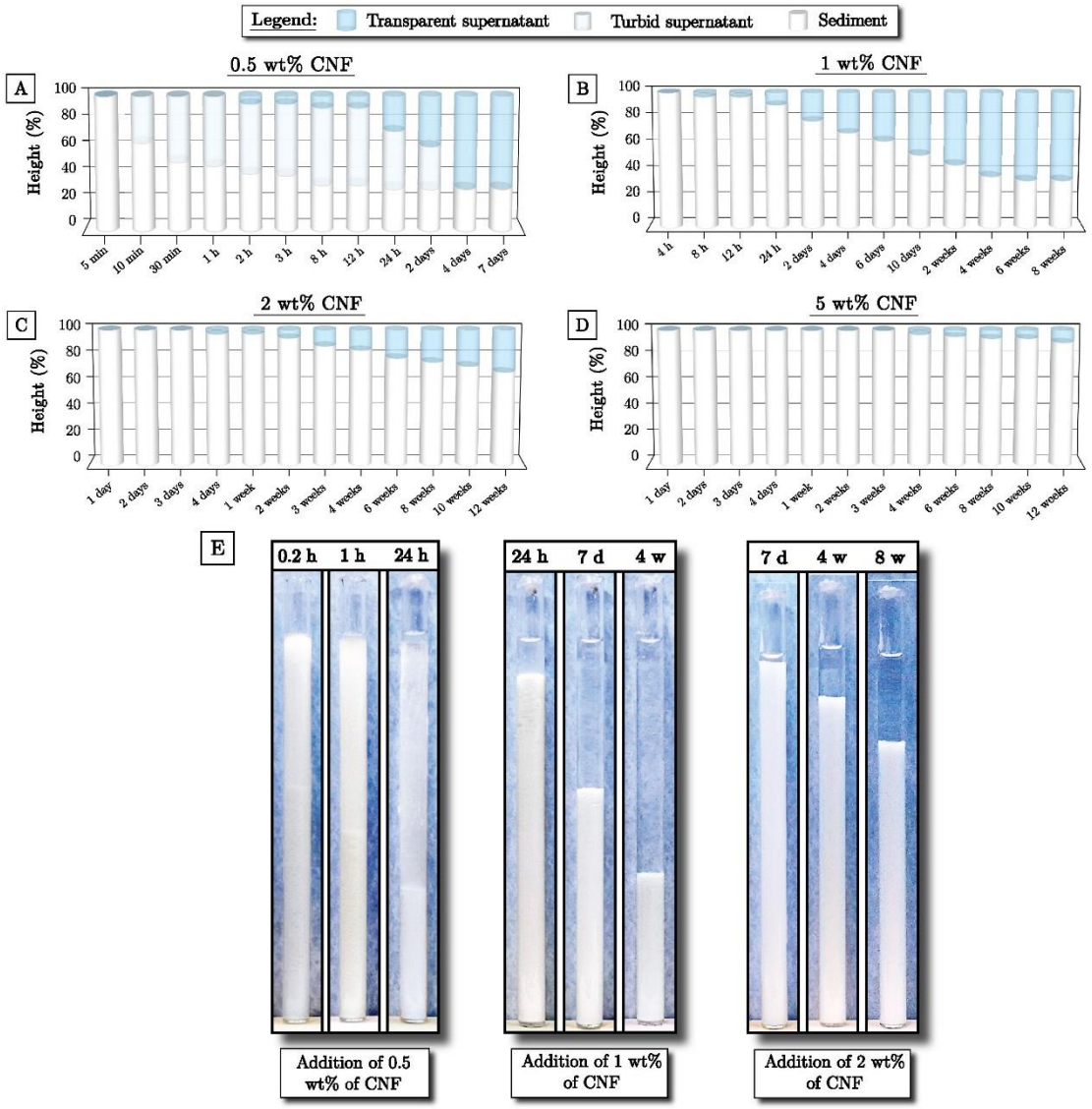

Figure 4.18: Sedimentation rates of $\varphi_A = 0.027$ 1.4NaPAA–MA aqueous suspensions (pH = 9) with added A) 0.5 wt% of CNF, B) 1 wt% of CNF, C) 2 wt% of CNF, D) 5 wt% of CNF. Pictures of sedimentation test of $\varphi_A = 0.027$ MA aqueous suspensions dispersed with 1.4 wt% of NaPAA at pH 9 and added 0.5 wt% of CNF (left), 1 wt% of CNF (middle) and 2 wt% CNF (right).

Additional increase of the CNF content further improved suspensions resistance towards sedimentation exhibiting significantly lower sedimentation rates. For example, suspension containing 1 wt % of CNF showed the first visible signs of sedimentation after 4 h (Figure 4.18B), while after the addition of CNF in the amount of 5 wt% of MA powder, no sedimentation could be observed for the first three weeks (Figure 4.18D). After 3 months, the same suspension barely sedimented, retaining over 90 % of its initial height.

4.3.5 Influence of Mg^{2+} and CNF addition on the zeta potential

The influence of addition of different amounts of Mg^{2+} cations or CNF on the zeta potential (ζ) of MA-containing suspensions at pH 9 was evaluated (Figures 4.19 and 4.20, respectively). In the case of CNF also the ζ at different pH values, but at constant amount of CNF (5 wt%) was determined (Figure 4.20B).

4.3.5.1 Influence of Mg^{2+} addition on the zeta potential

Addition of divalent cations (Mg^{2+}) to the suspension containing 1.4NaPAA–MA powder resulted in an interesting trend, which appeared to be reversed to the trend observed for viscosity values of the same suspensions (Figure 4.19). The absolute ζ value was the lowest at the same content of Mg^{2+} cations, where the viscosity was the lowest and vice versa.

At lower contents of Mg^{2+} cations (up to 20 mmol/mol), the absolute value ζ was decreasing almost linearly with the increasing Mg^{2+} content. The ζ increased from ≈ -55 mV before the addition of divalent cations to ≈ -20 mV after the addition of 20 mmol/mol of Mg^{2+}. This initial increase was followed by an increase of absolute ζ value (≈ –30 mV). The beginning of the latter decrease coincided with the onset of bridging flocculation, which occurred when the content of Mg^{2+} cations exceeded 22 mmol/mol (marked by a sharp increase of viscosity). On the other hand, when the content exceeded 40 mmol/mol, the absolute value of ζ started to decrease again (≈ –26.5 mV).

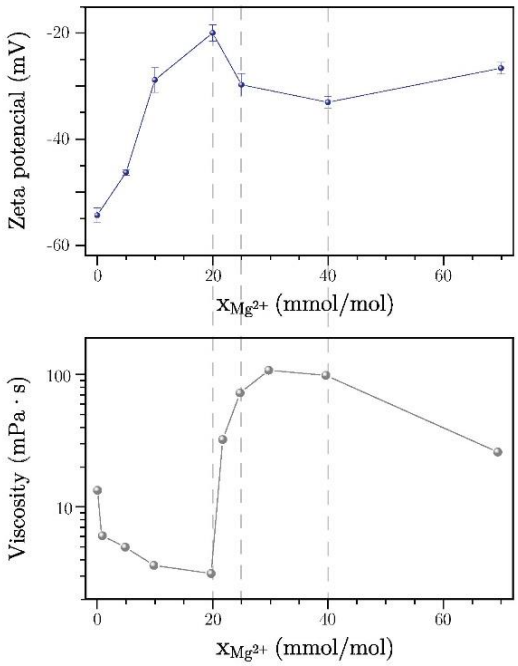

Figure 4.19: Zeta-potential curve of 1.4NaPAA–MA powder in diluted suspension at pH 9 with added different amounts of $MgCl_2$. For comparison, a curve showing viscosity (at 50 s^{-1} shear rate) as a function of $MgCl_2$ addition to φ_A=0.082 1.4NaPAA–MA aqueous suspension at pH 9 is also shown.

With regards to the obtained ζ and rheological data, we propose the following explanation of the ζ trend: the initial decrease of absolute ζ was caused by the shielding of negative charge of carboxylate groups on the PAA chains by the Mg^{2+} cations [84], [85]. Due to this charge shielding the coiling of PAA chains took place. Consequently, the thickness of polymer layer decreased, the shear plane moved closer to the surface of MA particle and the absolute value of ζ decreased [83]. The presence of divalent cations promotes the adsorption of PAA on the MA surface by creating bridges between the negatively charged surface of MA particles and the negatively charged NaPAA's carboxylate groups ($Al–O^- + R–COO^- + Mg^{2+} \rightleftharpoons Al–O\cdots Mg\cdots OOC–R$) [83], [84], [225], [226]. Consequently, the decrease of absolute value of ζ could also be partially ascribed to the shielding of MA particles negative surface charge by Mg^{2+}. When Mg^{2+} content exceeded 22 mmol/mol, the bridging flocculation was initiated and complexes of neutral salts were formed ($2R–COO^- + Mg^{2+} \rightleftharpoons (R–COO)_2Mg$). Formation of these complexes meant that the carboxylate groups, which prior to the bridging carried positive charge ($R–COOMg^+$), were now neutral and attributed to the slight increase of the of absolute ζ value. Above a certain content of divalent cations ($Mg^{2+} > 40$ mmol/mol), the dissolution of formed salt bridges started [78]. As a consequence, the of absolute value of ζ again decreased approaching the ζ value 1.4NaPAA–MA particles had before the onset of bridging flocculation (at 20 mmol/mol of $MgCl_2$ added).

4.3.5.2 Influence of CNF addition on the zeta potential

1.4NaPAA–MA suspension containing CNF in the range of 0.5–7 wt% exhibited an average ζ of –35.9±2.7 mV (marked by the dashed line in Figure 4.20A). This was slightly more negative in comparison to pure MA particles (-28 mV) [182]. On the other hand, a more negative ζ was observed for 1.4NaPAA–MA particles (≈ -55 mV). Since the absolute value of ζ was higher than 30 mV, the secondary particles (agglomerated clusters) repelled each other, meaning the suspensions had a more or less high degree of stability [68]. The scattering of results obtained for individual CNF contents showed no dependence from the amount of added CNF. The scattering was ascribed to the slight deviations in the suspensions properties, such as clustering/association of CNF after dispersion, occurring due to the hydrophobic interactions [227], degree of CNF swelling [228] or the amount of MA powder surface covered by the CNF network [20], [229].

To determine the effect of individual components, ζ of pure CNF and mixture of CNF and NaPAA at pH=9 was also determined. The value obtained for pure CNF was -43.8±0.74 mV. The value obtained after NaPAA was added to CNF was almost the same as in the case of pure CNF, i.e., -39.1±1.2 mV, indicating that NaPAA addition had little effect on the ζ of CNF fibres.

The difference between the ζ values for pure CNF or CNF/NaPAA system and the values of ζ obtained for systems containing 1.4NaPAA–MA and CNF could be a consequence of the difference in the suspensions concentrations. The concentration of CNF and NaPAA used for the determination of ζ was between 50 and 30 times higher in the suspensions without MA powder than in the suspensions containing MA powder. It was previously shown that an increase of the polysaccharide concentration lowers the absolute value of ζ [227]. However, the measurements of ζ could not be performed if the concentration of pure CNF or NaPAA/CNF was equal to the one used for the determination of ζ in the 1.4NaPAA–MA/CNF system. The number of particles was either under the detection limit or the concentration was too high to perform a valid measurement. Consequently, it was not possible to conclude if the ζ of pure CNF fibres was the same, higher or lower as the one obtained for the 1.4NaPAA–MA and CNF

systems. In other words, it was not possible to discern how and if the addition of 1.4NaPAA–MA particles affected CNF's ζ.

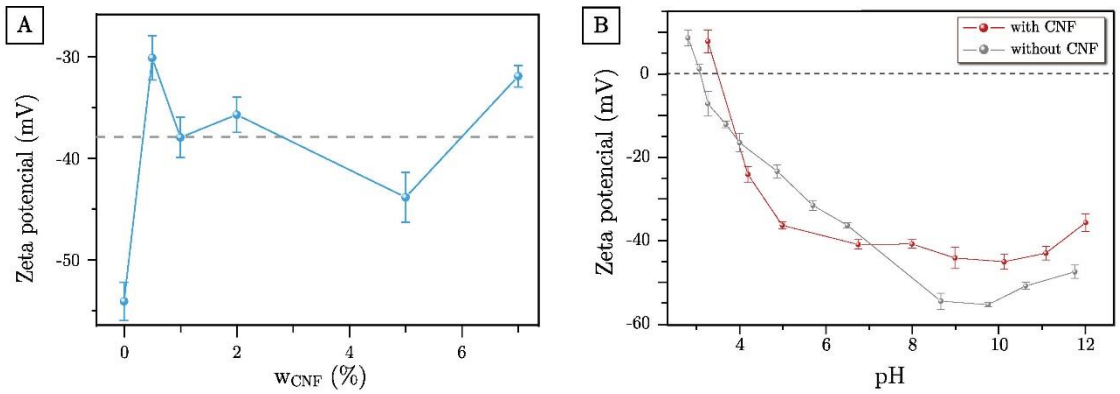

Figure 4.20: A) ζ curve of 1.4NaPAA–MA powder in diluted suspension at pH 9 and different amounts of CNF. The dashed line marks the average value of ζ. B) ζ curves of 1.4NaPAA–MA powder in diluted suspension at pH 9 with or without added CNF.

Still assuming that the difference in the suspensions concentration had a negligible effect on the measured ζ value the following explanation of the difference between individual values can be offered. The most plausible explanation of the decreased absolute ζ value of 1.4NaPAA–MA particles after the addition of CNF is that it occurred due to the CNF network partially covering the surface of NaPAA-dispersed MA particles. NaPAA molecules carry approximately 12 times more charge per unit of mass than CNF fibres. Thus when CNF covered MA surface, previously occupied by adsorbed NaPAA molecules, the absolute value of ζ decreased due to the adsorption of polymer with lower number of charged groups. Yet in order to confirm the validity of this explanation, the thickness of CNF layer, coating the MA particles, should be determined. The ζ of polymer-coated particles is influenced by the coating's thickness. In the case of a thick polymer layer, the ζ of the underlying particle is concealed and the measured ζ is only the potential of the coating layer. On the other hand, for thinner polymer layers, the value of ζ is the sum of both potentials, i.e., of the coating polymer and the underlying particle [229].

In the case of CNF also the ζ of 1.4NaPAA–MA at different pH values, but at a constant amount of CNF (5 wt%), was determined (Figure 4.20B). The most prominent change noticeable after the addition of CNF was an occurrence of a near-plateau region in the approximate pH range from 5 to 10. Occurrence of a plateau in this pH range is common for cellulose materials [228], [230], [231], and was ascribed to the fully dissociated carboxyl groups ($pK_a \approx 3.9$) [228], [232]. The highest absolute ζ was obtained at pH values between 9 and 10. This slight increase could be ascribed to the contribution of MA particles negative surface charge to the overall potential. As can be seen from the grey line in Figure 4.20B, the absolute value of ζ of 1.4NaPAA–MA particles was also the highest at this pH value. At even more alkaline values (pH >10) the absolute ζ slightly decreased. This decrease presumably occurred due to the compression of the electric double layer caused by the increased ionic strength. The latter occurred due to the increased concentration of NaOH, added to adjust the pH value [58]. When pH was lowered to neutral or acidic values (pH< 5), a step decrease of absolute value of ζ was observed. The decrease was ascribed to the protonation of carboxylate group ($R–COO^- \rightleftharpoons R–COOH$). Due to this neutralization of negative charge, the absolute ζ decreased. Afterwards, the CNF were not stable and tended to agglomerate if the pH was lowered below 3.5 (IEP). The IEP was slightly shifted after the addition of CNF, i.e., from 3.0 for 1.4NaPAA–MA system [182] to 3.5. The resemblance

between both IEPs is a consequence of the similarities in the chemical structure of NaPAA and cellulose [231]. Both substances contain carboxylate groups and possess similar pKa values, i.e., 3.9 for TEMPO-mediated cellulose [232] and 4.4 for NaPAA [233].

After the addition of CNF or Mg^{2+} the absolute value of ζ decreased in respect to the ζ value of 1.4NaPAA–MA particles, yet the decrease was more substantial after the addition of cations. The addition of CNF to 1.4NaPAA–MA aqueous suspensions decreased the absolute value of ζ (from -55 mV to approximately -36 mV). The former change was ascribed to the formed CNF coating on the MA particle surface. However, the ζ was not affected by the change of CNF concentration at constant 1.4NaPAA–MA content. On the other hand, the amount of added divalent cations had a pronounced influence on the ζ, which varied in the range of -40 mV and -20 mV.

4.4 Freeze-Casting of HMMA Monoliths

Three aqueous suspensions containing AlN-hydrolysis derived MA powder dispersed with NaPAA at pH of 9 were freeze-cast. One suspension contained only 1.4NaPAA–MA powder, while the other two were additionally stabilized by the addition of either Mg^{2+} cations or CNF.

Freeze-casting of aqueous suspensions containing only 1.4NaPAA–MA powder resulted in very fragile green bodies. As can be seen in Figure 4.21A, the monolith fragmented to pieces already during handling. Monolith prepared from aqueous suspension containing 1.4NaPAA–MA powder additionally stabilized through the triggering of interparticle associations (bridging flocculation) by the addition of divalent Mg^{2+} cations resulted in a green body with even poorer mechanical properties. The monoliths were extremely fragile, since they broke down into smaller pieces already during the freeze-drying stage (Figure 4.21B). Although interparticle associations were present in the suspension (interactions were formed between Mg^{2+} cations and carboxylate groups on the NaPAA chains adsorbed on the surface of MA particles), results suggest these interactions were not strong enough to produce rigid and self-standing green bodies. A more efficient binder is apparently needed in order to provide sufficient support to unsintered highly porous MA freeze-cast monoliths.

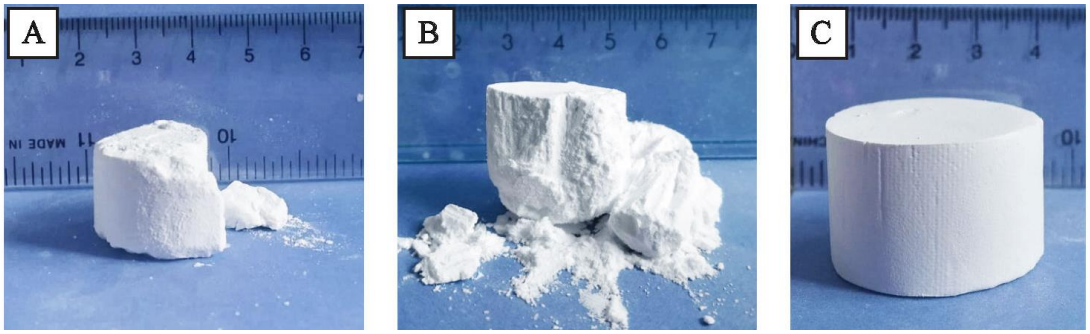

Figure 4.21: HMMA monolith prepared by freeze casting of A) aqueous suspension containing only 1.4NaPAA–MA powder ($\varphi_A = 0.082$), B) aqueous suspension containing 1.4NaPAA–MA powder ($\varphi_A = 0.082$) and 30 mmol/mol of Mg^{2+} cations, C) aqueous suspension containing 1.4NaPAA–MA powder ($\varphi_A = 0.082$) and 1 wt% of CNF.

On the other hand, monolith prepared by the addition of CNF to the suspension containing 1.4NaPAA–MA powder resulted in a stable green body (Figure 4.21C), showing potential for further studies, unlike the green bodies prepared from suspension stabilized by the addition of Mg^{2+} cations.

4.4.1 Fourier transform infrared spectroscopy (FTIR)

Fourier transform infrared spectroscopy (FTIR) was employed to study the nature of interactions between MA particles, NaPAA and CNF, owing to which the freeze-cast monoliths exhibited sufficiently high rigidness. Spectra of pure components, i.e., MA powder and freeze-dried CNF (Figure 4.22) were compared to the spectra of samples containing different mixtures of MA powder, NaPAA and CNF (Figures 4.24 and 4.25) in order to determine what type of interactions were formed between individual components in the final materials.

4.4.1.1 Spectra of pure components

In Figure 4.22A the bands of pure MA powder (γ–Al_2O_3) are shown. The band at 3294 cm^{-1} is characteristic for asymmetric stretching (ν_{as}) of (Al)O–H bonds [234], while the band at 3089 cm^{-1} belongs to the symmetric stretching (ν_s) of the same bonds [235]–[237]. Bands at 1145 and 1069 cm^{-1} can be assigned to the deformation of (Al)O–H bonds, i.e., δ_{as} and δ_s, respectively [235], [237]. The bands in the region below 1000 cm^{-1}, i.e., the bands at 731 and 566 cm^{-1}, can correspond to the stretching and bending vibrations of Al–O bonds from the octahedrally coordinated aluminum–oxygen complex (AlO_6) [238]. The band at 1641 cm^{-1} belongs to the vibrations (stretching) of O–H bond from adsorbed water molecules [235], [238], [239]. When water molecules are present a second band at ≈3490 cm^{-1} also appears [235], [238]. In the present case, this band might be deconvoluted from the wide band at 3294 cm^{-1}.

The weak bands at 2981 cm^{-1} and 1389 cm^{-1} could be ascribed to the stretching of C–H bond, indicative of a presence of residues of organic matter from the possible contamination, for example from ethanol used for cleaning of the FTIR set-up. The wide band occurring at ≈2100 cm^{-1} seen on the inset of Figure 4.22A was a combination band [238].

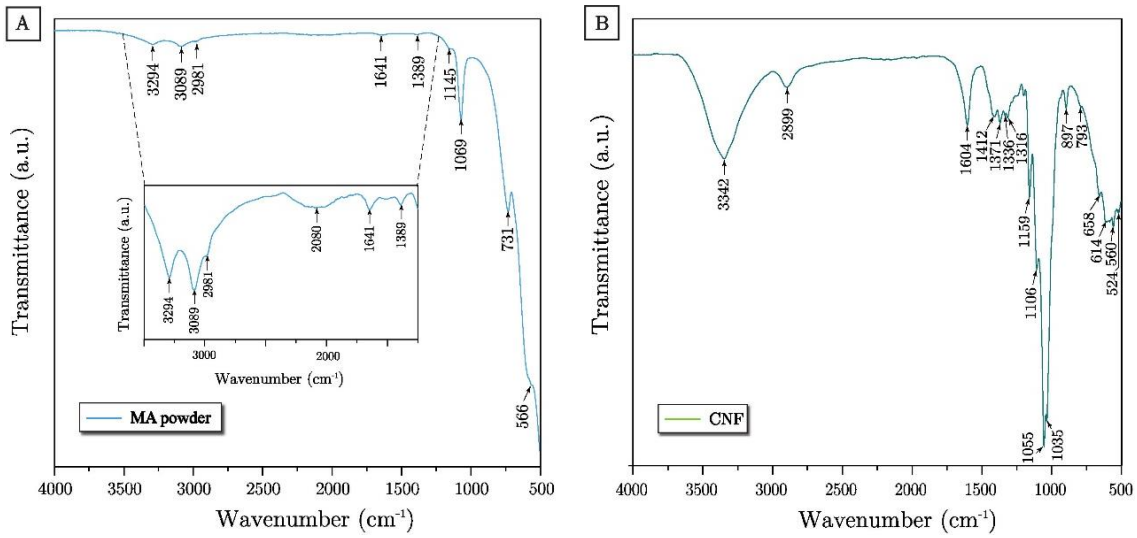

Figure 4.22: FTIR spectrum of A) MA powder and B) freeze-dried CNF.

Based on the chemical structure of cellulose (Figure 4.23) vibrations for hydroxyl group (–OH) of secondary alcohol, for carboxylate anion (R–COO^-) and for cyclohexane were expected. The connection between two individual rings forms an acetal bond (R–O–CH–O–R'), so bands for this group are also expected. The stretching and bending vibrations of these bonds frequently overlap, making band assignment a challenging task.

The wide band at 3342 cm^{-1} can be ascribed to the stretch of the O–H bond. The band's width at half maximum exceeds 300 cm^{-1} and its position between 3400 and 3300 cm^{-1} suggested that between individual OH groups intermolecular polymeric hydrogen bonds were formed [240]. In cellulose intra-molecular hydrogen bonds can also form between two OH groups [241]. The stretching vibration for intra-molecular hydrogen bond occurs between 3600 and 3500 cm^{-1} as a band of medium intensity. In CNF spectrum this band was most likely overlapping with the wide, more intense band for vibrations of inter-molecular hydrogen bonds.

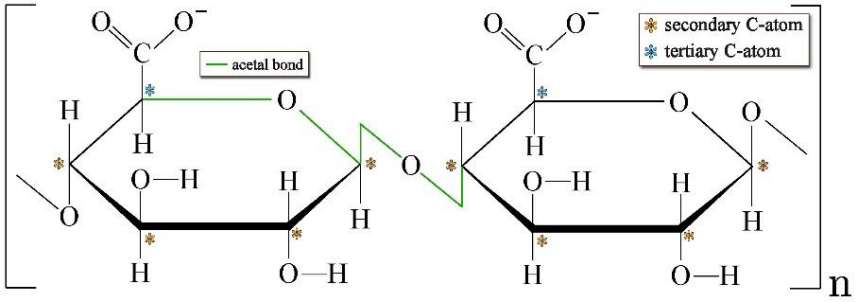

Figure 4.23: The structure of a monomer comprising TEMPO-mediated cellulose. The orange asterisks mark secondary carbon atoms (R_2–CH_2), while the blue asterisks mark tertiary carbon atoms (R_3–CH).

A much weaker band at 2899 cm^{-1} occurred due to the asymmetric and symmetric stretching of C–H bond [240], [242]. The vibrations appeared at a slightly higher frequency than in the unsubstituted CH_2 group. The shift occurred due to the presence of electron withdrawing groups, i.e., negative inductive effect of hydroxyl and also ether groups bound to the carbon atoms [242]. The sharp and strong band appearing at 1604 cm^{-1} belonged to the asymmetric stretching of the carboxylate anion (R–COO^-), while the band at 1412 cm^{-1} corresponded to the symmetric stretching of the same bonds [240], [242].

Bands at 1371 and 1336 cm^{-1} are characteristic for cellulose and occurred due to the in-plane deformations of C–H and O–H bonds, respectively [242], [243]. The weak band at 1315 cm^{-1} corresponded to the wagging of the CH_2 group [243]. The other band for vibration of C–H bond, either from secondary or tertiary carbon atom, occurred between 1422 and 719 cm^{-1} [242], yet their intensities are mostly weak and are thus commonly covered by other, more intense bands. The band at 1159 cm^{-1} occurred due to the asymmetric stretching of acetal bond, i.e., the "bridge" between two glucopyranose rings [240], [244], [245]. At lower wavelengths, vibrations of bonds between carbon and oxygen can be observed. The bands at 1106 and 793 cm^{-1} were attributed to the out-of-phase and in-phase stretching of C–C–O bonds, respectively [240], [242]. The vibrations at 1055, 1035 and 897 cm^{-1} can be ascribed to the C–O–H stretching, C–O–C ring skeletal vibration and asymmetric ring breathing, respectively [240], [242], [243]. The band for symmetric ring breathing, which usually occurs between 785 and 755 cm^{-1} [242], was overlapping with the band at 658 cm^{-1}. Bands at lowest wavelengths, i.e., 658 and 524 cm^{-1} are characteristic of the acetal bond deformation [240], [242]. The former could be overlapping with the band for O–H out-of-phase deformation [243]. The remaining bands at 614 and 560 cm^{-1} can be ascribed to the carboxylic anion scissoring and wagging deformation, respectively [242].

4.4.1.2 Spectra of composite samples

Spectrum of pure components, i.e., MA powder and CNF, were then compared to the spectrum of sample containing either only CNF and NaPAA (Figure 4.24) or to a spectrum

of a sample containing MA powder and CNF (Figure 4.25) to determine what type of interactions were formed between individual components in the final material.

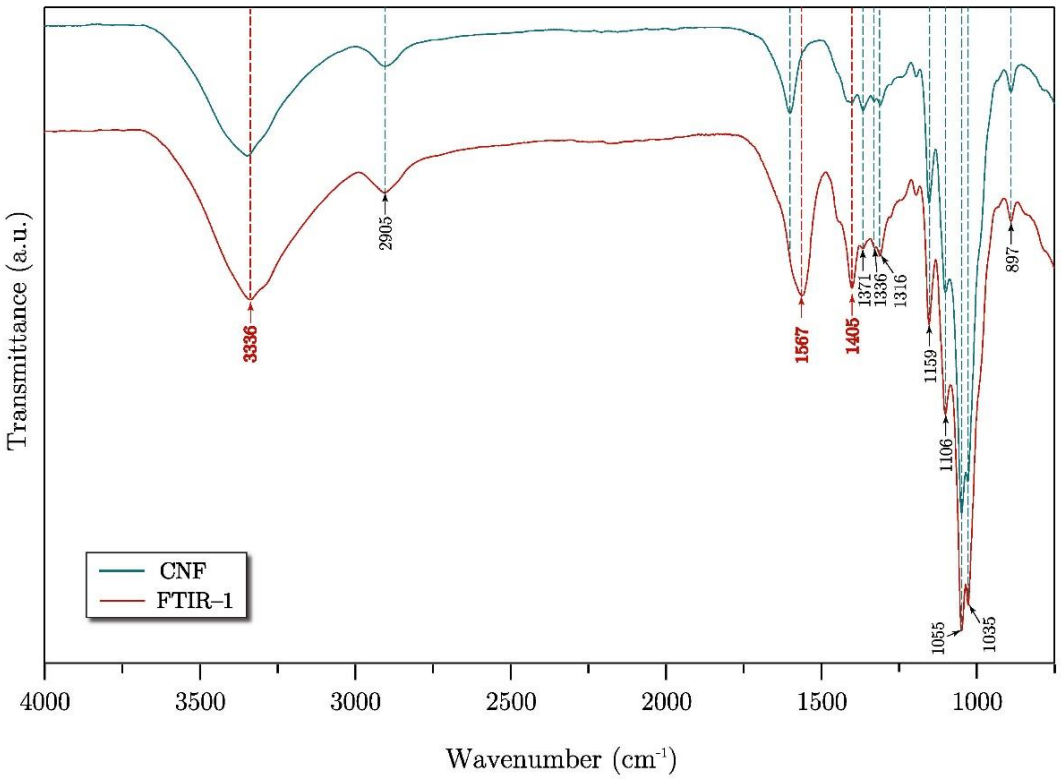

Figure 4.24: Comparison of FTIR spectrum of freeze-dried CNF and FTIR–1 to establish the type of interactions between CNF and NaPAA.

The chemical structure of NaPAA is much simpler in comparison to the structure of cellulose. In the NaPAA molecule, only vibrations of carboxylate anion and C–H vibrations for secondary and tertiary carbon atom are expected. However, the C–C skeletal vibration modes are usually weak and thus of little use in mid-infrared spectroscopy [242].

In the region below 1400 cm^{-1}, the spectra of CNF and sample containing CNF and NaPAA (FTIR–1) were practically identical. In Figure 4.24, the red dashed lines mark the bands not present or appearing at slightly different wavenumbers than in the spectrum of pure CNF. These bands occurred at 3336, 1567 and 1405 cm^{-1}. The band at 3336 cm^{-1} was shifted to a slightly lower wavenumber in comparison to the band's position in the spectrum of pure CNF (3342 cm^{-1}). Since the position and width of this band depends strongly on the type of hydrogen bond, it can be assumed that after the addition of NaPAA new hydrogen bonds between the oxygen atoms on NaPAA chains and hydroxyl groups on CNF were formed, thus lowering the band's wavenumber [240].

The bands occurring at 1567 and 1405 cm^{-1} corresponded to ν_{as} and ν_{s} of the carbon–oxygen bonds in carboxylate anion ($R–COO^{-}$), respectively. These vibrations could also be observed in the spectrum of pure CNF, but at slightly higher wavenumbers, i.e., 1604 and 1414 cm^{-1}. Both bands occurred at slightly lower wavenumbers in the spectrum of FTIR–1 due to the absence of electron withdrawing groups, i.e., hydroxyl and ether groups in the molecule of NaPAA. The bands for ν_{as} and ν_{s} of the carboxylate anion from CNF and from NaPAA were overlapping due to a very similar wavelength of both bond vibrations as can be seen in Figure 4.24. From the absence of newly formed bands, e.g., a strong band for the vibration of C=O (carbonyl) bond of the ester group, appearing between 1750 and 1735

cm^{-1} [240] it could be concluded that during suspension preparation, freezing or drying no reaction between CNF and NaPAA took place. However, individual molecules most likely interacted with each other via hydrogen bonding.

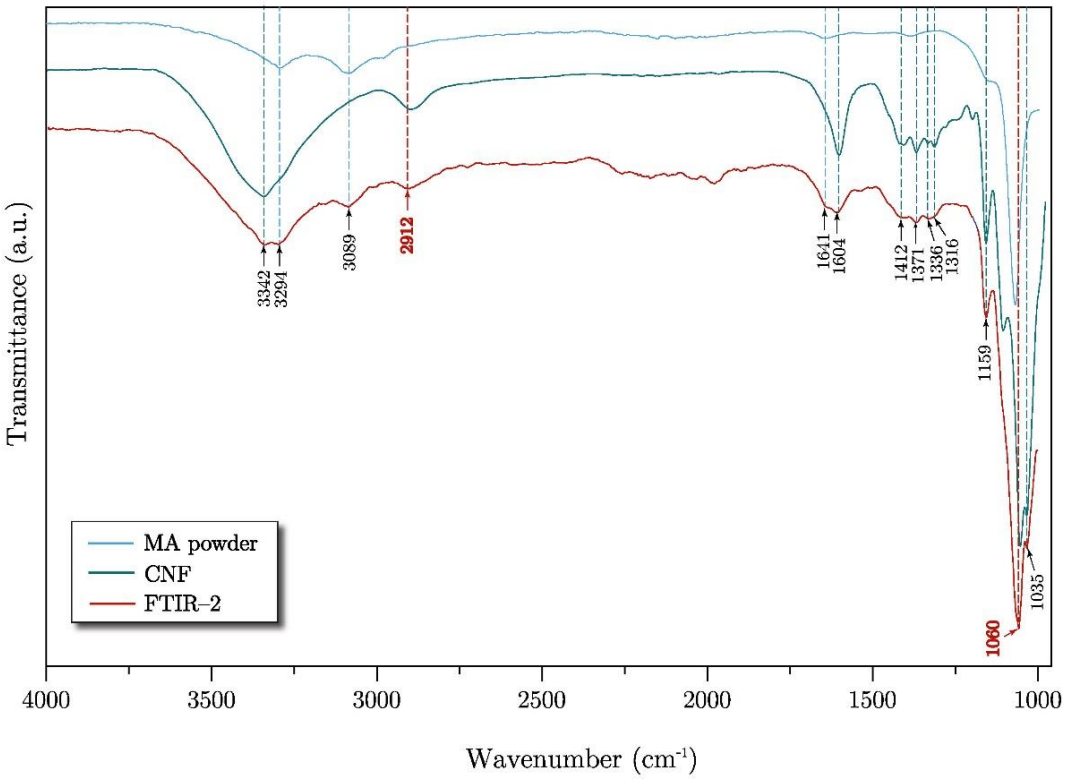

Figure 4.25: Comparison of FTIR spectrum of freeze-dried CNF, MA powder and FTIR–2 to establish the type of interactions between CNF and MA powder.

The interactions between MA and CNF were also studied by FTIR (Figure 4.25). On the spectrum of FTIR–2 (sample containing MA powder and CNF), no new bands could be observed, though two bands, i.e., at 2912 and 1060 cm^{-1}, appeared at slightly shifted wavelengths. The band at 2912 cm^{-1} could only be seen in the spectrum of pure CNF (Figure 4.22B), where it appeared at lower wavelength (2899 cm^{-1}). In CNF this band was ascribed to the asymmetric and symmetric stretching of the C–H bond. The shift to higher wavenumbers could be a consequence of the changes in the strength of hydrogen bonding and thus changes in the strength of negative inductive effect of hydroxyl groups, which cause the shift of this band to higher wavelengths [242]. On the other hand, the band at 1060 cm^{-1} (ascribed to vibrations of the –O–H bond) could be seen in both pure MA powder and pure CNF spectrum. However, both bands appeared at slightly different wavelengths, i.e., 1069 cm^{-1} (MA powder) and 1055 cm^{-1}(CNF). This observation can be explained by the presence of hydrogen bonds, which slightly decrease the vibration's frequency, with the decrease being proportional to the strength of the formed bonds [242]. Thus it can be postulated that the slight difference in the positions of all three –O–H bond vibration frequencies occurred due to the formation of different hydrogen bonds. In pure MA sample these bonds were formed between individual hydroxyl groups on the surface of MA particles. In pure CNF sample hydrogen bonds were formed between hydroxyl groups from individual CNF molecules. On the other hand, in the composite sample also hydrogen bonds between hydroxyl groups present on MA surface and hydroxyl groups from CNF

molecules could also be formed. This new type of hydrogen bonds could explain the shift of –O–H bond vibration band.

The –O–H bond vibration occurred at a lower wavelength in case of pure CNF, indicating that the hydrogen bonds between individual molecules of CNF were stronger than the hydrogen bonds formed between the OH group from a MA particle and the OH group from a CNF molecule. On the other hand, the position of –O–H vibration band at higher wavelength in the case of MA powder indicates that the strength of hydrogen bonds between two hydroxyl groups from MA powder was lower than the strength of hydrogen bonds formed between MA and CNF.

The FTIR measurements confirmed that interactions were formed between MA particles, NaPAA and CNF. While no chemical reaction took place, the components were to some degree interconnected through hydrogen bonding.

4.4.2 Freeze-casting of CNF-stabilized HMMA monoliths

Hierarchically macro-mesoporous alumina (HMMA) monoliths were prepared by employing freeze-casting of aqueous suspensions containing MA powder dispersed with NaPAA (1.4NaPAA–MA) and cellulose nanofibers. CNF were added in order to endow HMMA monoliths with mechanical stability as well as to prevent sedimentation and particle segregation during freezing [182]. The process of monoliths preparation is summarized in Chapter 3.4 and Figure 3.1.

In order to evaluate the influence of freezing rate (1 °C/min or 6 °C/min) and the ratio between water, MA powder and CNF on the final properties of freeze-cast HMMA monoliths, surface area, porosity, permeability, thermal conductivity and mechanical properties under compression were studied in detail.

4.4.2.1 Microstructural characterization

The main characteristic of porous materials prepared by unidirectional freezing of aqueous suspensions is the evolution of pore channels, a replica of the ice crystals formed during freezing [18], [51].

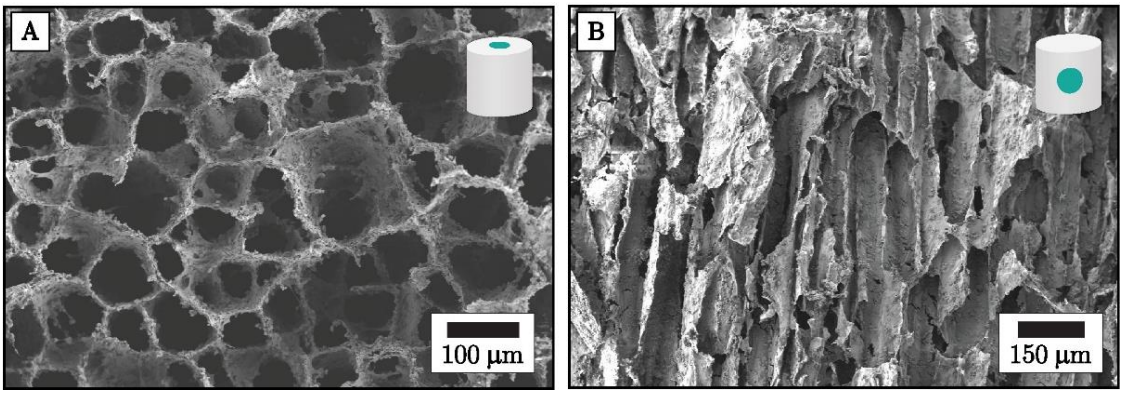

Figure 4.26: SEM of HMMA monolith containing $\varphi_A = 0.027$ of MA powder and 7 wt% CNF (FZC–5) viewed in A) axial direction (top view) and B) radial direction (side view).

HMMA monoliths prepared via freeze-casting possessed columnar-like porosity running parallel to the freezing direction as shown in Figure 4.26. The struts were composed of the CNF network in which MA particles were entangled in. The latter endowed the struts with mesoporosity. If a directional temperature gradient is applied to a suspension, the growth of solid crystals is directional rather than random, i.e., the crystals grow alongside the

direction of the temperature gradient [18]. Consequently, pore channels run continuously along one of the monolith's axis, mostly from the bottom to the top, resulting in a material with a long-range ordered porosity [27].

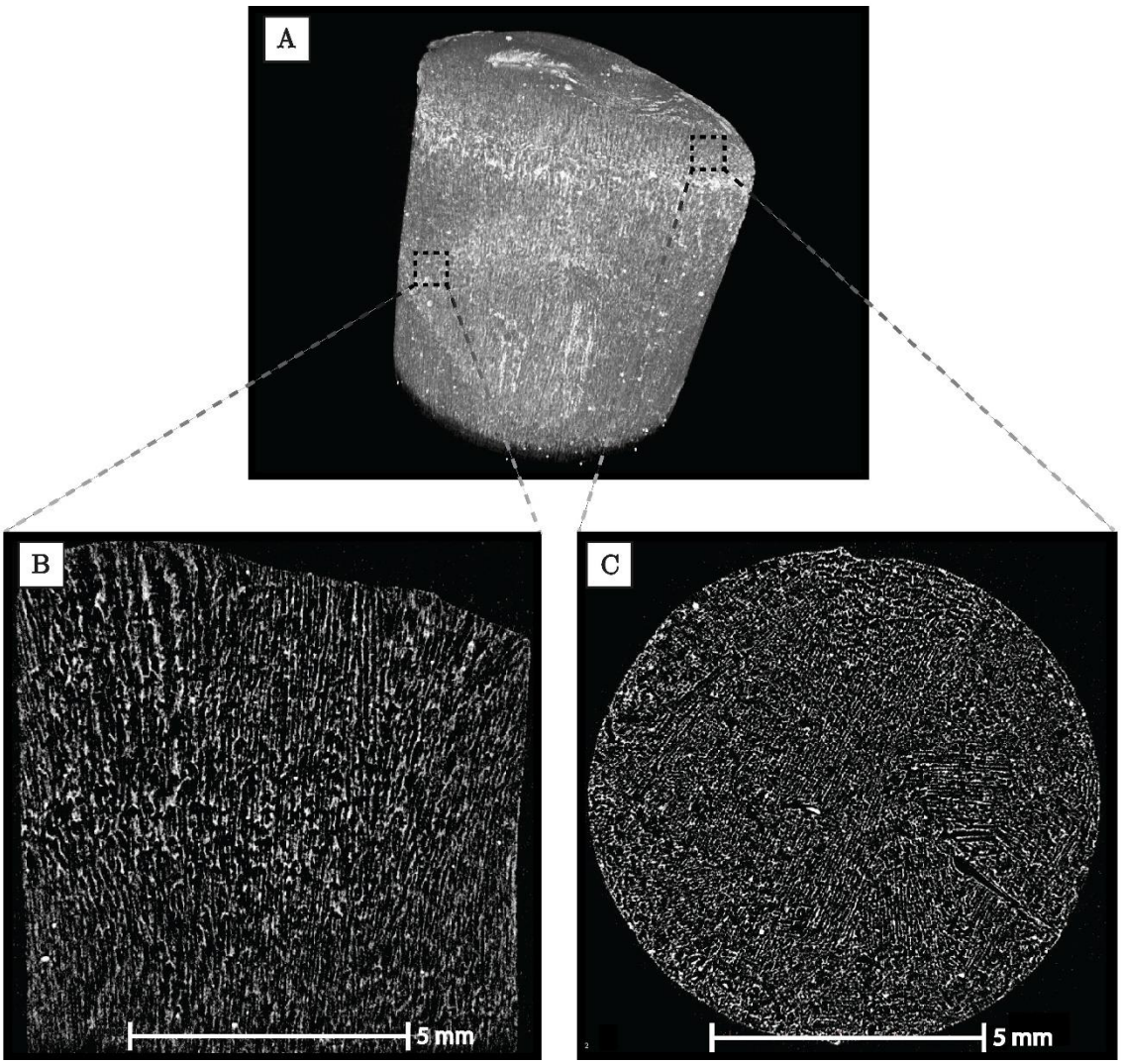

Figure 4.27: A) μ–CT image of monolith FZC–5 viewed in 3D. B) μ–CT image of monolith FZC–5 viewed in axial direction. C) μ–CT image of monolith FZC–5 viewed in radial direction.

The presence and the extent of the columnar-type of porosity in the HMMAs monoliths was inspected with the μ–CT analysis (Figure 4.27). In the direction parallel to the ice growth (axial direction, Figure 3.1), pores exhibited long-range order (Figure 4.27B). However, this was not the case in the direction perpendicular to the ice-growth front (radial direction, Figure 3.1), where the distribution and shape of pores looked rather random (Figure 4.27C). Yet a closer examination of these μ–CT images revealed that the distribution was not entirely random, but rather demonstrated some short-range order. Sections where pore walls were locally aligned were present, however no true long-range order could be observed. These randomly oriented, limited domains, consisting of organized channels/lamellae are characteristic for materials prepared by unidirectional freezing on a cold smooth plate, like the surface of a copper rod [18], [246].

The specific surface area (SSA) of freeze-cast monoliths containing MA powder (monoliths from FZC–2 to FZC–9; for composition see Table 3.1) was between 91 m^2/g and 134 m^2/g, while the freeze-cast monolith containing only CNF and NaPAA (FZC–1) had a much lower SSA of only 45 m^2/g. Although the SSA of monoliths containing MA powder was high compared to freeze-cast alpha-alumina porous ceramics [247] it was still lower than the surface area of the pure MA powder (180 m^2/g). A segment of the MA powder's surface area was lost presumably due to a partial coverage of the MA particle's surface with the CNF network as can be seen in Figure 4.28. Thus, the HMMA`s surface area (SSA) was irreversibly proportional to the amount of CNF (MA/CNF ratio). The higher the amount of CNF (lower MA/CNF ratio), the lower the SSA (Table 4.4). The freezing rate affected the SSA as well. SSA of two monoliths containing the same MA/CNF ratio frozen at two different rates, namely monoliths pairs FZC–5/FZC–6 (MA:CNF = 14:1) and FZC–7/FZC–8 (MA:CNF = 50:1), were compared. A higher surface area was observed for the monoliths frozen at the faster rate. The higher SSA of fast frozen monoliths was in accordance with the theoretical expectations, since a more rapid freezing rate results in the formation of a higher number of smaller pores. Thus a greater surface area of pore walls is formed, leading to a higher HMMA monolith's pore surface area [22].

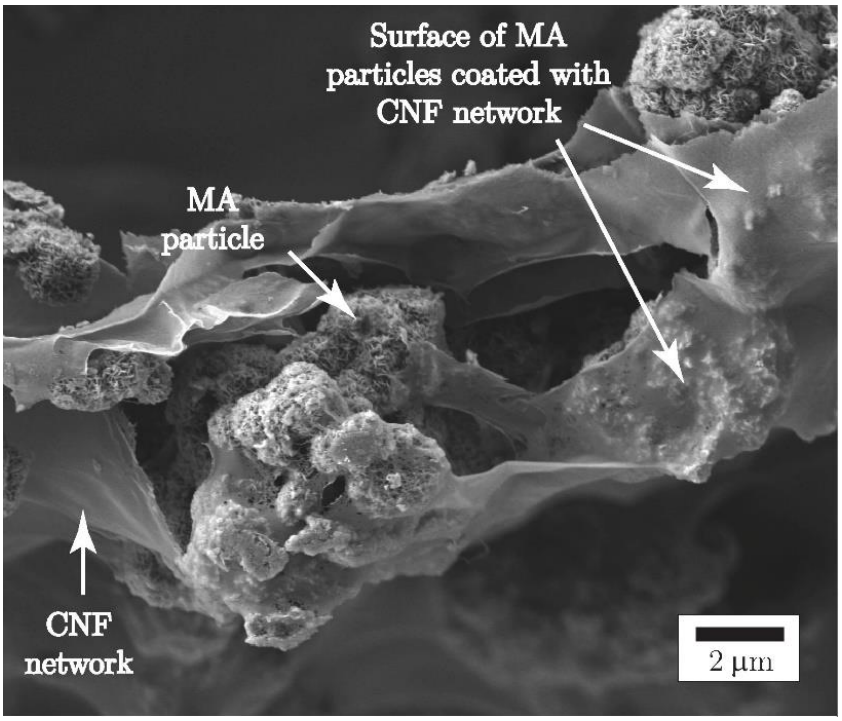

Figure 4.28: SEM image of MA particles entrapped in the CNF network.

SEM imaging fractions were performed to evaluate the influence of MA powder volume content in the freeze-cast slurries on the pore shape and the pore size of the HMMA monoliths. The results (Figure 4.29) showed that pore sizes started to decrease with increasing MA powder volume fraction (φ_A), while pore walls began to thicken. Also, when MA volume fraction was increased, the columnar structure became less distinctive. While at $\varphi_A = 0.054$ (Figure 4.29D) columnar porosity could still be distinguished, although its shape started to resemble a layer-like structure. It was also no longer as well defined as in HMMA monoliths with lower fractions of MA powder (Figure 4.29B and 4.29C).

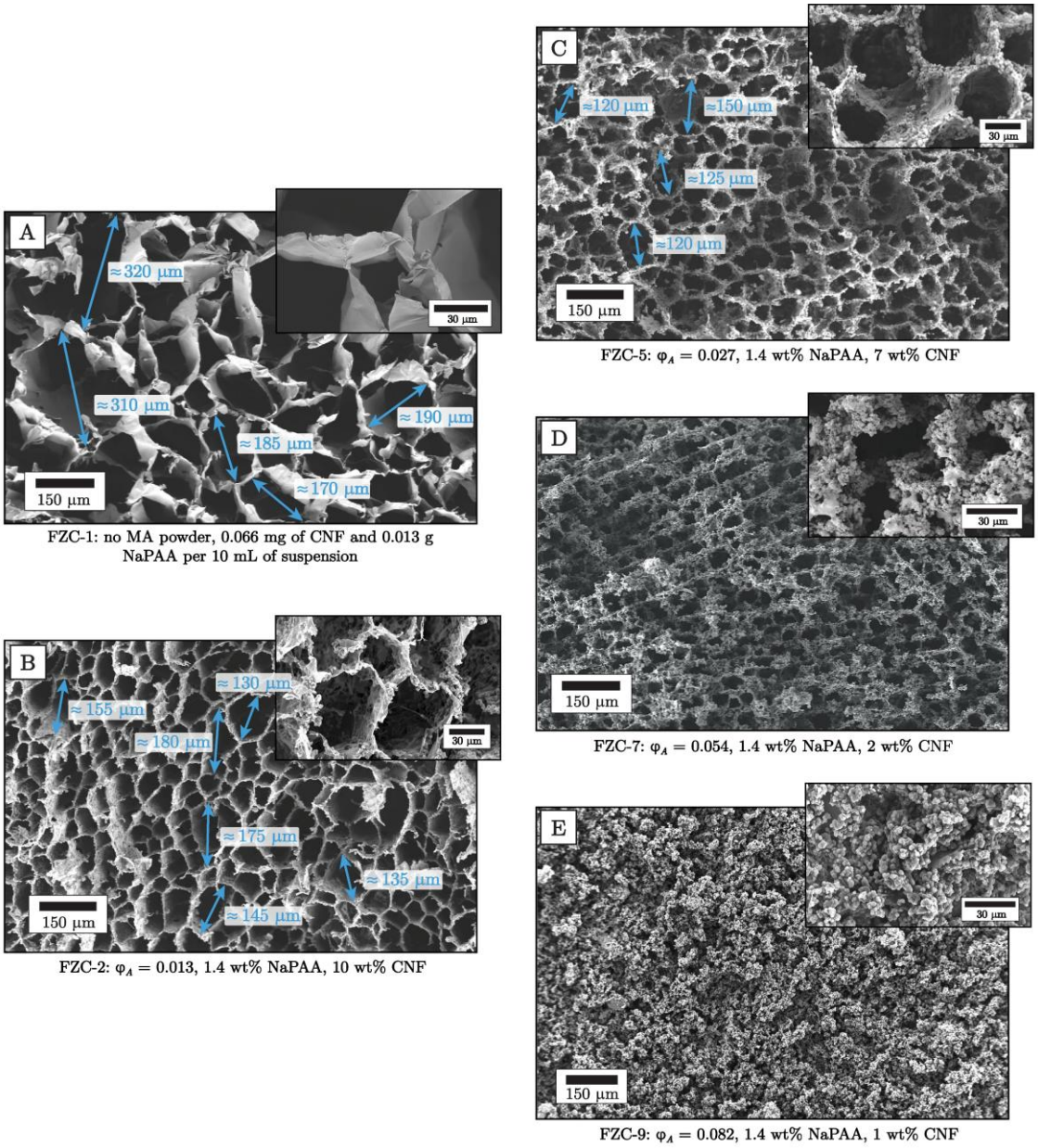

Figure 4.29: SEM images of freeze-cast monoliths A) FZC–1, B) FZC–2, C) FZC–5, D) FZC–7, and E) FZC–9, viewed in axial direction, i.e., perpendicular to the freezing direction. Arrows mark pores with a diameter above 115 µm.

When φ_A reached 0.082, the pores no longer exhibited long-range order (Figure 4.29E). The gradual transition, from well-defined columnar porosity present in monoliths FZC–1, FZC–2 and FZC–5, through poorly defined columnar-like pores present in monolith FZC–7, to the randomly shaped pores in monolith FZC–9, was ascribed to the insufficient mobility of the suspended MA particles. The insufficient mobility led to early entrapment of particles in the advancing freezing front [27] resulting in randomly shaped pores. The MA powder volume fraction was too high to enable undisturbed growth of ice crystals and thus a successful formation of columnar porosity.

Table 4.4: Summary of specific surface areas and porosities of HMMA monoliths prepared by freeze-casting.

Monolith	Geometric density ρ_{geom} (g/mL)	Geometric porosity* (%)	Mercury intrusion porosity (%)	Specific surface area (m^2/g)
FZC–1	0.011±0.001	99.2±0.1	96.6±0.3	45
FZC–2	0.056±0.002	98.5±0.1	96.5±0.3	91
FZC–3	0.056±0.001	98.5±0.0	96.1±0.1	/
FZC–4	0.097±0.002	97.5±0.1	96.2±0.6	105
FZC–5	0.108±0.007	97.1±0.2	96.8±0.2	100
FZC–6	0.109±0.010	97.1±0.3	96.2±0.4	117
FZC–7	0.172±0.006	95.6±0.2	94.4±0.5	128
FZC–8	0.177±0.003	95.4±0.1	94.3±0.1	138
FZC–9	0.272±0.002	93.1±0.1	90.8±0.9‡	134
MA–CIP200	1.158±0.003	70.7±0.1	71.0±0.1	138

*Geometrical porosity was calculated as: $(1- \rho_{geom}/\rho_{theor})\cdot 100\%$, where ρ_{theor} was the theoretical density, estimated from mass fractions and densities of the components. For calculation of ρ_{theor} values ρ_{CNF} = 1.46 g/mL and ρ_{MA} = 3.95 g/mL were used.

‡Sample was in part crushed during measurement. Accordingly, the results should be interpreted with care.

4.4.2.1.1 Influence of MA volume fraction on pore structure

Geometric and mercury-intrusion-based porosities were determined for all the freeze-cast HMMA monoliths presented in Table 4.4. The geometric density (ρ_G) of MA-powder-free FZC–1 sample was only 0.011 g/mL and comparable to the CNF aerogels densities already reported in the literature [248], [249]. On the other hand, the geometric densities of monoliths containing the lowest MA powder volume fraction, FZC–2 and FZC–3, were 5-times higher than the density of monolith FZC–1 with the value of 0.056 g/mL, which is equivalent to 98.5 % of the total geometric porosity. A further increase in the MA volume fraction caused the expected trend of increasing ρ_G and decreasing total porosity. The highest MA volume fraction in monolith FZC–9 reached the highest density of 0.272 g/mL.

The anticipated trend of total porosity decrease with the increase of MA volume fraction was also confirmed with mercury porosimetry. The results are presented in Table 4.4 and Figure 4.30. Deviations at volume fractions below 0.054 are observed. As-determined porosities appeared higher at higher MA volume fractions, while they should have decreased with increasing solid content [250]. A detailed examination of the intrusion curves at the lowest pressures/biggest pore sizes revealed a sharp increase of the dV/dlog(D) curve at pore diameters above 100 μm in the case of MA volume fraction below 0.054 (Figure 4.30A). Such increase indicates that pores larger than 115 μm (larger than the detection limit) are present in the sample. As a consequence, total porosities determined by Hg intrusion porosimetry for monoliths FZC–1, FZC–2 and FZC–3 were lower from the actual values. The presence of the pores bigger than 115 μm was also evident from the SEM images in Figures 4.30A–C. The ascent of the dV/dlog(D) curve at low pressures (pore diameters above 115 μm) was, on the other hand, not observed in the Hg intrusion measurements of

monoliths FZC–7 and FZC–9, thus suggesting that these monoliths did not possess pores with diameter exceeding 115 μm. Absence of the latter was also evident from the SEM images in Figures 4.29D and 4.29E.

While Hg-intrusion-determined porosities did not follow the expected decreasing trend with an increase of the MA solid volume fraction, the geometrical porosities (Table 4.4) changed with MA solid fraction per expectations. Due to the absence of pores with diameters exceeding 115 μm at higher φ_A also a close match between geometrical porosities and Hg-intrusion determined porosities was observed. On the other hand, substantial differences could be observed at lower volume fractions due to the fact that part of the total porosity was above the mercury-intrusion detection limit. Thus geometric porosities of monoliths FZC–1, FZC–2 and FZC–3 were closer to the real values and also followed the expected trend.

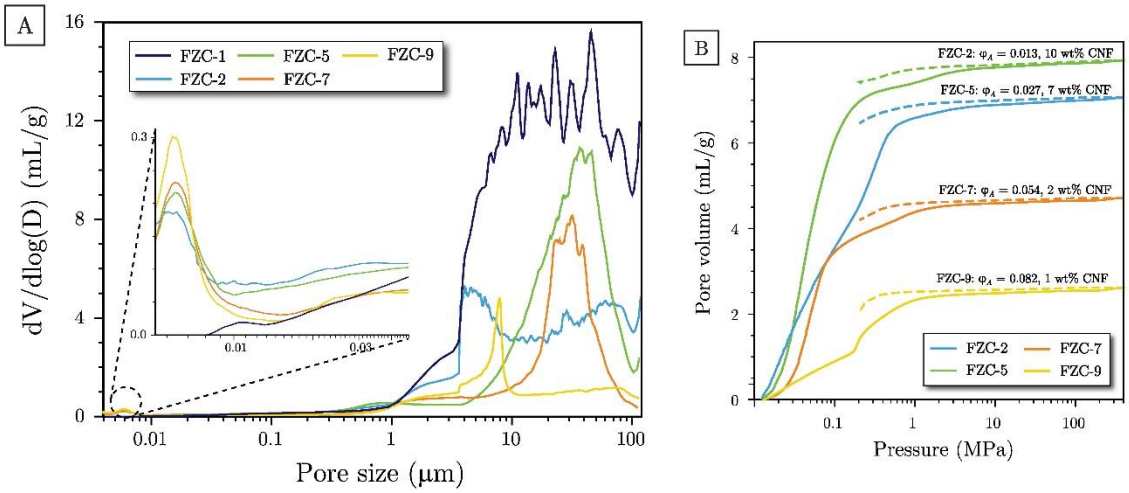

Figure 4.30: A) Pore size distribution in monoliths containing different volume fractions of MA powder all frozen at the rate of 1 °C/min. B) Hg intrusion (solid line) and extrusion (dashed line) curves of selected monoliths.

The MA powder volume fraction had an impact on the width of pore size distribution of monoliths frozen at the rate of 1 °C/min. Monolith FZC–1, which was prepared without MA powder, had the widest pore size distribution. Pore sizes were in the range from 1 μm to well over 115 μm (Figure 4.30A), with the biggest pores exceeding 300 μm as can be seen in Figure 4.29A. The pore size distribution in monolith FZC–2 was still very broad. The range was comparable to FZC–1. However, the pores were slightly smaller, especially the largest ones, which reached sizes of around 180 μm (Figure 4.29B). On the other hand, in the three monoliths with MA content of $\varphi_A \geq 0.054$, a much narrower pore size distribution was observed. In monolith FZC–5, the modal pore diameter was at 40.5 μm, while in FZC–7, which possessed even narrower pore size distribution, modal pore diameter appeared at 29.7 μm. The smallest modal pore diameter of 7.8 μm and the narrowest pore size distribution was detected in monolith FZC–9, which possessed the highest MA volume fraction. With increasing MA volume fraction, the number of pores exceeding 115 μm decreased together with their diameter until the solid content was high enough ($\varphi_A \geq 0.054$) to entirely prevent their formation.

Due to the intrinsic mesoporosity of MA particles, all freeze-cast monoliths (except FZC–1) beside macropores also possessed a substantial amount of mesoporosity, making them hierarchically porous as can be seen on the inset of Figure 4.30A. The approximate volume of mesopores was 0.12 mL/g and an average pore diameter was 6 nm. CNF on the

other hand is not mesoporous on its own as can be seen from the FZC–1 intrusion curve in the inset of Figure 4.30A. The volume of pores smaller than 50 nm determined in monolith FZC–1 was approximately 0.03 mL/g. Thus the addition of CNF and the consequent coverage of MA's surface and intrinsic mesopores was responsible for the decrease in mesoporosity of HMMA monoliths in comparison to the pure MA powder. Ma powder had a mesopore volume of 0.27 mL/g as determined by mercury intrusion porosimetry.

4.4.2.1.2 Influence of freezing rate on pore structure

The influence of the freezing rate on the porosity and pore size distribution was evaluated. The freezing rate (1 °C/min versus 6 °C/min) had no measurable influence on the total porosity when comparing samples containing the same MA/ CNF ratio (monoliths pairs FZC–5/FZC–6 and FZC–7/FZC–8; Table 4.4). However, the freezing rate still had a strong influence on the pore size distribution, as can be seen from the mercury intrusion porosimetry curves (Figure 4.31) and SEM images (Figure 4.32).

At the same MA/CNF ratio bigger pores with narrower, monomodal size distribution were formed in monoliths frozen at a slower rate. The modal pore diameters of slowly frozen monoliths were 40.5 and 29.7 µm for FZC–5 and FZC–7, respectively (Figure 4.31).

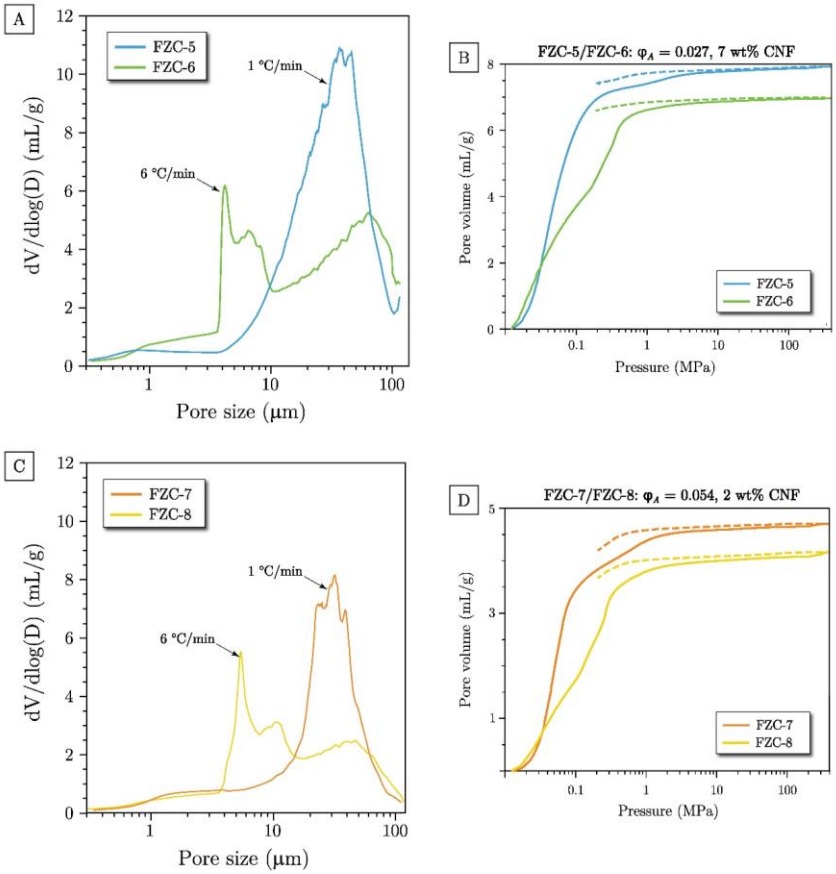

Figure 4.31: A) Pore size distribution of monoliths FZC–5 and FZC–6 containing the same MA/CNF ratio (MA:CNF = 14:1), frozen at different rates (1 °C/min or 6 °C/min, respectively). B) Hg intrusion (solid line) and extrusion (dashed line) curves for monoliths FZC–5 and FZC–6. C) Pore size distribution of monoliths FZC–7 and FZC–8 containing the same MA/CNF ratio (MA:CNF = 50:1), frozen at different rates (1 °C/min or 6 °C/min, respectively). D) Hg intrusion (solid line) and extrusion (dashed line) curves for monoliths FZC–7 and FZC–8.

On the other hand, when a faster freezing regime of 6 °C/min was used, a broader pore size distribution with bimodal nature evolved in both fast-frozen monoliths FZC–6 and FZC–8. The reason for the latter lies in water's crystallization process. At faster cooling rates, where ice formation is governed by the nucleation rather than crystal growth, the formation of smaller ice crystals is promoted [18]. Since the size of ice crystals determines the size of macropores in the final monolith, the faster freezing rates result in finer pore sizes. While modal pore diameters of 40.5 μm and 29.7 μm were determined in monoliths FZC–5 and FZC–7, respectively, the majority of macropores in monoliths FZC–6 and FZC–8 were in the size range of only a few micrometres, i.e., between 3 and 11 μm. The pore size distributions of fast-frozen monoliths FZC–6 and FZC–8 were quite similar. The clearest difference was in the modal diameter of pores above 20 μm, i.e., in the monolith FZC–6, the modal diameter was larger. This was in accordance with results obtained at a slow freezing rate, where with an increasing MA volume fraction modal diameter also decreased.

A predominating finer pore structure of monoliths frozen with a faster rate in comparison to pores formed at slower rates was also clearly evident from the SEM images in Figure 4.32.

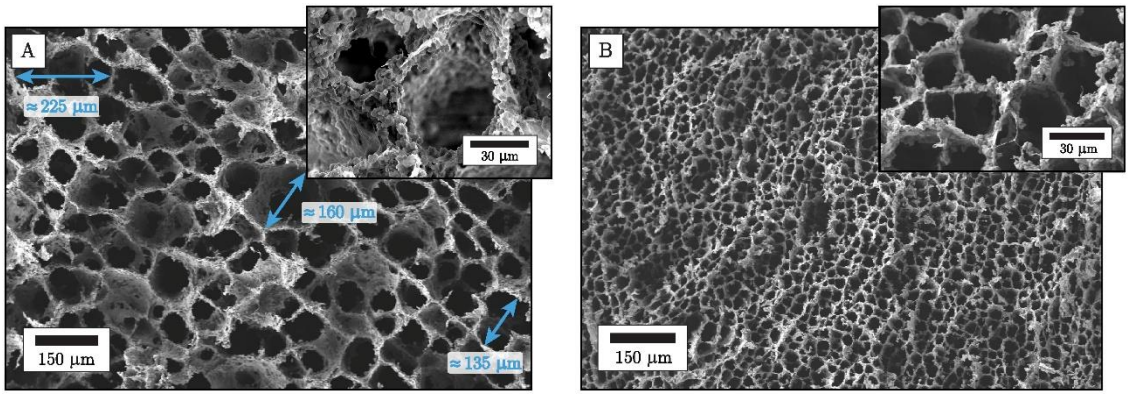

Figure 4.32: A) SEM images of HMMA monolith FZC–5. Arrows indicate pores with the diameter bigger than 115 μm. B) SEM images of HMMA monolith FZC–6.

However, bigger pores with the modal diameter at 48.4 μm (FZC–8) and 62.9 μm (FZC–6) could also be observed at a faster freezing regime (Figures 4.31A and 4.31C). It seems that the chosen rate was not fast enough to completely inhibit extensive ice crystal growth, resulting in the evolution of bimodal pore size distribution. The faster freezing was still too slow to entirely prevent the formation of pores with diameters above 10 microns, but it was apparently too fast to promote extensive crystal growth needed for the formation of ice columns with diameters exceeding 100 μm, present in monolith FZC–5 as indicated by the increase of dV/dlog(D) curve at low pressures (Figure 4.30 and 4.31A). In addition, the freezing rate had also affected the thickness of pore walls, which were considerably thinner in monoliths frozen at faster rates, as can be seen from the magnifications of SEM images in Figure 4.32 [251].

4.4.2.2 Permeability

Highly porous materials with columnar porosity possess good gas permeation properties (up to approximately 1×10^{-11} m^2 for Darcian permeability and up to approximately 1×10^{-5} m for non-Darcian permeability) [49], [252], [253]. Due to the latter freeze-cast materials are especially useful in high flow/pressure applications, since low pore tortuosity reduces the pressure drop.

FZC–5 and FZC–7 were tested for permeation properties in order to determine if MA powder volume fraction and CNF content influence the gas permeability. Results are shown in Figure 4.33. When pressure differences were plotted agains different air flows (Q/A), a higher pressure drop could be observed for monoliths FZC–5. Results suggest that FZC–7 had a slightly better overall gas permeability.

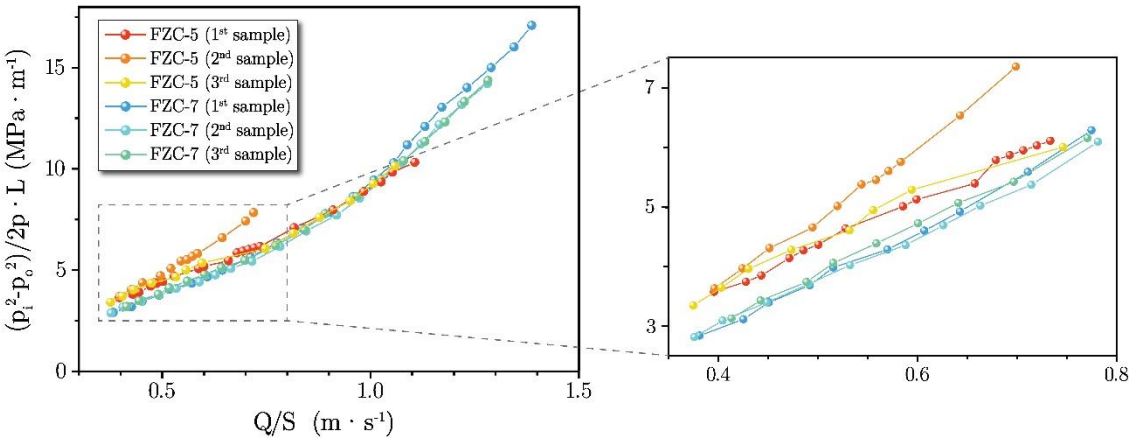

Figure 4.33: Specific air flow through monoliths versus pressure differential, shown for monoliths FZC–5 and FZC–7.

The permeability for both monoliths was calculated based on Forchheimer's equation for compressible fluids [196] described by Equation 3.1. There are two contributions to the overall permeability according to the Forchheimer's equation: Darcian permeability (k_1) and Non-Darcian permeability (k_2). Darcian permeability (k_1) arises due to viscous flow regime, while Non-Darcian permeability (k_2) corresponds to the inertial flow effects.

The decision to use Forchheimer's equation instead of Darcy's law [252] was based on the better fit between experimentally obtained and calculated data obtained by the least square method. The least square method yielded a better fit between pressure drop and gas velocity Q/A when quadric relationship (Forchheimer's equation) was used in contrast to when a linear equation (Darcy's law) was applied. The quadric relationship between the pressure drop and gas velocity (Figure 4.33) indicated that the inertia or Non-Darcian effects on the overall permeability should not be neglected.

Table 4.5: Summary of air permeability characteristics of freeze-cast HMMA monoliths.

HMMA monolith	Number of measurements	k_1 ($\times 10^{-12}$ m^2)	k_2 ($\times 10^{-7}$ m)
FZC-5	3	2.39 ± 0.19	9.15 ± 6.51
FZC-7	3	4.31 ± 0.47	2.23 ± 0.26

Permeability parameters k_1 and k_2 obtained for the two inspected HMMA monoliths were comparable to the values reported for freeze cast, sintered alumina monoliths [254], as well as to the typical values found for fibrous filters [196]. Obtained permeability properties were significantly better from the properties reported for alumina foams [255] or HMMA monoliths prepared by cold isostatic pressing of AlN-hydrolysis-derived-MA powder ($k_1 = 0.08 - 22.1\times10^{-16}$ m^2, $k_2 = 0.03 - 5390\times10^{-15}$ m) [110].

The Darcian permeabilities (k1) for FZC–5 and FZC–7 were 2.39×10-12 m2 and 4.31× 10-12 m2, respectively (Table 4.5). Parameters that influence the k1 are material's porosity and size of individual pores. The similarity of both latter parameters in tested monoliths (Table 4.4 and Figures 4.29C, 4.29D and 4.30A) explains the small difference between k_1 values.

On the other hand, the Non-Darcian permeability contribution was with 9.15×10^{-7} m higher for monolith FZC–5 in comparison to 2.23×10^{-7} m observed for monoliths FZC–7, accounting for a more than 300 % difference between Non-Darcian permeability. Unlike k_1 which is mostly determined by porosity and pore size, parameter k_2 is also susceptible to the changes of gas molecules velocity and flow [254]. On the SEM images on Figures 4.29C and 4.29D, an obvious transition from a columnar pore structure in monolith FZC–5 to more randomly shaped pores in monolith FZC–7 can be observed. Due to a higher alignment of the pores in monolith FZC–5, with the pore structure less tortuous, the air flow was not as obstructed as in the monolith FZC–7. Thus the resulting permeability in the former case was higher.

The variation of k_1 values between the measurements of identical HMMA monoliths was relatively low, indicating permeability characteristics have an acceptable reproducibility. However, for monolith FZC–5 a relatively high error between individual values of k_2 has to be addressed. This error could be ascribed to the limited strength of pore walls in the monoliths, since it was evident from the SEM images (Figures 4.29C and 4.29D) that the pore walls were considerably thinner in monolith FZC–5 in comparison to the monolith FZC–7. Thinner walls could have led to the warping or degradation of monolith's pore structure, consequently affecting the flow and velocity of gas molecules, which in turn affected k_2.

4.4.2.3 Compressive properties

The influence of MA volume fraction, CNF content and freezing rate on the stress-strain response of freeze-cast HMMA monoliths under compression in axial direction as well as radial direction were studied. The latter was carried out in order to establish the influence pore orientation has on mechanical behavior.

Table 4.6: Summary of compressive properties of freeze-cast HMMA monoliths.

HMMA monolith	**Axial direction**		**Radial direction**	
	Yield point (kPa)	Young's modulus (kPa)	Yield point (kPa)	Young's modulus (kPa)
FZC–1*	4	130	1±0	20±10
FZC–2	20±2	590±20	2±0	70±10
FZC–3	5±1	610±40	/	/
FZC–4*	28	930	/	/
FZC–5	52±6	1080±430	14±0	410±40
FZC–6*	40	1000	/	/
FZC–7	13±1	670±190	12±1	510±110
FZC–8*	14	620	/	/
FZC–9	2±0	150±40	2±0	130±60

*Axial compressive properties were determined from one measurement per batch.

4.4.2.3.1 Influence of MA/CNF ratio

The stress-strain curves of HMMA monoliths containing different MA/CNF ratios are shown in Figure 4.34. The shape of these curves is typically observed in compression of porous monoliths containing cellulose [256]. At low strains, a linear region stretching to various strains representing elastic deformation can be observed. In this region, the applied stress was predominantly caused by elastic bending of pore walls [257]. At the end of this region, yield point values were estimated and from them the compressive modulus calculated (Table 4.6) [257]. In the plateau region, which followed the linear zone, the porous structure, or more precisely pore walls collapsed under the constantly increasing stress.

Stress-strain curves and pictures taken during compression in axial direction at two different strains, i.e., 5 % and 15 % (images in Figure 4.34) show that MA/CNF ratio determined the compression behavior.

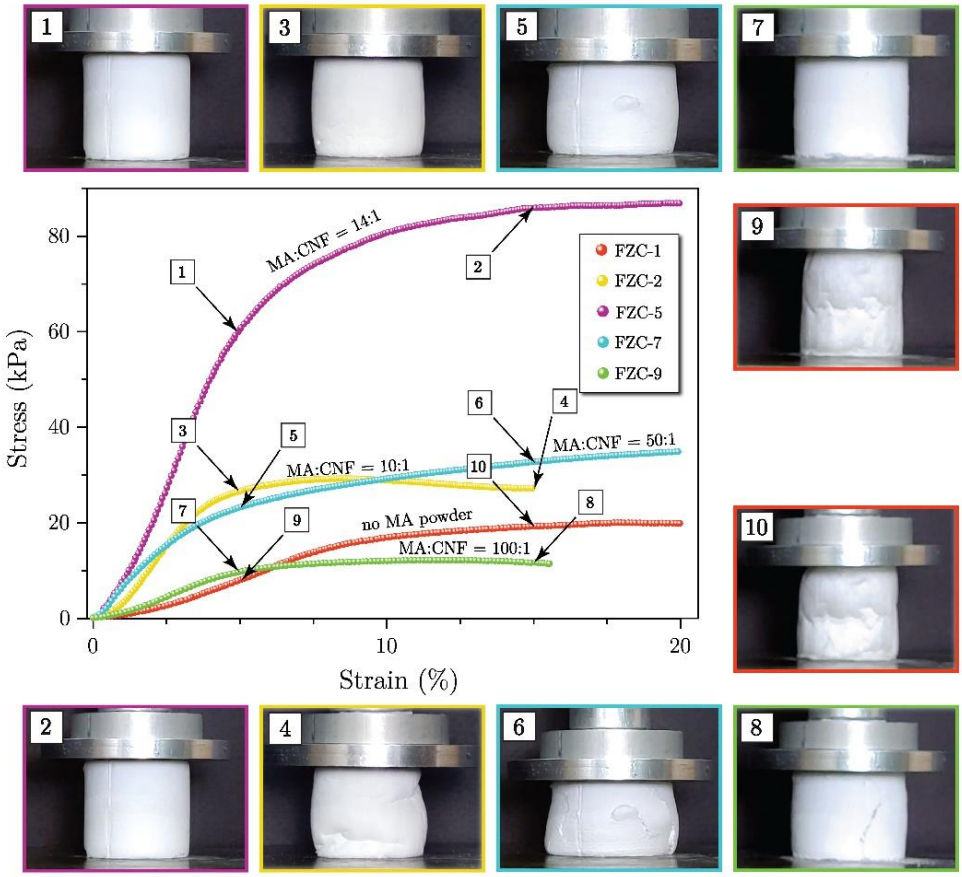

Figure 4.34: Stress-strain curves of monoliths containing different amounts of MA powder and CNF, compressed in the axial direction. Pictures 1-10 show compression of monoliths in the axial direction at 5 % and 15 % strain as indicated by the arrows on graph.

FZC–1 exhibited a yield point of 4 kPa, indicating that mechanical properties of CNF freeze-cast without containing MA powder possessed a relatively low compressive strength. However, after reinforcement of the CNF network with small amounts of MA powder (φ_A = 0.013), the yield point values were considerably increased to 20 kPa suggesting that MA particles endow CNF walls with strength as well as stiffness. The monoliths FZC–7 and FCZ–9 which contained 4.0 mg/1 mL or less of CNF in the suspension cracked during compression. On the other hand, FZC–1 and FCZ–2 containing 0.013 or less volume

fractions of MA powder caved in during compression. It can thus be concluded that a certain ratio between MA powder and CNF was required to achieve the stiffest response of such highly porous HMMA monolith. The stress-strain curve of FZC–5 exhibited the steepest linear region, while the images taken during compression show no visible exterior changes. Accordingly, the mass ratio between MA powder and CNF used to prepare FZC–5 (approximately 14:1) was apparently the closest to an optimal one in the view of the mechanical properties. Deviations from this mass ratio either in the favor of MA powder or CNF amount yielded monoliths with diminished compressive properties.

When comparing the results for axially compressed HMMA monoliths, a trend of decreasing yield point values with the decrease in the total CNF amount was observed (Fig. 4.32 and Table 4.6). The highest yield point value (52 kPa) was noticed for monoliths FZC–5, since they contained the highest CNF mass of 6.6 mg per 1 mL of suspension. In accordance with the observed trend, the lowest yield point value of 2 kPa was observed when the monoliths containing the lowest CNF mass (FZC–9), i.e., 3.0 mg/mL of suspension (Table 3.1), were compressed. Highest and lowest values of Young's moduli (E) were also observed for the same monoliths. The highest value of 1080 kPa was determined for the FZC–5, while FZC–9 exhibited the lowest value of Young's modulus of 150 kPa.

However, unlike yield point values that decreased directly with the decrease of the CNF content, Young's modulus values were also affected by the content of MA powder. Consequently, monoliths FZC–7 were with Young's modulus of 670 kPa more stiff than FZC–2, which with 590 kPa exhibited a slightly lower value due to lower content of MA powder. On the other hand, FZC–2 had a higher yield point value than FZC–7, i.e., 20 kPa in comparison to 13 kPa, due to a higher CNF content.

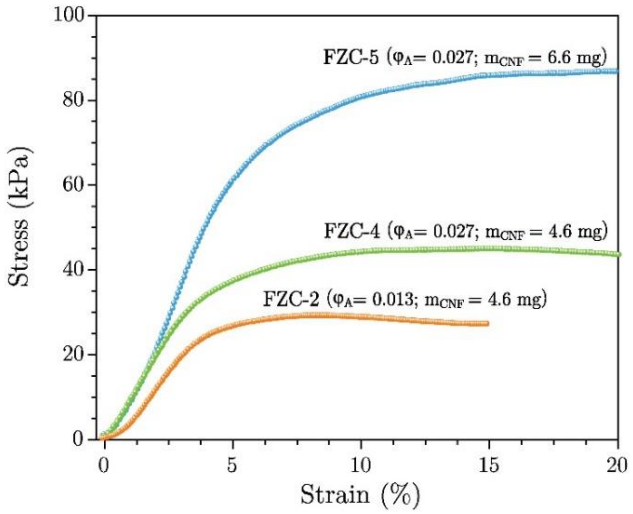

Figure 4.35: Influence of individual parameters, i.e., CNF content and MA volume fraction on compressive behavior of monoliths in the axial direction. Amount of CNF is given as mass of CNF (mg) per 1 mL of suspension.

In addition, the influence of the MA volume fraction and the CNF amount on the compressive properties were also evaluated (Figure 4.35). Stress-strain curves obtained for monoliths containing the same amount of MA powder (FZC–4 and FZC–5; φ_A=0.027) or the same amount of CNF (FZC–2 and FZC–4; m_{CNF}=4.6 mg/1 mL) were compared. A 100 % increase of the volume fraction (φ_A), i.e., from 0.013 (FZC–2) to 0.027 (FZC–4), increased the compressive yield point for 35 % (Table 4.6). On the other hand, when only CNF amount was increased by less than 50%, i.e., from 4.6 mg (FZC–4) to 6.6 mg (FZC–5) per 1 mL of suspension, the HMMA monoliths exhibited 90 % higher compressive

stresses, where the yield point was estimated to be ≈52 kPa. It follows that the contribution of CNF content to the overall compressive strength of freeze-cast HMMA monoliths was much more significant than the contribution of MA powder content. However, MA powder must still be added to reinforce the CNF walls.

Porous ceramic materials with anisotropic pore structure exhibit different mechanical properties perpendicular to pore orientation as opposed to the direction parallel to it [17], [258]. Since HMMA monoliths possessed a distinct anisotropic pore structure (Figures 4.26, 4.27 and 4.29), compressive properties of selected monoliths were also evaluated in the radial direction to study the influence of pore orientation on the compressive strength (Figure 4.36). It can be observed from the pictures taken during compression in radial direction (pictures in Figure 4.36) that the monoliths FZC–7 and FCZ–9 cracked and that the monoliths FZC–1 and FCZ–2 caved in, similar as when compressed in the axial direction. Thus, same conclusions regarding the composition of monoliths can be drawn – when a MA powder/CNF ratio of approximately 15:1 is achieved, the best possible compressive properties will be achieved in both axial as well as radial direction.

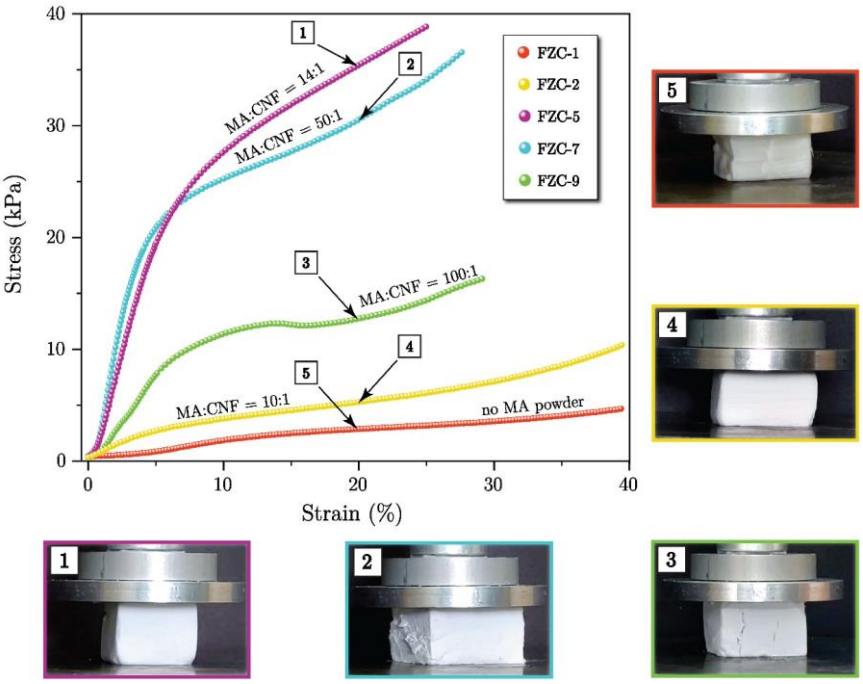

Figure 4.36: Stress-strain curves of monoliths containing different amounts of MA powder and CNF, compressed in the radial direction. Pictures 1-5 show compression of monoliths in the radial direction at 20 % strain as indicated by the arrows on graph.

Comparison of yield point values obtained in the axial and radial direction for the same monoliths showed yield point decrease with increasing MA volume fraction (Table 4.6). The differences between the axial and radial compressive strength were observed for monoliths with a more pronounced anisotropic structure (FZC–1, FZC–2, and FZC–5). On the other hand, for monoliths FZC–7 and FZC–9, which contained higher MA volume fractions, where a well-defined columnar porosity could not evolve and thus exhibited a less distinctive structural anisotropy, the obtained stress-strain curves and yield points values were more similar in both directions (Figure 4.29 and Table 4.6). Comparable observations for materials with anisotropic pores structures were already reported for other materials with columnar porosity [17]. The monoliths containing lower MA powder volume fractions (φ_A below 0.054), which resulted in distinctively columnar pore structure,

exhibited notably better mechanical properties in the direction parallel to the pore walls. For example, monoliths FZC–5 prepared with $\varphi_A = 0.027$ having yield point values of 52 kPa in the axial direction and 14 kPa in the radial direction were determined. However, there was almost no difference between yield point values for monoliths FZC–7 obtained in the axial direction (13 kPa) and the radial direction (12 kPa).

Due to the distinctive anisotropy there were substantial differences between the axial and the radial Young's modulus. In monoliths FZC–5, the Young's modulus determined with axial compression (1080 kPa) was more than 50% higher than in the radial direction (410 kPa). In contrast, there was a considerably smaller difference between axial and radial Young's modulus in monoliths containing higher MA volume fractions, e.g., monoliths FZC–7 exhibited values of 670 kPa (axially) and 510 kPa (radially). The disappearance of differences between radial and axial mechanical properties can be ascribed to the disappearing of structure's anisotropy with increasing MA volume fraction.

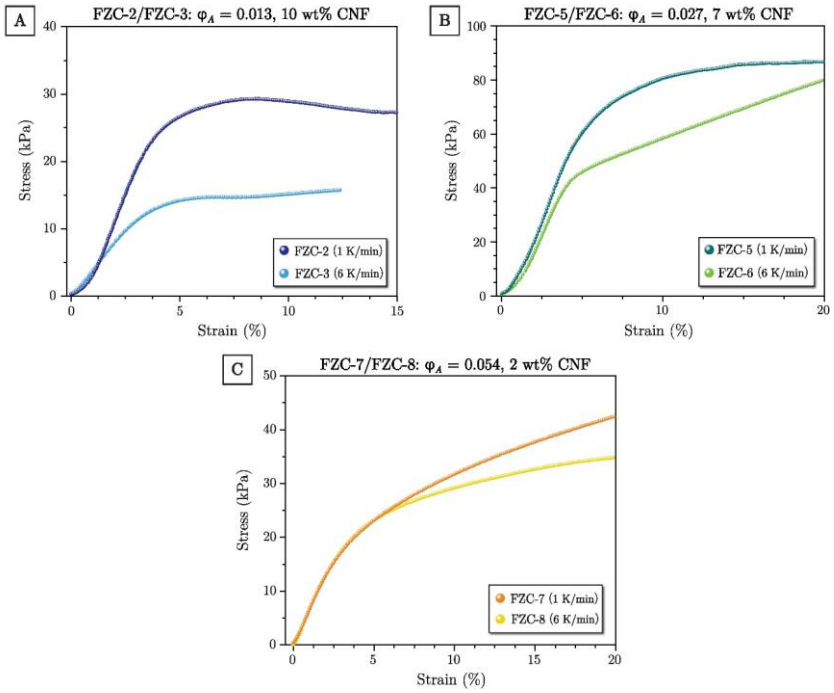

Figure 4.37: A) Stress-strain curves of monolith pair FZC–2/FZC–3, B) stress-strain curves of monolith pair FZC–5/FZC–6, C) stress-strain curves of monolith pair FZC–7/FZC–8. All monolith pairs contain the same amount of MA powder and CNF, but were frozen at two different rates.

The influence of freezing rate on compressive properties was also studied. It was found out that it had a considerable effect on compressive properties in the axial direction as can be seen form the stress-strain curves in Figure 4.37 and Table 4.6. When comparing monolith pairs in Figures 4.37A, 4.37B and 4.37C (monoliths containing same MA/CNF ratios, yet frozen at different rates), a clear trend of disappearing differences between slow and fast frozen monoliths with increasing MA powder volume fraction between monoliths frozen at different regimes can be discerned. For example, HMMA monoliths containing lower MA volume fractions ($\varphi_A = 0.013$) exhibited higher yield points if consolidated at a slower freezing rate (1 °C/min) as is clearly visible in Figure 4.37A. When volume fraction was increased from 0.013 to 0.054, the differences between yield points of slowly and fast frozen monoliths notably decreased (Figure 4.37B). The influence of freezing rate was not discernable after MA powder content reached the volume fraction of 0.054 (Figure 4.37C).

Improved compressive properties of monoliths FZC–2 and FZC–5 frozen at a slower rate can be explained by the greater thickness of monolith pore walls, formed at slower freezing rates (Figure 4.32). Consequently, these monoliths could withstand higher compressive loads.

4.4.2.4 Thermal properties

To monoliths prepared by freeze-casting thermal properties were determined. Additionally, HMMA monoliths were prepared by cold isostatic pressing (CIP), for the purpose of comparing the thermal properties of dry-pressed specimens with the properties of samples prepared via freeze-casting.

As was the case in mechanical properties evaluation, the anisotropic structure of freeze-cast HMMA monoliths had also led to direction-dependent thermal properties. While Hot Disk indeed enables simultaneous determination of thermal conductivity in-plane (axial) and through the plane (radial) of an anisotropic material, the as-determined radial thermal conductivity (λ_r) is only valid if the material's structure is homogeneous, consisting of evenly shaped and distributed pores along x- and z-axis, as marked in Figure 3.2. As can be seen from SEM and μ–CT images in Figures 4.26 and 4.27, that was not the case for freeze-cast HMMA monoliths. Consequently, the λ_a and λ_r had to be determined in separate measurements. An exception was the monolith MA–CIP200, which possessed a homogeneous pore structure, and thus the axial and radial thermal conductivity could be determined in a single measurement.

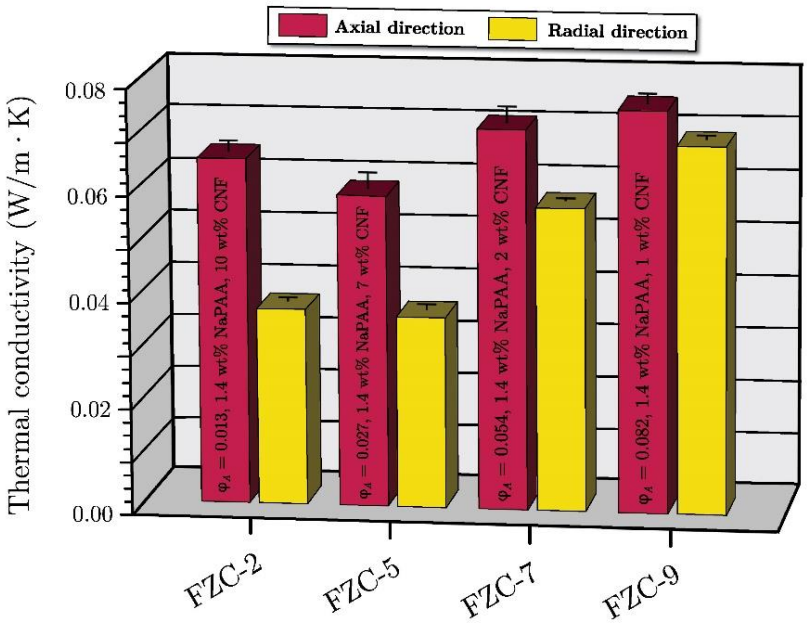

Figure 4.38: Effective thermal conductivity of selected HMMA monoliths measured in the axial direction (λ_a) and radial direction (λ_r).

In the axial direction, a relatively low thermal conductivity (λ_a) of HMMA monoliths of 0.068±0.009 W/m·K was measured, which is about 30 % lower when compared to the thermal conductivity of freeze-cast and sintered α–Al_2O_3 porous ceramicw of similar porosity [259]. However, this is still higher than the reported λ of highly porous pure CNF aerogels (≈ 0.04 W/m·K) [260].

As can be seen in Figure 4.38, an increase in the volume fraction of MA powder from 0.013 to 0.082 had negligible effect on the axial thermal conductivity. Thermal conductivity

increased from 0.065 W/m·K to 0.077 W/m·K (Table 4.7). On the other hand, thermal conductivity in the radial direction displayed a more distinctive dependence on the MA powder volume fraction. An increase of λ_r from 0.037 W/m·K (FZC–5) to 0.057 W/m·K (FZC–7) could be observed if φ_A was increased from 0.027 to 0.054. The different sensitivity of λ_a and λ_r from the MA volume fraction can be explained by solid conduction of the pore walls [261]. A higher volume fraction resulted in an increased content of MA particle in the pore walls. As a consequence, the walls were thicker, while pore diameters decreased, leading to a higher solid conduction in the radial direction and thus to a higher radial thermal conductivity. While MA volume fraction did affect thermal conductivity, any dependence of λ_a and λ_r on the MA/CNF ratio could not be observed. An increase in the MA/CNF ratio from MA:CNF = 10:1 to MA:CNF = 20:1 (monoliths FZC–2, FZC–4 and FZC–5) caused practically no change of the thermal conductivity in any of the tested directions (Table 4.7). Consequently, it was observed that the increase in thermal conductivity was not MA/CNF-ratio-dependent, but was dependent on the increase of MA powder content when exceeding $\varphi_A > 0.054$.

Table 4.7: Summary of thermal properties of selected HMMA monoliths.

HMMA monolith	λ_a	λ_r	c_p
	W/m·K	W/m·K	kJ/kg·K
FZC–2	0.065±0.002	0.037±0.001	1.288±0.007
FZC–4	0.065±0.001	0.038±0.001	1.224±0.007
FZC–5	0.059±0.003	0.037±0.001	1.343±0.015
FZC–7	0.072±0.003	0.057±0.002	1.223±0.008
FZC–9	0.077±0.002	0.069±0.001	1.139±0.008
MA–CIP200	0.327±0.004	0.356±0.006	1.000±0.022

When comparing axial and radial thermal conductivities of FZC–2 and FZC–5, it was observed that the thermal conductivity in the axial direction was almost twice as high as in the radial direction (Table 4.7). The reason for these differences lies in the anisotropy of the structure of monoliths FZC–2 and FZC–5 (Figure 4.29). The solid conduction of the pore walls in the axial direction and perhaps even natural convection along the same direction, caused the value λ_a to be higher than the value λ_r. On the other hand, the differences between λ_a and λ_r of monoliths containing larger amounts of MA powder, namely FZC–7 and FZC–9, were much smaller. With increasing MA volume fraction, the pore walls thickened and pore diameters decreased, causing the structure to become more isotropic (monoliths FZC–7 and FCZ–9) and consequently much smaller differences between λ_a and λ_r could be observed.

4.4.2.4.1 Thermal imaging

For the purpose of comparing the thermal properties of highly porous freeze-cast HMMA monoliths with the thermal properties of HMMA monoliths of intermediate porosity, the latter were consolidated by CIP (MA–CIP200).

As-prepared monoliths had a porosity of 70.8 % (which is 25 % lower than the porosity of freeze-cast HMMA monoliths) and possessed a thermal conductivity of 0.327 W/m·K (Tables 4.4 and 4.7), which was more than 5-times higher than the thermal conductivity observed in monolith FZC–5. This higher thermal conductivity possessed by CIP-

consolidated HMMA monoliths can be explained by a lower total porosity in comparison to the freeze-cast HMMA monoliths.

Thermographic imaging was performed in order to provide a visual representation of the differences between thermal conductivity of CIP-consolidated (MA–CIP200) and freeze-cast HMMA (FZC–5) monoliths (Figure 4.39). As seen from Figure 4.39, the outer layer of MA–CIP200 was heated to a much higher temperature than the outer layer of the freeze-cast monolith in the same time interval of 30 min, i.e., more than 94 °C in comparison to 64.5 °C. On the other hand, after cooling down for 10 min only minor differences between the outer layer temperatures of the two monoliths could be observed, with both monoliths reaching an almost room temperature (≈ 22 °C).

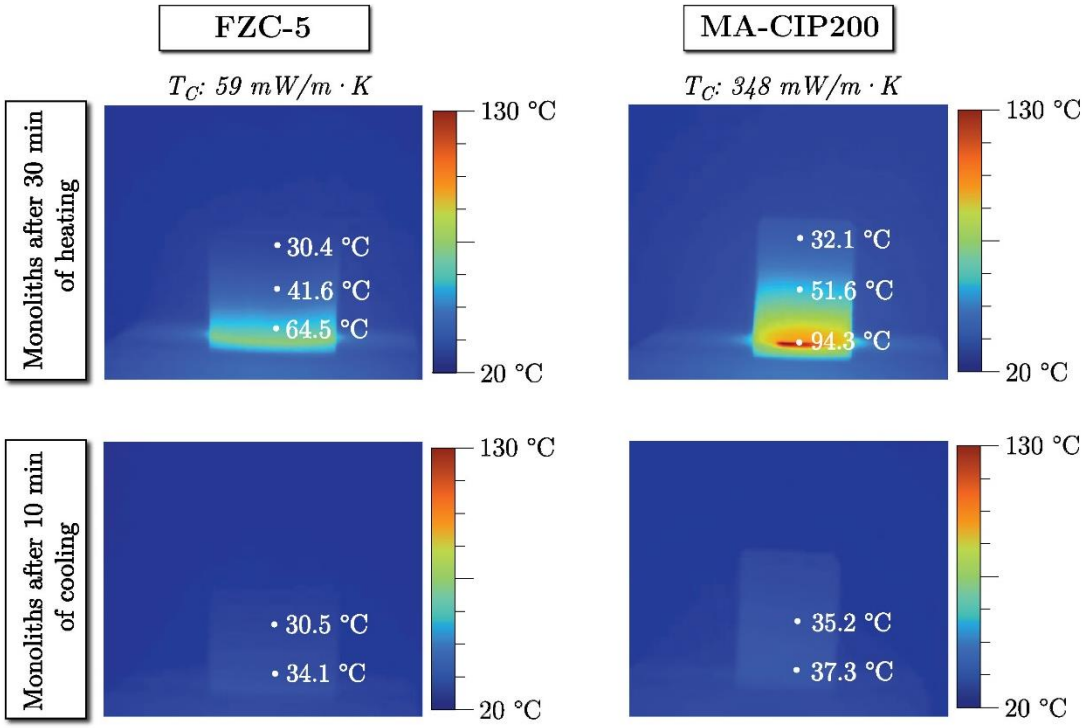

Figure 4.39: Thermographic images of freeze-cast monolith FZC–5 and CIP consolidated monoliths MA–CIP200 after heating for 30 min and after subsequent cooling down for 10 min. The colors in the images represent the temperature distribution on the monolith's surface.

Chapter 5

Conclusions

The research presented in the doctoral dissertation was focused on the understanding of the dispersive properties of AlN-powder-hydrolysis-derived γ–Al_2O_3 (MA) powder, the behavior of aqueous suspensions containing such hierarchically assembled, mesoporous MA powder, the behavior of suspension consolidation by using the freeze casting method, and the several properties of freeze-cast monoliths relevant for highly porous ceramics.

In conclusion, by exploiting **AlN powder hydrolysis** hierarchically assembled, micro-sized, globular MA particles with flower-like structure of high surface area (≈180 m^2/g) and high mesoporosity (0.47 mL/g) were prepared. MA powder was then dispersed in water with NaPAA used as dispersant. The optimal amount of NaPAA was determined with viscosity measurements and proved to be pH-dependent. Namely, 1.4 wt% of dry MA powder mass when pH of suspension was set to 9 and 2.8 wt% when pH was set to 6. The suspension containing a solid volume fraction φ_A=0.126, at both tested pH values, represented the maximum solid volume fraction achievable. The maximum volume fraction was relatively low due to the particles' irregular (non-spherical) shape and their high porosity. However, if the envelope volume fraction φ_E, assuming non-porous particles, was considered, the maximum volume fraction was considerably higher (φ_m = 0.453).

Due to the size of MA particles (average particle size of 8.9 μm), it was not possible to prepare stable MA suspensions. The suspensions were prone to immediate sedimentation and segregation. Two mechanisms for triggering interparticle associations through bridging flocculation for limiting or even preventing suspension sedimentation and segregation were investigated. Namely, the addition of divalent cations (Mg^{2+}, Ca^{2+}) or a secondary fibrous phase (CNF):

- ∴ Addition of ≥ 20 mmol/mol of **Mg^{2+} cations** only partially prevented sedimentation, but it completely prevented segregation on the account of bridging between NaPAA carboxylate groups and divalent cations.
- ∴ Addition of **cellulose nanofibers** (> 1 wt% of MA powder mass) completely prevented both sedimentation and segregation over longer periods of time. A clear supernatant and ≈90 % of the initial suspension's height could be observed after 12 weeks as a result of the interparticle bridging and through MA particle entrapment.

Rheological measurements and sedimentation tests showed CNF was a superior additive for the stabilization of suspensions containing MA particles.

Hierarchically macro-mesoporous alumina (HMMA) monoliths were prepared by exploiting freeze-casting as a consolidation technique. The weak interparticle associations triggered by the addition of divalent cations were not sufficiently strong to yield stable porous MA green bodies, which collapsed during the freeze-drying stage. On the other hand, the addition of CNF endowed highly porous MA green bodies with remarkable

mechanical strength. FTIR studies showed, that MA powder, NaPAA and CNF interacted through intermolecular bonds, most probably hydrogen. Thus, the enhanced mechanical stability could be almost exclusively attributed to the entrapment of MA particles into the CNF network.

HMMA monoliths containing 1.4NaPAA–MA powder and CNF possessed anisotropic structure, displayed high, hierarchical porosity (93.1–99.2 %), with macropores shaped as columnar structures of diameter varying from approximately 1 to 300 µm, depending on the consolidation parameters. The average diameter of mesopores, however, was much more uniform (≈ 6 nm), being the result of intrinsic MA powder properties and as such was not affected by the consolidation parameters. A relatively high surface area (91-138 m^2/g) was obtained owing to beneficial surface properties of the MA powder. The surface area was affected by the processing parameters, especially the MA/CNF ratio. The high content of columnar-shaped pores contributed to a high permeability (k_1 = 2.39–4.31×10^{-12} m^2 in k_2 = 2.23–9.15×10^{-7} m) and low, anisotropic thermal conductivity (0.036-0.077 W/m·K) of the HMMA monoliths. Selected monoliths (FZC–5 and FZC–6) exhibited high insulative properties and compressive strengths (up to 52 kPa) rarely seen in highly porous and green (not sintered or thermally treated) ceramic materials.

The following conclusions were drawn with respect to studying the influence of processing parameters (MA powder volume fraction, MA/CNF ratio and freezing rate) on density (porosity), permeability, thermal and mechanical properties of HMMA:

- ∴ The MA/CNF ratio only affected compressive properties. MA/CNF ratio of 14:1 yielded the best compressive strength (FZC–5).
- ∴ The freezing rate had a pronounced effect on the surface area, marco-pore size distribution as well as compressive properties, when MA content (φ_A) was ≤ 0.054. Surface area was lower, when a slower freezing rate was used. On the other hand, higher compressive strengths were observed at a slower freezing rate.
- ∴ MA volume fraction had a pronounced effect on the surface area, which increased with increasing MA content. It also affected total porosity and pore size. Both parameters decreased with increasing MA volume fraction. Additionally, MA powder content was the only parameter that had influenced the thermal conductivity. A slight increase of λ was observed only after a certain, high enough increase in the MA volume fraction ($\varphi_A > 0.054$).

In perspective, the addition of CNF to MA suspensions prior to consolidation not only prevented sedimentation and segregation during the freezing process but also endowed green bodies with high permeability, low thermal conductivity and sufficient mechanical stability, thus eliminating any need for additional calcination or sintering steps.

Appendix A

Characterization Methods

A.1 Rheology

Rheology is an interdisciplinary field concerned with the deformation of matter and behavior of its flow [262]. Its usefulness is vast, ranging from scientific research to industrial applications. It is mostly used for basic applications, such as prediction of pressure drop in the pipes during flow and determination of quality of input materials and final products. It is also a helpful tool in the developments of products with more complicated flow characteristics, such as paints, cements or chocolate [263]–[265].

When a fluid begins to move, layers are formed inside the flow. Individual layers move with different velocities as illustrated in Figure A.1, where a fluid is placed between two parallel plates. When the upper plate is pushed with a force F, the fluid is split into layers that move at different velocities (v). The topmost layer, which is in contact with the upper plate's surface moves with the same velocity as the plate. Each following layer moves a bit slower. Reducing speed is a consequence of friction between two adjacent layers, and the viscosity is a measure of this friction.

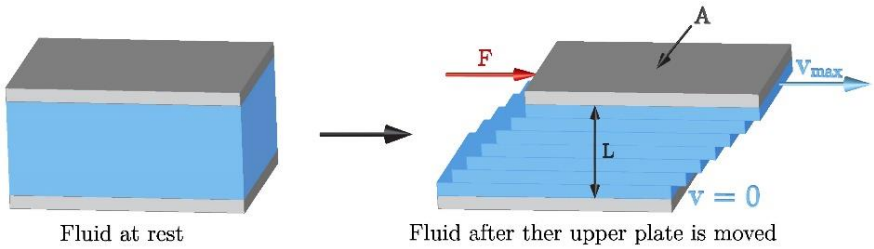

Figure A.1: Illustration of a fluid between two parallel plates at rest (left) and flowing under the influence of externally applied force (right).

Viscosity is therefore a measure of a fluid's resistance to flow [266]. Based on Figure A.1, viscosity can be defined as the ratio between the product of force (F) and thickness of fluid (L) and the product of area of the moving plate (A) and velocity of the fluid's topmost layer (v):

$$\eta = \frac{F \cdot L}{v \cdot A} \tag{A.1}$$

The ratio between the force F and the plate's area A is known as shear stress (τ):

$$\tau = \frac{F}{A} \tag{A.2}$$

and the ratio between fluid's thickness L and topmost layer's velocity v defines shear rate ($\dot{\gamma}$):

$$\dot{\gamma} = \frac{v}{L} \tag{A.3}$$

When Eq. (A.2) and (A.3) are inserted into Eq. (A.1), Equation A.4 is obtained. The latter defines the viscosity as a ratio between shear stress τ and shear rate $\dot{\gamma}$ [262]:

$$\eta = \frac{\tau}{\dot{\gamma}} \tag{A.4}$$

Viscosity of individual fluids differs greatly, with the reasons varying from chemical composition to size and shape of particles in the case of suspensions. Additionally, influence of measuring parameters such as temperature and time of shearing should be taken into account [262]. Based on rheological behaviour materials can be roughly divided into one of the three groups: [267]

- ∴ viscous materials (liquids that flow at low stress)
- ∴ elastic materials (solids that deform under applied external stress, but return to the original state once the stress is removed)
- ∴ viscoelastic materials (materials that exhibit both viscous and elastic characteristics. For example, they behave as liquids as well as solids, but one type of behaviour prevails).

When rheological properties are studied, relationship between shear rate and viscosity (or shear stress) is the most commonly investigated. Based on these relationships fluids can be divided into two subgroups:

- ∴ ***Newtonian fluids:*** the ratio between shear stress and shear rate is linear and viscosity is independent from shear rate. This type of behaviour is typical for pure liquids (e.g., water, glycerol, petrol, mineral oils etc.) and some diluted suspensions [69], [268].
- ∴ ***Non-Newtonian fluids:*** the ratio between shear stress and shear rate is not linear and the viscosity is shear rate or shear time dependent. Into this group, the majority of fluids can be classified, for example, cements, concentrated suspensions, paints, pastes, gels, etc. [268], [269].

Non-Newtonian fluids exhibit different shear-dependent behaviors. When viscosity changes with shear rate we talk about plastic, pseudo-plastic or dilatant flow behavior (Figure A.2A). If shear stress and viscosity change with time at a constant shear rate, we talk about thixotropic or rheopectic fluids (Figure A.2B) [262]. Shear rate dependent flow behavior is very common, while fluids with shear-time dependent behavior are much rarer.

For pseudo-plastic fluids shear stress increases with shear rate and viscosity decreases. The so-called shear-thinning behavior can be observed. Plastic fluids exhibit same dependency from shear rate as pseudo-plastic. However, unlike pseudo-plastic fluids which flow at low shear stress, plastic fluids do not. In the latter, critical value of shear stress, known as yield stress (τ_0), must first be achieved before the flow can occur [262]. A special subgroup of plastic fluids is the so-called Bingham plastics. These fluids also exhibit yield stress, but unlike for plastic fluids the relationship between shear stress and shear rate is linear [268].

The behavior of dilatant fluids is the opposite of the pseudo-plastic behavior. With increasing shear rate, the viscosity also increases, due to a phenomenon known as shear-thickening. Like in pseudo-plastic fluids, flow occurs at low shear stress. Unlike shear-thinning, the occurrence of shear-thickening is in most applications unwanted, since it causes problems like blockage of pipes during pumping, inhomogeneous pouring of slurries, etc. [267].

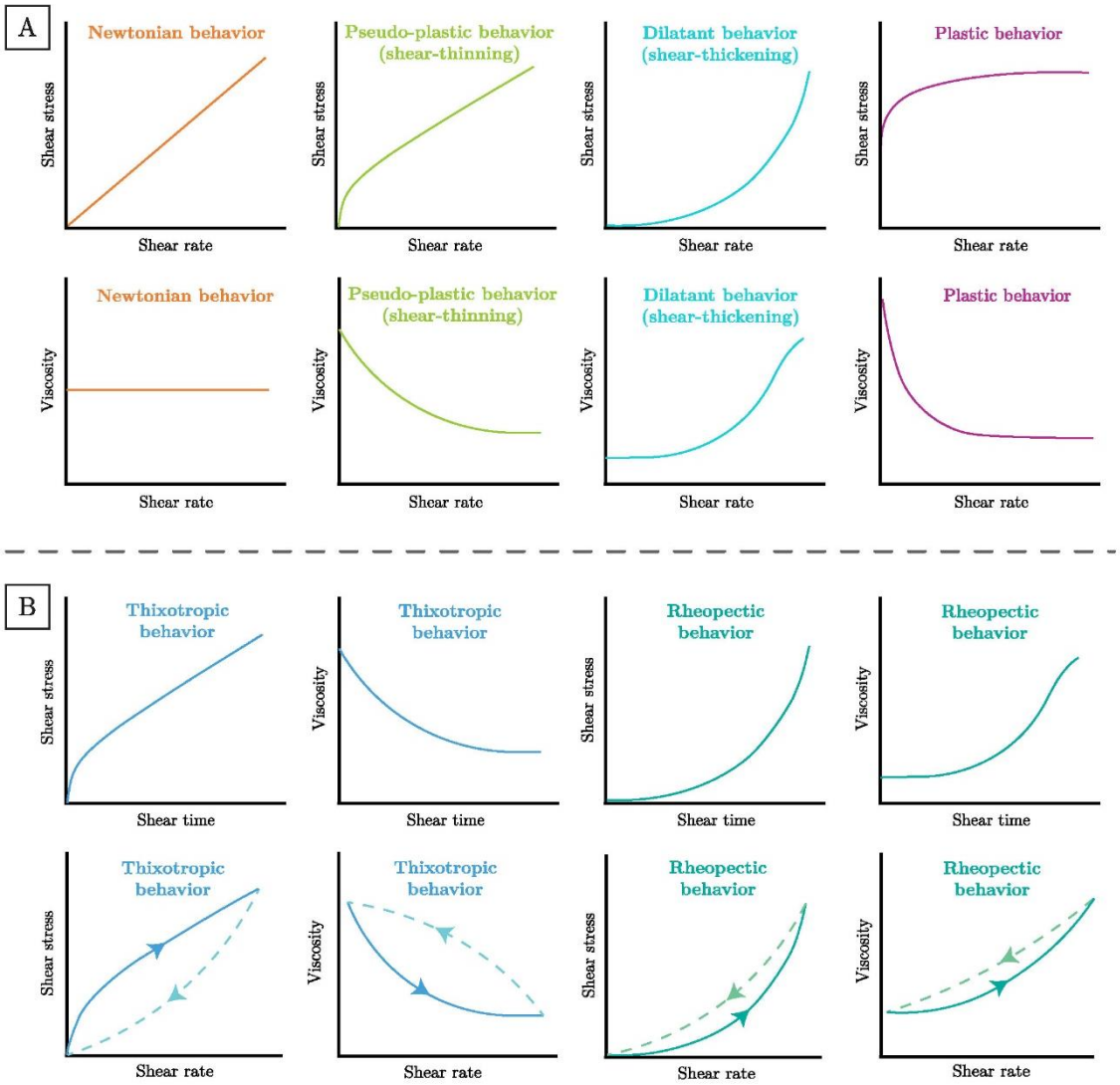

Figure A.2: Rheograms of Newtonian and non-Newtonian fluids with shear time-independent (A) and shear time-dependent (B) flow.

As already mentioned, the viscosity and shear stress of some fluids also change with shearing time at a constant shear rate. If with time viscosity decreases, then we are talking about thixotropic fluids. If viscosity increases with shearing time (shear-thickening), the fluid exhibits rheopectic behavior. After the applied shear forces are removed, thixotropic and rheopectic fluids return back to its original state.

A.1.1 Influence of particles on rheological properties

If particles are dispersed in a liquid, the flow of the latter is obstructed. A spherical particle will force the liquid to flow around it, elongating the streamlines (Figure A.3) and as a result the friction is higher. Consequently, the viscosity of such suspensions increases in comparison to a pure liquid [269]. In suspensions, aside from standard parameters determining viscosity such as temperature and type of liquid, parameters like particle concentration, interactions, shape, size and size distribution have a pronounced effect on the viscosity.

Addition of particles to the liquid will increase its resistance to flow. The higher the number of particles (higher solid volume fractions), the less space is available for particles

to glide pass each other. Hence the number of mechanical interactions is increased, resulting in a higher friction and a higher viscosity (Figure A.4A) [269]. At low particle concentrations (diluted suspensions), there are practically no mechanical interactions between individual particles. Aside from a slight increase in viscosity in comparison to pure liquid, no major changes in rheological behavior are observed. For example, a liquid that exhibits Newtonian type of flow will behave the same after the addition of low concentrations of particles. On the other hand, when there is a high concentration of particles dispersed in a fluid, not only an increase of viscosity is observed, but also the behavior of the flow changes. Typically, a change to shear-thinning behavior is observed when the particles are able to arrange in layers perpendicular to the shear plane [69]. However, in some concentrated suspensions particles are not able to rearrange in such formation and as a result shear-thickening behavior is observed [262].

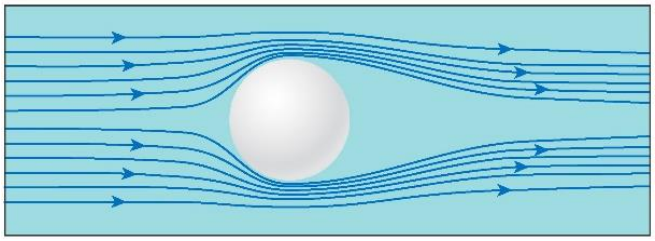

Figure A.3: Streamlines formed around a spherical particle dispersed in a liquid medium.

Interparticle interactions also have a substantial influence on rheology. In diluted suspensions, their contribution is negligible, since the distances between individual particles are too big in order for interactions to develop. However, in the case of concentrated suspensions type and strength of interactions play an important role. Viscosity of stable suspensions, where repulse interactions are predominant, will be lower in comparison to a suspension in which interactions are mostly attractive. The latter will lead to particle agglomeration and thus to a more obstructed movement [267], [270].

Another parameter that changes the viscosity of suspensions is particle size. At the same number of particles, the ones with bigger size will cause higher increase in viscosity (Figure A.4B) due to the higher solid volume fraction. Therefore, the friction between individual particles is more pronounced. On the other hand, if two suspensions contain the same solid volume fraction, the suspension with smaller particles will possess higher viscosity, since the number of particles and consequently the number of interactions will be higher. The particle size distribution also affects viscosity. If particles size is polydispersed, the space packing is much more effective, since smaller particles fill the space between bigger particles. Consequently, at the same volume fraction suspensions with monodispersed particles, where packing is less effective (regardless of particle size), possess higher viscosity than suspensions with polymodal distribution (Figure A.4C).

Particle shape also has a pronounced and complex effect on rheological behavior, especially in concentrated suspensions [267]. Any deviation from spherical shape causes changes in rheological behavior. Based on the orientation of non-spherical particles the flow can be more or less obstructed. For example, if we have oval-shaped particles, the viscosity at low shear rates will be higher than in the case of spherical particles, due to a random orientation of particles. On the other hand, at higher shear rates oval-shaped particles orient easier in the direction of the flow than spherical particles, the phenomena known as preferential orientation (Figure A.4D). Consequently, the shear-thinning is much more pronounced. At higher shear rates the viscosity of suspensions containing oval-shaped

particles is noticeably lower than the viscosity of suspensions containing spherical particles. Apart from flow obstruction, the shape of particles also indirectly changes flow behavior.

Additionally, the non-spherical particles have a higher surface area than spherical particles and thus there are more physical as well as more mechanical interactions between the former. For example, the friction due to sharp edges causes the viscosity to increase in comparison to suspensions containing smooth spherical particles (Figure A.4E).

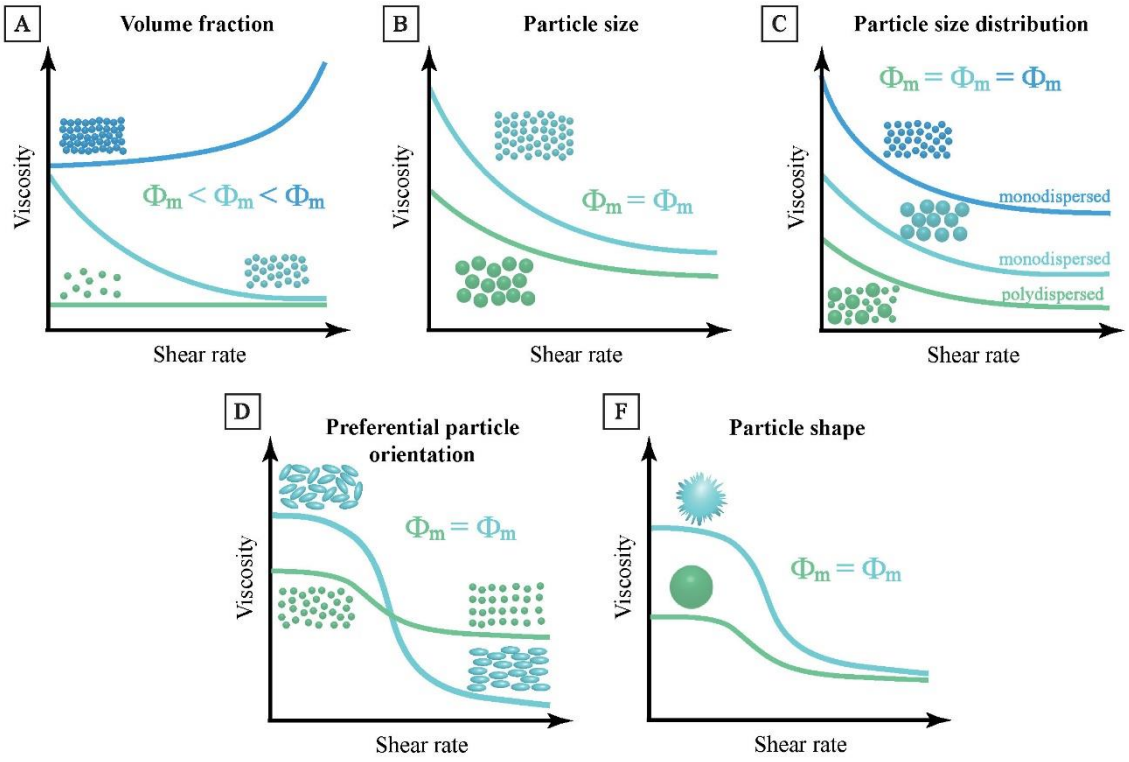

Figure A.4: Illustrations showing the change of viscosity with shear rate as influenced by A) different volume fractions, B) particle size at the same solid volume fraction, C) particle size distribution at the same solid volume fraction, D) preferential orientation of particles on viscosity and rheological behavior of suspensions at the same solid volume fraction, and E) particle shape at the same solid volume fraction.

A.1.2 Rheometry

Rheometry is an experimental technique used for characterization of rheological properties [216]. Rheological measuring instruments can be divided into relative and absolute. In relative measurements, the viscosity is determined based on comparison to a standard value (falling ball viscosity, penetrometers, Ford cup, etc.). In absolute measurements rheological data can be determined based on the measurement parameters and geometry of measuring cell. This group includes viscometers and rheometers.

Two basic principles of absolute measurements exist: rotational (transient) and oscillatory (dynamic) [60], illustrated in Figure A.5. In the first principle, the rheological data is collected in a short time period (usually a couple of minutes or a couple of dozen minutes) during which shear is continuously applied. The applied shear can be constant or a function of time. In oscillatory measurements, the fluid is not subjected to continuous shear, but is rather exposed to it in well-defined periodic short time intervals, mostly sinusoid [216]. The two principles look fairly similar, yet they provide different rheological information about the investigated material.

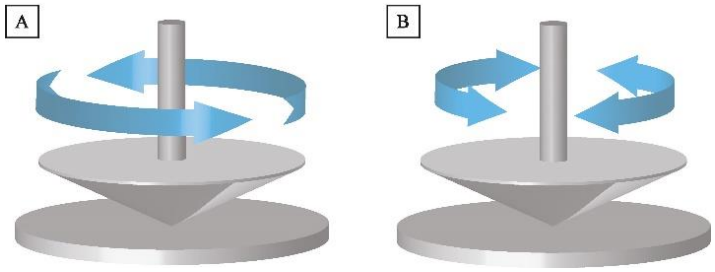

Figure A.5: A) Rotational measurement principle. B) Oscillatory measurement principle.

Rotational measurements are performed at so-called destructive shear conditions, where due to a continuous shearing at relatively high shear rates the inner structure of a fluid is deformed or even destroyed [60], [269]. As a result, a shear rate and shear stress or viscosity relationship is obtained. From the latter, also the type of rheological behavior and potential yield stress can be determined. During the measurement, either shear rate or shear stress is controlled, where the first principle is used for fluids with no yield stress (Newtonian, dilatant or pseudo-plastic fluids), while the shear stress controlled measurement is used when determining the yield point (pseudo-plastic flow behavior) [216]. However, not all materials can be characterized with the rotational test. The method can be used only on materials with prevailing viscous component.

Oscillatory tests are performed at low shear forces, where the inner structure is only slightly perturbed and not deformed or destroyed like in the case of rotational tests. Oscillatory measurements are mostly used to obtain information about the structure of fluid, like interactions between molecules or particles [60]. Rotational tests enable only characterization of materials with a prevailing viscous component, while oscillatory measurements enable characterization of a broader material spectra including those with a prevailing elastic component. As a result of oscillatory measurement, a complex shear modulus (G*), storage modulus (G') and loss modulus (G'') are obtained [216]. Storage modulus describes the elastic (solid-like) materials, and the loss modulus represents the viscous (liquid) part [268]. Since G* is the vector sum of G' and G'', it describes the complete rheological behavior, composed of both viscous and elastic part.

Aside from the measurement principle (rotational and oscillatory), the geometry of measuring system (MS) also plays an important role. The most common measuring systems are concentric cylinder (CC), cone-and-plate (CP) and parallel-plate (PP) [216] illustrated on Figure A.6. CC–MS consists of an inner and outer cylinder, with the latter being hollow as seen in Figure A.6A. It is especially useful for characterization of liquids, since unlike in CP and PP systems, in the former, liquid cannot flow from the MS, even at high shear rates. However, for CC–MS, a rather large amount of sample is needed and also the method is less appropriate for the testing of past-like fluids [216]. CP–MS system is composed of a stationary horizontal plate and a nearly flat cone. Its main advantage is a small amount of sample needed for the analysis. Additionally, throughout the entire shear gap (the distance between rotating and static part of MS), shearing conditions are homogeneous. On the other hand, CP–MS cannot be used for suspensions containing particles above a certain size. Also dispersion medium evaporation, flow inhomogeneity, discharge of the gap etc. can occur at the edge of the cone [216]. PP–MS consist of two parallel horizontal plates, where the lower plate is stationary like in the case of CP system, while the upper plate represents the rotating part. With PP–MS characterization of rheological properties of suspensions containing larger particles, hardening materials and samples exhibiting 3D structures is possible. The same unwanted events as in CP–MS can occur at the edge of the upper plate. Additionally, unlike in CP–MS, the shear conditions are not constant

throughout the shear gap but rather a shear gradient evolves. In PP–MS shear rate increases from zero in the center of the upper plate to the maximum value at its edge.

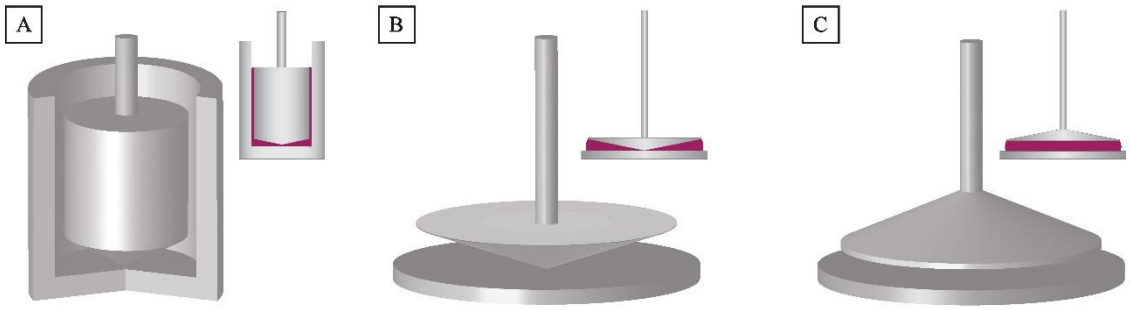

Figure A.6: Illustrations of A) concentric cylinder measuring system (CC–MS), B) cone-and-plate measuring system (CP–MS) and C) parallel-plate measuring system (PP–MS).

The choice of an appropriate measuring system geometry thus depends on many factors. Parameters like fluid's viscosity, the available amount of sample, desired shear rate, required precision in temperature control, particle size, possibility of a dispersion medium evaporation or sedimentation should be considered when planning a rheological experiment [269].

A.2 Zeta Potential

When particles, either colloidal or non-colloidal, are dispersed in polar liquid media, such as water, a charge will develop on the surface of particles. This charge can be either positive or negative, although the latter is more common [271]. Due to the charged surface, a reorganization of ions in the dispersion medium occurs to ensure electrical neutrality of the system as a whole [61]. As a consequence, an ionic layer forms around each particle known as electric double layer (EDL). EDL consists of an excess of ions charged oppositely as the particle surface and a deficiency of ions carrying the charge of the same sign [61], [63]. With the distance from the particle the repulsive interactions between its surface and same-charged ions starts to fade until at a long enough distance (some 10 nanometers) they completely disappear. At such distance, the number of positively and negatively charged ions is again the same.

As the name indicates, two layers are formed around a dispersed particle, namely Stern layer and diffusive layer. The former exists right next to the particle surface and is separated from the diffusive layer by the Stern plane (Figure A.7) [64]. Ions in Stern layer are assumed to be immobilized, due to the strong interactions with the charged surface. Part of these ions can even adsorb on the surface. Ions located in the inner part of the diffuse layer are also assumed to be immobilized. They are separated from the movable part of the diffuse layer by a sharp boundary named slip plane [65]. It represents the boundary between the part of dispersion medium and the containing ions that moves with the particle and the part that moves independently from the particle [66]. However, the location of the slip plane is not accurately known. It is assumed that its location is only little further from the surface than the Stern plane (Figure A.7) [61].

Based on the distance from the particle surface the potential changes. On the particle surface, the potential, known as the Nernst potential (ψ_0), has the highest value [67]. This value decreases linearly through the Stern layer, reaching the value known as the Stern potential (ψ_d) on the Stern plane [65], [67]. From this point onwards, the potential decreases exponentially with the distance from the particle surface [56]. The surface

(Nernst) potential cannot be measured [67]. It can however be estimated from the measurement of potential on the slip plane, known as electrokinetic or zeta potential (ζ) [59], [65]. The specific distribution of ions around a charged particle thus enables the assessment of an approximate charge on its surface [66].

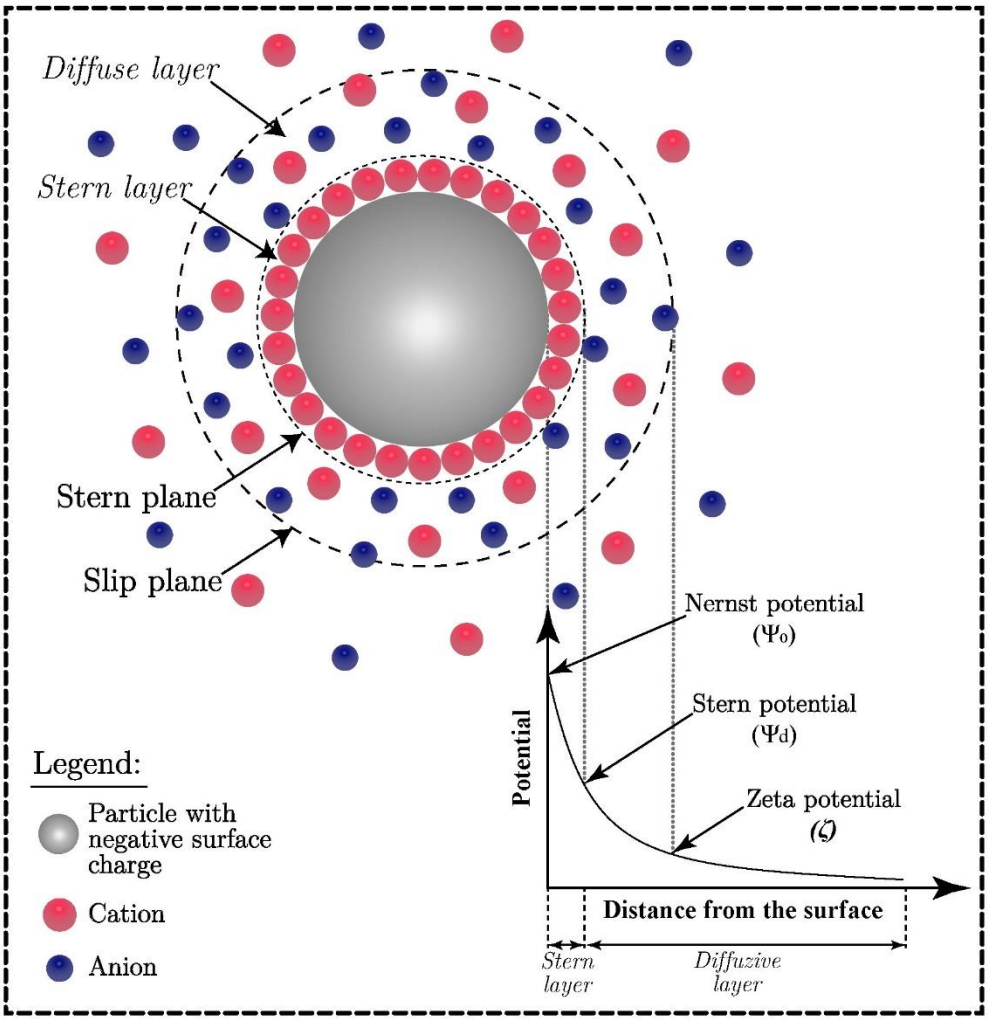

Figure A.7: Structure of an electrical double layer formed around a negatively charged particle.

Zeta potential is defined as a difference between the potential of EDL of electrophoretically mobile particles and the potential of dispersant surrounding them. In other words, it is the difference between the potentials of layers inside and outside of the slip plane, when the particles and the liquid phase move tangentially in respect to each other [56], [61], [67].

Zeta potential can be obtained from electrokinetic measurements by three main measuring principles, namely streaming potential, electro-osmosis and electrophoresis. The latter principle is the most widely applied [61], [70]. In electrophoresis, the dispersion medium (liquid) is at rest, while the particles move under the influence of externally applied electric field, in the direction of the oppositely charged electrode [61], [66]. This movement of charged particles (electrophoretic mobility) or more precisely their velocity is mostly measured using light scattering detection (detector used in the majority of commercially available instruments, e.g., Malvern, Zetasizer®) [67]. Considering some assumptions, the ζ can then be calculated from particle mobility [61].

The value of ζ depends on many factors, such as particle surface, concentration and type of ions present in the liquid phase, type of liquid used for dispersion, etc. [66]. Especially important is the concentration of ions, which depends on the suspension's pH. Therefore, the ζ is always given as a value at specific pH. One of the most important values is the isoelectric point (IEP), which is defined as the pH value where the ζ is equal to zero. Dispersed particles will, due to the absence of charge, agglomerate when pH of a suspension is close to the value of IEP. In order to prepare stable suspensions, their pH should be either higher or lower than IEP.

The value of isoelectric point depends on surface properties. For example, materials with acidic groups on the surface will have IEP at low pH values, while the presence of alkaline groups moves IEP to higher pH values (Figure A.8). However, the determination of isoelectric point is not an easy task. The best method is through the titration of suspension with acid and alkaline solutions, i.e., measurement of a selected number of ζ throughout the entire pH range [271]. As a result, a dependence of ζ from solution's pH is obtained (Figure A.8). As depicted in Figure A.8, when pH value is moved to higher or lower values in respect to the IEP, the absolute value of ζ starts to increase. After a certain pH, where ζ reaches its maximum value, a consequent decrease in its absolute value can be observed at very acidic and very alkaline pH. At these values, due to a high ionic strengths, the EDL is more compressed, which results in lower absolute ζ values [58].

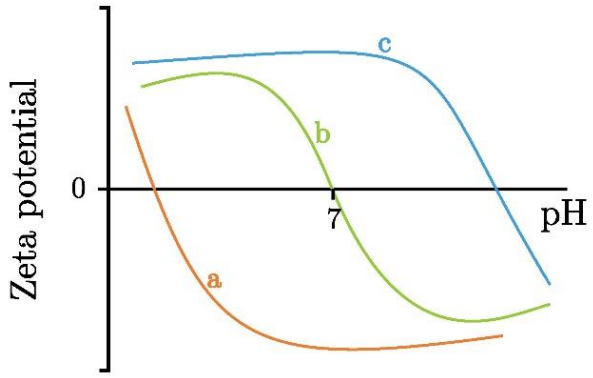

Figure A.8: Zeta potential in dependence from solution pH for particles with present acidic surface groups (a), for amphoteric particles (b) and particles with basic surface groups (c).

Since a lot of suspension's properties are directly or indirectly related to the charge on the surface of particles, determination of ζ has become extremely useful, providing information such as suspension stability, influence of dispersant addition, type of interparticle interactions, etc. [271]. Its use in the estimation of suspension's stability is especially popular [67]. For example, particles with ζ between 0 and $\pm$10 mV are in most cases highly unstable and agglomerate quickly, while the particles with ζ between $\pm$10 and $\pm$30 mV are reasonably stable. They will remain dispersed over shorter time periods, but will agglomerate eventually. On the other hand, when ζ exceeds $\pm$30 mV, particles are highly stable and not likely to agglomerate [67], [68].

A.3 Mercury Intrusion Porosimetry

Mercury intrusion porosimetry (MIP) is a routinely used technique for characterization of materials, especially porous [272]. It enables determination of a wide range of pore sizes from approximately 3.5 nm and up to several hundred micrometers [4], [273]. MIP is considered as a standard method for the characterization of macroporous materials. All of

the alternative techniques, like liquid porosimetry, X-ray tomography, theoretical modeling etc., are less suitable for the characterization of pores in macro range [4].

MIP is in itself relatively easy to perform, the analysis time is short and results generally have a good reproducibility, with under 1% standard deviation [274]. This technique provides a wide range of information obtainable from a single run, such as bulk and skeletal density, pore size distribution and total pore volume [274].

Some additional parameters like surface area, compressibility and permeability or, in the case of powder materials, particle size distribution can also be obtained. Yet, these data analyses are more complex and require an experienced user [4], [274]. Additionally, noticeable deviations from the actual state can easily arise due to numerical models used in calculation, e.g., particle size can be estimated from pore sizes by predicting powder particle packing structure. However, any deviations of the particle shape from spherical will lead to a false result [274]. Alternative techniques, such as gas sorption for determination of surface area or dynamic light scattering used for characterization of particle size, should be used to verify the exactness of the results obtained with the advanced modeling of MIP data.

MIP exploits the non-wetting nature of mercury (contact angle $> 90^{o}$), which means that the pressure must be applied in order to force the intrusion of mercury into pores. With increasing pressure mercury can intrude into smaller and smaller pores. This inverse relationship between the pore diameter (d_{pore}) and mercury intrusion/extrusion at applied pressure is described in Eq. (A.5) and is known as Washburn equation [4], [273], [274]:

$$p = -\frac{4 \cdot \gamma \cdot cos\theta}{d_{pore}} \tag{A.5}$$

where p is the applied pressure, d_{pore} the diameter of the pore, γ the surface tension of mercury and θ the contact angle between the solid surface and mercury. For the surface tension, a value of 0.485 $N \cdot m^{-1}$ at 25 °C is generally accepted [274].

To solve Eq. (A.5), surface tension of mercury and contact angle for the sample tested must be known. Analysis parameters (temperature and pressure) have little effect on the value of γ [275], causing insignificant errors in the determination of pore sizes. The contact angle, on the other hand, has a bigger impact on the results, since its value depends on the surface properties of tested material [4], [274]. The value of θ can be evaluated experimentally, yet even little differences in material's composition, such as the presence of impurities or differences in crystalline structure, have a substantial influence on the contact angle. Thus it is recommended that for a general porosity evaluation, a standard value of 140° is used, regardless of the sample material. Standard value of θ enables easier comparison between mercury intrusion obtained porosities from the different studies [4], [274].

All mercury porosimetry machines work on the same principle, as illustrated in Figure A.9. First the dilatometer containing a sample is evacuated to avoid the presence of moisture or any air pocket formation during mercury filling. Then the dilatometer (cell and stem) is filled with mercury. When pressure is increased, mercury starts to penetrate into the pores and as a consequence the height of the mercury in the capillary stem decreases. After the pressure is decreased, extrusion of mercury occurs and the height of the mercury column in the stem starts to increase. The change in the mercury column height is monitored through capacitance measurements between a metal coating on the outer side of glass stem and mercury column inside the stem [274]. Since the stem's inner diameter is precisely defined, the change in mercury column height can be used to calculate the intruded volume. The intrusion and extrusion volumes at specific pressures are monitored and then converted into pore size – pore volume relation [274].

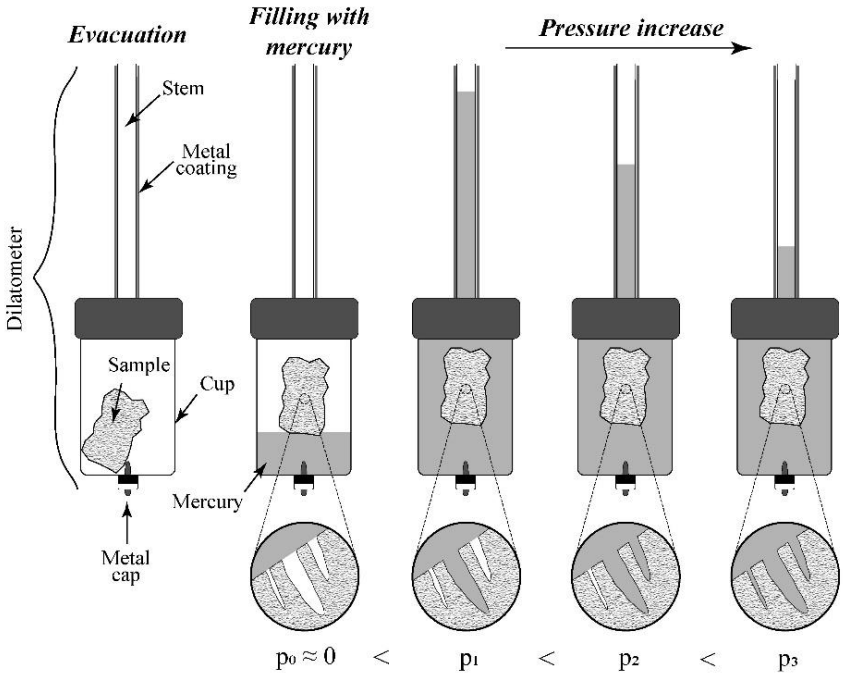

Figure A.9: Illustration of a typical penetrometer (dilatometer) and the principle of mercury intrusion measurement, with an illustration of pore filling sequence.

Since the intrusion of mercury is pressure-controlled, also the pore size range that can be determined with this technique is limited by the achievable pressures [273]. Commercially available porosimeters enable measurements in the pressure range of 3 kPa to 400 MPa, corresponding to a cylindrical pore diameter of a little below 500 µm to 3.6 nm, for $\theta = 140°$ [4], [274]. The upper pressure limit is set to 400 MPa by the majority of manufacturers in order to avoid safety issues [273]. On the other hand, the lower limit is set by the head pressure of mercury on the material tested [274]. Due to its height, the sample is subjected to a certain starting pressure caused by mercury. This head pressure also depends on the geometry of the penetrometer (also called dilatometer). Different positions of mercury capillary in regards to the cup containing sample are possible [276], [277]. The above-mentioned upper pore diameter of 500 µm cannot be measured for all samples or with every machine. Thermo Fischer Scientific specifies the upper pore size limit at 116 µm, other producers like Micromeritics® claim the upper limit to be 500 µm or over 900 µm as claimed by Anton Paar. Although the latter limit is very questionable since the mercury head pressure limits measurable range to 500 µm or lower [274].

In order to avoid complex mathematical problems, a cylindrical shape of pores is assumed when modeling MIP data [273], [274]. Since the real pore shape is usually rather different, the former postulation is in many cases the main reason for substantial differences between real and experimentally determined pore sizes. Postulation of a cylindrical shape is especially problematic in the case of so-called “ink-bottle” pores, in which the opening is much narrower than the inner part (Figure A.10). Mercury porosimetry can only measure the largest opening connecting the pore to the material surface [274]. Consequently, the differences arise between the measured and actual (inner) diameter, with the measured diameter being much smaller than the inner diameter (Figure A.10A). This difference occurs due to much higher pressures, which is needed for mercury to intrude an “ink-bottle” pore in comparison to a cylindrical pore of the same inner diameter (Figure A.10B).

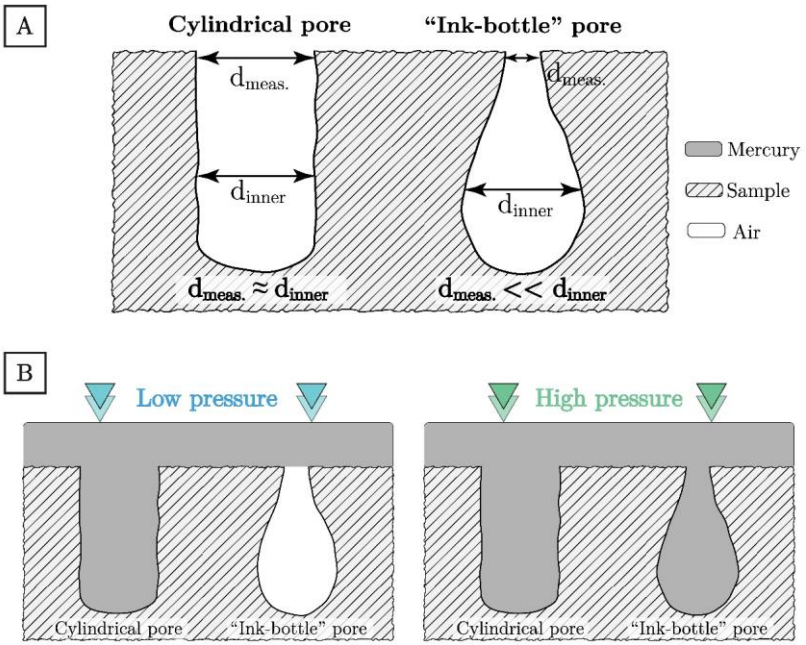

Figure A.10: A) Influence of the pore shape on the relationship between the diameter measured with mercury intrusion porosimetry ($d_{meas.}$) and the inner diameter of the pore (d_{inner}). B) "Ink-bottle" pores with the same inner diameter as cylindrical pores are filled at much higher pressures than the latter.

Due to the above-mentioned assumption and the considerable influence of the preset experimental parameters on the results, MIP is more of a comparative technique than an absolute method [4], [274]. The results and conclusions made from this technique should be regarded accordingly.

Results of MIP are usually shown as intrusion and extrusion volumes as a function of applied pressure (Figure A.11). The volume of intruded mercury can be plotted as a cumulative (total) volume ($V_{cum.}$), which tells us the volume of all pores filled at a certain pressure. Intruded volume can also be plotted as incremental volume ($V_{incr.}$), which denotes the volume of pores with a specific diameter [4]. It is calculated by subtracting the cumulative volume at specific pressure from the cumulative volume determined at a slightly higher pressure.

The shape of an intrusion-extrusion curve depends on many factors, such as sample type (powder or bulk materials), pore size, pore volume, etc. The most common curve shapes are shown in Figure A.11.

When a powder material is analyzed, the curve can be divided into several regions (Figure A.11A). The increase of the $V_{cum.}$ in the region I occurs due to particle rearrangement within the powder bed. A much more prominent increase in the region II is the consequence of mercury intrusion into interparticle voids. Intrusion in region III happens due to the presence of intraparticle porosity. In Figure A.11A, there is a clear distinction between inter- and intraparticle pores, allowing for a precise distinction between both pore types. Determination of particle size as well as envelope density (density of particles including closed and open pores) is thus possible [273], [274]. In the majority of cases this demarcation is rather distinct, since the size of interpores greatly exceeds the size of intraparticle pores. However, some materials possess inter- and intrapores of the same proportions. In such cases, the demarcation is not possible and porosity of particles or particle size cannot be determined accurately [273].

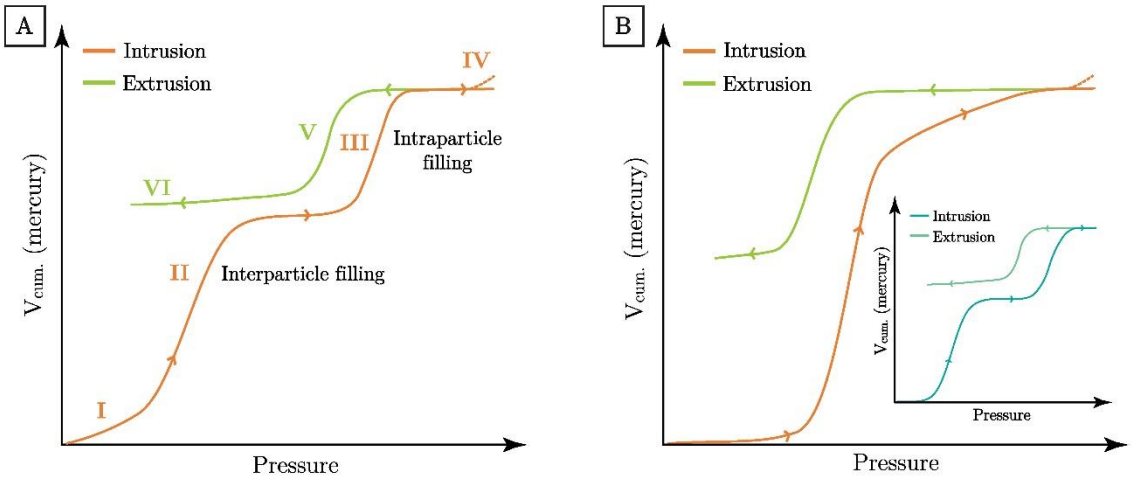

Figure A.11: Mercury intrusion and extrusion curves showing cumulative volume as a function of pressure for powder sample (A) and for bulk sample (B). Inset shows intrusion/extrusion curve for a bulk sample with bimodal pore size distribution.

At the highest pressures, a small increase at the end of the intrusion curve can occur (IV). This increase indicates that the sample was compressed. For most solids, the contribution due to the compressibility is negligible. Yet it should not be disregarded in the case of polymers or sol-gel materials [274]. For such samples, a correction for compressibility should be implemented [273].

When the pressure is decreased, the extrusion of mercury starts. A hysteresis loop occurs (V), since extrusion and intrusion do not occur at the same pressure. Also some of the mercury usually remains trapped in the sample pores, hence the loop is not closed (VI) [4].

Intrusion-extrusion curve for bulk samples is similar to the one observed in powder samples, except no intrusion due to particles rearrangement or filling of interparticle voids occurs.

As illustrated in Figure A.11, hysteresis between intrusion and extrusion curve is observed in practically all sample types. There are several explanations of this phenomena, but three of them are accepted by the majority of the research community. These theories are contact angle hysteresis, “ink-bottle” theory and the percolation-connectivity model [274]. The first one postulates that hysteresis occurs due to a difference in the contact angle of mercury during intrusion and extrusion. The validity of this theory is however somewhat questionable, since it cannot explain all of the observations. “Ink-bottle” theory is based on the assumption that the pore opening is narrower than the diameter of the cavity (as shown in Figure A.10A). Consequently, the pressure needed to force mercury intrusion is controlled by the pore opening and not the diameter of the cavity. When extrusion starts, the mercury network breaks at the pore neck (narrow paths), and consequently a significant amount of the mercury remains trapped inside such pores. This theory adequately explains why after extrusion $V_{cum.}$ is not equal or close to zero. Yet it cannot explain the shift between the pressure at which the intrusion starts and the pressure needed for extrusion from the same pores. In an ideal system, where pores have a uniform, cylindrical shape intrusion and extrusion should occur at the same pressure [274]. The percolation-connectivity model is in a way an improved “ink-bottle” theory. This theory’s main assumption is that a network of interconnected pores exists. Unlike in intrusion, where there is a continuous flow of mercury during pore filling, during extrusion, some of the mercury remains trapped. This means that a new interface must be formed when mercury

is retracting from the pores. Since the formation of an interface requires energy, occurrence of an energy-barrier is to be expected. Thus for extrusion to start, the pressure must be lower in comparison to the pressure needed for intrusion, in order to compensate for the energy needed to form a new mercury surface [274].

In summary, mercury intrusion porosimetry is currently still the main method for the analysis of macropores due to its simplicity, short analysis times, good reproducibility and extensive information that can be obtained from a single measurement. However, some drawbacks and limitations should be emphasized [4], [273], [274]:

- ∴ MIP is only capable of determining the largest pore entrance, but not the actual pore size (problem of "ink-bottle" pores).
- ∴ Pores with a diameter smaller than 3.5 nm (assuming $\theta = 140°$) cannot be determined. The technique is therefore not suitable for characterization of micropores.
- ∴ The largest measurable pore size is limited by the sample height and the measurement setup (mercury "head-pressure").
- ∴ Some metals, such as gold or silver, and some alloys can react with mercury forming amalgams. This can lead to an immense change of contact angle.
- ∴ Mercury is a hazardous chemical and should be handled with care.

Despite the mentioned drawbacks mercury porosimetry remains the main method for the characterization of macro-porous materials, since a comparable alternative technique is yet to be established [4].

A.4 Gas Adsorption

Gas adsorption is one of the most commonly used techniques for the determination of (large) specific surface areas and characterization of meso- and microporous samples [278], [279]. This technique is based on the coverage of the material's surface with a gaseous film, which enables a detailed determination of surface morphology and pore shape at the atomic level [280].

When a clean solid surface comes into contact with gas (or vapors), adsorption will always occur to some degree. Gas molecules (adsorbate) adsorb on the surface of a solid material (adsorbent). The adsorbed amount depends on the interaction potential between the adsorbate and the adsorbent and temperature and pressure [280]. Adsorption can be chemical (irreversible) or physical (reversible), depending on the strength of the interactions. In the case of chemical adsorption (chemisorption), the interaction potential between gas molecules and solid surface is rather high, and in most cases chemical bonds are formed. On the other hand, in the case of physical adsorption (physisorption), interaction potential is much lower and van der Waals forces are the predominant type of interactions. Molecules of gas are more localized in the case of chemisorption and cannot freely migrate about the surface, while physisorbed molecules are not bound to a specific site and can cover an entire surface. Also their adsorption process is fully reversible, meaning the adsorption as well as the desorption process can be studied [280]. Due to a more suitable characteristics of physisorption, gas adsorption is mainly based on the latter principle, yet for characterization of some materials chemisorption is used [276], [280].

A number of gases can be used as adsorbates, e.g., nitrogen, hydrogen, carbon monoxide, helium, krypton, argon etc., yet nitrogen is the most widely used [276], [278], [279]. Also, since physical adsorption of gases is more pronounced at lower temperatures, the adsorption measurements are conducted in liquid nitrogen (≈77 K) [281].

Prior to any gas adsorption measurement, any contaminating molecule physisorbed to the sample's surface must be removed. Most commonly this is accomplished by a vacuum

treatment of a sample material or by purging it with an inert gas. Both procedures are carried out at elevated temperatures [280].

Gas adsorption technique can be carried out in two different modes: static and flow. The majority of commercially available machines are based on the static mode [276], [279]. Flow mode is a modification of a conventional gas chromatography. The amount of adsorbed gas is measured by passing the gas phase through a thermal conductivity cell [276], [279]. In the static approach, the quantity of adsorbed gas can be measured by a volumetric or a gravimetric method [279]. Especially when nitrogen is used, the amount of adsorbed gas is mainly determined by the volumetric method [279]. In this variation, a known volume of gas is supplied to the measuring cell containing sample. After the gas is added the adsorption starts. The latter is always accompanied by a pressure drop; thus the system must be allowed to equilibrate. When the equilibrium state is reached, i.e., when the rate of gas adsorption is the same as the rate of desorption, the amount of gas adsorbed is calculated. The adsorbed volume is the difference between the total volume of gas added and the volume of gas needed to fill the "dead space" (the volume of the measuring cell from which the volume of a sample is subtracted) [278], [281]. The gravimetric determination, on the other hand, is based on measuring the difference in sample mass prior to and after the adsorption. The major advantage in comparison to the volumetric approach is that the cell calibration (determination of the "dead space") is eliminated. Yet, the principle is less popular than the volumetric method, due to a delicate nature of the gravimetric apparatus [276].

The process of adsorption is repeated point-by-point at multiple different volumes/pressures of adsorbate gas and before each measurement the system is allowed to reach equilibrium. When the highest (preset) value of relative pressure is reached, the process is repeated in reverse. The amount of added adsorbate gas is gradually (step-wise) decreased and information about the desorption process is obtained.

Results are plotted as an adsorption-desorption isotherm, where the amounts of adsorbed gas are given as a function of equilibrium pressure of the adsorbate gas or as the function of partial gas pressure (P/P_0) at the equilibrium state [279]. P_0 being the saturation pressure of the adsorbate gas. By implementation of a suitable theoretical model surface area and pore volumes can then be calculated [280].

When an isotherm is obtained the first step is the identification of the isotherm type [279]. From it, the basic material characteristics can be established. For example, is the sample porous or nonporous, is the porosity in micro or meso range, etc. It can also be established whether the adsorbed molecules form one or multiple layers. In monolayer adsorption all adsorbed molecules are in contact with the surface or adsorbent, while in multilayer adsorption, some of the adsorbed molecules are only in contact with other adsorbed molecules and not in the direct contact with the solid surface [279].

The categorization into types is especially important when choosing the appropriate theoretical model for further processing of the obtained data [282]. The type of isotherm is determined by the nature of solid material tested and also by the properties of adsorbate gas [281]. By current IUPAC classification, which is based on a prior classification system established by Brunauer [283], there are six types of isotherms in the gas-solid systems (Figure A.12) [279]. The majority of adsorption isotherms can be allocated into one of these six classes, some systems, for example supercritical gases, are not similar to any of the standard isotherm types [282]. The current classification only consists of adsorption isotherms behaving as monotonic functions of pressure. This means that through the entire pressure range, the function is either increasing or decreasing. Yet some experimentally obtained isotherms of supercritical gases are not monotonic but show a maximum [282].

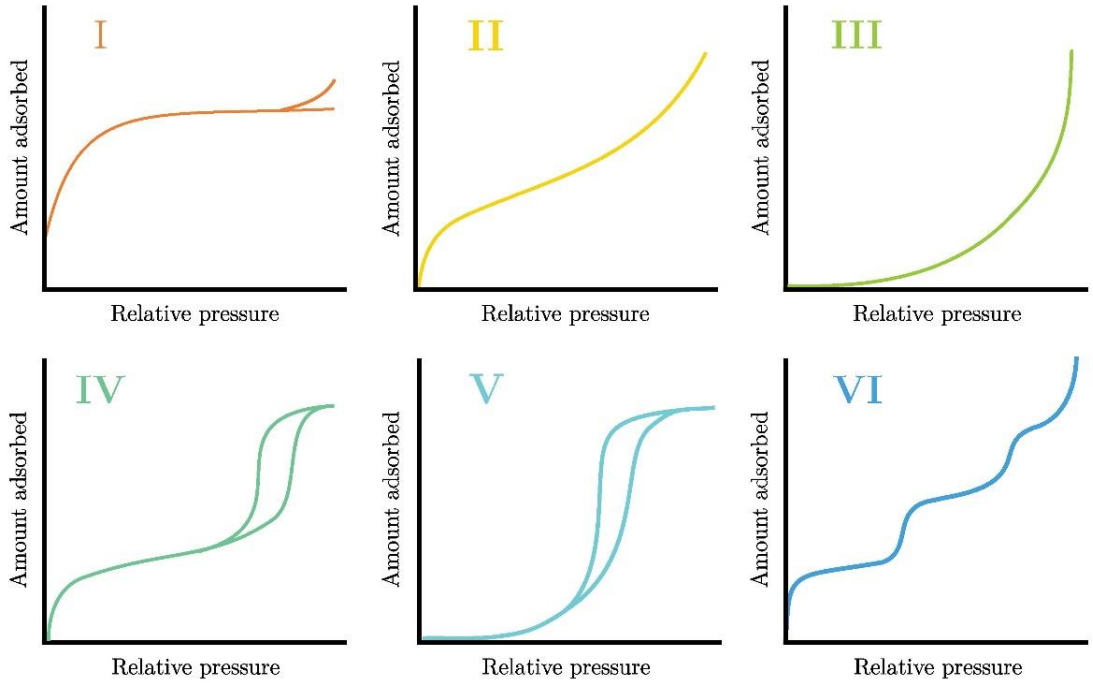

Figure A.12: IUPAC classification of adsorption isotherms in gas-solid systems.

Type I isotherm can be recognized by a pronounced initial adsorption (at low relative pressures), followed by a plateau region. This shape is characteristic for gas adsorption on microporous substrates, where the adsorbed layer is no more than a few molecular layers thick [276]. The increase at low pressures is due to the filling of micropores. The following plateau region indicates that little to none adsorption occurs once the micropores are filled. This means that the exposed surface area of such materials consists almost exclusively of micropores, and there is practically no external surface area [280].

Type II is characteristic for nonporous or macroporous materials. The curve has an inflection point at low relative pressures, which usually marks that monolayer surface coverage is complete. With further increase of pressure multilayer adsorption starts [279], [280].

Systems that exhibit isotherm of type III are not common. Two conditions must be met in order to obtain type III isotherm, namely the substrate must be non-porous and the interactions between adsorbent and adsorbate must be much weaker than between individual molecules of adsorbate [279]. In such materials, the adsorption is much faster at higher pressures where monolayer coverage is complete and multilayer adsorption starts [276].

For type IV, a (closed) hysteresis loop is a characteristic feature. The desorption and adsorption branches differ due to the presence of mesopores [276], [279]. Just like in the case of type II, also for type IV there is an inflection point that marks the pressure where monolayer surface coverage is finished. The notable increase in the adsorbed amount at higher pressures as well as the appearance of hysteresis loop indicate that the filling of mesopores has started.

Systems with type V isotherm have similar properties as systems described with type III, i.e., weak adsorbate-adsorbent interactions. Yet type V isotherm exhibits a hysteresis loop similar to type IV, indicating the substrate must be mesoporous and not non-porous as in the case of type III [279], [280]. Just like class III also class V materials are not common [279].

Type VI isotherm is characteristic for multilayer adsorption. The substrate must be non-porous and its surface of uniform shape. The height of each step is an indication of the monolayer capacity of individual adsorbed layers [279].

A.4.1 Surface area determination

Surface area is by its definition the accessible area of solid material's surface per unit mass and is usually given in square meters per gram [3]. There are a number of gas adsorption methods for the determination of the surface area, yet the Brunauer, Emmett and Teller (BET) method is the most commonly used [276], [281]. This theory is an extension of Langmuir's theory [284] for the calculation of adsorbate monolayer capacity (V_m) from the adsorption isotherm [276]. The main limitation of Langmuir's model is that the adsorption is restricted to a monolayer. Yet in real systems, there is no pressure value at which the surface would be completely covered with precisely one layer [280]. Usually a second and higher layers start to form before the monolayer coverage is complete [276]. The assumptions made by the BET model enable the experimental determination of V_m despite the fact that a complete monolayer coverage is never accomplished without at least partial formation of multilayers. BET is thus an extension of Langmuir's theory to multilayer adsorption [280]. Eq. (A.6) presents the BET equation:

$$\frac{P}{V_a(P_0-P)} = \frac{1}{V_m \cdot C} + \frac{C-1}{V_m \cdot C} \cdot \left(\frac{P}{P_0}\right) \tag{A.6}$$

where P_0 is the saturation pressure of the gas, P is the pressure of the adsorbate at equilibrium, V_a is the volume of gas adsorbed at pressure P, C is a constant and V_m is the volume of gas needed to achieve monolayer surface coverage [281].

In most cases, if $P/(V_a \cdot (P_0 - P))$ is plotted versus P/P_0, a straight line is obtained within the partial pressure range 0.05 to 0.35. For accurate determination of the surface area five or more points should be measured inside this range of partial pressures. From the slope and intercept of this line the volume of a monolayer V_m can be determined. Specific surface area (SSA) of the sample can then be calculated from Eq. A.7 [281]:

$$SSA = \frac{N_A \cdot V_m \cdot A_N}{V_0 \cdot m} \tag{A.7}$$

where N_A is the Avogadro constant, A_N the molecular cross-sectional area, V_0 the molar volume of gas and m sample mass. For nitrogen, which is the most commonly used adsorbate, the molecular cross-sectional area of 16.2×10^{-20} m^2 is assumed [279][281]. The majority of the commercial machines available today use BET method for the calculation of SSA and usually enable its determination in the range from 0.01 m^2/g up to a couple of thousands m^2/g [276].

However, not all types of isotherms are suitable for the BET analysis. It is unlikely to obtain a correct SSA value from type I and III isotherms. On the other hand, BET-determined surface areas from types II and IV are close to the actual values [279].

A.4.2 Pore volume and pore size distribution

While mercury porosimetry is the first choice for characterization of macroporous materials, gas adsorption is the most widely used technique for the characterization of micro- meso- and very small macropores [285]. If nitrogen is used as an adsorbate gas, the pores with sizes ranging from 0.5 nm and up to 200 nm can be characterized [285], [286].

When pore sizes and pore volumes are determined by gas adsorption, the choice of the appropriate theoretical model for isotherm analysis is of paramount importance. Different

models should be applied for microporous and mesoporous materials. The reason lies in the pore filling mechanism. In mesopores, the prevailing mechanism is capillary condensation, which occurs at higher relative pressures. On the other hand, micropores are filled at lower relative pressures by a volume-filling process [287].

For the determination of pore size distribution in meso range the most widely used model is the one developed by Barret, Joyner and Halenda [288], known as the BJH model. The BJH model is based on Kelvin equation, with the applied correction for multilayer adsorption. The model also assumes a cylindrical pore shape [281]. However, the computed results obtained by applying this model are only valid for type IV isotherms [279]. The decision which branch of the isotherm (adsorption or desorption) should be selected for BJH calculations is more or less a matter of personal choice [279]. Yet, the desorption part of an isotherm is closer to the thermodynamically stable system than the adsorption part, and is consequently used more often [278]. Even though several authors reported considerable errors resulting from the implementation of the BJH model, with mesopore sizes being mostly underestimated [289], [290], it is still widely used due to its accessibility in the commercially available software programs [285].

BJH model is widely applied, yet it is limited to the pores with diameters larger than 2 nm, since the model cannot accurately predict the diameters and volumes of micropores [291]. Thus a number of alternative theoretical models able to determine micropore volume from adsorption isotherm of type I were developed [280], [292]. Among the most widely used are the t-method [293] and α_s-method [294].

A.5 Thermal Conductivity

Heat transfer occurs through one of three modes: radiation, convection, and gas conduction. All three modes are present simultaneously when the temperature gradient occurs, but usually one predominates. Also at room temperatures radiation can be neglected [295]. For solid material conduction is the primary heat transfer mechanism [296]. Consequently, among a variety of thermal properties of solid materials thermal conductivity (λ) and thermal diffusivity (κ) are the most commonly determined. Another important characteristic is specific heat capacity (c_p) [296].

A number of different experimental methods have been developed for characterization of above-mentioned properties [297]. There are five main methods for the determination of thermal conductivity: radial heat flow method, calorimeter method, hot wire method, guarded hot-plate method and flash method [298].

In all techniques, a temperature gradient is established and the response of the material to this gradient monitored. However, between techniques, parameters such as sample size and measurement time differ [296]. Based on measurement principle thermal conductivity determination methods can be divided into two main categories: transient and steady-state. If the temperature is independent of the recording time, the method is categorized as steady-state, while in the transient state measurement recorded temperatures vary with time [297]. The radial heat flow, calorimetry and the guarded hot-plate are examples of steady-state methods, whereas the flash and hot-wire methods are based on the transient state measurement principle [297]–[299].

Transient state techniques present several advantages in comparison to steady-state methods. In transient state experimental times needed to determine thermal transport properties are considerably shorter [296], [297], with the measurements completed in seconds rather than minutes or hours needed for steady-state techniques [296]. Also a broader range of the thermal conductivity can be measured in transient-state (from 0.01 to 400 $Wm^{-1}K^{-1}$) [300].

Additionally, in a steady-state experiment the thermal conductivity and thermal diffusivity cannot be determined in a single measurement. Contrarily with transient methods both parameters can be measured simultaneously.

A.5.1 Transient plane source technique

Transient plane source (TPS) techniques are an improved modification of the hot-wire transient state method [301], [302].

The experimental setup for both techniques (hot wire and TPS) is similar. The electrical heating element which also serves as a temperature monitor is placed between two identical flat pieces of the material under investigation. A small constant electrical power is supplied to the heating element, which emits it as heat in all directions into the surrounding investigated material. The change in the temperature of the heating element is accurately determined by measuring its electrical resistance [299]. Through the monitoring of the temperature increase it is possible to determine the thermal conductivity and thermal diffusivity of the tested material [299], [303]. If the investigated material is highly thermally conductive, the temperature increase will be lower than if the material is thermally insulative [298].

However, in the hot-wire method, a thin refractory wire (e.g., platinum or nickel-chrome) is used as a heating element [298]. In TPS methods, the heat flow originates from a plane heating element, such as a rectangular metal foil [304]–[306] or a thin metal foil disk with a bifilar spiral pattern [297], [302]. The first one is called the hot strip technique, while the second one is known as the hot disk.

The advantage of TPS methods over hot wire is that when using TPS, both thermal conductivity and thermal diffusivity can be determined with a good accuracy. On the other hand, with the hot-wire method, only thermal conductivity is determined with high accuracy, whilst the thermal diffusivity is estimated with lower precision [297], [302].

Additionally, there are also differences between the applicability of mentioned TPS techniques, namely hot disk technique possesses two main advantages over the hot strip method. Firstly, due to the sensor design, the resistance in the hot disk sensor is higher than in the hot strip sensor. Consequently, the temperature change is recorded with higher sensitivity and accuracy [299]. The second advantage is that the hot disk technique allows the use of samples with smaller dimensions. Theoretical model used in the hot strip method assumes the infinitely long strip. This means that samples must have a large length–to–width ratio (up to the ratio of 20:1), so the required sample dimensions are much larger than in the case of the hot disk method [299]. Consequently, the hot disk technique is nowadays commercially available and widely used in academic research for the characterization of new materials as well as on the industrial level [299] for optimization of the production process and for on-line monitoring of the quality control during production [296].

As already stated, the hot disk technique uses a thin metal disk as a continuous plane heat source [299]. Such sensor consists of a nickel double spiral, which is approximately 10 μm thick with a diameter ranging from 0.5 to 30 mm depending on the sensor type [302]. The metal spiral is sandwiched between two thin sheets of electrically insulating material, typically polyimide (Kapton) or mica. The choice of insulating material depends on the measurement temperature range. For temperatures from 30 K to 450 K, a Kapton insulated sensor is used, while for higher temperatures (450 K–1200 K), mica sensors are more appropriate [297]. The schematics of experimental configuration and of a Kapton sensor are shown in Figure A.13A and A.13B, respectively.

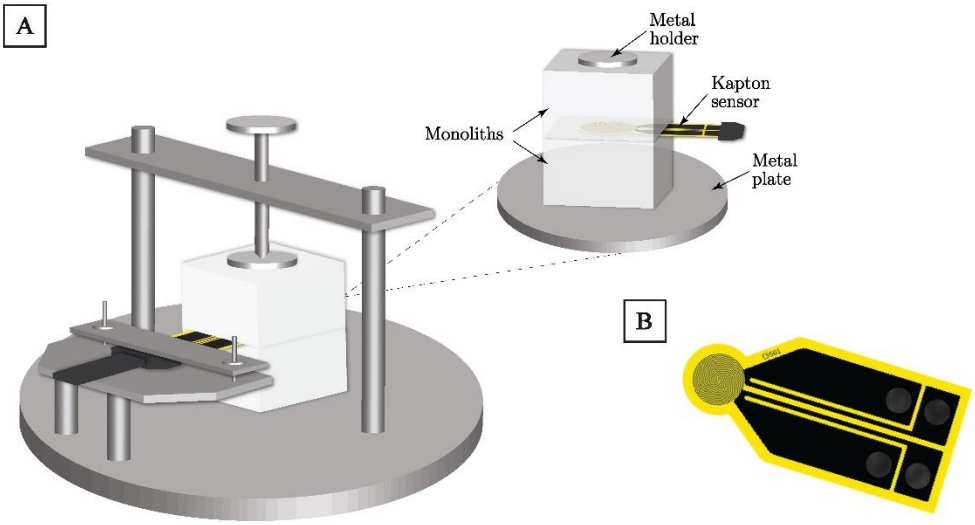

Figure A.13: A) Illustration of the hot disk measurement setup for the determination of thermal conductivity. B) Schematic of a Kapton sensor with a diameter of 6.4 mm. The image was obtained from the HotDisk® website (https://www.hotdiskinstruments.com).

This commercially available technique can be used over a wide temperature range [299], [303], and on a variety of sample shapes and sizes. Samples can be relatively small, ranging from 3 millimeters on, while the thickness can range from thin films to bulk materials [296], [297], [301]. Aside from bulk and thin film materials, hot disk can also be used to determine thermal properties of liquids [307], [308], powders [309] and anisotropic materials [19], [310].

This technique also enables the determination of a broad range of thermal properties from 0.005 W/mK to 500 W/mK for thermal conductivity and from 5×10^{-8} m^2 s^{-1} to 10^{-4} m^2 s^{-1} for thermal diffusivity.

Anisotropic properties can be found in many materials and products, such as wood, fibrous foams, and Li-ion batteries [19], [311], [312]. Thermal properties of such materials are direction-dependent. Hot disk enables simultaneous characterization of thermal properties in-plane (axial) and through the plane (radial) of a sample. As a result, two thermal conductivities are obtained, one for each direction. The measurement is based on the same principle as isotropic measurement, but the specific heat capacity of the material must be determined beforehand due to the applied mathematical model [310]. However, the as-determined radial λ is only accurate for orthotropic materials, that is materials with homogeneous structure in one plane but different from the structure in the other plane. In other words, properties along the x- and z-axes must be identical, but differ from those in the y-axis (Figure 3.2),

However, despite the many advantages of the hot disk technique, its accuracy in the determination of low thermal conductivity is limited. It has been pointed out that due to the insulative layer on the sensor, the experimental error can be significant when thermally insulative materials are tested. Especially if thermal conductivity is lower than 0.05 W/mK [313], [314]. For such materials thermal conductivity determined with the hot disk method was up to 50 % higher from the value determined with steady-state methods [314].

The hot disk technique also offers an additional option of specific heat capacity determination in a separate measurement (Figure A.14A). Heat capacity specifies the material's ability to store heat [315], with low c_p indicating a material with high thermal conductivity and vice versa. It is especially important to know its exact value when thermal properties are being determined to the materials with anisotropic structure [316]. For the determination of specific heat capacity, a special sensor with a golden cylinder is needed

(Figure A.14B). When measuring c_p, first a reference measurement is performed, where an empty cylinder, thermally insulated with polystyrene, is heated, and the temperature recorded continuously. Then the cylinder must be left to cool down, after which a sample of known mass and volume is placed inside it. The cylinder containing sample is again thermally insulated with polystyrene and heated over the same time interval as the reference measurement. Electrical heating power must be adjusted, so that the temperature increase is as similar as possible to the one recorded during reference measurement. Again the temperature increase is recorded. From the known mass and volume of the sample and the information about the difference between temperature increase in empty golden cylinder and the one containing sample, c_p can be calculated.

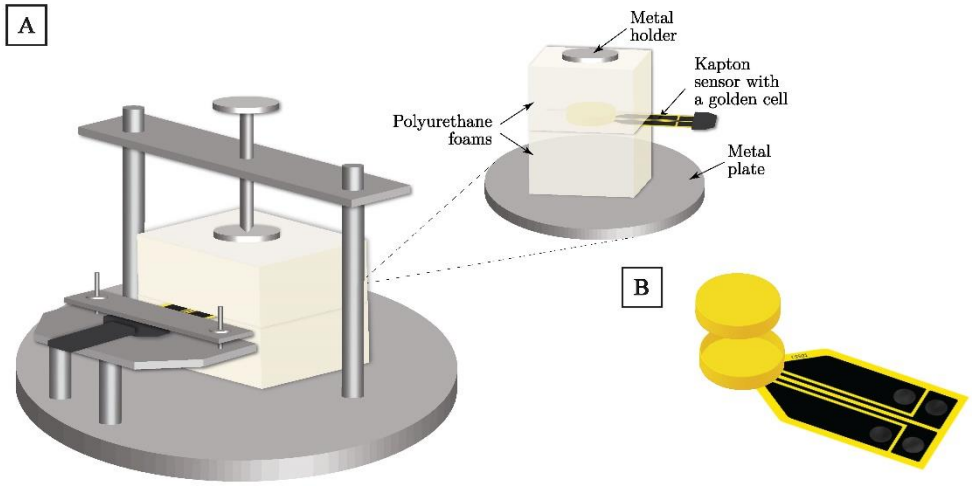

Figure A.14: A) Illustration of the hot disk measurement setup for the determination of specific heat capacity. B) Schematic of a cell-sensor for the determination of material's specific heat capacity.

A.6 Permeability

Permeability is a property that defines the easiness with which a fluid can flow under pressure gradient through the pores in a material [196]. Permeability is of great importance in porous ceramics, especially if the material is to be used in (gas)filtration, or as membranes where larger pressure drops should be prevented [252], [317].

In order to pass a fluid through a material, the latter has to possess a suitable number of pore channels. Thus permeability is mainly a function of material porosity and shape and size of pores [252]. Among porous materials, the ones with aligned pore channels, running unidirectionally throughout the entire material, usually exhibit the highest permeability [317].

Darcy's law, discovered in the middle of the 19th century, was the first equation to describe the flow of a fluid through a porous media. From it Eq. (A.8) for the determination of permeability (for compressible fluids) can be derived: [196], [252]

$$\frac{p_i^2 - p_0^2}{2p \cdot L} = \frac{\eta}{k_1} \cdot \left(\frac{Q}{S}\right) = \frac{\eta}{k_1} \cdot v_s \tag{A.8}$$

where p_i and p_0 are the inlet and outlet fluid pressures, respectively. η is the fluid's viscosity, Q the volumetric air flow rate at the sample exit and S is the cross-sectional area normal to the flow. The quotient between Q and S is the fluid's superficial velocity v_s. L is the

thickness of the material, p is the fluid's pressure at which μ and v_s are determined (usually it is the same as p_i or p_o) and k_1 the Darcian permeability.

According to Eq. (A.8), the flow velocity is linearly proportional to the decrease of pressure [252]. Yet the latter equation was derived from results of experiments conducted at low flow velocities, where the pressure drop (the left side of Equation A.8) is almost entirely the consequence of viscous effects. Viscous effects occur due to the friction between fluid layers and the pore walls [252], [318], and are defined by constant k_1 [252]. However, if the velocity of a fluid is increased, the flow velocity and the pressure drop are no longer in linear dependence and deviations from Darcy's law occur [252].

Forchheimer noticed that at high flow velocities, when the flow changes from laminar to turbulent, the relationship between pressure and velocity drop is a parabolic function [319]. Hence he proposed a modified version of Eq. (A.8):

$$\frac{p_i^2 - p_o^2}{2p \cdot L} = \frac{\eta}{k_1} \cdot \left(\frac{Q}{S}\right) + \frac{\rho}{k_2} \cdot \left(\frac{Q}{S}\right)^2 = \frac{\eta}{k_1} \cdot v_s + \frac{\rho}{k_2} \cdot v_s^2 \tag{A.9}$$

where ρ is the density of a compressible fluid and k_2 the non-Darcian permeability [320].

The Forchheimer equation takes into consideration that the pressure loss occurs due to the viscous (k_1) and the inertial effects [252]. The latter is described by the non-Darcian permeability k_2. The non-linear behavior observed by Forchheimer is the consequence of the contribution of inertial effects which arise at higher fluid velocities [321]. Inertial effects occur when fluid flow is disturbed and changes direction, for example when the pore structure is tortuous (the pore channels have many turns) [196].

The main limitation of Darcy's law is hence that the reliable permeability values are only obtained at low flow velocity when the flow is laminar [319]. On the other hand, the Forchheimer's equation enables the determination of permeability in a wider range of fluid's velocities and for turbulent flows [320]. Still, due to its simplicity, Darcy's law is still widely used, especially for measurements conducted at low pressures [252].

It should be noted that the form of Equations (A.8) and (A.9) only applies for compressible fluids, like air. The expressions on the left side of both equations have to be modified in the case an incompressible fluid is used for conducting the experiments [318]. Unlike incompressible fluids (liquids), compressible fluids (gases) expand during flow through a porous material. The velocity of fluid exiting the material is therefore higher than the velocity at material's entrance. Consequently, the pressure profile of liquids and gases differs and modifications of Eq. (A.8) and Eq. (A.9) are needed in order to account for the different flow behavior [196].

Experimentally the permeability is determined in a test where a fluid is forced to flow through a porous material [196]. A sample, which is mostly in the shape of a cylinder or disk of thickness L and exposed surface area S, is sealed between two chambers as illustrated in Figure A.14. The inlet (p_i) and outlet (p_o) pressures and volumetric flow rate (Q) are measured. The superficial fluid velocity can be determined by dividing the flow rate with the exposed surface area (v_s= Q/S) [196].

After the results are obtained, the pressure drop is plotted against fluid's velocity. If the relationship is linear, Darcy's model is used, and if the dependence follows a parabolic curve, the Forchheimer's equation should be implemented. In the latter case, the data should be fitted by the least-square method to a parabolic function $y = ax + bx^2$, where y is $(p_i^2 - p_o^2)/2pL$ (for compressible fluids), and x the v_s. Parameters a and b are the Darcian and non-Darcian permeability, respectively, and are calculated from the fitted curve [196].

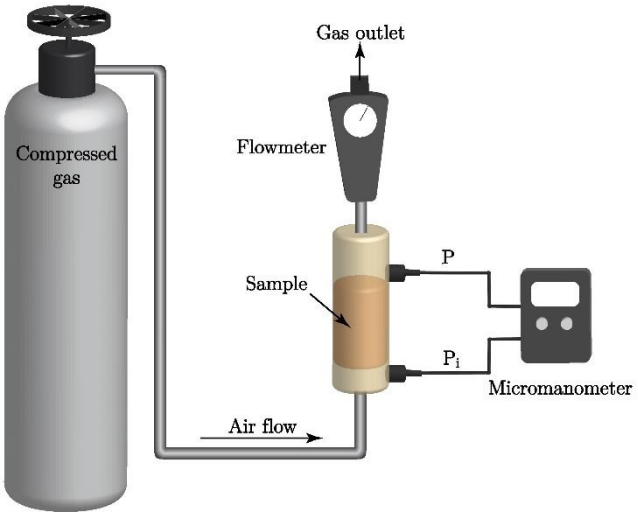

Figure A.15: Illustration of a basic permeability test set-up. The depicted set-up is for gas permeability testing.

Permeability tests can be performed in several different set-ups, with Figure A.15 illustrating one of the simplest, most commonly used set-ups for the characterization of ceramic foams [196], [322]. Naturally the most appropriate test configuration depends on the properties of the material tested.

A.7 X-Ray Microtomography

X-ray microtomography is a non-destructive imaging technique used for obtaining 3D images of materials. The combination of X-ray scanning and data processing enables reconstruction of the internal structure. The technique's formal name is actually electronic computed X-ray tomography, but it is more commonly known as computed tomography (CT) [278]. In the past, CT has been mostly used in medicine, where the resolution of 300 µm was sufficient. On the other hand, for material science much higher resolutions are needed, so this technique was not suitable until the emergence of the third generation of synchrotron radiation facilities. Then the resolutions could be pushed to the micrometer level, and it was possible to routinely obtain resolutions as low as 1 µm [278], [323]. When the resolution is lower than 20 µm, we are talking about micro computed tomography (µ–CT) [324].

Today µ–CT enables characterization of microstructural features, such as pores and cracks, and detection of other phases [323]. It is especially useful in the characterization of porous materials [324], where parameters like porosity, pore shape, average pore size and pore interconnectivity can be estimated from the reconstructed 3D images [278]. µ–CT is also very useful for the evaluation of the impact of deformation on pore structure. For example, individual µ–CT images of the internal structure of highly porous materials, e.g., foams, can be recorded prior, during and after the compression test. Resulting images show how the pore structure changes under externally applied forces [278][325].

There is a variety of different setups, yet they all include a source of X-rays, a rotating platform on which the sample is fixed, an X-ray detector and a computer to process the obtained data and to show the reconstructed images [278], [323], [324]. The basic principle of X-ray tomography is layer-by-layer scanning of a material. X-rays transmitted through different layers are recorded by X-ray detector, converted into digital image recordings.

Then with the help of computer processing, images of individual layers are configured into a 3D image [278].

A μ–CT image consists of a number of pixels in different shades of gray. The pixel's shade indicates the X-ray absorption coefficient. The darker the shade, the lower the absorption in this area, while brighter shades represent parts with high absorption. The pores and other low density areas are dark, with the high density areas such as pore walls represented by the whiter shades [278].

A.8 Fourier-Transform Infrared Spectroscopy

Infrared (IR) spectroscopy is a study of interaction between material and infrared light. Infrared light has a wide range of wavelengths. Between wavenumbers 14000 and 4000 cm^{-1} is the near IR light spectrum, 4000 and 400 cm^{-1} is the mid IR and from 400 to 4 cm^{-1} the far IR spectrum. The majority of the molecules have a strong absorbance especially in the mid IR region, which is why these wavelengths are the most commonly used in IR spectroscopy.

Absorbance at a specific wavelength ($A(\lambda)$) is calculated from the intensity of the background spectrum (I_0) and the intensity of the sample spectrum (I) according to the following Equation (A.10):

$$A(\lambda) = log\left(\frac{I_0}{I}\right) \tag{A.10}$$

In absorbance spectrum, absorbance is plotted as a function of wavenumbers. The latter appear in a descending trend from the left to the right side of the x-axis. In such spectrum the bands point upwards and the topmost point denotes their wavenumber. Instead of the absorbance, percent transmittance (%T) can also be plotted on the y-axis. %T is a measure for the amount of light that was transmitted by the sample. It is calculated by Equation (A.11):

$$\%T = 100 \cdot \left(\frac{I}{I_0}\right) \tag{A.11}$$

Unlike in the absorbance spectrum, the bands in %T spectrum point downwards and the lowest point of the band determines the wavelength. For the identification of unknown samples either absorbance or %T spectrum can be used, with the decision between the two being almost entirely a matter of personal preferences.

Absorbance spectrum can also be used for quantitative analysis. Concentration of individual components in the sample can be determined, since the area of a band is proportional to its concentration. In order to perform quantitative analysis, first a number of samples with known concentrations must be measured to prepare a calibration line relating absorbance to concentration [83]. The concentration can then be calculated from Equation (A.12), known as the Beer's Law:

$$A(\lambda) = \varepsilon(\lambda) \cdot l \cdot c \tag{A.12}$$

where $A(\lambda)$ and $\varepsilon(\lambda)$ are the absorbance and the absorptivity at some specific wavelength, respectively, l the path length and c the concentration.

An absorbance spectrum can be used for both, quantitative and qualitative analysis. The transmittance spectrum is on the other hand only suitable for qualitative analysis, since the size of transmittance bands is not linearly proportional to concentration [83].

The wide use of IR is mainly due to its simplicity, relatively inexpensive equipment, short analysis times and good sensitivity. Additional advantage is the strong absorbance, especially in mid IR spectrum [83]. Among the most widely used is the Fourier-transform infrared (FTIR) spectroscopy, which is a variation of IR spectroscopy using a mathematical function known as Fourier transformation to convert the raw data into a spectrum [83].

There are some limitations of IR spectroscopy. The main issue represents characterization of samples consisting of a number of different molecules. The more complex the sample, the more difficult it is to ascribe individual bands to a specific molecule in order to identify it. Another disadvantage is that a chemical species without bond vibrations (such as noble gases, monatomic ions, homonuclear diatomic molecules, e.g., nitrogen and oxygen) will not produce an infrared spectrum. Also the IR spectroscopy is very sensitive to the presence of water. Even in small quantities its broad and intense absorption bands conceal the majority of the bands indicative of other molecules present in the sample [83].

Analysis of infrared spectrum provides a lot of information about the molecular composition of sample. Bands positions are indicative of the molecular structure. Almost every chemical bond/functional group absorbs IR light of different wavelengths, where the absorption bands then appear [240]. The majority of chemical bonds will produce multiple bands at different wavelengths after the absorption of IR radiation, since there are several possible vibration modes [326]. The number of different vibrational modes increases with complexity of the molecule in question. For each possible vibration mode, a band at a specific wavelength will appear. A specific vibration requires a specific amount of energy, provided by absorption of IR radiation of specific wavelength. Vibration modes are divided into two main groups, namely bond stretching and bond bending (Figure A.16) [326].

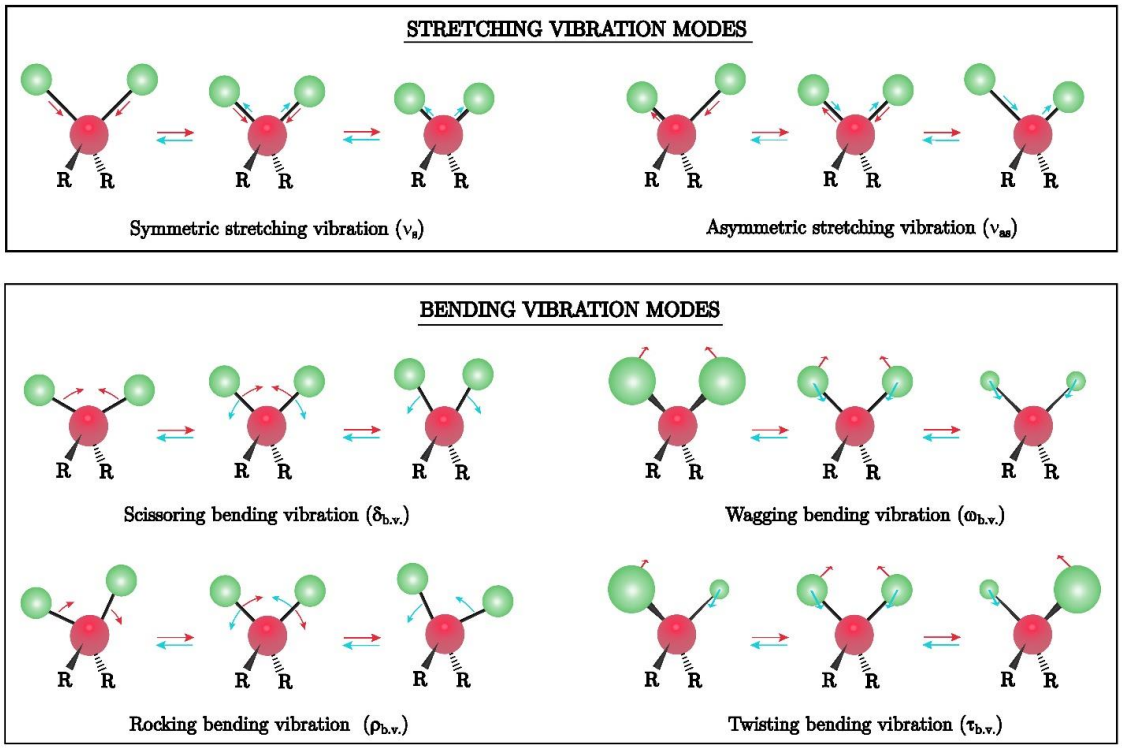

Figure A.16: Schematic representation of bond vibration modes in a tetravalent atom (e.g., R_2CH_2).

In the stretching mode, only the bond length is changed and this change can be either symmetrical (ν_s) or asymmetrical (ν_{as}). In the former mode, two (or more) bonds stretch out and contract at the same time. If the stretching is asymmetrical then while one bond stretches, the other gets shorter. On the other hand, in the bond bending vibrations, the angle between two bonds changes. There are four main types of bond bending, namely scissoring ($\delta_{b.v.}$), rocking ($\rho_{b.v.}$), wagging ($\omega_{b.v.}$) and twisting ($\tau_{b.v.}$) deformation. In scissoring vibration, two atoms move towards and away from each other. In rocking vibration, on the other hand, two atoms move simultaneously in two directions, like a pendulum. These two types of vibration are also known as in-plane deformations or bending modes [242]. In wagging and twisting, the two atoms move out of the plane in which the bonds are located. These two types of bending are also known as out-of-plate deformations. In wagging, both atoms move out or behind the plane simultaneously. In twisting mode, one atom moves out of the plane, while the other simultaneously moves behind the bond plane.

A.9 Compressive Strength

Strength is a measure of the amount of load a material can withstand before failure [327] and is one of key material properties. If the strength is not sufficiently high, other material's properties are irrelevant, since the material cannot be used in practically any application [328]. Depending on the loading type, four main strengths are defined: compressive, tensile, bending and shear [328].

Compressive strength is determined in compression tests, where the most simple is a uniaxial compression test (Figure A.17) [329]. Yet in order to perform a valid compression test special care must be taken to ensure compression is not encompassed by shear [330]. Occurrence of shearing can be minimized by planar compression, where the load is applied only in downward direction. For such tests the sample must have a smooth surface. The presence of any bumps or dents would lead to a non-uniformly distributed stress across material's surface and consequently the results would not reflect the true compressive properties [330].

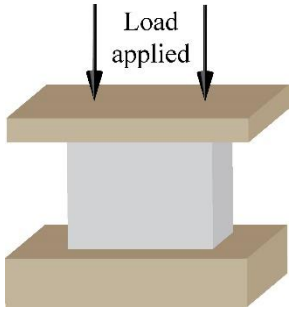

Figure A.17: Illustration of an uniaxial compression test setup.

As a result of a compression test, a stress-strain curve is obtained. In compressive testing the stress (σ) occurs as a consequence of applied load (force) and is defined as the ratio between the load (force) applied (F) and the contact surface area of the sample (A) as presented in Eq. (A.13): [331]

$$\sigma = \frac{F}{A} \tag{A.13}$$

Strain on the other hand is a measure of deformation caused by the applied load and is expressed by Eq. (A.14):

$$\varepsilon = \frac{X}{l} \tag{A.14}$$

where ε is the strain, X the decrease in the sample length due to compression and l the original sample length. Strain is dimensionless and could be elastic or plastic. The former denotes a reversible deformation, where after the load is removed, the sample returns to its original shape. On the other hand, if the strain is plastic, the deformation is permanent [328].

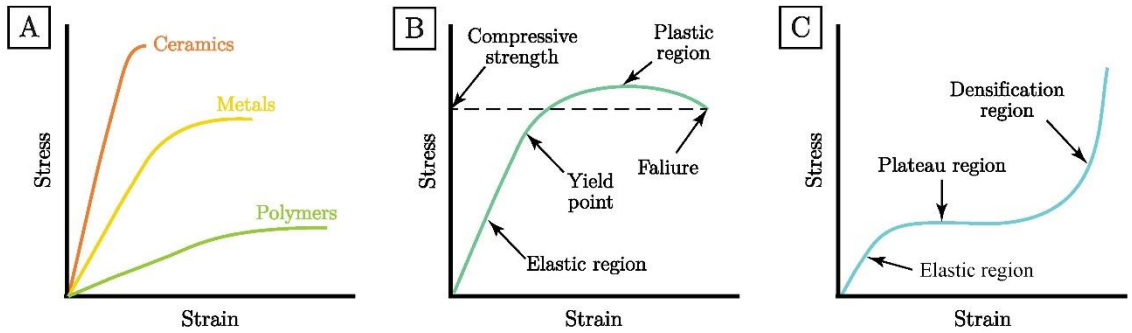

Figure A.18: A) Compression strain-stress curves for different types of material. B) Typical regions of a compression stress-strain curve. C) Compression stress-strain curve of a porous material.

The shape of the stress-strain curve obtained by compression tests depends on the type of material. Typical curve shapes for ceramic, metal and polymer with a detailed description of stress-strain curve segments can be seen in Figures A.18A and A.18B, respectively. Regardless of the material's type there are some similarities in the shape of stress-strain curves. Initial part of the graph is always linear, where the stress and strain are proportional. In this section, the deformation is elastic. Also for all types the yield point marks the end of elastic region, where the strain becomes plastic and the deformation permanent. The end of the stress-strain curve is the point of failure, where the material can no longer withstand the load and breaks. This point determines the compressive strength of a given material. Although the stress-strain relationship is linear for all material types at lower strains, there are big differences in the lines slope, pointing to big differences in compressive properties. For example, ceramics have a much higher yield point than polymers, yet unlike in polymers the plastic region in ceramics is virtually non-existent (Figure A.18A).

In the linear region, Hooke's law may be applied to determine Young's modulus or modulus of elasticity (E). The latter is a measure of the extent of strain that arises due to a given stress, as defined by Eq. (A.15) [328]:

$$E = \frac{\sigma}{\varepsilon} \tag{A.15}$$

When Eq. (A.13) and (A.14) are inserted into Eq. (A.15), the Young's modulus can be calculated by Equation (A.16):

$$E = \frac{F \cdot X}{A \cdot l} \tag{A.16}$$

The curves in Figure A.18A are characteristic for the non-porous materials. For porous material however, the shape of the stress-strain curve is different [327], as can be seen in Figure A.18C. The degree of porosity, pore shape and pore size as well as their spatial distribution have a great influence not only on the strength of material but also on the

slope of the linear part in the stress-strain curve. Through the latter also the Young's modulus is affected [257], [332]. When porous materials like foams are compressed, three characteristic regions in the stress-strain curve can be observed. The shape is similar in all types of materials and also their composites [256], [257], [333], [334]. Like in dense materials the dependence between stress and strain is firstly linear until reaching a yield point. The linear (elastic) region is in majority limited to small strains of 5 % or less [333]. The deformation in this region mostly manifests as an elastic bending of pore walls [257]. After the yield point is reached, a plateau zone starts, where the stress is more or less constant. The plateau zone is a manifestation of the pore walls collapse [257], [333]. The length of constant-stress zone depends on the degree of porosity, where a material with high porosity exhibits a longer and a more flat plateau than a less porous material [334]. The third part of the curve is a densification region, where the pore walls crush together [333]. In this region, the stress increases abruptly with small increases in the strain.

References

[1] G. M. Gladysz and K. K. Chawla, *Voids in Materials*. Amsterdam: Elsevier, 2015.

[2] D. J. Green and P. Colombo, "Cellular ceramics: Intriguing structures, novel properties, and innovative applications," *MRS Bull.*, vol. 28, no. 4, pp. 296–300, 2003.

[3] J. Rouquerol *et al.*, "Recommendtions for the Characterization of Porous Solids," *Pure Appl. Chem*, vol. 66, no. 8, pp. 1739–1758, 1994.

[4] J. Rouquerol *et al.*, "Liquid intrusion and alternative methods for the characterization of macroporous materials (IUPAC Technical Report)," *Pure Appl. Chem.*, vol. 84, no. 1, pp. 107–136, 2012.

[5] D. J. Green, "Porous Ceramic Processing," in *Encyclopedia of Materials: Science and Technology*, K.H. Jürgen Buschow, R. W. Cahn, M. C. Flemings, B. Ilschner, E. J. Kramer, S. Mahajan, and P. Veyssière, Eds. Oxford: Elsevier, 2001, pp. 7758–7761.

[6] P. S. Liu and G. F. Chen, "Fabricating Porous Ceramics," in *Porous Materials*, Oxford: Elsevier, 2014, pp. 221–302.

[7] M. Scheffler and P. Colombo, Eds., *Cellular Ceramics: Structure, Manufacturing, Properties and Applications*. Weinheim: Wiley-VCH, 2005.

[8] T. Ohji and M. Fukushima, "Macro-porous ceramics: processing and properties," *Int. Mater. Rev.*, vol. 57, no. 2, pp. 115–131, 2012.

[9] P. Colombo, "Conventional and novel processing methods for cellular ceramics," *Philos. Trans. R. Soc. A*, vol. 364, pp. 109–124, Jan. 2006.

[10] P. Colombo, "Ceramic Foams: Fabrication, Properties and Applications," *Key Eng. Mater.*, vol. 206–213, pp. 1913–1918, Dec. 2001.

[11] S. Deville, "Properties and Applications of Ice-Templated Materials," in *Freezing Colloids: Observations, Principles, Control, and Use*, Cham: Springer International Publishing, 2017, pp. 439–548.

[12] G. M. Gladysz and K. K. Chawla, "Cellular Materials," in *Voids in materials: From unavoidable defects to designed cellular materials*, Amsterdam: Elsevier, 2015, pp. 103–130.

[13] S. Barg, C. Soltmann, M. Andrade, D. Koch, and G. Grathwohl, "Cellular Ceramics by Direct Foaming of Emulsified Ceramic Powder Suspensions," *J. Am. Ceram. Soc.*, vol. 91, no. 9, pp. 2823–2829, 2008.

[14] T. Tomita, S. Kawasaki, and K. Okada, "Effect of Viscosity on Preparation of Foamed Silica Ceramics by a Rapid Gelation Foaming Method," *J. Porous Mater.*, vol. 12, pp. 123–129, 2005.

[15] S. Barg, D. Koch, and G. Grathwohl, "Processing and Properties of Graded Ceramic Filters," *J. Am. Ceram. Soc.*, vol. 92, no. 12, pp. 2854–2860, 2009.

[16] W. L. Li, K. Lu, and J. Y. Walz, "Freeze casting of porous materials: review of critical factors in microstructure evolution," *Int. Mater. Rev.*, vol. 57, no. 1, pp. 37–60, Jan. 2012.

[17] K. L. Scotti and D. C. Dunand, "Freeze casting – A review of processing, microstructure and properties via the open data repository," *Prog. Mater. Sci.*, vol. 94, pp. 243–305, 2018.

[18] S. Deville, "Freeze-casting of porous ceramics: A review of current achievements and issues," *Adv. Eng. Mater.*, vol. 10, no. 3, pp. 155–169, 2008.

[19] B. Wicklein *et al.*, "Thermally insulating and fire-retardant lightweight anisotropic foams based on nanocellulose and graphene oxide," *Nat. Nanotechnol.*, vol. 10, no. 3, pp. 277–283, 2015.

[20] H. Hudelja, T. Konegger, B. Wicklein, J. Čretnik, F. Akhtar, and A. Kocjan, "Freeze-casting of highly porous cellulose-nanofiber-reinforced γ-Al2O3 monoliths," *Open Ceram.*, vol. 5, p. 100069, 2021.

[21] H. Tamon, T. Akatsuka, H. Mori, and N. Sano, "Synthesis of Zeolite Monolith with Hierarchical Micro/Macropores by Ice-Templating and Steam-Assisted Crystallization," *Chem. Eng. Trans.*, vol. 32, pp. 2059–2064, 2013.

[22] A. Ojuva, F. Akhtar, A. P. Tomsia, and L. Bergström, "Laminated adsorbents with very rapid CO2 uptake by freeze-casting of zeolites," *ACS Appl. Mater. Interfaces*, vol. 5, no. 7, pp. 2669–2676, 2013.

[23] J. Dhainaut, S. Deville, I. Amirouche, and M. Klotz, "A Reliable Method for the Preparation of Multiporous Alumina Monoliths by Ice-Templating," *Inorganics*, vol. 4, no. 1, p. 6, 2016.

[24] S. R. Mukai, H. Nishihara, and H. Tamon, "Formation of monolithic silica gel microhoneycombs (SMHs) using pseudosteady state growth of microstructural ice crystals," *Chem. Commun.*, vol. 4, no. 7, pp. 874–875, 2004.

[25] S. Deville, *Ice-Templating: Processing Routes, Architectures, and Microstructures.* Cham: Springer International Publishing, 2017.

[26] S. Yunoki *et al.*, "Control of pore structure and mechanical property in hydroxyapatite/collagen composite using unidirectional ice growth," *Mater. Lett.*, vol. 60, no. 8, pp. 999–1002, Apr. 2006.

[27] S. Deville, E. Saiz, and A. P. Tomsia, "Ice-templated porous alumina structures," *Acta Mater.*, vol. 55, no. 6, pp. 1965–1974, 2007.

[28] J. Verma, M. Vijayakumar, and R. Mitra, "Processing and microstructure of freeze-cast silica foams," *Mater. Lett.*, vol. 153, pp. 168–170, Aug. 2015.

[29] K. K. Mallick and J. Winnett, "Preparation and Characterization of Porous Bioglass® and PLLA Scaffolds for Tissue Engineering Applications," *J. Am. Ceram. Soc.*, vol. 95, no. 9, pp. 2680–2686, 2012.

[30] Q. Fu, M. N. Rahaman, B. S. Bal, and R. F. Brown, "Proliferation and function of MC3T3-E1 cells on freeze-cast hydroxyapatite scaffolds with oriented pore architectures," *J. Mater. Sci. Mater. Med.*, vol. 20, no. 5, pp. 1159–1165, 2009.

[31] M. N. Rahaman and Q. Fu, "Manipulation of porous bioceramic microstructures by freezing of suspensions containing binary mixtures of solvents," *J. Am. Ceram. Soc.*, vol. 91, no. 12, pp. 4137–4140, 2008.

[32] K. S. Kamyshnaya and T. A. Khabas, "Developing porous ceramics on the base of zirconia oxide with thin and permeable pores by crystallization of organic additive method," *IOP Conf. Ser. Mater. Sci. Eng.*, vol. 156, no. 1, 2016.

[33] S. M. Miller, X. Xiao, and K. T. Faber, "Freeze-cast alumina pore networks: Effects of freezing conditions and dispersion medium," *J. Eur. Ceram. Soc.*, vol. 35, no. 13, pp. 3595–3605, 2015.

[34] S. Flauder, U. Gbureck, and F. A. Müller, "Structure and mechanical properties of β-TCP scaffolds prepared by ice-templating with preset ice front velocities," *Acta Biomater.*, vol. 10, no. 12, pp. 5148–5155, 2014.

[35] S. M. H. Ghazanfari and A. Zamanian, "Phase transformation, microstructural and mechanical properties of hydroxyapatite/alumina nanocomposite scaffolds produced by freeze casting," *Ceram. Int.*, vol. 39, no. 8, pp. 9835–9844, Dec. 2013.

[36] X. Liu, M. N. Rahaman, and Q. Fu, "Oriented bioactive glass (13-93) scaffolds with controllable pore size by unidirectional freezing of camphene-based suspensions: Microstructure and mechanical response," *Acta Biomater.*, vol. 7, no. 1, pp. 406–416, 2011.

[37] F. C. Technique, "Porous Ceramic Bodies with Interconnected Pore Channels by a Novel Freeze Casting Technique," *J. Am. Ceram. Soc.*, vol. 88, no. 5, pp. 1108–1114, 2005.

[38] J. Han, C. Hong, X. Zhang, J. Du, and W. Zhang, "Highly porous ZrO2 ceramics fabricated by a camphene-based freeze-casting route: Microstructure and properties," *J. Eur. Ceram. Soc.*, vol. 30, no. 1, pp. 53–60, Jan. 2010.

[39] Y. Koh, J. Song, E. Lee, and H. Kim, "Freezing Dilute Ceramic/Camphene Slurry for Ultra-High Porosity Ceramics with Completely Interconnected Pore Networks," *J. Am. Ceram. Soc.*, vol. 89, no. 10, pp. 3089–3093, 2006.

[40] A. Macchetta, I. G. Turner, and C. R. Bowen, "Fabrication of HA/TCP scaffolds with a graded and porous structure using a camphene-based freeze-casting method," *Acta Biomater.*, vol. 5, no. 4, pp. 1319–1327, May 2009.

[41] T. Y. Yang, H. B. Ji, S. Y. Yoon, B. K. Kim, and H. C. Park, "Porous mullite composite with controlled pore structure processed using a freeze casting of TBA-based coal fly ash slurries," *Resour. Conserv. Recycl.*, vol. 54, no. 11, pp. 816–820, 2010.

[42] H. J. Choi, T. Y. Yang, S. Y. Yoon, B. K. Kim, and H. C. Park, "Porous alumina/zirconia layered composites with unidirectional pore channels processed using a tertiary-butyl alcohol-based freeze casting," *Mater. Chem. Phys.*, vol. 133, no. 1, pp. 16–20, 2012.

[43] T. Xu and C.-A. Wang, "Control of pore size and wall thickness of 3-1 type porous PZT ceramics during freeze-casting process," *Mater. Des.*, vol. 91, pp. 242–247, Feb. 2016.

[44] D. Ghosh, N. Dhavale, M. Banda, and H. Kang, "A comparison of microstructure and uniaxial compressive response of ice-templated alumina scaffolds fabricated from two different particle sizes," *Ceram. Int.*, vol. 42, no. 14, pp. 16138–16147, 2016.

[45] Y. Zou, C. Gaudillere, J. E. Escribano, J. M. Serra, and J. Malzbender, "Microstructure, mechanical behavior and flow resistance of freeze-cast porous 3YSZ substrates for membrane applications," *J. Eur. Ceram. Soc.*, vol. 37, no. 9, pp. 3167–3176, 2017.

[46] S. Deville *et al.*, "Ice Shaping Properties, Similar to That of Antifreeze Proteins, of a Zirconium Acetate Complex," *PLoS One*, vol. 6, no. 10, p. e26474, Oct. 2011.

[47] M. K. Lee, N.-O. Chung, and J. Lee, "Membranes with through-thickness porosity prepared by unidirectional freezing," *Polymer (Guildf).*, vol. 51, no. 26, pp. 6258–6267, Dec. 2010.

[48] H. Lu, C. Li, B. Zhang, X. Qiao, and C. Y. Liu, "Toward highly compressible graphene aerogels of enhanced mechanical performance with polymer," *RSC Adv.*, vol. 6, no. 49, pp. 43007–43015, 2016.

[49] M. Fukushima, M. Nakata, Y. Zhou, T. Ohji, and Y. Yoshizawa, "Fabrication and properties of ultra highly porous silicon carbide by the gelation-freezing method," *J. Eur. Ceram. Soc.*, vol. 30, no. 14, pp. 2889–2896, 2010.

[50] M. Fukushima and Y. I. Yoshizawa, "Fabrication and morphology control of highly porous mullite thermal insulators prepared by gelation freezing route," *J. Eur. Ceram. Soc.*, vol. 36, no. 12, pp. 2947–2953, 2016.

[51] S. Deville, "Ice-templating, freeze casting: Beyond materials processing," *J. Mater. Res.*, vol. 28, no. 17, pp. 2202–2219, 2013.

[52] S. Deville, E. Saiz, and A. P. Tomsia, "Freeze casting of hydroxyapatite scaffolds for bone tissue engineering," *Biomaterials*, vol. 27, no. 32, pp. 5480–5489, 2006.

[53] T. Waschkies, R. Oberacker, and M. J. Hoffmann, "Control of Lamellae Spacing During Freeze Casting of Ceramics Using Double-Side Cooling as a Novel Processing Route," *J. Am. Ceram. Soc.*, vol. 92, no. S1, pp. S79–S84, Jan. 2009.

[54] D. J. Shaw, *Introduction to colloid and surface chemistry*. Oxford: Butterworth-Heinemann, 1992.

[55] A. Pettersson, G. Marino, A. Pursiheimo, and J. B. Rosenholm, "Electrosteric Stabilization of Al2O3, ZrO2, and 3Y–ZrO2 Suspensions: Effect of Dissociation and Type of Polyelectrolyte," *J. Colloid Interface Sci.*, vol. 228, no. 1, pp. 73–81, Aug. 2000.

[56] R. J. Pugh, "Dispersion and Stability of Ceramic Powders in Liquids," in *Surface and colloid chemistry in advanced ceramics processing*, R. J. Pugh and L. Bergström, Eds. Boca Raton: CRC Press, 1994, pp. 127–192.

[57] T. Tadros, "General Principles of Colloid Stability and the Role of Surface Forces," in *Colloid Stability*, vol. 1, Weinheim, Germany: Wiley-VCH Verlag GmbH & Co. KGaA, 2014, pp. 1–22.

[58] B. P. Singh, S. Bhattacharjee, L. Besra, and D. K. Sengupta, "Evaluation of dispersibility of aqueous alumina suspension in presence of Darvan C," *Ceram. Int.*, vol. 30, no. 6, pp. 939–946, 2004.

[59] J. A. Lewis, "Colloidal processing of ceramics," *Adv. Appl. Ceram.*, vol. 83, no. 10, pp. 246–253, 2012.

[60] T. F. Tadros, "Correlation of viscoelastic properties of stable and flocculated suspensions with their interparticle interactions," *Adv. Colloid Interface Sci.*, vol. 68, pp. 97–200, Nov. 1996.

[61] B. Dobiáš, "Electrical phenomena at the solid-liquid interface," in *Solid-Liquid Dispersions (Surfactant science series)*, M. J. Schick and A. T. Hubbard, Eds. Boca Raton: CRC Press, 1999, pp. 157–205.

[62] T. Bakarič, *Processing of porous Pb(Zr0.53Ti0.47)O3 ceramics with a designed microstructure and patterning of thick films by inkjet printing.* Jožef Stefan International Postgraduate School, Ljubljana, Slovenia, 2016.

[63] L. Bergström, "Surface Characterization of Ceramic Powders," in *Surface and Colloid Chemistry in Advanced Ceramics Processing*, R. J. Pugh and L. Bergström, Eds. Boca Raton: CRC Press, 1994, pp. 70–125.

[64] J. N. Israelachvili, "Electrostatic Forces between Surfaces in Liquids," in *Intermolecular and Surface Forces*, J. N. Israelachvili, Ed. Waltham: Academic Press, 2011, pp. 291–339.

[65] J. Lyklema, "Molecular interpretation of electrokinetic potentials," *Curr. Opin. Colloid Interface Sci.*, vol. 15, no. 3, pp. 125–130, 2010.

[66] A. V. Delgado, F. Gonzalez-Caballero, R. J. Hunter, L. K. Koopal, and J. Lyklema, "Measurement and interpretation of electrokinetic phenomena," *J. Colloid Interface Sci.*, vol. 309, no. 2, pp. 194–224, 2007.

[67] S. Bhattacharjee, "DLS and zeta potential – What they are and what they are not?," *J. Control. Release*, vol. 235, pp. 337–351, Aug. 2016.

[68] A. Kumar and C. K. Dixit, "Methods for characterization of nanoparticles," in *Advances in Nanomedicine for the Delivery of Therapeutic Nucleic Acids*, S. Nimesh, R. Chandra, and N. Gupta, Eds. Cambridge: Woodhead Publishing, 2017, pp. 44–58.

[69] T. Tadros, "Interparticle interactions in concentrated suspensions and their bulk (Rheological) properties," *Adv. Colloid Interface Sci.*, vol. 168, no. 1–2, pp. 263–277, Oct. 2011.

[70] T. F. Tadros, "Electrokinetic Phenomena and Zeta Potential," in *Dispersion of Powders in Liquids and Stabilization of Suspensions*, Weinheim: Wiley, 2012, pp. 63–84.

[71] B. P. Singh, R. Menchavez, C. Takai, M. Fuji, and M. Takahashi, "Stability of dispersions of colloidal alumina particles in aqueous suspensions," *J. Colloid Interface Sci.*, vol. 291, no. 1, pp. 181–186, Nov. 2005.

[72] J. Davies and J. G. P. Binner, "The role of ammonium polyacrylate in dispersing concentrated alumina suspensions," *J. Eur. Ceram. Soc.*, vol. 20, no. 10, pp. 1539–1553, 2000.

[73] K. K. Das and P. Somasundaran, "A kinetic investigation of the flocculation of alumina with polyacrylic acid," *J. Colloid Interface Sci.*, vol. 271, no. 1, pp. 102–109, 2004.

[74] J. Cesarano and I. A. Aksay, "Processing of Highly Concentrated Aqueous alpha-Alumina Suspensions Stabilized with Polyelectrolytes," *J. Am. Ceram. Soc.*, vol. 71, no. 12, pp. 1062–1067, 1988.

[75] A. Dakskobler, K. Kočevar, and T. Kosmač, "Short-range repulsive potential developed by the addition of Mg(II) ions to aqueous alumina slurries," *J. Eur. Ceram. Soc.*, vol. 21, no. 13, pp. 2361–2368, 2001.

[76] R. J. Nap, S. H. Park, and I. Szleifer, "Competitive calcium ion binding to end-tethered weak polyelectrolytes," *Soft Matter*, vol. 14, no. 12, pp. 2365–2378, 2018.

[77] N. Volk, D. Vollmer, M. Schmidt, W. Oppermann, and K. Huber, "Conformation and Phase Diagrams of Flexible Polyelectrolytes," in *Advances in Polymer Science*, vol. 166, 2004, pp. 29–65.

[78] M. O. de la Cruz, L. Belloni, M. Delsanti, J. P. Dalbiez, O. Spalla, and M. Drifford, "Precipitation of highly charged polyelectrolyte solutions in the presence of multivalent salts," *J. Chem. Phys.*, vol. 103, no. 13, pp. 5781–5791, 1995.

[79] P.-Y. Hsiao and E. Luijten, "Salt-Induced Collapse and Reexpansion of Highly Charged Flexible Polyelectrolytes," *Phys. Rev. Lett.*, vol. 97, no. 14, p. 148301, Oct. 2006.

[80] A. Kocjan and Z. Shen, "Colloidal processing and partial sintering of high-performance porous zirconia nanoceramics with hierarchical heterogeneities," *J. Eur. Ceram. Soc.*, vol. 33, no. 15–16, pp. 3165–3176, Dec. 2013.

[81] A. Dakskobler and T. Kosmač, "Weakly flocculated aqueous alumina suspensions prepared by the addition of Mg(II) ions," *J. Am. Ceram. Soc.*, vol. 83, no. 3, pp. 666–668, 2000.

[82] A. Dakskobler and T. Kosmač, "Destabilisation of an alkaline aqueous alumina suspension by the addition of magnesium acetate," *Colloids Surfaces A Physicochem. Eng. Asp.*, vol. 195, no. 1–3, pp. 197–203, 2001.

[83] K. Vermöhlen, H. Lewandowski, H.-D. Narres, and M. . Schwuger, "Adsorption of polyelectrolytes onto oxides — the influence of ionic strength, molar mass, and Ca2+ ions," *Colloids Surfaces A Physicochem. Eng. Asp.*, vol. 163, no. 1, pp. 45–53, Mar.

2000.

[84] L. Dupont, A. Foissy, R. Mercier, and B. Mottet, "Effect of Calcium Ions on the Adsorption of Polyacrylic Acid onto Alumina," *J. Colloid Interface Sci.*, vol. 161, pp. 445–464, 1993.

[85] J. Sun, L. Bergström, and L. Gao, "Effect of Magnesium Ions on the Adsorption of Poly(acrylic acid) onto Alumina," *J. Am. Ceram. Soc.*, vol. 84, no. 11, pp. 2710–2712, 2001.

[86] I. Michaeli, "Ion binding and the formation of insoluble polymethacrylic salts," *J. Polym. Sci.*, vol. 48, no. 150, pp. 291–299, 1960.

[87] L. Mureşan, P. Sinha, P. Maroni, and M. Borkovec, "Adsorption and surface-induced precipitation of poly(acrylic acid) on calcite revealed with atomic force microscopy," *Colloids Surfaces A Physicochem. Eng. Asp.*, vol. 390, no. 1–3, pp. 225–230, 2011.

[88] M. A. Faers and G. R. Kneebone, "Application of rheological measurements for probing the sedimentation of suspension concentrate formulations," *Pestic. Sci.*, vol. 55, pp. 312–325, 1999.

[89] T. F. Tadros and A. Zsednai, "Application of Depletion Flocculation for Prevention of Formation of Dilatant Sediments," *Colloids and Surfaces*, vol. 43, pp. 105–116, 1990.

[90] R. Buscall, J. W. Goodwin, R. H. Ottewill, and T. F. Tadros, "The Settling of Particles through Newtonian and Non-Newtonian Media," *J. Colloid Interface Sci.*, vol. 85, no. 1, pp. 78–86, 1981.

[91] C.-T. Liao, Y.-F. Wu, W. Chien, J.-R. Huang, and Y.-L. Chen, "Modeling shear-induced particle ordering and deformation in a dense soft particle suspension," *J. Phys. Condens. Matter*, vol. 29, no. 43, p. 435101, Nov. 2017.

[92] D. Klemm *et al.*, "Nanocellulose as a natural source for groundbreaking applications in materials science: Today's state," *Mater. Today*, vol. 21, no. 7, pp. 720–748, 2018.

[93] B. Fan, S. Chen, Q. Yao, Q. Sun, and C. Jin, "Fabrication of cellulose nanofiber/AlOOH aerogel for flame retardant and thermal insulation," *Materials (Basel).*, vol. 10, no. 3, pp. 1–10, 2017.

[94] D. Klemm *et al.*, "Nanocelluloses: A new family of nature-based materials," *Angew. Chemie - Int. Ed.*, vol. 50, no. 24, pp. 5438–5466, 2011.

[95] A. Dufresne, "Nanocellulose: A new ageless bionanomaterial," *Mater. Today*, vol. 16, no. 6, pp. 220–227, 2013.

[96] K. De France, Z. Zeng, T. Wu, and G. Nyström, "Functional Materials from Nanocellulose: Utilizing Structure–Property Relationships in Bottom-Up Fabrication," *Adv. Mater.*, vol. 33, no. 28, p. 2000657, Jul. 2021.

[97] A. E. J. de Nooy, A. C. Besemer, and H. van Bekkum, "On the Use of Stable Organic Nitroxyl Radicals for the Oxidation of Primary and Secondary Alcohols," *Synthesis (Stuttg).*, vol. 10, pp. 1153–1176, 1996.

[98] Ú. Fillat *et al.*, "Assessing cellulose nanofiber production from olive tree pruning residue," *Carbohydr. Polym.*, vol. 179, pp. 252–261, Jan. 2018.

[99] A. Hajian, S. B. Lindström, T. Pettersson, M. M. Hamedi, and L. Wågberg, "Understanding the Dispersive Action of Nanocellulose for Carbon Nanomaterials," *Nano Lett.*, vol. 17, no. 3, pp. 1439–1447, 2017.

[100] Y. Li *et al.*, "Strong transparent magnetic nanopaper prepared by immobilization of Fe3O4 nanoparticles in a nanofibrillated cellulose network," *J. Mater. Chem. A*, vol. 1, no. 48, p. 15278, 2013.

[101] S. Gupta, F. Martoïa, L. Orgéas, and P. Dumont, "Ice-Templated Porous Nanocellulose-Based Materials: Current Progress and Opportunities for Materials Engineering," *Appl. Sci.*, vol. 8, no. 12, p. 2463, Dec. 2018.

[102] X. Zhang, Z. Lu, J. Zhao, Q. Li, W. Zhang, and C. Lu, "Exfoliation/dispersion of low-temperature expandable graphite in nanocellulose matrix by wet co-milling," *Carbohydr. Polym.*, vol. 157, pp. 1434–1441, Feb. 2017.

[103] T.-M. Tenhunen *et al.*, "Enhancing the Stability of Aqueous Dispersions and Foams Comprising Cellulose Nanofibrils (CNF) with CaCO3 Particles," *Nanomaterials*, vol. 8, no. 9, p. 651, Aug. 2018.

[104] A. M. Zhivkov and R. P. Hristov, "Stability of aqueous suspensions of alumina particles with adsorbed (carboxymethyl)cellulose," *Colloids Surfaces A Physicochem. Eng. Asp.*, vol. 529, pp. 523–530, Sep. 2017.

[105] T. Nagaoka, K. Kita, and N. Kondo, "Preparation of alumina ceramics from a slurry with cellulose nanofibers," *J. Ceram. Soc. Japan*, vol. 126, no. 3, pp. 198–201, 2018.

[106] E. Kontturi *et al.*, "Advanced Materials through Assembly of Nanocelluloses," *Adv. Mater.*, vol. 30, no. 24, p. 1703779, Jun. 2018.

[107] R. J. Moon, A. Martini, J. Nairn, J. Simonsen, and J. Youngblood, "Cellulose nanomaterials review: Structure, properties and nanocomposites," *Chem. Soc. Rev.*, vol. 40, no. 7, pp. 3941–3994, 2011.

[108] M. Trueba and S. P. Trasatti, "γ-Alumina as a Support for Catalysts: A Review of Fundamental Aspects," *Eur. J. Inorg. Chem.*, vol. 2005, no. 17, pp. 3393–3403, Sep. 2005.

[109] G. Busca, "The surface of transitional aluminas : A critical review," *Catal. Today*, vol. 226, pp. 2–13, 2014.

[110] A. Kocjan, T. Konegger, and A. Dakskobler, "Hierarchical macroporous-mesoporous gamma-alumina monolithic green bodies with high strength," *J. Mater. Sci.*, vol. 52, no. 19, pp. 11168–11178, 2017.

[111] G. Busca, "Structural, Surface, and Catalytic Properties of Aluminas," in *Advances in Catalysis*, F. C. Jentoft, Ed. London: Academic Press, 2014, pp. 319–404.

[112] L. Liu, S.-Z. Luo, B. Wang, and Z. Guo, "Investigation of small molecular weight poly(acrylic acid) adsorption on γ-alumina," *Appl. Surf. Sci.*, vol. 345, pp. 116–121, 2015.

[113] P. Euzen *et al.*, "Alumina," in *Handbook of Porous Solids*, F. Schüth, K. S. W. Sing, and J. Weitkamp, Eds. Weinheim: Wiley, 2002, pp. 1591–1677.

[114] T. J. Webster, R. W. Siegel, and R. Bizios, "Osteoblast adhesion on nanophase ceramics.," *Biomaterials*, vol. 20, no. 13, pp. 1221–1227, 1999.

[115] Á. Maquieira, E. M. Brun, M. Garcés-García, and R. Puchades, "Aluminum oxide nanoparticles as carriers and adjuvants for eliciting antibodies from non-immunogenic haptens," *Anal. Chem.*, vol. 84, no. 21, pp. 9340–9348, 2012.

[116] Y. Zhao, R. L. Frost, W. N. Martens, and H. Y. Zhu, "Growth and surface properties of boehmite nanofibers and nanotubes at low temperatures using a hydrothermal synthesis route," *Langmuir*, vol. 23, no. 19, pp. 9850–9859, Sep. 2007.

[117] X. Zhang, M. Honkanen, E. Levänen, and T. Mäntylä, "Transition alumina nanoparticles and nanorods from boehmite nanoflakes," *J. Cryst. Growth*, vol. 310, no. 15, pp. 3674–3679, 2008.

[118] S. C. Kuiry, E. Megen, S. D. Patil, S. a Deshpande, and S. Seal, "Solution-based chemical synthesis of boehmite nanofibers and alumina nanorods.," *J. Phys. Chem. B*, vol. 109, no. 9, pp. 3868–3872, 2005.

[119] S. C. Shen *et al.*, "Steam-Assisted Solid Wet-Gel Synthesis of High-Quality Nanorods of Boehmite and Alumina," *J. Phys. Chem. C*, vol. 111, no. 2, pp. 700–707, 2007.

[120] T. He, L. Xiang, and S. Zhu, "Hydrothermal preparation of boehmite nanorods by selective adsorption of sulfate.," *Langmuir*, vol. 24, no. 15, pp. 8284–8289, 2008.

[121] D. H. M. Buchold and C. Feldmann, "Nanoscale gamma-AlO(OH) hollow spheres: synthesis and container-type functionality.," *Nano Lett.*, vol. 7, no. 11, pp. 3489–3492, 2007.

[122] Y. Liu *et al.*, "Hydrothermal synthesis of microscale boehmite and gamma nanoleaves alumina," *Mater. Lett.*, vol. 62, no. 8–9, pp. 1297–1301, Mar. 2008.

[123] W. Cai, J. Yu, S. Gu, and M. Jaroniec, "Facile hydrothermal synthesis of hierarchical boehmite: Sulfate-mediated transformation from nanoflakes to hollow microspheres," *Cryst. Growth Des.*, vol. 10, no. 9, pp. 3977–3982, 2010.

[124] S. Xuan, F. Wang, X. Gong, S.-K. Kong, J. C. Yu, and K. C.-F. Leung, "Hierarchical core/shell Fe3O4@SiO2@γ-AlOOH@Au micro/nanoflowers for protein immobilization," *Chem. Commun.*, vol. 47, no. 9, p. 2514, 2011.

[125] H. Cölfen and M. Antonietti, "Mesocrystals: Inorganic Superstructures Made by Highly Parallel Crystallization and Controlled Alignment," *Angew. Chemie Int. Ed.*, vol. 44, no. 35, pp. 5576–5591, Sep. 2005.

[126] S. Wintzheimer *et al.*, "Supraparticles: Functionality from Uniform Structural Motifs," *ACS Nano*, vol. 12, no. 6, pp. 5093–5120, 2018.

[127] W. Cai, J. Yu, C. Anand, A. Vinu, and M. Jaroniec, "Facile synthesis of ordered mesoporous alumina and alumina-supported metal oxides with tailored adsorption and framework properties," *Chem. Mater.*, vol. 23, no. 5, pp. 1147–1157, 2011.

[128] G. J. B. Voss *et al.*, "Mesostructured alumina as powders and thin films," *J. Mater. Chem. A*, vol. 2, no. 25, pp. 9727–9735, 2014.

[129] C. Pecharromán, A. Esteban-Cubillo, R. Torrecillas, and U. S. Moya, "Micro/nano composites: A simple and safe way to fabricate nanomaterials," *Int. J. Nanotechnol.*, vol. 4, no. 3, pp. 282–297, 2007.

[130] A. B. D. Nandiyanto and K. Okuyama, "Progress in developing spray-drying methods for the production of controlled morphology particles: From the nanometer to submicrometer size ranges," *Adv. Powder Technol.*, vol. 22, no. 1, pp. 1–19, 2011.

[131] L. H. Edelson and A. M. Glaeser, "Role of Particle Substructure in the Sintering of Monosized Titania," *J. Am. Ceram. Soc.*, vol. 71, no. 4, pp. 225–235, Apr. 1988.

[132] S. C. Kuiry, E. Megen, S. D. Patil, S. A. Deshpande, and S. Seal, "Solution-based chemical synthesis of boehmite nanofibers and alumina nanorods," *J. Phys. Chem. B*, vol. 109, no. 9, pp. 3868–3872, 2005.

[133] X. Bokhimi, J. Sánchez-Valente, and F. Pedraza, "Crystallization of sol-gel boehmite via hydrothermal annealing," *J. Solid State Chem.*, vol. 166, no. 1, pp. 182–190, 2002.

[134] X. Bokhimi, A. Morales, and J. S. Valente, "Sulfate ions and boehmite crystallization in a sol made with aluminum tri-sec-butoxide and 2-propanol," *J. Phys. Chem. C*, vol. 111, no. 1, pp. 103–107, 2007.

[135] S. M. Kim, Y. J. Lee, K. W. Jun, J. Y. Park, and H. S. Potdar, "Synthesis of thermo-stable high surface area alumina powder from sol-gel derived boehmite," *Mater. Chem. Phys.*, vol. 104, no. 1, pp. 56–61, 2007.

[136] B. E. Yoldas, "Alumina Sol Preparation From Alkoxides," *Am. Ceram. Soc. Bull.*, vol. 54, no. 3, pp. 289–290, 1975.

[137] F. Vaudry, S. Khodabandeh, and M. E. Davis, "Synthesis of Pure Alumina Mesoporous Materials," *Chem. Mater.*, vol. 8, no. 7, pp. 1451–1464, 1996.

[138] W. Deng, M. W. Toepke, and B. H. Shanks, "Surfactant-assisted synthesis of alumina with hierarchical nanopores," *Adv. Funct. Mater.*, vol. 13, no. 1, pp. 61–65, 2003.

[139] R. W. N. D. Filho, G. De Araujo Rocha, C. R. Montes, and A. C. Vieira-Coelho, "Synthesis and characterization of boehmites obtained from gibbsite in presence of different environments," *Mater. Res.*, vol. 19, no. 3, pp. 659–668, 2016.

[140] Z. Shi, W. Jiao, L. Chen, P. Wu, Y. Wang, and M. He, "Clean synthesis of hierarchically structured boehmite and γ-alumina with a flower-like morphology," *Microporous Mesoporous Mater.*, vol. 224, pp. 253–261, Apr. 2016.

[141] X. Y. Chen, Z. J. Zhang, X. L. Li, and S. W. Lee, "Controlled hydrothermal synthesis of colloidal boehmite (γ-AlOOH) nanorods and nanoflakes and their conversion into γ- Al2O3 nanocrystals," *Solid State Commun.*, vol. 145, no. 7–8, pp. 368–373, 2008.

[142] J. Lee, H. Jeon, D. G. Oh, J. Szanyi, and J. H. Kwak, "Morphology-dependent phase

transformation of γ-Al2O3," *Appl. Catal. A Gen.*, vol. 500, pp. 58–68, 2015.

[143] S. C. Shen, W. K. Ng, Z. Y. Zhong, Y. C. Dong, L. Chia, and R. B. H. Tan, "Solid-based hydrothermal synthesis and characterization of alumina nanofibers with controllable aspect ratios," *J. Am. Ceram. Soc.*, vol. 92, no. 6, pp. 1311–1316, 2009.

[144] Y. Feng *et al.*, "One-step synthesis of hierarchical cantaloupe-like AlOOH superstructures via a hydrothermal route," *Cryst. Growth Des.*, vol. 8, no. 4, pp. 1426–1429, 2008.

[145] D. Mishra, S. Anand, R. K. Panda, and R. P. Das, "Hydrothermal preparation and characterization of boehmites," *Mater. Lett.*, vol. 42, no. 1, pp. 38–45, 2000.

[146] S. Musić, D. Dragčević, and S. Popović, "Hydrothermal crystallization of boehmite from freshly precipitated aluminum hydroxide," *Mater. Lett.*, vol. 40, no. 6, pp. 269–274, 1999.

[147] P. Pardo, F. J. Serrano, O. Vallcorba, J. M. Calatayud, J. M. Amigó, and J. Alarcón, "Enhanced Lateral to Basal Surface Ratio in Boehmite Nanoparticles Achieved by Hydrothermal Aging," *Cryst. Growth Des.*, vol. 15, no. 7, pp. 3532–3538, 2015.

[148] Y. Zhao, R. L. Frost, W. N. Martens, and H. Y. Zhu, "Growth and Surface Properties of Boehmite Nanofibers and Nanotubes at Low Temperatures Using a Hydrothermal Synthesis Route," *Langmuir*, vol. 23, no. 19, pp. 9850–9859, 2007.

[149] Z. Tang *et al.*, "Synthesis of flower-like Boehmite (γ-AlOOH) via a one-step ionic liquid-assisted hydrothermal route," *J. Solid State Chem.*, vol. 202, pp. 305–314, 2013.

[150] Y. Yang, H. Liang, L. Liu, and Z. Yang, "Facile hydrothermal synthesis of uniform 3D γ-AlOOH architectures assembled by nanosheets," *Cryst. Res. Technol.*, vol. 45, no. 2, pp. 195–198, 2010.

[151] Y. Li, J. Liu, and Z. Jia, "Fabrication of boehmite AlOOH nanofibers by a simple hydrothermal process," *Mater. Lett.*, vol. 60, no. 29–30, pp. 3586–3590, Dec. 2006.

[152] T. Kim, J. Lian, J. Ma, X. Duan, and W. Zheng, "Morphology controllable synthesis of γ-alumina nanostructures via an ionic liquid-assisted hydrothermal route," *Cryst. Growth Des.*, vol. 10, no. 7, pp. 2928–2933, 2010.

[153] Y. Mathieu, B. Lebeau, and V. Valtchev, "Control of the morphology and particle size of boehmite nanoparticles synthesized under hydrothermal conditions," *Langmuir*, vol. 23, no. 18, pp. 9435–9442, 2007.

[154] C. Kaya, J. . He, X. Gu, and E. . Butler, "Nanostructured ceramic powders by hydrothermal synthesis and their applications," *Microporous Mesoporous Mater.*, vol. 54, no. 1–2, pp. 37–49, Jul. 2002.

[155] T. Tsuchida, "Hydrothermal synthesis of submicrometer crystals of boehmite," *J. Eur. Ceram. Soc.*, vol. 20, no. 11, pp. 1759–1764, 2000.

[156] M. M. Amini and M. Mirzaee, "Effect of solution chemistry on preparation of boehmite by hydrothermal assisted sol-gel processing of aluminum alkoxides," *J. Sol-Gel Sci. Technol.*, vol. 36, no. 1, pp. 19–23, 2005.

[157] T.-Z. Ren, Z.-Y. Yuan, and B.-L. Su, " Microwave-Assisted Preparation of Hierarchical Mesoporous−Macroporous Boehmite AlOOH and γ-Al 2 O 3 ," *Langmuir*, vol. 20, no. 4, pp. 1531–1534, 2004.

[158] Q. Liu, A. Wang, X. Wang, P. Gao, X. Wang, and T. Zhang, "Synthesis, characterization and catalytic applications of mesoporous γ-alumina from boehmite sol," *Microporous Mesoporous Mater.*, vol. 111, no. 1–3, pp. 323–333, 2008.

[159] I. U. Haq, K. Akhtar, and Z. U. Khan, "Characterization of Monodispersed γ-Al2O3 Particles, Synthesized by Homogeneous Precipitation under Reflux Boiling," *High Temp. Mater. Process.*, vol. 34, no. 4, pp. 325–332, 2015.

[160] K. M. Parida, A. C. Pradhan, J. Das, and N. Sahu, "Synthesis and characterization of nano-sized porous gamma-alumina by control precipitation method," *Mater. Chem. Phys.*, vol. 113, no. 1, pp. 244–248, 2009.

[161] B. Pacewska, M. Keshr, and O. Kluk, "Aluminium nitrate as a precursor of mesoporous aluminium oxides," *J. Therm. Anal. Calorim.*, vol. 74, no. 2, pp. 595–603, 2003.

[162] F. Petrakli, M. Arkas, and A. Tsetsekou, "α-Alumina nanospheres from nano-dispersed boehmite synthesized by a wet chemical route," *J. Am. Ceram. Soc.*, vol. 101, no. 8, pp. 3508–3519, 2018.

[163] L. Zhong, Y. Zhang, and Y. Zhang, "Cleaner synthesis of mesoporous alumina from sodium aluminate solution," *Green Chem.*, vol. 13, no. 9, pp. 2525–2530, 2011.

[164] Y. Li, Y. Zhang, C. Yang, and Y. Zhang, "Precipitating sandy aluminium hydroxide from sodium aluminate solution by the neutralization of sodium bicarbonate," *Hydrometallurgy*, vol. 98, no. 1–2, pp. 52–57, 2009.

[165] A. Kocjan, T. Konegger, and A. Dakskobler, "Hierarchical macroporous–mesoporous γ-alumina monolithic green bodies with high strength," *J. Mater. Sci.*, vol. 52, no. 19, pp. 11168–11178, 2017.

[166] A. Kocjan, "The hydrolysis of AlN powder – a powerful tool in advanced materials engineering," *Chem. Rec.*, vol. 18, no. 7–8, pp. 1232–1246, 2018.

[167] T. Kosmac, S. Novak, and M. Sajko, "Hydrolysis-assisted solidification (HAS): A new setting concept for ceramic net-shaping," *J. Eur. Ceram. Soc.*, vol. 17, no. 2–3, pp. 427–432, 1997.

[168] A. Dakskobler, A. Kocjan, and T. Kosmač, "Porous alumina ceramics prepared by the hydrolysis-assisted solidification method," *J. Am. Ceram. Soc.*, vol. 94, no. 5, pp. 1374–1379, 2011.

[169] K. Krnel, A. Kocjan, and T. Kosmac, "A simple method for the preparation of nanostructured aluminate coatings," *J. Am. Ceram. Soc.*, vol. 92, no. 10, pp. 2451–2454, 2009.

[170] P. Jevnikar, M. Golobič, A. Kocjan, and T. Kosmač, "The effect of nano-structured alumina coating on the bond strength of resin-modified glass ionomer cements to zirconia ceramics," *J. Eur. Ceram. Soc.*, vol. 32, no. 11, pp. 2641–2645, 2012.

[171] M. Egashira, Y. ShImizu, Y. Takao, R. Yamaguchi, and Y. Ishikawa, "Effect of Carboxylic Acid Adsorption on the Hydrolysis and Sintered Properties of Aluminum Nitride Powder," *J. Am. Ceram. Soc.*, vol. 77, no. 7, pp. 1793–1798, 1994.

[172] K. Krnel and T. Kosmač, "Reactivity of aluminum nitride powder in dilute inorganic acids," *J. Am. Ceram. Soc.*, vol. 83, no. 6, pp. 1375–1378, 2000.

[173] K. Tsugeki, S. Yan, H. Maeida, K. Kusakabe, and S. Morooka, "Silica coating of aluminium nitride particles by radio-frequency plasma chemical vapour deposition," *J. Mater. Sci. Lett. Vol.*, vol. 13, pp. 43–45, 1994.

[174] P. Bowen, J. G. Highfield, A. Mocellin, and T. A. Ring, "Degradation of Aluminum Nitride Powder in an Aqueous Environmet," *J. Am. Ceram. Soc.*, vol. 73, no. 3, pp. 724–728, 1990.

[175] O. Levenspiel, "Fluid-Particle Reactions: Kinetics," in *Chemical reaction engineering*, New York: Wiley, 1999, pp. 566–588.

[176] A. Kocjan, K. Krnel, and T. Kosmač, "The influence of temperature and time on the AlN powder hydrolysis reaction products," *J. Eur. Ceram. Soc.*, vol. 28, no. 5, pp. 1003–1008, 2008.

[177] A. Kocjan, A. Dakskobler, K. Krnel, and T. Kosmač, "The course of the hydrolysis and the reaction kinetics of AlN powder in diluted aqueous suspensions," *J. Eur. Ceram. Soc.*, vol. 31, no. 5, pp. 815–823, 2011.

[178] S. Fukumoto, T. Hookabe, and H. Tsubakino, "Hydrolysis behavior of aluminum nitride in various solutions," *J. Mater. Sci.*, vol. 35, no. 11, pp. 2743–2748, 2000.

[179] G. C. Bye and J. G. Robinson, "Crystallization Processes in Aluminium Hydroxide Gels," *Kolloid-Zeitschrift und Zeitschrift fur Polym.*, vol. 198, pp. 53–60, 1964.

[180] A. Kocjan, A. Dakskobler, and T. Kosmač, "Evolution of aluminum hydroxides in diluted aqueous aluminum nitride powder suspensions," *Cryst. Growth Des.*, vol. 12, no. 3, pp. 1299–1307, 2012.

[181] B. E. Yoldas, "Hydrolysis of aluminium alkoxides and bayerite conversion," *J. Appl. Chem. Biotechnol.*, vol. 23, no. 11, pp. 803–809, 2007.

[182] H. Hudelja, B. Wicklein, D. Kuščer, and A. Kocjan, "Triggering the aqueous interparticle association of γ–Al2O3 hierarchical assemblies using divalent cations and cellulose nanofibers," *J. Eur. Ceram. Soc.*, vol. 41, no. 1, pp. 590–598, 2021.

[183] S. Hartmann, A. Sachse, and A. Galarneau, "Challenges and Strategies in the Synthesis of Mesoporous Alumina Powders and Hierarchical Alumina Monoliths," *Materials (Basel).*, vol. 5, no. 12, pp. 336–349, Feb. 2012.

[184] D. Han, X. Li, L. Zhang, Y. Wang, Z. Yan, and S. Liu, "Hierarchically ordered meso/macroporous γ-alumina for enhanced hydrodesulfurization performance," *Microporous Mesoporous Mater.*, vol. 158, pp. 1–6, Aug. 2012.

[185] X. Li, M. Sun, J. C. Rooke, L. Chen, and B.-L. Su, "Synthesis and applications of hierarchically porous catalysts," *Chinese J. Catal.*, vol. 34, no. 1, pp. 22–47, Jan. 2013.

[186] A. Corma, "From microporous to mesoporous molecular sieve materials and their use in catalysis," *Chem. Rev.*, vol. 97, no. 6, pp. 2373–2419, 1997.

[187] A. Ojuva *et al.*, "Mechanical performance and CO2 uptake of ion-exchanged zeolite A structured by freeze-casting," *J. Eur. Ceram. Soc.*, vol. 35, no. 9, pp. 2607–2618, 2015.

[188] Y. Zhang, H. Liang, C. Y. Zhao, and Y. Liu, "Macroporous alumina monoliths prepared by filling polymer foams with alumina hydrosols," *J. Mater. Sci.*, vol. 44, no. 3, pp. 931–938, 2009.

[189] Y. Tokudome, K. Fujita, K. Nakanishi, K. Miura, and K. Hirao, "Synthesis of monolithic Al2O3 with well-defined macropores and mesostructured skeletons via the sol-gel process accompanied by phase separation," *Chem. Mater.*, vol. 19, no. 14, pp. 3393–3398, 2007.

[190] Y. S. Han, J. B. Li, and Y. J. Chen, "Fabrication of bimodal porous alumina ceramics," *Mater. Res. Bull.*, vol. 38, no. 2, pp. 373–379, 2003.

[191] B. Gaweł and G. Øye, "Hierarchical γ-alumina monoliths with macro- and meso porosity prepared by using cross-linked dextran gel beads as the template," *Mater. Lett.*, vol. 95, pp. 86–88, Mar. 2013.

[192] M. Sobhani, H. Tavakoli, M. D. Chermahini, and M. Kazazi, "Preparation of macro-mesoporous γ-alumina via biology gelatin assisted aqueous sol-gel process," *Ceram. Int.*, vol. 45, no. 1, pp. 1385–1391, 2019.

[193] L.-L. Li, W.-T. Duan, Q. Yuan, Z.-X. Li, H.-H. Duan, and C.-H. Yan, "Hierarchical γ-Al2O3 monoliths with highly ordered 2D hexagonal mesopores in macroporous walls," *Chem. Commun.*, vol. 41, pp. 6174–6176, 2009.

[194] K. Zhang, Z. Fu, T. Nakayama, and K. Niihara, "Structural evolution of hierarchically macro/mesoporous Al2O3 monoliths under heat-treatment," *Microporous Mesoporous Mater.*, vol. 153, pp. 41–46, May 2012.

[195] G. G. Brown *et al.*, *Unit operations*. New York: John Wiley & Sons, 1951.

[196] M. Innocentini, P. Sepulveda, and F. Ortega, "Permeability," in *Cellular Ceramics*, M. Scheffler and P. Colombo, Eds. Weinheim: Wiley, 2005, pp. 313–341.

[197] A. A. Ditts, I. B. Revva, N. Y. Grishko, and R. V. Tarnovskiy, "Influence of dispersion state of initial AlN powder on the hydrolysis process in air environment," *IOP Conf. Ser. Mater. Sci. Eng.*, vol. 156, no. 1, p. 012040, Nov. 2016.

[198] R. K. Iler, "Fibrillar Colloidal Boehmite; Progressive Conversion to Gamma, Theta, and Alpha Aluminas," *J. Am. Ceram. Soc.*, vol. 44, no. 12, pp. 618–624, 1961.

[199] S. Chibowski, M. Wiśniewska, and E. O. Mazur, "The effect of temperature on the adsorption and conformation of polyacrylic acid macromolecules at the ZrO2-polymer solution interface," *Powder Technol.*, vol. 141, no. 1–2, pp. 12–19, 2004.

[200] A. U. Khan, N. Mahmood, and P. F. Luckham, "Rheological Characterization of Alumina Ceramic Suspensions in Presence of a Dispersant and a Binder," *J. Dispers. Sci. Technol.*, vol. 33, no. 8, pp. 1210–1217, 2012.

[201] K. K. Das and P. Somasundaran, "Flocculation-dispersion characteristics of alumina using a wide molecular weight range of polyacrylic acids," *Colloids Surfaces A Physicochem. Eng. Asp.*, vol. 223, no. 1–3, pp. 17–25, 2003.

[202] Y. Hirata, J. Kamikakimoto, A. Nishimoto, and Y. Ishihara, "Interaction between a-Alumina Surface and Polyacrylic Acid," *J. Ceram. Soc. Japan*, vol. 100, no. 1, pp. 7–12, 1992.

[203] S. Chibowski, M. Wísniewska, and T. Urban, "Influence of solution pH on stability of aluminum oxide suspension in presence of polyacrylic acid," *Adsorption*, vol. 16, no. 4–5, pp. 321–332, 2010.

[204] M. Wiśniewska, S. Chibowski, and T. Urban, "Effect of the type of polymer functional groups on the structure of its film formed on the alumina surface - Suspension stability," *React. Funct. Polym.*, vol. 72, no. 11, pp. 791–798, 2012.

[205] M. Montero, T. Molina, M. Szafran, R. Moreno, and M. I. Nieto, "Alumina porous nanomaterials obtained by colloidal processing using d-fructose as dispersant and porosity promoter," *Ceram. Int.*, vol. 38, no. 4, pp. 2779–2784, 2012.

[206] J. Cesarano, I. Aksay, and A. Bleier, "Stability of α-Al203 Suspensions with Poly(methacrylic acid) Polyelectrolyte," *J. Am. Ceram. Soc.*, vol. 71, no. 4, pp. 250–255, 1988.

[207] J. G. P. Binner and A. M. McDermott, "Rheological characterisation of ammonium polyacrylate dispersed, concentrated alumina suspensions," *Ceram. Int.*, vol. 32, no. 7, pp. 803–810, 2006.

[208] M. J. Edirisinghe, H. M. Shaw, and K. L. Tomkins, "Flow behaviour of ceramic injection moulding suspensions," *Ceram. Int.*, vol. 18, no. 3, pp. 193–200, 1992.

[209] S. Mueller, E. W. Llewellin, and H. M. Mader, "The rheology of suspensions of solid particles," *Proc. R. Soc. A*, vol. 466, no. 4, pp. 1201–1228, 2010.

[210] J. S. Laskowski, "Surface chemistry fundamentals in fine coal processing," in *The Coal Handbook: Towards Cleaner Production*, vol. 1, D. Osborne, Ed. Elsevier, 2013, pp. 347–421.

[211] A. Zamorategui, S. Sugita, R. Zárraga, S. Tanaka, and K. Uematsu, "Evaluation of dispersability of gamma alumina prepared by homogeneous precipitation," *J. Ceram. Soc. Japan*, vol. 120, no. 1403, pp. 290–294, 2012.

[212] C. D. Cwalina and N. J. Wagner, "Material properties of the shear-thickened state in concentrated near hard-sphere colloidal dispersions," *J. Rheol. (N. Y. N. Y).*, vol. 58, no. 4, pp. 949–967, 2014.

[213] G. Chatté *et al.*, "Shear thinning in non-Brownian suspensions," *Soft Matter*, vol. 14, no. 6, pp. 879–893, 2018.

[214] J. F. Berret, R. Gamez-Corrales, J. Oberdisse, L. M. Walker, and P. Lindner, "Flow-structure relationship of shear-thickening surfactant solutions," *Europhys. Lett.*, vol. 41, no. 6, pp. 677–682, 1998.

[215] W. J. Tseng and C. H. Wu, "Aggregation, rheology and electrophoretic packing

structure of aqueous Al_2O_3 nanoparticle suspensions," *Acta Mater.*, vol. 50, no. 15, pp. 3757–3766, 2002.

[216] T. G. Mezger, *The Rheology Handbook: For users of rotational and oscillatory rheometers*. Hannover: Vincentz Network, 2006.

[217] I. M. Krieger and T. J. Dougherty, "A Mechanism for Non-Newtonian Flow in Suspensions of Rigid Spheres," *Trans. Soc. Rheol.*, vol. 3, no. 1, pp. 137–152, 1959.

[218] M. Corcione, "A semi-empirical model for predicting the effective dynamic viscosity of nanoparticle suspensions," *Heat Transf. Eng.*, vol. 33, no. 7, pp. 575–583, 2012.

[219] Z. Soua, O. Larue, E. Vorobiev, and J. L. Lanoisellé, "Estimation of floc size in highly concentrated calcium carbonate suspension obtained by filtration with dispersant," *Colloids Surfaces A Physicochem. Eng. Asp.*, vol. 274, no. 1–3, pp. 1–10, 2006.

[220] F. Ferrini, D. Ercolani, B. de Cindio, L. Nicodemo, L. Nicolais, and S. Ranaudo, "Shear viscosity of settling suspensions," *Rheol. Acta*, vol. 18, no. 2, pp. 289–296, 1979.

[221] Karl Wefers, C. Misra, and P. R. Bridenbaugh, *Oxides and Hydroxides of Aluminum*. Alcoa Laboratories, 1987.

[222] R. Schweins, G. Goerigk, and K. Huber, "Shrinking of anionic polyacrylate coils induced by Ca2+, Sr 2+ and Ba2+: A combined light scattering and ASAXS study," *Eur. Phys. J. E*, vol. 21, no. 2, pp. 99–110, 2006.

[223] N. B. Wyatt and M. W. Liberatore, "The effect of counterion size and valency on the increase in viscosity in polyelectrolyte solutions," *Soft Matter*, vol. 6, no. 14, pp. 3346–3352, 2010.

[224] Y. Liu, K. Gordeyeva, and L. Bergström, "Steady-shear and viscoelastic properties of cellulose nanofibril–nanoclay dispersions," *Cellulose*, vol. 24, no. 4, pp. 1815–1824, 2017.

[225] D. Santhiya, G. Nandini, S. Subramanian, K. A. Natarajan, and S. G. Malghan, "Effect of polymer molecular weight on the adsorption of polyacrylic acid at the aluminum-water interface," *Colloids Surfaces A Physicochem. Eng. Asp.*, vol. 133, pp. 157–163, 1998.

[226] A. Sommerauer, D. L. Sussman, and W. Stumm, "The role of complex formation in the flocculation of negatively charged sols with anionic polyelectrolytes," *Kolloid-Zeitschrift Zeitschrift für Polym.*, vol. 225, no. 2, pp. 147–154, 1968.

[227] M. G. Carneiro-da-Cunha, M. A. Cerqueira, B. W. S. Souza, J. A. Teixeira, and A. A. Vicente, "Influence of concentration, ionic strength and pH on zeta potential and mean hydrodynamic diameter of edible polysaccharide solutions envisaged for multinanolayered films production," *Carbohydr. Polym.*, vol. 85, no. 3, pp. 522–528, Jun. 2011.

[228] M. R. Kulterer *et al.*, "Functional polysaccharide composite nanoparticles from cellulose acetate and potential applications," *Adv. Funct. Mater.*, vol. 22, no. 8, pp. 1749–1758, 2012.

[229] G. V Lowry *et al.*, "Guidance to improve the scientific value of zeta- potential measurements in nanoEHS," *Environ. Sci. Nano*, vol. 3, no. 5, pp. 953–965, 2016.

[230] V. Mikulcová, R. Bordes, A. Minařík, and V. Kašpárková, "Pickering oil-in-water emulsions stabilized by carboxylated cellulose nanocrystals – Effect of the pH," *Food Hydrocoll.*, vol. 80, pp. 60–67, Jul. 2018.

[231] M. Reischl, K. Stana-Kleinschek, and V. Ribitsch, "Electrokinetic investigations of oriented cellulose polymers," *Macromol. Symp.*, vol. 244, pp. 31–47, 2006.

[232] M. Spaic, D. P. Small, J. R. Cook, and W. Wan, "Characterization of anionic and cationic functionalized bacterial cellulose nanofibres for controlled release applications," *Cellulose*, vol. 21, no. 3, pp. 1529–1540, 2014.

[233] J. E. Gebhardt and D. W. Fuerstenau, "Flotation behavior of hematite fines flocculated with polyacrylic acid," *Mining, Metall. Explor.*, vol. 3, no. 3, pp. 164–170, Aug. 1986.

[234] S. A. Hosseini, A. Niaei, and D. Salari, "Production of γ-Al₂O₃ from Kaolin," *Open J. Phys. Chem.*, vol. 1, no. 2, pp. 23–27, 2011.

[235] H. Hou, Y. Xie, Q. Yang, Q. Guo, and C. Tan, "Preparation and characterization of γ-AlOOH nanotubes and nanorods," *Nanotechnology*, vol. 16, no. 6, pp. 741–745, 2005.

[236] R. L. Oréfice and W. L. Vasconcelos, "Sol-Gel Transition and Structural Evolution on Multicomponent Gels Derived from the Alumina-Silica System," *J. Sol-Gel Sci. Technol.*, vol. 9, no. 3, pp. 239–249, 1997.

[237] R. L. Frost, J. T. Kloprogge, and S. C. Russell, "Dehydroxylation of Aluminum (Oxo)hydroxides Using Infrared Emission Spectroscopy. Part II: Boehmite," *Appl. Spectrosc.*, vol. 53, no. 5, pp. 572–582, 1999.

[238] G. K. Priya, P. Padmaja, K. G. K. Warrier, A. D. Damodaran, and G. Ã. Aruldhas, "Dehydroxylation and high temperature phase formation in sol-gel boehmite characterized by Fourier transform infrared spectroscopy," *J. Mater. Sci. Lett.*, vol. 16, pp. 1584–1587, 1997.

[239] D. S. Maciver, H. H. Tobin, and R. T. Barth, "Catalytic aluminas I. Surface chemistry of eta and gamma alumina," *J. Catal.*, vol. 2, no. 6, pp. 485–497, 1963.

[240] D. Lin-Vien, N. B. Colthup, W. G. Fateley, and J. G. Grasselli, *The Handbook of Infrared and Raman Characteristic Frequencies of Organic Molecules*. San Diego: Academic Press, 1991.

[241] Tetsuo Kondo, "Hydrogen Bonds in Cellulose and Cellulose Derivatives," in *Polysaccharides: Structural Diversity and Functional Versatility*, S. Dumitriu, Ed. New York: Marcel Dekker, 2004, pp. 69–98.

[242] G. Socrates, *Infrared and Raman Characteristic Group Frequencies*. New York: John Wiley & Sons, 2004.

[243] M. Poletto, V. Pistor, M. Zeni, and A. J. Zattera, "Crystalline properties and

decomposition kinetics of cellulose fibers in wood pulp obtained by two pulping processes," *Polym. Degrad. Stab.*, vol. 96, no. 4, pp. 679–685, Apr. 2011.

[244] R. H. Marchessault, "Application of infra-red spectroscopy to cellulose and wood polysaccharides," *Pure Appl. Chem.*, vol. 5, no. 1–2, pp. 107–130, 1962.

[245] V. Tserki, P. Matzinos, S. Kokkou, and C. Panayiotou, "Novel biodegradable composites based on treated lignocellulosic waste flour as filler. Part I. Surface chemical modification and characterization of waste flour," *Compos. Part A*, vol. 36, pp. 965–974, 2005.

[246] E. Munch, E. Saiz, A. P. Tomsia, and S. Deville, "Architectural control of freeze-cast ceramics through additives and templating," *J. Am. Ceram. Soc.*, vol. 92, no. 7, pp. 1534–1539, 2009.

[247] Y. M. Tan, O. Cervantes, S. W. Nam, J. D. Molitoris, and J. P. Hooper, "Dynamic fragmentation of cellular, ice-templated alumina scaffolds," *J. Appl. Phys.*, vol. 119, no. 2, 2016.

[248] H. Sehaqui, Q. Zhou, and L. A. Berglund, "High-porosity aerogels of high specific surface area prepared from nanofibrillated cellulose (NFC)," *Compos. Sci. Technol.*, vol. 71, no. 13, pp. 1593–1599, 2011.

[249] C. Antonini *et al.*, "Ultra-porous nanocellulose foams: A facile and scalable fabrication approach," *Nanomaterials*, vol. 9, no. 8, pp. 1–14, 2019.

[250] D. F. Souza *et al.*, "Synthesis and structural evaluation of freeze-cast porous alumina," *Mater. Charact.*, vol. 96, pp. 183–195, 2014.

[251] S. A. Barr and E. Luijten, "Structural properties of materials created through freeze casting," *Acta Mater.*, vol. 58, no. 2, pp. 709–715, 2010.

[252] J. Kim, J. H. Ha, J. Lee, and I. H. Song, "Effect of pore structure on gas permeability constants of porous alumina," *Ceram. Int.*, vol. 45, no. 5, pp. 5231–5239, 2019.

[253] M. D. M. Innocentini, P. Sepulveda, and F. S. Ortega, "Permeability," in *Cellular ceramics*, M. Scheffler and P. Colombo, Eds. Wiley VCH, Weinheim, 2005, pp. 313–341.

[254] D. F. Souza, E. H. M. Nunes, J. A. Queiroga, and W. L. Vasconcelos, "Microstructural characterization and gas permeation performance of freeze-cast alumina supports," *J. Eur. Ceram. Soc.*, vol. 38, no. 11, pp. 4020–4025, 2018.

[255] M. D. M. Innocentini, V. P. Rodrigues, R. C. O. Romano, R. G. Pileggi, G. M. C. Silva, and J. R. Coury, "Permeability optimization and performance evaluation of hot aerosol filters made using foam incorporated alumina suspension," *J. Hazard. Mater.*, vol. 162, no. 1, pp. 212–221, Feb. 2009.

[256] B. Yuan *et al.*, "Transparent and flame retardant cellulose/aluminum hydroxide nanocomposite aerogels," *Sci. China Chem.*, vol. 59, no. 10, pp. 1335–1341, 2016.

[257] L. Wang and M. Sánchez-Soto, "Green bio-based aerogels prepared from recycled cellulose fiber suspensions," *RSC Adv.*, vol. 5, no. 40, pp. 31384–31391, 2015.

[258] R. Rice, "Mechanical Properties," in *Cellular Ceramics*, M. Scheffler and P.

Colombo, Eds. Wiley VCH, Weinheim, 2005, pp. 291–312.

[259] F. He *et al.*, "Alumina aerogels with unidirectional channels under different freezing temperatures during freeze casting——Part II: Anisotropic mechanical and thermal conductive properties," *Ceram. Int.*, vol. 46, no. 16, pp. 25691–25696, 2020.

[260] T. Wu *et al.*, "Dual-porous cellulose nanofibril aerogels via modular drying and cross-linking," *Nanoscale*, vol. 12, no. 13, pp. 7383–7394, 2020.

[261] B. Wicklein *et al.*, "Thermally insulating and fire-retardant lightweight anisotropic foams based on nanocellulose and graphene oxide," *Nat. Nanotechnol.*, vol. 10, no. 3, pp. 277–283, 2015.

[262] H. A. Barnes, J. F. Hutton, and K. Walters, Eds., *An Introduction to Rheology*, First edit. Amsterdam: Elsevier, 1989.

[263] T. A. Strivens, "The rheology of paints," in *Paint and Surface Coatings: Theory and Practice*, R. Lambourne and T. A. Strivens, Eds. Cambridge: Woodhead Publishing, 1987, pp. 575–597.

[264] P. F. G. Banfill, "Rheology of Fresh Cement and Concrete," in *Proceedings of an International Conference, Liverpool*, 1991.

[265] M. Wells, "Controlling the rheology of chocolate and fillings," in *Science and Technology of Enrobed and Filled Chocolate, Confectionery and Bakery Products*, G. Talbot, Ed. Cambridge: Woodhead Publishing Limited, 2009, pp. 255–284.

[266] B. Faure, "Particle interactions at the nanoscale: From colloidal processing to self-assembled arrays," Stockholm University, Stockholm, Sweden, 2012.

[267] L. Bergström, "Rheology of Concentrated Suspensions," in *Surface and colloid chemistry in advanced ceramics processing*, R. J. Pugh and L. Bergström, Eds. New York: Marcel Dekker, 1994, pp. 193–224.

[268] H. A. Barnes, *A handbook of elementary rheology*. Aberystwyth: University of Wales, 2000.

[269] J. Mewis and N. J. Wagner, *Colloidal suspension rheology*. Cambridge: Cambridge University Press, 2011.

[270] B. P. Singh, S. Bhattacharjee, and L. Besra, "Influence of surface charge on maximizing solids loading in colloidal processing of alumina," *Mater. Lett.*, vol. 56, no. 4, pp. 475–480, 2002.

[271] R. J. Hunter, "Zeta potential in colloid science: principles and applications," in *Colloid science*, R. H. Ottewill and R. L. Rowel, Eds. London: Academic Press, 1981.

[272] J. Kenvin, J. Jagiello, S. Mitchell, and J. Pérez-Ramírez, "Unified method for the total pore volume and pore size distribution of hierarchical zeolites from argon adsorption and mercury intrusion," *Langmuir*, vol. 31, no. 4, pp. 1242–1247, 2015.

[273] C. A. Leon y Leon, "New perspectives in mercury porosimetry," *Adv. Colloid Interface Sci.*, vol. 76–77, pp. 341–372, 1998.

[274] H. Giesche, "Mercury Porosimetry: A General (Practical) Overview," *Part. Part.*

Syst. Charact., vol. 23, no. 1, pp. 9–19, Jun. 2006.

[275] T. R. Hogness, "The surface tensions and densities of liquid mercury, cadmium, zinc, lead, tin and bismuth.," *J. Am. Chem. Soc.*, vol. 43, no. 7, pp. 1621–1628, 1921.

[276] T. Allen, *Particle Size Measurement*. London: Chapman & Hall, 1997.

[277] Micromeritics Instrument Corporation, "Physical Characterization of Materials Using Porosimetry," *AZoNano*, 2019. [Online]. Available: https://www.azonano.com/article.aspx?ArticleID=2641. [Accessed: 10-Nov-2020].

[278] P. S. Liu and G. F. Chen, "Characterization Methods: Basic Factors," in *Porous Materials: Processing and Applications*, P. S. Liu and G. F. Chen, Eds. Oxford: Butterworth-Heinemann, 2014, pp. 411–492.

[279] K. S. W. Sing, "Recommendations: Reporting Physisorption Data for Gas/Solid Systems with Special Reference to the Determination of Surface Area and Porosity," *Pure Appl. Chem.*, vol. 54, no. 11, pp. 2201–2218, 1982.

[280] S. Lowell and J. E. Shields, *Powder Surface Area and Porosity*. Dordrecht: Springer, 1991.

[281] M. Palacios, H. Kazemi-Kamyab, S. Mantellato, and P. Bowen, "Laser diffraction and gas adsorption techniques," in *A Practical Guide to Microstructural Analysis of Cementitious Materials*, K. Scrivener, R. Snellings, and B. Lothenbach, Eds. Boca Raton: CRC Press, 2016, pp. 445–484.

[282] M. D. Donohue and G. L. Aranovich, "Classification of Gibbs adsorption isotherms," *Adv. Colloid Interface Sci.*, vol. 76–77, pp. 137–152, 1998.

[283] S. Brunauer, *The Adsorption of Gases and Vapors. Volume I: Physical Adsorption*. London: Oxford university press, 1945.

[284] I. Langmuir, "The Adsorption of Gases on Plane Surfaces of Glass, Mica and Platinum," *J. Am. Chem. Soc.*, vol. 40, no. 9, pp. 1361–1403, 1918.

[285] J. Groen, "Critical appraisal of mesopore characterization by adsorption analysis," *Appl. Catal. A Gen.*, vol. 268, no. 1–2, pp. 121–125, Aug. 2004.

[286] J. C. Groen, L. A. A. Peffer, and P. Javier, "Pore size determination in modified micro- and mesoporous materials . Pitfalls and limitations in gas adsorption data analysis," *Miroporous mesoporous Mater.*, vol. 60, pp. 1–17, 2003.

[287] K. Sing, "The use of nitrogen adsorption for the characterisation of porous materials," *Colloids Surfaces A Physicochem. Eng. Asp.*, vol. 187–188, pp. 3–9, 2001.

[288] E. P. Barrett, L. G. Joyner, and P. P. Halenda, "The Determination of Pore Volume and Area Distributions in Porous Substances. I. Computations from Nitrogen Isotherms," *J. Am. Chem. Soc.*, vol. 71, no. 1, pp. 373–380, 1951.

[289] J. Choma, M. Jaroniec, W. Burakiewicz-Mortka, and M. Kloske, "Critical appraisal of classical methods for determination of mesopore size distributions of MCM-41 materials," *Appl. Surf. Sci.*, vol. 196, pp. 216–223, 2002.

[290] P. I. Ravikovitch and A. V Neimark, "Characterization of nanoporous materials from adsorption," *Colloids Surfaces A Physicochem. Eng. Asp.*, vol. 188, pp. 11–21,

2001.

[291] A. Saito and H. C. Foley, "Curvature and Parametric Sensitivity in Models for Adsorption in Micropores," *Am. Inst. Chem. Eng. Journals*, vol. 37, no. 3, pp. 429–436, 1991.

[292] S. J. Gregg and K. S. W. Sing, *Adsorption, Surface Area, and Porosity*. London: Academic Press, 1982.

[293] B. C. Lippens and J. H. de Boer, "Studies on pore systems in catalysts: V. The t method," *J. Catal.*, vol. 4, no. 3, pp. 319–323, 1965.

[294] K. S. W. Sing, "Utilisation of adsorption data in the BET region," in *Surface Area Determination*, . H. Everett and R. H. Ottewill, Eds. Boston: Butterworth-Heinemann, 1970, pp. 25–42.

[295] B. E. Yoldas, M. J. Annen, and J. Bostaph, "Chemical engineering of aerogel morphology formed under nonsupercritical conditions for thermal insulation," *Chem. Mater.*, vol. 12, no. 8, pp. 2475–2484, 2000.

[296] N. Mathis, "Transient thermal conductivity measurements: Comparison of destructive and nondestructive techniques," *High Temp. - High Press.*, vol. 32, no. 3, pp. 321–327, 2000.

[297] M. Gustavsson, J. S. Gustavsson, S. E. Gustafsson, and L. Hälldahl, "Recent developments and applications of the hot disk thermal constants analyser for measuring thermal transport properties of solids," *High Temp. - High Press.*, vol. 32, no. 1, pp. 47–51, 2000.

[298] R. F. Speyer, "Thermal Conductivity," in *Thermal Analysis of Materials*, New York: Marcel Dekker, 1994, pp. 227–242.

[299] Y. He, "Rapid thermal conductivity measurement with a hot disk sensor," *Thermochim. Acta*, vol. 436, no. 1–2, pp. 122–129, Oct. 2005.

[300] M. Antunes, V. Realinho, J. I. Velasco, E. Solórzano, M. Á. Rodríguez-Pérez, and J. A. De Saja, "Thermal conductivity anisotropy in polypropylene foams prepared by supercritical CO2 dissolution," *Mater. Chem. Phys.*, vol. 136, no. 1, pp. 268–276, 2012.

[301] M. Gustavsson, E. Karawacki, and S. E. Gustafsson, "Thermal conductivity, thermal diffusivity, and specific heat of thin samples from transient measurements with hot disk sensors," *Rev. Sci. Instrum.*, vol. 65, no. 12, pp. 3856–3859, 1994.

[302] S. E. Gustafsson, "Transient plane source techniques for thermal conductivity and thermal diffusivity measurements of solid materials," *Rev. Sci. Instrum.*, vol. 62, no. 3, pp. 797–804, 1991.

[303] Q. Zheng, S. Kaur, C. Dames, and R. S. Prasher, "Analysis and improvement of the hot disk transient plane source method for low thermal conductivity materials," *Int. J. Heat Mass Transf.*, vol. 151, p. 119331, Apr. 2020.

[304] S. E. Gustafsson, E. Karawacki, and M. N. Khan, "Transient hot-strip method for simultaneously measuring thermal conductivity and thermal diffusivity of solids and

fluids," *J. Phys. D. Appl. Phys.*, vol. 12, no. 9, pp. 1411–1421, 1979.

[305] S. E. Gustafsson, E. Karawacki, and M. A. Chohan, "Thermal transport studies of electrically conducting materials using the transient hot-strip technique," *J. Phys. D. Appl. Phys.*, vol. 19, no. 5, pp. 727–735, 1986.

[306] R. Singh, N. S. Saxena, and D. R. Chaudhary, "Simultaneous measurement of thermal conductivity and thermal diffusivity of some building materials using the transient hot strip method," *J. Phys. D. Appl. Phys.*, vol. 18, no. 1, pp. 1–8, 1985.

[307] R. J. Warzoha and A. S. Fleischer, "Determining the thermal conductivity of liquids using the transient hot disk method. Part I: Establishing transient thermal-fluid constraints," *Int. J. Heat Mass Transf.*, vol. 71, pp. 779–789, Apr. 2014.

[308] H. Nagai, F. Rossignol, Y. Nakata, T. Tsurue, M. Suzuki, and T. Okutani, "Thermal conductivity measurement of liquid materials by a hot-disk method in short-duration microgravity environments," *Mater. Sci. Eng. A*, vol. 276, no. 1–2, pp. 117–123, Jan. 2000.

[309] M. Yuan, T. T. Diller, D. Bourell, and J. Beaman, "Thermal conductivity of polyamide 12 powder for use in laser sintering," *Rapid Prototyp. J.*, vol. 19, no. 6, pp. 437–445, 2013.

[310] A. Elkholy, H. Sadek, and R. Kempers, "An improved transient plane source technique and methodology for measuring the thermal properties of anisotropic materials," *Int. J. Therm. Sci.*, vol. 135, pp. 362–374, Jan. 2019.

[311] A. Dupleix, A. Kusiak, M. Hughes, and F. Rossi, "Measuring the thermal properties of green wood by the transient plane source (TPS) technique," *Holzforschung*, vol. 67, no. 4, pp. 437–445, 2013.

[312] B. Koo *et al.*, "Toward lithium ion batteries with enhanced thermal conductivity," *ACS Nano*, vol. 8, no. 7, pp. 7202–7207, 2014.

[313] R. Coquard, E. Coment, G. Flasquin, and D. Baillis, "Analysis of the hot-disk technique applied to low-density insulating materials," *Int. J. Therm. Sci.*, vol. 65, pp. 242–253, Mar. 2013.

[314] J. A. De Saja, O. Almanza, and M. A. Rodríguez-Pérez, "Applicability of the Transient Plane Source Method To Measure the Thermal Conductivity of Low-Density," *J. Polym. Sci. Part B Polym. Phys.*, vol. 42, pp. 1226–1234, 2004.

[315] A. Bouguerra, A. Aït-Mokhtar, O. Amiri, and M. B. Diop, "Measurement of thermal conductivity, thermal diffusivity and heat capacity of highly porous building materials using transient plane source technique," *Int. Commun. Heat Mass Transf.*, vol. 28, no. 8, pp. 1065–1078, 2001.

[316] A. A. Trofimov, J. Atchley, S. S. Shrestha, A. O. Desjarlais, and H. Wang, "Evaluation of measuring thermal conductivity of isotropic and anisotropic thermally insulating materials by transient plane source (Hot Disk) technique," *J. Porous Mater.*, vol. 27, no. 6, pp. 1791–1800, Dec. 2020.

[317] T. Ohji, "Porous Ceramic Materials," in *Handbook of Advanced Ceramics*, S. Somiya, Ed. Waltham: Academic Press, 2013, pp. 1141–1142.

[318] M. D. M. Innocentini, A. R. F. Pardo, and V. C. Pandolfelli, "Influence of Air Compressibility on the Permeability Evaluation of Refractory Castables," *J. Am. Ceram. Soc.*, vol. 83, no. 6, pp. 1536–1538, 2000.

[319] J. R. Fanchi, "Porosity and Permeability," in *Integrated Reservoir Asset Management*, J. R. Fanchi, Ed. Burlington: Gulf Professional Publishing, 2010, pp. 49–69.

[320] M. D. M. Innocentini, V. R. Salvini, V. C. Pandolfelli, and J. R. Coury, "Assessment of Forchheimer's Equation to Predict the Permeability of Ceramic Foams," *J. Am. Ceram. Soc.*, vol. 82, no. 7, pp. 1945–1948, 1999.

[321] P. Philipset and H. L. Schram, "Non-Darcian Airflow through Ceramic Foams," *J. Am. Ceram. Soc.*, vol. 32, pp. 728–732, 1991.

[322] E. A. Moreira, M. D. M. Innocentini, and J. R. Coury, "Permeability of ceramic foams to compressible and incompressible flow," *J. Eur. Ceram. Soc.*, vol. 24, pp. 3209–3218, 2004.

[323] E. Maire, J.-Y. Buffière, L. Salvo, J. J. Blandin, W. Ludwig, and L. J. Michel, "On the Application of Microtomography in the Filed of Material Science," *Adv. Eng. Mater.*, vol. 3, no. 8, pp. 539–546, 2001.

[324] J. Baruchel, J.-Y. Buffiere, E. Maire, Pa. Merle, and G. Peix, *X-Ray Tomography in Material Science*. Paris: Hermes science publications, 2000.

[325] E. Maire, "Computed X-ray Tomography," in *Handbook of Cellular Metals: Production, Processing, Applications*, H.-P. Degischer and B. Kriszt, Eds. Weinheim: Wiley-VCH, 2002, pp. 145–155.

[326] B. Schrader, *Infrared and Raman Spectroscopy*. Weinheim: VCH, 1995.

[327] S. N. Patnaik and D. A. Hopkins, *Strength of Materials*. Boston: Butterworth-Heinemann, 2004.

[328] P. A. Claisse, "Strength of materials," in *Civil Engineering Materials*, Boston: Butterworth-Heinemann, 2016, pp. 9–22.

[329] M. F. Ashby and D. R. H. Jones, Eds., "Mechanical Properties of Ceramics," in *International Series on Materials Science and Technology*, Boston: Butterworth-Heinemann, 2013, pp. 327–344.

[330] J. T. Bauman, "Stress-Strain Testing," in *Rubber Components: Guide for Design Engineers*, J. T. Bauman, Ed. Cincinnati: Hanser, 2008, pp. 43–67.

[331] T. H. G. Megson, Ed., "Stress and Strain," in *Structural and Stress Analysis*, Boston: Butterworth-Heinemann, 2019, pp. 165–201.

[332] R. Danzer, T. Lube, R. Morrell, and P. Supancic, "Mechanical Properties of Ceramics," in *Handbook of Advanced Ceramics*, S. Somiya, Ed. Oxford: Academic Press, 2013, pp. 609–632.

[333] D. R. H. Jones and M. Ashby, "Properties of Composites and Foams," in *In International Series on Materials Science and Technology, Engineering Materials 2*, M. F. Ashby and D. R. H. Jones, Eds. Boston: Butterworth-Heinemann, 2013,

pp. 477–492.

[334] B. Jiang, Z. Wang, and N. Zhao, "Effect of pore size and relative density on the mechanical properties of open cell aluminum foams," *Scr. Mater.*, vol. 56, no. 2, pp. 169–172, 2007.

Bibliography

Publications Related to the Thesis

H. Hudelja, T. Konegger, B. Wicklein, J. Čretnik, F. Akhtar, A. Kocjan, Freeze-casting of highly porous cellulose-nanofiber-reinforced γ-Al_2O_3 monoliths, *Open Ceram.*, vol. 5, pp. 100069, 2021, doi:10.1016/j.oceram.2021.100069.

H. Hudelja, B. Wicklein, D. Kuščer, A. Kocjan, Triggering the aqueous interparticle association of γ-Al_2O_3 hierarchical assemblies using divalent cations and cellulose nanofibers, *J. Eur. Ceram. Soc.*, vol. 41, pp. 590-598, 2021, doi: 10.1016/j.scitotenv.2020.137421.

Journal Articles

D. Lisjak, P. Hribar Boštjančič, P. Hribar Boštjančič, A. Mertelj, A. Mavrič, A. Mavrič, M. Valant, M. Valant, J. Kovač, H. Hudelja, H. Hudelja, A. Kocjan, D. Makovec, Formation of Fe(III)-phosphonate Coatings on Barium Hexaferrite Nanoplatelets for Porous Nanomagnets, *ACS Omega*, vol. 5, pp. 14086–14095, 2020, doi:10.1021/acsomega.0c01597.

Conference Paper

D. Lisjak, P. Hribar, A. Mertelj, A. Mavrič, M. Valant, H. Hudelja, A. Kocjan, D Makovec, Porous nanomagnets made by coating barium hexaferrite nanoplatelets with phosphonic acids. In Zbornik povzetkov [Elektronski vir] = Book of abstracts / Slovenski kemijski dnevi 2020 = 26th Annual Meeting of the Slovenian Chemical Society, 16-18 september 2020, Portorož, Slovenija. 2020, p. 49. [COBISS.SI-ID 29648643]

H. Hudelja, A. Kocjan, Freeze casting of feather-light, cellulose-nanofiber-reinforced Al_2O_3 foams. In Conference guide [Elektronski vir] / 44th International Conference and Exposition on Advanced Ceramics and Composites, January 26-31, 2020, Daytona Beach, Florida. 2020, p. 197. [COBISS.SI-ID 33238567]

H. Hudelja, A. Kocjan, Feather-light, cellulose-nanofiber-reinforced γ-Al_2O_3 foams [Elektronski vir]. In Program in knjiga povzetkov [Elektronski vir] = Program and book of abstracts / 27. Mednarodna konferenca o materialih in tehnologijah, 16.-18. oktober 2019, Portorož, Slovenija = 27th International Conference on Materials and Technology, 16-18 October 2019, Portorož, Slovenia. 2019, p. 66. [COBISS.SI-ID 302184704]

Kocjan, H. Hudelja, Freeze casting of ultralight, cellulose-nanofiber-reinforced γ-Al_2O_3 foams. In Shaping 7, 11-13 September 2019, Aveiro, Portugal [Elektronski vir]: book of abstracts. 2019, p. 49. [COBISS.SI-ID 33295143]

H. Hudelja, A. Kocjan, Freeze casting of highly-porous γ−Al_2O_3 foams. In Book of abstracts [Elektronski vir] / XVI. Conference of the European Ceramic Society, ECerS 2019, 16-20 June, 2019, Torino, Italy. 2019, p. 61. [COBISS.SI-ID 32507687]

H. Hudelja, A. Kocjan, Can nanoparticles be tamed? [Elektronski vir]. In Knjiga povzetkov [Elektronski vir] / 11. študentska konferenca Mednarodne podiplomske šole Jožefa Stefana in 13. dneva mladih raziskovalcev (Konferenca KMBO), 15. in 16. april 2019, Planica, Slovenija: science of the future how to stay up-tod-date with your research! = Book of abstracts = 11th Jožef Stefan International Postgraduate School Students' Conference and 13th Young Researchers' Day, 15th and 16th May 2019, Planica, Slovenia. 2019, p. 56. [COBISS.SI-ID 32350247]

O. Kovalenko, S. D. Škapin, M. Maček, S. Tkachenko, L. Čelko, D. Vengust, N. Daneu, A. Kocjan, H. Hudelja, M. Spreitzer, S. Umerova, D. I. Baranovskyi, A. Ragulya, Impact of the barium tytanyl oxalate precipitation condition on the aggregate formation characteristics. In Program and the Book of abstracts / Eighteenth Young Researchers' Conference Materials Sciences and Engineering, 4-6 December, 2019, Belgrade, Serbia. 2019, p. 35. [COBISS.SI-ID 58730243]

Other Publications

Hudelja, Hermina, Načrtovanje procesa kristalizacije aktivne farmacevtske učinkovine z uporabo in-line tehnik = Crystalization process development of active pharmaceutical ingredient using in-line monitoring techniques: magistrsko delo. Faculty of Chemistry and Chemical Technology, University of Ljubljana, 2016. [COBISS.SI-ID 1537123779]

Hudelja, Hermina, Diels-Alderjeve reakcije nekaterih 2H-piran-2-onov = Diels-Alder reactions of selected 2H-pyran-2-ones: diplomsko delo. Faculty of Chemistry and Chemical Technology, University of Ljubljana, 2013. [COBISS.SI-ID 36952069]

Biography

The author of this doctoral dissertation Hermina Hudelja was born on 8th of December 1990 in Novo mesto, Slovenia. After finishing Gymnasium in 2009, she was admitted to the Faculty of Chemistry and Chemical Technology, University of Ljubljana. She finished her bachelor studies in September 2013 and continued with her studies at the Faculty of Chemistry and Chemical Technology where she finished her master studies in 2016. In October 2016 she enrolled into a doctoral study program Nanosciences and Nanotechnologies at the Jožef Stefan International Postgraduate School, Ljubljana, Slovenia. The topic of her dissertation was preparation and characterization of hierarchically porous γ–Al_2O_3 materials. During her PhD she was awarded two grants for her research from JECS Trust for a two-months exchange with Luleå University of Technology and for attending the Winter Workshop 2020 organized by the American Ceramic Society in Daytona Beach, Florida. Her oral presentation at 27th International Conference on Materials and Technology (27th ICM&T) was awarded with a second place.